

REVIEW ARTICLE

Raman spectroscopy of graphene and carbon nanotubes

R. Saito^a, M. Hofmann^b, G. Dresselhaus^c, A. Jorio^d, and M.S. Dresselhaus^{b,e,*}

^aDepartment of Physics, Tohoku University, Sendai 980-8578, Japan; ^bDepartment of Electrical Engineering and Computer Science, Massachusetts Institute of Technology, Cambridge, MA 02139-4307, USA; ^cFrancis Bitter Magnet Laboratory, Massachusetts Institute of Technology, Cambridge, MA 02139-4307, USA; ^dDepartamento de Física, Universidade Federal de Minas Gerais, Belo Horizonte - MG, 30123-970, Brazil; ^eDepartment of Physics, Massachusetts Institute of Technology, Cambridge, MA 02139-4307, USA

(Received 28 June 2010; final version received 5 April 2011)

This paper reviews progress that has been made in the use of Raman spectroscopy to study graphene and carbon nanotubes. These are two nanostructured forms of sp^2 carbon materials that are of major current interest. These nanostructured materials have attracted particular attention because of their simplicity, small physical size and the exciting new science they have introduced. This review focuses on each of these materials systems individually and comparatively as prototype examples of nanostructured materials. In particular, this paper discusses the power of Raman spectroscopy as a probe and a characterization tool for sp^2 carbon materials, with particular emphasis given to the field of photophysics. Some coverage is also given to the close relatives of these sp^2 carbon materials, namely graphite, a three-dimensional (3D) material based on the AB stacking of individual graphene layers, and carbon nanoribbons, which are one-dimensional (1D) planar structures, where the width of the ribbon is on the nanometer length scale. Carbon nanoribbons differ from carbon nanotubes in that nanoribbons have edges, whereas nanotubes have terminations only at their two ends.

PACS: 78.30.-j Raman Spectroscopy; 61.48.Gh Structure of graphene; 61.48.De Structure of nanotubes; 71.38.-k Polarons and electron-phonon interactions.

Keywords: resonance Raman spectroscopy; carbon nanotubes; graphene nanoribbons; electron-phonon interaction

	Contents	PAGE
1.	Basic concepts	417
1.1.	Overview of sp^2 carbon materials	417
1.1.1.	Graphite	417
1.1.2.	Fullerenes	418
1.1.3.	Carbon nanotubes	419
1.1.4.	Graphene	420
1.1.5.	Nanoribbons	421
1.1.6.	Raman spectroscopy for sp^2 carbon materials	421
1.2.	Various photo-physical processes	423
1.2.1.	Valence-to-conduction band transitions and excitons	423
1.2.2.	Optical transitions including impurity levels	424
1.2.3.	Optical phonons	425
1.2.4.	Free carrier processes	425

*Corresponding author. Email: millie@mgm.mit.edu

1.3. Interactions for optical processes	425
1.3.1. Photon-induced electron–phonon interaction	425
1.3.2. Electron–phonon interaction in infrared absorption	426
1.3.3. Dipole–phonon interaction in non-radiative decay	426
1.3.4. Dipole–photon interaction in photoluminescence	427
1.3.5. Rayleigh scattering	427
1.3.6. Brillouin scattering	427
1.3.7. Raman scattering	427
1.3.8. First- and higher-order Raman processes	428
1.4. Characteristics of the Raman effect	428
1.4.1. Raman spectra and the Raman excitation profile	429
1.4.2. Incident and scattered resonance conditions	429
1.4.3. Stokes and anti-Stokes Raman processes	429
1.4.4. The Raman spectra and spectral width: Lorentzian lineshape	430
1.4.5. The Breit–Wigner–Fano (BWF) lineshape	431
1.4.6. The effect of defects on spectral broadening	432
1.4.7. The Raman resonance window	432
1.5. Raman measurements of low-dimensional materials	433
1.5.1. Cutting lines and van Hove singularities of the density of states	434
1.5.2. Dimensionality and the resonance Raman effect	434
1.5.3. Coherence time and length in Raman processes	435
2. Experimental progress of Raman spectroscopy and related optics	435
2.1. Electrons and phonons in graphene	436
2.1.1. The hexagonal crystal structure of graphene	436
2.1.2. The electronic structure and optical transitions	436
2.1.3. Phonons and the el–ph interaction in graphene	437
2.2. Electrons and phonons in 1D carbon nanostructures	438
2.2.1. 1D carbon structures	438
2.2.2. π bands and phonons in carbon nanotubes and nanoribbons	438
2.2.3. Optical transitions	438
2.2.4. Type I and II semiconductor nanotubes	438
2.2.5. 1D exciton, exciton–photon and exciton–phonon interactions	439
2.3. The optical measurement techniques	440
2.3.1. Light absorption	440
2.3.2. Resonance Rayleigh scattering	441
2.3.3. Photoluminescence excitation spectra	442
2.3.4. Electro-luminescence	443
2.3.5. Infrared absorption spectroscopy	444
2.3.6. Coherent phonon spectroscopy	444
2.4. Raman spectroscopy of sp^2 carbons	445
2.4.1. Historical background	445
2.4.2. Raman spectra of graphite and graphene: G - and G' -bands	446
2.4.3. First-order RBM, G^+ and G^- Raman spectra of SWNTs	446
2.4.4. The defect-induced Raman spectral features: D - and D' -bands	447
2.5. Laser Raman scattering measurements	447
2.5.1. The Raman setup	447
2.5.2. Polarized and micro Raman measurements	447
2.5.3. Confocal Raman spectroscopy and Raman imaging	448
2.5.4. Characterization of the sample edges and the imaging of defects	448
2.5.5. Resonance Raman spectroscopy	449
2.5.6. The Raman excitation profile	449

2.5.7. The Kataura plot	449
2.6. Other measurement techniques related to Raman spectroscopy	450
2.6.1. Surface-enhanced Raman spectroscopy	450
2.6.2. Surface and interference enhanced Raman spectroscopy	451
2.6.3. Near-field enhanced Raman spectroscopy	451
2.6.4. Tip enhanced Raman spectroscopy	451
2.6.5. Simultaneous atomic force microscopy, near-field Raman and PL imaging	452
2.6.6. Coherent anti-Stokes Raman spectroscopy (CARS)	452
2.7. Kohn anomaly in graphene and carbon nanotubes	453
2.7.1. Kohn-anomaly of the <i>G</i> -band of graphene	453
2.7.2. Kohn anomaly of bi-layer graphene	453
2.7.3. Kohn anomalies of SWNTs	454
2.8. Classification of Raman processes	455
2.8.1. First-order Raman process	455
2.8.2. Two-phonon second-order Raman process	455
2.8.3. One-phonon and one-elastic second-order Raman process	456
2.8.4. Double resonance Raman spectra	456
2.8.5. Dispersive behavior of the phonon energy in DR Raman processes	457
2.8.6. The inter-valley double resonance Raman scattering processes	458
2.8.7. Forward and backward scattering	458
2.8.8. DR q circles in 2D graphene	460
2.8.9. Dispersive behavior of the <i>G'</i> - and <i>G*</i> -band	461
2.8.10. Double resonance, overtone and combination modes	462
2.9. Summary	462
3. Calculation method of resonance Raman spectra	464
3.1. Overview of calculations reviewed in this section	464
3.1.1. Raman scattering and phonon energy dispersion	465
3.1.2. Electronic energy bands	465
3.1.3. The double resonance process	465
3.1.4. Electron–photon and electron–phonon interactions	465
3.1.5. Excitons	466
3.1.6. Resonance window and the Kohn Anomaly	466
3.2. Tight-binding calculation for phonons	466
3.3. Simple tight-binding calculation for the electronic structure	468
3.3.1. Extended tight-binding calculation for the graphene electronic structure	471
3.4. Calculations of matrix elements	471
3.4.1. The electron–photon matrix element	471
3.4.2. Electric dipole vector for graphene	472
3.4.3. Calculation of the electron–phonon interaction	474
3.5. Calculation of excitonic states	477
3.5.1. The Bethe–Salpeter equation for exciton states	477
3.5.2. Exciton–photon matrix element	479
3.5.3. The exciton–phonon interaction	479
3.6. The resonance Raman process	480
3.6.1. Matrix elements for the resonance Raman process	480
3.6.2. Matrix elements for double resonance Raman scattering	480
3.6.3. Resonance window width	481
3.6.4. <i>G</i> -band intensity for semiconducting SWNTs	483
3.6.5. <i>G</i> -band intensity for metallic SWNTs: The Kohn Anomaly	484
4. Raman spectra of graphene	487
4.1. The <i>G</i> -band and <i>G'</i> -band intensity ratio	488

4.2. Layer number dependence of G' -band	488
4.2.1. The number of graphene layers with AB stacking	488
4.2.2. Characterization of the graphene stacking order by the G' spectra	490
4.3. D -band and G -band intensity ratio and other disorder effects	491
4.3.1. Ar^+ ion bombardment on graphene	491
4.3.2. The D to G intensity ratio and the L_D dependence	492
4.3.3. The D to G intensity ratio: the “local activation” model	493
4.3.4. The Local Activation Model and the Raman Integrated Areas	495
4.3.5. Modeling disorder effects in the Raman linewidths and frequency shifts: the spatial correlation model for defects	497
4.3.6. Evolution of overtone and combination modes	500
4.3.7. Disorder and the number of layers	501
4.4. Edge phonon Raman spectroscopy	501
4.5. Polarization effects in graphene nanoribbons	503
5. Raman spectra of carbon nanotubes	504
5.1. The radial breathing mode and the Kataura plot	504
5.1.1. The RBM frequency	505
5.1.2. The RBM for double wall carbon nanotubes	506
5.1.3. The Raman excitation profile for the RBM	508
5.1.4. The RBM spectra of SWNT bundles	510
5.1.5. (n, m) dependence of RBM intensity – experimental analysis	511
5.1.6. The experimental Kataura plot	513
5.2. Exciton environmental effect	513
5.2.1. The effect of the dielectric constant κ on E_{ij}	514
5.2.2. Screening effect: a general κ function	515
5.2.3. Effect of the environmental dielectric constant κ_{env} on E_{ij}	518
5.3. Splitting of the G mode	518
5.3.1. The G-band eigenvectors and curvature	518
5.3.2. The six G-band phonons – confinement effect	519
5.3.3. The diameter dependence of the G band phonon frequencies	522
5.4. Kohn Anomaly effect on the G-band and the RBM mode	524
5.4.1. G-band Kohn anomaly	524
5.4.2. Chemical doping and the G band	525
5.4.3. Substrate interaction and the G band	525
5.4.4. Theoretical approach to the Kohn Anomaly	525
5.4.5. RBM band and G-band Kohn anomaly	527
5.5. Double resonance effect and quantum confinement	528
5.5.1. The G' -band in SWNT bundles	529
5.5.2. The (n, m) dependence of the G' -band; phonon trigonal warping	530
5.6. Near-field Raman spectroscopy	533
6. Challenges of Raman spectroscopy in graphene and carbon nanotubes	533
6.1. The novelties of graphene	534
6.2. The novelties of carbon nanotubes	535
6.3. Near-field Raman spectroscopy and microscopy	536
6.4. Time-dependent Raman and coherent phonon spectroscopy	536
6.5. Conclusion and messages for the future	536
Acknowledgements	537
Notes	537
References	538

This review of the Raman spectroscopy of graphene and carbon nanotubes starts with a brief presentation of background material to set the stage for a discussion of the present status of knowledge on this topic by providing a broad overview of the field in Section 1. This is followed, in Section 2, by an overview discussion of experimental progress that has been made in recent years using many experimental techniques. Advances in the theoretical understanding needed to interpret the many new results that appear daily on the photo-physics of graphene and carbon nanotubes are reviewed in Section 3. The detailed consideration of the Raman spectroscopy of graphene and carbon nanotubes is presented in Sections 4 and 5, both individually and comparatively, while Section 6 looks at future developments in this field. A textbook helpful for understanding background material relevant to this review article has recently been published [1].

Hereafter in, Section 1, we provide background to Raman spectroscopy in general, giving special attention to resonance Raman spectroscopy, with illustrations of the various photo-physical phenomena, which are given in terms of graphene and carbon nanotubes. Raman measurements in low-dimensional (one- and two-dimensional) systems are then discussed in general terms, giving specific examples of the differences and similarities between the Raman spectra for graphene and carbon nanotubes in relation to other sp^2 carbons. Finally, we discuss what can be learned from the Raman spectrum from one laser line in comparison to what can be learned from using a continuum of laser lines.

1. Basic concepts

In this section, we introduce the basic concepts of Raman spectroscopy, starting with where they stand within the broad picture of light–matter interactions and then considering their general characteristics. The concepts of first-order and higher-order scattering processes, Stokes vs. anti-Stokes processes, lineshapes, resonance and coherent processes are introduced, as well as the classical treatment of the Raman effect. Subsequently, we present a historical description of the Raman spectroscopy used to study and characterize graphitic materials, from graphite to single-walled carbon nanotubes (SWNTs) and graphene. This brief introduction to the Raman spectroscopy of sp^2 nanocarbons should be useful to general readers who may not be so familiar with Raman spectroscopy.

1.1. Overview of sp^2 carbon materials

We start this section with a brief history of several important carbon materials.

1.1.1. Graphite

Carbon materials have been the objects of study and use for many years [2]. Three-dimensional (3D) graphite is one of the longest known forms of pure carbon, naturally occurring on the surface of the earth as a mineral (as, for example, in the mineral deposits of Ticonderoga (New York) graphite, Ceylon (Sri Lanka) and the large graphite deposits in Minas Gerais, Brazil). Structurally, graphite is a layered material, with individual graphene layers, as shown in Figures 1 and 2(a). These individual graphene layers are stacked in the ABAB Bernal stacking order in the most common form of graphite, as shown in Figure 2(b) to illustrate the relative in-plane atomic arrangements of the A and B carbon atoms within the layer plane and in adjacent layers. Here, one type of carbon atom (labeled A) is aligned on top of another A atom in the direction perpendicular to the graphene layer, while the other type (the B carbon atom) is aligned in every other layer¹ [2], so that the graphene planes are arranged in the so-called ABAB Bernal stacking sequence, as shown in Figure 2(c) [6], where a carbon atom is found on adjacent layer planes over the empty center of a hexagon. This AB stacking order (Figure 2(c)) also applies to bi-layer graphene prepared by the

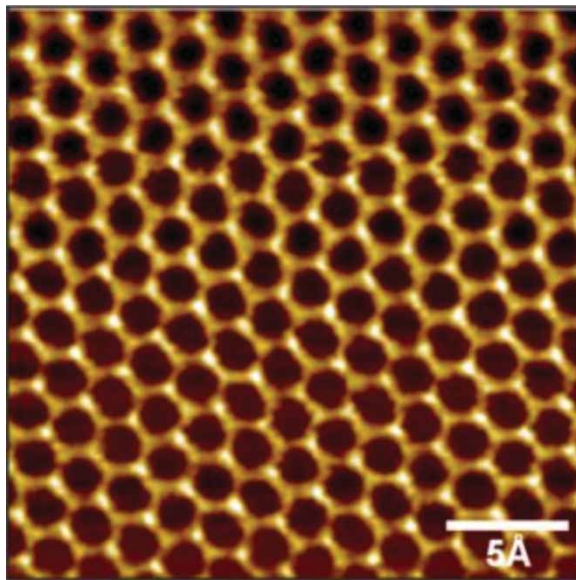


Figure 1. STM image of graphite. Notice the different brightness for the A and B atoms (see footnote 1). Reprinted from Carbon, 48(5), M.M. Lucchese *et al.* pp. 1592–1597 [3]. Copyright © (2010) Elsevier.

mechanical exfoliation method [7,8], while Figure 2(d) shows the stacking arrangement of trilayer graphene. In graphite, layers 1 and 3 are crystallographically equivalent and are translated from one another by the out-of-plane lattice parameter $c = 0.670$ nm (see Figure 2(d)), thus generating hexagonal graphite. Another related crystalline arrangement is the less common form known as rhombohedral graphite [9], which has an ABC stacking order, consisting of three layers and a lattice constant of 1.005 nm.

Of all materials, graphite has the highest melting point (4200 K), the highest thermal conductivity (3000 W/mK) and a high room-temperature electron mobility (30,000 cm²/V s) [10,11]. 3D graphite was synthesized for the first time in 1960 by Arthur Moore and co-workers [12–16] and their high-temperature, high-pressure synthesis method yielded the material commonly known as highly oriented pyrolytic graphite (HOPG). Graphite and its related carbon fibers [17–19] have been used commercially for decades [20]. Carbon fiber applications range from use as conductive fillers, and as mechanical structural reinforcements in composites (e.g., in the aerospace industry), to their use as electrode materials for making steel, exploiting their good electrical conductivity and in lithium ion battery applications exploiting their high resiliency [20,21].

1.1.2. Fullerenes

In 1985, the discovery of another unique sp² carbon system took place, the observation of the C₆₀ fullerene molecule [22]. The fullerene molecule consists of 60 carbon atoms with mostly sp² bonding and appropriate π bonding to form a closed surface with full icosahedral symmetry. Because of topological restrictions, fullerenes, in general, have 12 pentagonal rings and any numbers of hexagonal rings, thereby generating a large variety of C_n fullerene molecules. The C₆₀ molecule with full icosahedral symmetry can be regarded as the first isolated carbon nanosystem. Fullerenes stimulated and motivated a large scientific community into new research directions from the time of their discovery up to the end of the twentieth century, but fullerene-based applications

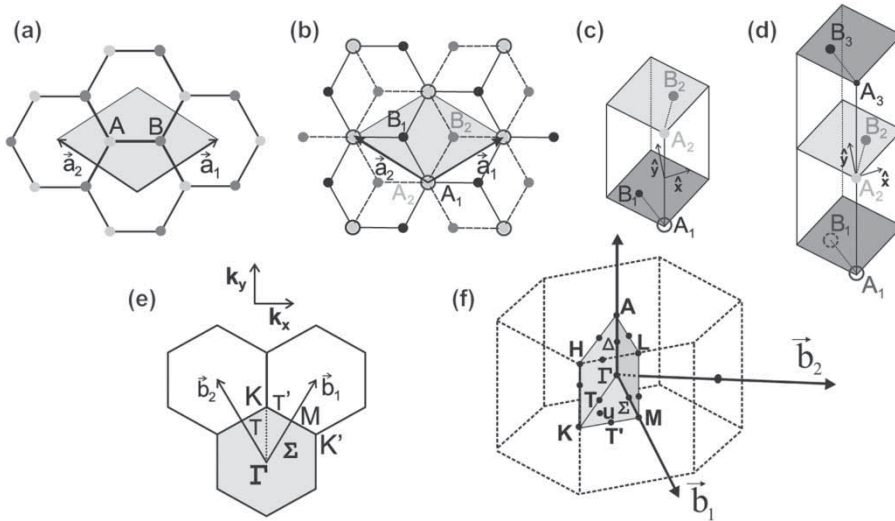


Figure 2. (a) Top view of the real space unit cell of mono-layer graphene showing the inequivalent carbon atoms A and B and the graphene unit vectors \mathbf{a}_1 and \mathbf{a}_2 . (b) Top view of the real space bi-layer graphene structure. The light/dark gray dots and black circles/black dots represent the carbon atoms in the upper and lower layers, respectively, of bi-layer graphene (2-LG). (c) The unit cell and the x and y unit vectors of bi-layer graphene and (d) the same as (c) but for trilayer graphene. (e) The reciprocal space unit cell showing the first Brillouin zone with its high symmetry points and lines, such as the line T connecting Γ to K . (f) The Brillouin zone for 3D graphite showing high symmetry points and axes. Here Δ is a high symmetry point along the axis connecting points A and Γ , and u is a general point in the $KM\Gamma$ plane. Adapted figure with permission from A. Jorio *et al.* Spectroscopy in Graphene Related System, 2010 [1] Copyright © Wiley-VCH Verlag GmbH & Co. KGaA; and with permission from L. M. Malard *et al.*, *Physical Review B* 79, p. 125426, 2009 [4]. Copyright © (2009) by the American Physical Society; and with permission from Physics Reports 473, L.M. Malard *et al.* pp. 51–87 [5]. Copyright © (2009) Elsevier.

remain sparse to date. In this review, we do not mention fullerenes much. See [23] for more information on fullerenes.

1.1.3. Carbon nanotubes

Carbon nanotubes arrived actively on the scene in 1991 following the footsteps of the emergence of the C_{60} fullerene molecule. Since their emergence, carbon nanotubes have evolved into one of the most intensively studied materials, now being held responsible for co-triggering the nanotechnology revolution. The strong entry of nanotubes on the scene in 1991 was through a report of the observation of multi-walled carbon nanotubes (MWNTs) on the cathode of a carbon arc used to produce fullerenes [24]. Actually, carbon nanotubes had been identified in the 1970s in the core structure of vapor-grown carbon fibers as very small carbon filaments [25–27] and carbon fibers were reported even earlier in the 1950s in the Russian literature [28] (see Figure 3). However, single-walled carbon nanotubes (SWNTs), the most widely studied carbon nanostructure in the 1995–2005 timeframe, were first synthesized systematically in 1993 [30,31]. Carbon nanotube research took off at this point in time. The great interest in the fundamental properties of carbon nanotubes and in their exploitation through a wide range of applications is due to their unique structural, chemical, mechanical, thermal, optical, optoelectronic and electronic properties [21,32,33]. The growth of an SWNT at a specific location and point in a given direction and the growth of a huge



Figure 3. Early transmission electron microscopy images of carbon nanotubes [29]. The early reported observations of nanotubes (a) in 1952 [28] and (b) in 1976 [25]. (c) Observation of SWNTs that launched the field in 1993 [30,31] together with an example of their observation. Adapted figure with permission from Carbon 14(2), A. Oberlin *et al.*, pp. 133–135 [25]. Copyright © (1976) Elsevier; and with permission from Carbon 44, M. Monthieux and V.L. Kuznetsov, pp. 1621–1623 [29]. Copyright © (2006) Elsevier; and with permission from Macmillan Publishes Ltd. Nature [30]. Copyright © (1993); and with permission from Macmillan Publishes Ltd. Nature [31], Copyright © (1993).

amount of millimeter-long nanotubes with nearly 100% SWNT purity (absence of other carbon forms) have now been achieved [34], and further improvements in nanotube synthesis are evolving rapidly at this time. Substantial success with the separation of nanotubes by their (n, m) structural indices, metallicity (semiconducting or metallic) and by their length has been achieved by different methods, especially by the density gradient approach of Hersam and Arnold [35]. Advances have been made with doping either n-type or p-type nanotubes for the modification of their properties, as summarized in reference [36,37]. Studies on nanotube mechanical properties [37,38], optical properties [39–45], magnetic field-dependent properties [46], optoelectronics [47,48], transport properties [49] and electrochemistry [50,51] have exploded, revealing many rich and complex fundamental excitonic and other collective phenomena [21]. Nanotube-based quantum transport phenomena, including quantum information applications, spintronics and superconducting effects, have also been explored [49]. After more than a decade and a half of intense activity in carbon nanotube research, more and more attention is now being focussed on the practical applications of the many unique and special properties of carbon nanotubes [20]. Further background information on the synthesis, structure, properties and applications of carbon nanotubes can be found in [1,21] and some of these topics are further emphasized in the present review.

1.1.4. Graphene

The interest in a single atomic layer of sp^2 carbon (called graphene; see Figure 1) goes back to the pioneering theoretical work of Wallace in 1947 [52] which was for many years used as a model system for all sp^2 carbons. This very early work provides a framework for comparing the structures of graphite, fullerenes, carbon nanotubes and other sp^2 nanocarbons. The synthesis of single-layer graphene was actually reported by Boehm in 1962 [53], but this early discovery was neither confirmed nor followed up for many years.

More recently, mono-layer graphene was synthesized from nano-diamonds in 2001 [54] and from SiC [55]. The material synthesized from nano-diamonds is generally a few-layer graphene material but thin ribbon specimens of mono-layer thickness are also contained in such samples. In the studies on these nanoribbons, emphasis was given to the properties of edges of the nanoribbons and especially to the magnetic properties of these edges [54,56–59]. The graphene prepared from heating SiC to 1300 °C emphasized the 2D electron gas properties of this graphene in an electric field, but did not especially focus on the number of layers [55].

The widespread study of graphene was launched by the preparation of mono-layer graphene by Novoselov *et al.* [7], using a simple Scotch tape method to prepare and transfer mono-layer graphene from the *c*-face of graphite to a suitable substrate such as SiO₂ for the measurement of the electrical and optical properties of mono-layer graphene [60]. The Novoselov and Geim studies of transport in few-layer graphene in 2004 [7] led to a renewed interest in mono-layer and

few-layer graphene and to an in-depth study of the unique properties of this material in the mono-layer and bi-layer limit. Surprisingly, this very basic system, which had been conceptually utilized by researchers over a period of many decades, suddenly appeared on the experimental scene, demonstrating many novel physical properties that were not even imagined previously [60,61]. The discovery of these novel properties launched a rush into the study of graphene science in the first decade of the twenty-first century, and culminating in the 2010 Nobel Prize in physics [62].

Besides the outstanding mechanical properties [63] (breaking strength ~ 40 N/m, Young's modulus ~ 1.0 TPa) and thermal properties [64,65] (room temperature thermal conductivity ~ 3000 W m⁻¹ K⁻¹ [65]), the scientific interest in graphene was stimulated [66,67] by the widespread report of the relativistic (massless) electronic properties of the conduction electrons (and holes) in a single layer less than 1 nm thick, with a state-of-the-art mobility reaching $\mu = 200,000$ cm²/V s at room temperature for freely suspended graphene [66–71]. Other unusual properties have been predicted and demonstrated experimentally, such as the minimum conductivity and the half-integer quantum Hall effect in mono-layer graphene [72] and the integer quantum Hall effect in bi-layer graphene [73], ambipolar transport by either electrons or holes by the variation of a gate potential, operation as a transparent conductor [47,74], Klein tunneling [75–82], negative refractive index and Veselago lensing [80], anomalous Andreev reflections at metal–superconductor junctions [76,81–84], anisotropies under antidot lattices [85] or periodic potentials [86], and a metal–insulator transition via hydrogenation of graphene [87]. Applications such as fillers for composite materials, as super-capacitors, batteries, interconnects and field emitters are being developed, although it is still too early to say to what extent graphene will be able to compete with carbon nanotubes and other established materials systems in the applications world [88]. Although nanotubes and graphene are both carbon-based nanostructures, they have different properties related to the planar aspects of graphene and the tubular aspects of nanotubes, and this basic difference should distinguish their optimal usage in applications.

1.1.5. Nanoribbons

Graphene nanoribbons are of particular interest for introducing a bandgap into graphene-related systems. Bandgaps are needed for many electronics applications of nanomaterials. Since graphene can be patterned using, for example, high-resolution lithography [55,89], nanocircuits with graphene–nanoribbon interconnects can be fabricated. Many groups are now fabricating devices using graphene and also graphene nanoribbons, which have a long length and a small nanoscale width, and where the ribbon edges play an important role in both determining their electronic structure and exhibiting unusual spin polarization properties [56]. Nanoribbons of small widths exhibit 1D behavior analogous to carbon nanotubes, but have a high density of electronic states at the Fermi level for the case of well-defined zigzag edges. This high density of electronic states allows us to experimentally distinguish zigzag nanoribbons from armchair and chiral nanoribbons which do not exhibit this property. While lithographic techniques have limited resolution for the fabrication of small width nanoribbons (<20 nm wide), chemical [90] and synthetic [91] methods have been employed successfully, including the unzipping of SWNTs as a route to produce carbon nanoribbons [92,93]. Carbon nanoribbons have been shown to be especially sensitive for the study of edge structures and edge properties and edge reconstruction effects [94].

1.1.6. Raman spectroscopy for sp^2 carbon materials

Raman spectroscopy is the inelastic scattering of light, usually associated with the emission (Stokes process) or absorption (anti-Stokes process) of phonons [95]. By knowing the energy shift of the scattered light relative to the incident light, which yields Raman spectra in cm⁻¹ (see Figure 4),

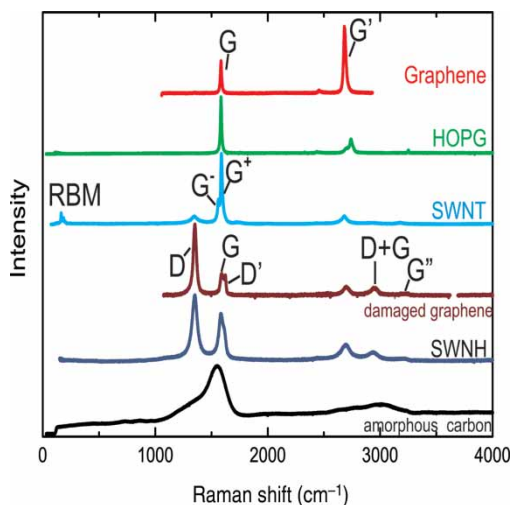


Figure 4. Raman spectra from several sp^2 nanocarbon and bulk carbon materials. From top to bottom: crystalline mono-layer graphene, HOPG, an SWNT bundle sample, damaged graphene, single-wall carbon nanohorns (SWNH). The most intense Raman peaks are labeled in a few of the spectra [1,96]. Note that some authors call the G' by $2D$ and the G'' by $2D'$ [97]. Reprinted with permission from M.S. Dresselhaus *et al.*, Nano Letters 10, pp. 953–973, 2010 [96]. Copyright © (2010) American Chemical Society.

we can obtain the phonon frequency which is useful for identifying the origin of an unknown structure of a newly discovered molecule or of a new material in chemistry [98]. Among all possible phonon modes for sp^2 carbons, only a limited number of phonons are Raman-active modes (namely those with A , E_1 and E_2 symmetry for carbon nanotubes, and E_{2g} for graphite) [99–101]. A common metric used to characterize the defect density in a material is the ratio of the intensities of the disorder-induced D-band to the symmetry-allowed G-band ratio (I_D/I_G) [102]. Study of the D- and G-band modes by Raman spectroscopy (see Figure 4) yields information about the crystal structure of the material and about many of its interesting physical properties.

Raman spectroscopy for the various sp^2 carbon materials (see Figure 4) has been mainly used for sample characterization and these different carbon materials exhibit characteristic differences related to the small differences in their structures. The fundamental sp^2 carbon material is mono-layer graphene which has the simplest and most fundamental spectrum showing the two Raman-allowed features that appear in all sp^2 carbon materials – the first-order G-band and the second-order symmetry-allowed G' -band,² where the symbol G is used to denote “graphitic.” The next most commonly observed feature is the D-band that is a defect-activated Raman mode. The D-band occurs at about 1350 cm^{-1} at 2.41 eV laser excitation energy (E_{laser}) and is highly dispersive as a function of E_{laser} (see Section 2.8.9). Since the graphite melting temperature is very high (over 4200 K) and since no actual carbon materials are defect-free, the D/G-band intensity ratio (I_D/I_G) provides a sensitive metric for the degree of disorder in sp^2 carbon materials over a wide temperature range. In the case of fullerenes, a special Raman-active phonon mode related to the vibrations of a pentagonal ring (1469 cm^{-1}) is particularly sensitive for understanding the molecular structure [23]. In the case of carbon nanotubes, it is common to survey unknown samples using Raman spectroscopy to check for the presence of nanotubes in the sample by observing the cylindrical-specific, Raman-active-mode radial breathing mode (RBM) in which atoms around the circumference of a single wall carbon nanotube (SWNT) are vibrating in a breathing mode in the radial direction (see Figure 4) [32,100,103–110]. This vibrational mode is unique to carbon nanotubes and serves to sensitively identify their presence in a given sample. Since the RBM frequency

ω_{RBM} is inversely proportional to the nanotube diameter d_t , we can thus estimate the diameter distribution of the nanotubes that are contained in a given sample [111]. When we observe an isolated nanotube, we can use its Raman spectrum to obtain its detailed structure, which involves identification of the spatial orientation, the diameter and the chiral angle of the nanotube, as well as the nanotube (n, m) chirality assignment. This (n, m) assignment is based on the concept of the resonance Raman effect (see Section 1.5.2). In the case of graphene [112–114], the intensity ratio ($I_{G'}/I_G$) and the lineshape of the G'-band (along with other indicators) can be used for identifying the number of graphene layers (see Section 4.2.1). For graphene ribbons, we can use Raman spectroscopy to study the edge structure of the ribbons [94,115] to yield information about the structure and properties of graphene ribbons (see Section 4.4). For all these reasons, Raman spectroscopy is very sensitive for the characterization of sp^2 carbons.

Since most carbon materials are not soluble in water, Raman spectroscopy is useful as an *in situ*, non-contact, non-destructive measurement tool that can be used at room temperature and under ambient operating conditions, as well as for freely suspended carbon nanotubes and graphene samples. Combining the continuing advances in optical techniques with new theoretical developments that are rapidly developing, Raman spectroscopy studies of graphene and carbon nanotubes have provided a great deal of information about their solid-state properties, which are the main subjects of this review, including their behavior as a function of temperature, pressure and Fermi energy [1].

1.2. Various photo-physical processes

In this section, various optical processes that are useful for the characterization of nanostructures are very briefly discussed. The Raman effect [116,117] is briefly mentioned in this section, but is further discussed in Sections 1.4–1.5.

When focusing light into a material (molecule or solid), part of the energy just passes through the sample (by transmission), while the remaining photons interact with the system through light absorption, reflection, light emission or light scattering. The amount of light that will be transmitted, as well as the details for all the light–matter interactions, are determined by the electronic and vibrational properties of the material. Furthermore, different phenomena occur when focusing light with different energy photons into a given material [95,118], because different photon energies will be related to the different optical transitions occurring in the medium. As an example of the richness of light–matter interactions, an overview of various optical absorption mechanisms for a semiconducting material is shown in Figure 5. Using this figure as a guide, examples are given for the many different effects that might occur when light interacts with a material. Starting from the high-energy side of the diagram moving to mechanisms important at lower energies, Figure 5 shows the absorption coefficient as a function of the energy of the photon which yields the absorption spectra and enumerates the dominant photo-physical processes that are involved in the various photon energy regimes in Figure 5 [95].

1.2.1. Valence-to-conduction band transitions and excitons

A photon (having an energy in the 1–5 eV range) can be absorbed by an electron making a transition from the valence band to the conduction band, as shown in Figure 5. Such a transition generates a free electron in the conduction band, leaving behind a “hole” in the valence band, where we use the nomenclature for electrons and holes as used in semiconductor physics [119].

Photons with an energy smaller than the energy gap can generate a transition to an exciton level, thereby creating an exciton which corresponds to an electron bound to a hole through the Coulomb interaction. Although excitonic levels in model semiconducting systems such as GaAs

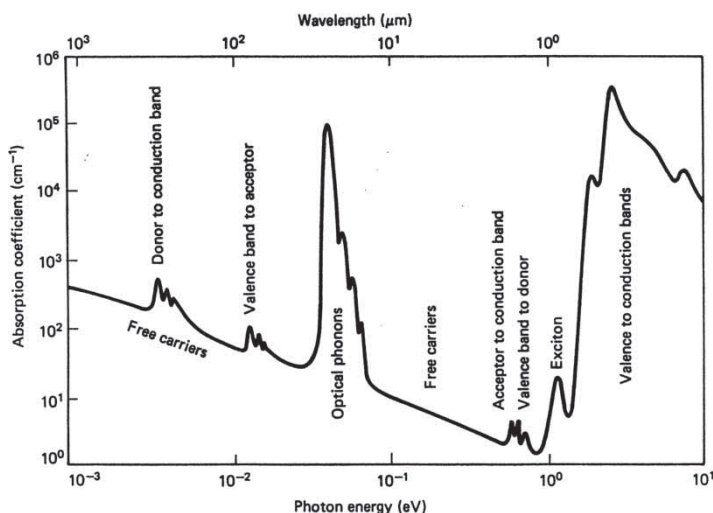


Figure 5. Photo-physical mechanisms operative for various regions of the electromagnetic spectrum as photons in various energy ranges interact with materials. Reprinted figure with permission from A. Jorio *et al.* Spectroscopy in Graphene Related Systems, 2010 [1]. Copyright © Wiley-VCH Verlag GmbH & Co. KGaA.

have excitonic levels of a few meV below the bandgap, the excitonic levels in carbon nanotubes are much larger (on the order of a few hundred meV), emphasizing the greater importance of excitonic effects in low-dimensional nanosystems. Optical absorption in the case of carbon nanotubes was predicted by Ando to be excitonic as far back as 1997 [120] and the importance of excitons in nanotubes was demonstrated experimentally by the two photon experiments carried out by the Heinz group in 2005 [121] and a similar result was independently obtained by the Berlin group [122]. These experiments confirm theoretical concepts that excitonic effects would be enhanced in low-dimensional systems. Although excitonic effects were found to be much larger in semiconducting nanotubes than in metallic nanotubes, excitons nevertheless have been found in these works to also dominate optical absorption processes in metallic nanotubes.

1.2.2. Optical transitions including impurity levels

Impurities can form states within the bandgap of semiconducting materials. If the impurity atom has more valence electrons than the atom it replaces, then this impurity will act as an electron donor making the nanotube an n-type semiconductor. However, if the impurity atom has fewer electrons, then it will behave like an electron acceptor giving rise to a p-type semiconductor. Light can be absorbed, generating electronic transitions from the valence band to such donor impurity levels, or optical transitions can be made by taking electrons from an acceptor level to the conduction band of a semiconductor. For semiconducting carbon nanotubes, typical photon energies for these impurity levels are in the 10–100 meV range about a band edge, but they usually occur over an energy range smaller than the energy gap.

Optical transitions to conduction band impurity levels or from valence band shallow acceptor levels can also be responsible for light absorption. The corresponding photon energy would be significantly lower than the stronger excitations from the dominant bright allowed state. In materials, such as carbon nanotubes, the lowest energy transitions however involve dark exciton states, thereby lowering the intensity of these transitions.

1.2.3. *Optical phonons*

Optical absorption by phonons typically occurs when the incident photon energy coincides with the energy of optical phonons, corresponding, in general, to 50 meV to 0.2 eV for first-order processes. These absorption processes generally occur in the infrared energy range and play a major role in the field of infrared spectroscopy for both molecules and solid-state systems.

In sp^2 carbon systems, the harmonics and combination modes of symmetry-allowed optical phonons are clearly observed in the Raman spectra through double resonance (DR) processes. Thus phonon-related effects can be observed over a photon energy range up to ~ 350 meV for the observation of phonon-related effects. It is noted that Raman processes and infrared absorption processes generally occur at different photon energies because, in general, different phonons are Raman- and infrared-active for high symmetry materials such as sp^2 carbons.

1.2.4. *Free carrier processes*

Free carriers provide another mechanism for optical absorption. Free carriers are dominant in metallic systems and are present in doped semiconducting systems through electrons and/or holes. These carriers can also absorb light, usually occurring over a broad energy range from 1 to 10 meV. Other free carrier processes not shown explicitly in Figure 5 also occur. In a higher energy region (1–10 eV), collective excitations of electrons also occur, giving rise to plasmon absorption. At much higher energies in the ultraviolet and X-ray range, transitions from core levels also take place, generating photo-excited electrons, which can be observed by ultraviolet photo-electron spectroscopy (UPS) and X-ray photo-electron spectroscopy (XPS), depending on the energy of these deeper levels. By measuring the momentum and energy of photo-electrons for a given momentum and energy, information can be obtained about the momentum and energy of the incident electron in the valence energy band, by the angle-resolved photo-emission spectroscopy (ARPES) technique, which has been widely used for observing electron energy dispersion in single layer and multi-layer graphene [123–126].

1.3. *Interactions for optical processes*

In this section, we focus on the different phenomena occurring through light–matter interactions [95] (see Figure 6). The potential energy profile of an atom is modified by the electric field of the incident photon, so that the energy and momentum of the incident light are changed in a scattering process and a resulting photoluminescence or fluorescence process that frequently occurs after absorption by an atom gives important information about this interaction. However, typical times for the occurrence of such photoluminescence or fluorescence processes are much longer (in ns or ms, respectively) than for typical light scattering events (in ps). We now briefly review the various light–matter interactions.

1.3.1. *Photon-induced electron–phonon interaction*

Two kinds of light scattering processes are the elastic and inelastic scattering processes, which are called the Rayleigh and the Raman scattering, respectively. In the case of Rayleigh scattering, only the direction of the light is changed with no change in photon energy, while in the case of Raman scattering, either phonon creation or annihilation occurs in the scattering process. When the electric field associated with the photon interacts with an atom, the electron and the ion core move in opposite directions to each other to form a dipole and this oscillating dipole interacts with the incident photon to generate the scattered light. The coupling of the dipole with the electric field of the photon creates a phonon which is described by an electron phonon

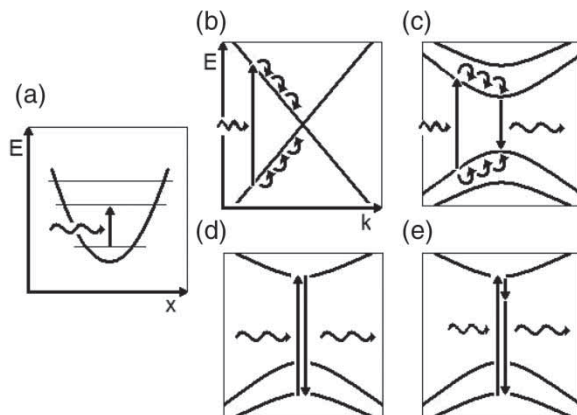


Figure 6. The light–matter interaction, showing the most commonly occurring processes. The waved arrows indicate incident and scattered photons. The vertical arrows denote photon-induced transitions between (a) vibrational levels and (b–e) electronic states. Curved arrow segments indicate electron–phonon (el–ph) (hole–phonon) scattering events. In (e), the shortest vertical arrow also indicates an el–ph transition in Raman scattering. In (d, e), the processes are resonant if the incident (or scattered) photon energy exactly matches the energy difference between initial and excited electronic states. When far from the resonance window where resonance occurs, the optical transition is called a virtual transition. The intensity for resonance Raman scattering can be much larger for vertical processes that are resonant than those that are not resonant [1,95]. Reprinted figure with permission from A. Jorio *et al.* Spectroscopy in Graphene Related Systems, 2010 [1]. Copyright © Wiley-VCH Verlag GmbH & Co. KGaA.

(el–ph) interaction that occurs in the Raman scattering process. In this process the electron is excited to a virtual state, for which the stable geometry of the chemical bond is no longer identical to that of the ground state. This perturbation generates a force resulting in atomic motion, thereby providing a quantum explanation for the el–ph interaction. If the incident photons are introduced through a sufficiently short light pulse with a duration comparable to the frequency of the phonon, then all atoms start to move at the same time as a result of the el–ph interaction, thereby creating a coherent motion of the atoms which can be detected by a second pulse of light at a frequency at which the material is transparent. This sensitive technique is known as coherent phonon spectroscopy.

1.3.2. Electron–phonon interaction in infrared absorption

When the photon energy matches the energy for allowed phonon creation, the photon can transfer energy directly to create an acoustic or optical phonon (see Figure 6(a)). This resonance process is called infrared (IR) absorption, since the phonons that are created have energies corresponding to IR photon frequencies. IR-active phonon modes are phonon modes that have the symmetry of a vector [1], which describes the vibration of an oscillating dipole moment of the ions in the material. The dipole moment is directly coupled to the electric field associated with the incident and scattered photons. We describe this interaction by an electromagnetic interaction perturbation Hamiltonian between the vibrating atoms and the photons that induce the vibration. Since all the atoms in nanocarbon materials are neutral carbon atoms, the dipole moment for IR absorption is generated by photo-excited electrons created by the optical electric field.

1.3.3. Dipole–phonon interaction in non-radiative decay

For higher photon energies, the photons are absorbed by exciting an electron–hole (e–h) pair, as shown in Figure 6(b). The photo-excited electron (or hole) then loses energy to electrons in the

bottom (top) of the conduction (valence) energy band by creating multiple phonons of different frequencies through el-ph coupling, in which the phonons are selected such that the initial and final electronic states satisfy both energy and momentum conservation requirements. In the case of a metal, such photo-excited electrons (together with their holes) will decay down (up) to the ground states without emitting a photon, and such processes are called non-radiative decay process as shown in Figure 6(b). In graphene or metallic carbon nanotubes, non-radiative decay that generates heat frequently occurs and can have a special character because of their linear $E(k)$ dispersion relation.

1.3.4. Dipole-photon interaction in photoluminescence

If the material has an energy gap between the occupied (valence) and unoccupied (conduction) bands, the photo-excited electron quickly (on a ps timescale) decays to the bottom of the conduction band by an el-ph process and then to its ground state by emitting a photon with the bandgap energy on a ns timescale, in a light emission process (see Figure 6(c)). This emission process is called photoluminescence, and the energy decrease from the incident photon to the scattered photon is generally called a Stokes process because of the decreased energy of the emitted photon.³ In order to get photoluminescence emission, an interaction between the dipole moment of the atom with the electric field of the photon is essential in which the dipole-selection rule must be satisfied for the electronic excited states. When the energy gap is smaller than the optical phonon energy, no photoluminescence occurs, but phonon emission can occur by an inter-band el-ph interaction. In this case, the quantum efficiency for photon generation by the photo-excited electrons is suppressed significantly.

1.3.5. Rayleigh scattering

In the Rayleigh scattering process, a photon is virtually⁴ absorbed by a material and the oscillating electric field of the photon just shakes the electrons. In this case, the electrons just scatter that energy back to another photon having the same energy as the incident photon. When the incident and scattered photons have the same energy, the scattering process is said to be “elastic” and is named Rayleigh scattering (see Figure 6(d)). Elastic scattering occurs by an interaction of the electric field of the photons with the crystal or atomic potential and it can occur even for the case of real absorption, in which the Rayleigh scattering intensity is enhanced significantly, and such a process is called the resonance Rayleigh scattering [44].

1.3.6. Brillouin scattering

In solid materials, a further distinction is made between the inelastic scattering by acoustic phonons (called Brillouin scattering) and by optical phonons (called Raman scattering). Brillouin scattering occurs by an el-ph interaction with acoustic phonons or with any other low-energy excitation such as a magnon. The concept of Brillouin scattering does not apply to molecular systems for which the acoustic phonon would represent a translation of the molecule. Since Brillouin scattering generally appears in a lower energy region than that for an optical phonon, a special experimental set-up based on low-frequency instrumentation is required for observing Brillouin scattering, namely a set-up that very strongly suppresses the presence of the Rayleigh signal. When the Brillouin scattering is stimulated by the electric field of the laser light itself, a strong Brillouin signal is obtained which is known as stimulated Brillouin scattering.

1.3.7. Raman scattering

The inelastic scattering of light is called the Raman effect, named in honor of the discoverer of the Raman effect in 1927, commonly attributed to Sir Chandrasekhara Venkata Raman (1888–1970),

an Indian scientist who was awarded the Nobel Prize in Physics in 1930 for his work on “the scattering of light and for the discovery of the effect named after him”. In the Raman process, an incident photon with energy $E_i = E_{\text{laser}}$ and momentum $k_i = k_{\text{laser}}$ reaches the sample and is scattered, resulting in a photon with a different energy E_s and a different momentum k_s . For energy and momentum conservation,

$$E_s = E_i \pm E_q \quad \text{and} \quad k_s = k_i \pm q, \quad (1)$$

where E_q and q are the energy and momentum change during the scattering event induced by electromagnetic excitation of the medium. The quantities E_q and q can be considered to be the energy and the momentum of the phonon.

The Raman process which emits (absorbs) a phonon is called a first-order Raman process. In order to recombine an electron at k_s with a hole at k_i , the wavevector q should be almost zero. Thus, only phonons near the Γ point (zone-centered phonon) in the phonon dispersion relation can be Raman-active modes. However, when we consider second-order Raman processes in which two scattering events are involved, the restriction for $q = 0$ is relaxed. Further, the photo-excited electrons in sp^2 carbons are located in k space near the hexagonal corners of the 2D Brillouin zone (BZ), named the K and K' points, where the states of lowest energy are located. Here, there are two possibilities for $q \neq 0$ scattering: intra-valley ($K \rightarrow K, K' \rightarrow K'$) and inter-valley scattering ($K \rightarrow K', K' \rightarrow K$). We will show (see Section 2.8.4) that a double resonance Raman process involving excitations near the K and K' points in the 2D BZ yields a large Raman signal.

1.3.8. First- and higher-order Raman processes

The order of the Raman process is given by the number of scattering events that are involved in the Raman process. The most usual case is the first-order Stokes Raman scattering process, where the photon energy excitation creates one phonon in the crystal with a very small momentum ($q \approx 0$). If two, three or more scattering events occur in the Raman process, then the process is called second-, third-, or higher-order, respectively. The first-order Raman process gives the basic quantum of vibration, while higher-order processes give very interesting information about overtones and combination modes. In the case of overtones, the Raman signal appears at nE_q ($n = 2, 3, \dots$) and the Raman signal from combination modes appears at the sum of the different phonon energies ($E_{q1} + E_{q2}$, etc). An interesting point in the higher-order Raman signal in a solid material is that the restriction for $q \approx 0$ in a first-order Raman scattering process is relaxed. The photo-excited electron at k can be scattered to $k + q$ and can go back to its original position at k after the second scattering event by scattering a phonon with wavevector $-q$, which allows the recombination of the photo-excited electrons with their corresponding holes. The probability for selecting a pair of q and $-q$ phonons is usually small and not very important for solids. However, we see in Section 2.8.4–2.8.10 that, under special resonance conditions (the DR condition) commonly occurring in sp^2 nanocarbons, we can expect a clear Raman signal from $q \neq 0$ scattering events.

1.4. Characteristics of the Raman effect

Next, we very briefly define in this section a number of the important characteristics of the Raman effect that will be commonly used throughout this article. We first discuss the Raman spectra giving special emphasis to low-dimensional systems, thereby introducing the concept of the Raman excitation profile which relates the laser frequencies over which resonant processes take place (Section 1.4.1 and 1.4.2). This leads to a discussion of Stokes and anti-Stokes spectra and the difference between the two (Section 1.4.3), followed by a discussion of the spectral width of particular phonon features in the Raman spectra (Section 1.4.4–1.4.6). Finally, we discuss

in Section 1.4.7, the characteristics of the Raman excitation profile, particularly the resonance window width.

1.4.1. Raman spectra and the Raman excitation profile

When we use one laser energy and observe the intensity of the scattered photons as a function of the shift of energy in cm^{-1} from the incident light (the Raman shift), this plot is called a Raman spectrum, from which we determine the phonon energy and its spectral width. The Raman spectrum is observed by passing the scattered light through a monochromator which divides the light entering the instrument into the scattered light on the lower energy side relative to the incident light (the so-called Stokes Raman spectra) and the scattered light on the higher energy side (the so-called anti-Stokes Raman spectra). At the zero energy shift, we generally see a strong Rayleigh signal which can be eliminated by using a so-called notch filter⁵ or a (triple) monochromator.⁶

When we have an experimental laser system where the photon energy can be tuned (or changed), the Raman intensity for a low-dimensional sp^2 carbon system such as carbon nanotubes will show a sharp maximum at the resonance energy where the laser energy matches that of the excited states of the nanotubes. This resonant enhancement of the Raman intensities is called the resonance Raman effect. We denote the measurement of the Raman spectral intensity as a function of the laser energy as the Raman resonance window or the Raman excitation profile. The *resonance window* thus defined is normally expressed as the energy width at full-width at half-maximum (FWHM) intensity of the Raman intensity in the Raman excitation profile (which is a plot of the Raman intensity vs. E_{laser} in units of eV).

1.4.2. Incident and scattered resonance conditions

In the resonance excitation profile for an individual carbon nanotube, sharp maxima in the intensity are observed when the laser energy E_{laser} matches an optical transition energy E_{ii} . For a Raman-active phonon with an energy E_q , we expect two resonance conditions: $E_{\text{laser}} = E_{\text{ii}}$ and $E_{\text{laser}} = E_{\text{ii}} + E_q$ (for Stokes), which we call the incident and scattered resonance conditions, respectively. In the incident resonance condition, the initial photon absorption becomes a “real” absorption process, while in the scattered resonance condition, the final photon emission becomes a “real” emission process. For all Raman-active phonons, the resonance energy for the incident resonance is commonly E_{ii} , while the resonance energies for the scattered phonons depend on E_q . When the resonance window width in the Raman excitation profile is larger than E_q , we can see only one resonance peak. In the case of carbon nano-materials, a typical resonance window width is 50 meV and thus we can see two distinct peaks for optical phonons (0.2 eV), but not for RBM phonons (10–20 meV) in the case of SWNTs. It is important to note that the scattered resonance condition for the anti-Stokes Raman process is given by $E_{\text{laser}} = E_{\text{ii}} - E_q$.

1.4.3. Stokes and anti-Stokes Raman processes

The Stokes (S) and anti-Stokes (aS) processes for phonon scattering exhibit different Raman intensity behaviors from each other because the phonon number in the Stokes process is increased from n to $n + 1$ and this phonon creation process can always be carried out. However in the anti-Stokes process, a phonon is annihilated so that for the process to progress, phonons must be present to be annihilated and this may not be possible if the phonon energy is large compared to $k_{\text{B}}T$ where k_{B} is the Boltzmann constant. The average number of available phonons n at a

temperature T with energy E_q is given by the Bose–Einstein distribution function

$$n = \frac{1}{e^{E_q/k_B T} - 1}. \quad (2)$$

Of particular significance, room temperature (300 K) corresponds to $25.85 \text{ meV} = 208.5 \text{ cm}^{-1}$. For carbon nanotubes the energies of the RBM phonons are comparable in energy to room temperature while the G-band and the D-band phonons are of much higher energies than the room temperature energy. Of particular significance is the relative magnitude of E_q relative to $k_B T$. Most Raman spectra are conveniently taken at room temperature (300 K),

As stated above, the probability for the S and aS processes differs because in the Stokes process the system goes from n phonons to $n + 1$, while in the anti-Stokes process (aS) the system goes from $n + 1$ to n . Using time reversal symmetry, the matrix elements for the transition $n \rightarrow n + 1$ (S) and $n + 1 \rightarrow n$ (aS) are the same, and the intensity ratio between the S and aS signals I_S/I_{aS} from one given phonon can be obtained by

$$\frac{I_S}{I_{aS}} \propto \frac{n + 1}{n} = e^{E_q/k_B T}. \quad (3)$$

When we use Equation (3) for evaluating E_q or T , we must be careful not to be close to the resonance conditions for either the S or aS process. If E_{laser} corresponds to the resonance condition for $E_{\text{laser}} = E_{ii}$ for the incident photon, then all phonons will be in resonance in the Raman scattering process. But for $E_{\text{laser}} = E_{ii} \pm E_q = E_S$ only the scattered light is in resonance and although each phonon will be in resonance in the Raman spectrum of the nanotube, each phonon will be in resonance at a different E_S value.

1.4.4. The Raman spectra and spectral width: Lorentzian lineshape

A Raman spectrum is a plot of the scattered intensity I_S as a function of $E_{\text{laser}} - E_S$ (Raman shift, see Figure 7), and the energy conservation relation given by Equation (1) is a very important aspect of Raman spectroscopy. The Raman spectra will show peaks at a phonon energy $\pm E_q$, and in Figure 7 the energy of the Stokes process is shown at positive energy, while the anti-Stokes process is shown at negative energy in Figure 7. Thus, in the spectrometer (grating) which divides the scattered light into different directions, the anti-Stokes signal appears in the opposite position relative to the Stokes signal when measured from the central Rayleigh signal.

The Raman lineshape contains a wealth of information about the electrons and phonons for the various sp^2 nanocarbon systems. The Raman spectrum for semiconducting tubes exhibits a peak intensity $I(\omega)$ at a phonon energy of E_q displaced from E_{laser} . An expression for the frequency dependence of the phonon excitation can be obtained using a model based on a harmonic oscillator damped by some other interactions (similar to a mass-spring system inside a liquid). Therefore, the shape of the Raman peak will be the response of a damped harmonic oscillator with an eigenfrequency ω_q that is forced by an external field oscillating with a frequency ω . Considering the damping frequency to be given by Γ_q , the intensity $I(\omega)$ of a forced damped harmonic oscillator model of the phonon excitation is a Lorentzian curve

$$I(\omega) = \frac{I_0}{\pi \Gamma_q} \frac{1}{(\omega - \omega_q)^2 + \Gamma_q^2} \quad (4)$$

in the limit where the frequency $\omega_q \gg \Gamma_q$, where Γ_q is the damping term.⁷

The full width at half maximum intensity (*Raman spectral width*) is given by $\text{FWHM} = 2\Gamma_q$. The center of the Lorentzian lineshape gives the natural phonon frequency ω_q , and Γ_q is related to

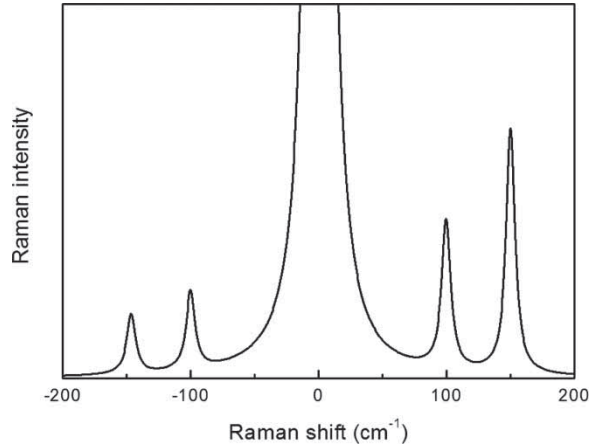


Figure 7. Schematics showing the Rayleigh line (at 0 cm^{-1}) and the Raman spectrum. The Rayleigh intensity is always much stronger and it has to be filtered out for any meaningful Raman experiment. The Stokes process (positive frequency peaks) are usually stronger than the anti-Stokes process (negative frequency peaks) due to phonon creation/annihilation statistics. Reprinted from Carbon, 48(5), M.M. Lucchese *et al.* pp. 1592–1597 [3]. Copyright © (2010) Elsevier.

the damping or the energy uncertainty or the phonon lifetime. The damping of the amplitude (as characterized by Γ_q) is observed as E_{laser} is tuned (and thus as the scattered light energy is varied). The damping of $I(\omega)$ thus provides information on the phonon lifetime, Δt . The uncertainty principle $\Delta E \Delta t \sim \hbar$ gives an uncertainty in the value of the phonon energy, as measured in the Raman spectrum, which corresponds to the spectral FWHM of $2\Gamma_q$. Therefore, Γ_q is the inverse of the lifetime for a phonon, and Raman spectra in this way provide information on phonon lifetimes.

There are two origins for the finite phonon lifetime: the anharmonic potential and the el-ph interaction, each of which are discussed below. This is followed by a further discussion of the lineshapes $I(\omega)$ observed for phonons.

(i) *Anharmonic potential*

Anharmonicity of the inter-atomic potential for the phonon occurs for large \mathbf{r} far from the potential minimum. In this regime, the wave vector q of the phonon is no longer a good quantum number and phonon scattering occurs by emitting a phonon (third-order process) or by phonon-phonon scattering (fourth-order anharmonicity). Anharmonicity gives the main contribution to the thermal expansion process (third-order process) and to the thermal conductivity (fourth-order process).

(ii) *Electron-phonon interaction*

Another possible interaction is the el-ph interaction in which a phonon excites an electron in the valence band to the conduction band or scatters a photo-excited electron to other unoccupied states. The former el-ph process works for electrons in the valence band, while the latter el-ph process works for electrons in excited states. Thus, the origins of the finite lifetime of the phonon are different from each other for the case of electron and hole excitation, and is one mechanism for breaking the symmetry between electrons and holes in graphene.

1.4.5. The Breit-Wigner-Fano (BWF) lineshape

In specific cases, the Raman spectra can deviate from the simple Lorentzian lineshape in Equation (4). One obvious case is when the feature is actually composed of more than one phonon

contribution. Then the Raman peak will be a convolution of several Lorentzian peaks, depending on the frequency and weight of each phonon contribution.

One case of importance occurs when the lattice vibration couples to free electrons, as occurs in graphene or metallic nanotubes when an el-ph interaction takes place. In this case, additional line broadening and even distorted (asymmetric) lineshapes can result, and this effect is known as the Kohn anomaly (KA) [127]. In cases where phonons are coupled to the continuum excitation spectra of free electrons, the Raman peak may exhibit a so-called Breit–Wigner–Fano (BWF) lineshape, given by [128,129]

$$I_{\text{BWF}}(\omega) = I_0 \frac{[1 + (\omega - \omega_{\text{BWF}}/q_{\text{BWF}}\Gamma_{\text{BWF}})]^2}{1 + [(\omega - \omega_{\text{BWF}}/\Gamma_{\text{BWF}})]^2}, \quad (5)$$

where $1/q_{\text{BWF}}$ is a measure of the interaction of a discrete level (the phonon) with a continuum of states (the electrons). Here ω_{BWF} is the BWF peak frequency at the maximum intensity I_0 , and Γ_{BWF} is the frequency half width-half maximum for the intensity profile of the BWF peak. Such effects are observed in certain metallic sp^2 carbon materials and are discussed later, in connection with metallic carbon nanotubes.

1.4.6. The effect of defects on spectral broadening

In a perfect system, the one-phonon Raman intensity $I_0(\omega)$ associated with a vibrational mode of wavevector \mathbf{q}_0 and frequency $\omega(\mathbf{q}_0)$ is well described by a Lorentzian function

$$I_0(\omega) \propto \frac{1}{[\omega - \omega(\mathbf{q}_0)]^2 + [\Gamma_0/2]^2}, \quad (6)$$

as described above. A disordered distribution of point defects as would be produced by ion implantation, however, will scatter phonons and will also add a contribution to the FWHM by coupling phonons of wavevector \mathbf{q}_0 to those of wavevector $\mathbf{q}_0 + \delta\mathbf{q}$ [130]. In the limit of low levels of disorder, the coupling will be most effective for small δq , so the phonon wave packet in k -space can be described by a Gaussian function $\exp[-(\mathbf{q} - \mathbf{q}_0)^2 L_{\text{pc}}^2/4]$ centered at \mathbf{q}_0 and having a width proportional to $1/L_{\text{pc}} \approx \delta q$. Therefore, in real space L_{pc} is a measure of the phonon coherence length, which should also be a good measure of the average distance between point defects. Then, the Raman intensity for the disordered graphene $I(\omega)$ can be written as [130–134]

$$I(\omega) \propto \int_{\text{BZ}} d^2q \frac{W(\mathbf{q}) \exp[-(\mathbf{q} - \mathbf{q}_0)^2 L_{\text{pc}}^2/4]}{[\omega - \omega(\mathbf{q})]^2 + [\Gamma_0/2]^2}, \quad (7)$$

where the integral is taken over the 2D BZ of graphene and $W(\mathbf{q})$ is a weighting function that describes the wavevector dependence of the el-ph coupling for the Raman process.

1.4.7. The Raman resonance window

Here, we consider the Raman excitation profile or the Raman resonance window, including the width of the resonance window γ_r . Both the lineshape and the width of the resonance window are considered when obtaining information from the excitation profile. In principle, the Raman intensity $I(E_{\text{laser}})$ for a 1D or zero-dimensional carbon sp^2 system shows a dependence on the laser energy E_{laser} in the Raman excitation profile associated with resonances of E_{laser} with the

incident E_{ii} and scattered light $E_{ii} \pm E_q$ according to

$$I(E_{\text{laser}}) = \left| \frac{A}{(E_{\text{laser}} - E_{ii} - i\gamma_r)(E_{\text{laser}} - (E_{ii} \pm E_q) - i\gamma_r)} \right|^2, \quad (8)$$

where the resonant lineshape $I(E_{\text{laser}})$ consists of two peaks at $E_{\text{laser}} = E_{ii}$ (*incident resonance condition*) and $E_{\text{laser}} = E_{ii} \pm E_q$ (*the scattered resonance condition*). Here γ_r is the FWHM width discussed below. Experimentally it is not always possible to resolve the observed $I(E_{\text{laser}})$ lineshape into two peaks.

The FWHM width of each peak in the Raman excitation profile is the resonance window width γ_r , and is related to the lifetime of an electron in its excited states. If the lifetime of the photo-excited electron is finite, then the resonance condition in the Raman excitation profile may show departures from Equation (8) which assumes $\gamma_r \ll E_q$. The finite lifetime of the photo-excited electron is subject to the uncertainty relation $\Delta E \Delta t \sim \hbar$.

The photo-excited carrier can be relaxed from the excited states by several processes, each occurring according to different time scales:

- The Coulomb interaction between electrons (10–100 fs).
- The electron–phonon interaction for all possible phonons (with lifetimes < 1 ps).
- The electron–photon interaction (with lifetimes < 1 ns).

When we consider the Coulomb interaction for a given electron, the other electrons should excite the first electron to an unoccupied state. Thus, the Coulomb interaction depends on the metallicity of the material. In the case of carbon nanotubes, the interaction between two excitons that is relevant to this term is known as the Auger process. On the other hand, a photo-excited electron has a definite lifetime for emitting any energy–momentum conserved phonon. Thus, the el–ph interaction of the electron from a state k (a photo-excited state) to the energy–momentum conserved $k + q$ (phonon emitting electron state) is important. Note that γ_r (the resonance window width, Eq. (8)) is physically different from Γ_q (the Raman spectral width, Eq. (4)).

1.5. Raman measurements of low-dimensional materials

The resonance Raman effect is especially important in low-dimensional nano-systems since the density of states becomes singular (because of the presence of van Hove singularities in 1D systems, see Figure 8) and the spectral energies become discrete. The latter effect is important for decreasing the resonance window width since the number of energy–momentum conserved intermediate states becomes small and thus the corresponding lifetime of the photo-excited carrier becomes long. These are the reasons why we can observe Raman spectra even from a single molecule or, for the case of carbon sp^2 nanostructures, we can even see Raman spectra from an individual carbon nanotube.

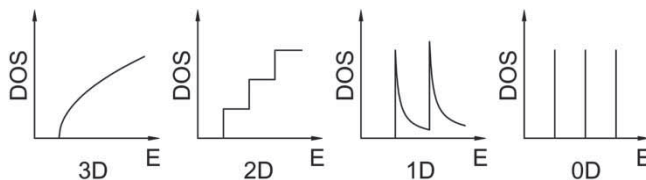


Figure 8. Typical electronic density of states for 3D, 2D, 1D and 0D systems.

1.5.1. *Cutting lines and van Hove singularities of the density of states*

When the 2D sheets of graphene are rolled up to form 1D nanotubes, different subbands in the 1D reciprocal space of the nanotube can be extended into the 2D reciprocal space of a single sheet of the parent bulk layered material as a set of parallel equi-distant cutting lines [32,135,136]. This procedure is shown in Figure 9(a) for states near the K point.

Figure 9(b) shows the electronic density of states (DOS) related to the nanotube electronic band structure plotted schematically in Figure 9(a). Each of N cutting lines in Figure 9(a) (except for the one that crosses the degenerate K point) gives rise to a local maximum in the DOS $g(E)$ in Figure 9(b), known as a (1D) van Hove singularity (vHS), given by

$$g(E) = \frac{2}{N} \sum_{\mu=1}^N \int \left[\frac{\partial E_{\mu}(k)}{\partial k} \right]^{-1} \delta[E_{\mu}(k) - E] dk. \tag{9}$$

The four vHSs in Figure 9(b) are labeled by $E_i^{(v)}$ and $E_i^{(c)}$ for the electronic subbands in the valence and conduction bands, correspondingly. The presence of vHSs in the DOS of 1D structures makes these structures behave differently from their related 3D and 2D counterpart materials, as can be seen in Figure 8. A finite density of states between the first singularities in the valence band and conduction band for metallic nanotubes is shown in Figure 9(b).

1.5.2. *Dimensionality and the resonance Raman effect*

The electronic DOS profiles for systems of different dimensionality (3D, 2D, 1D, and 0D) are very different from one another, as shown in Figure 8. The typical DOS dependence on energy near an

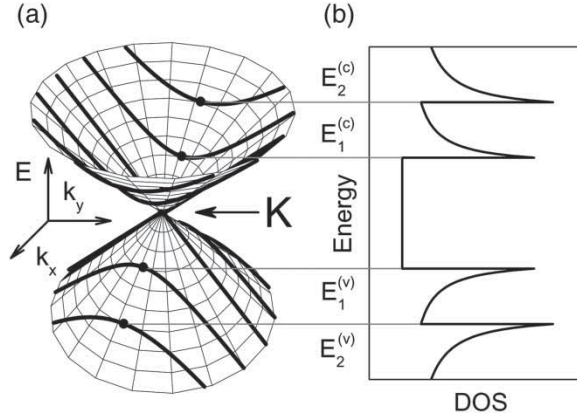


Figure 9. (a) The energy–momentum contours for the valence and conduction bands for a 2D system, with each band obeying a linear dependence for $E(k)$ and forming a degenerate point K where the valence and conduction bands touch to define a zero gap semiconductor. The cutting lines of these contours denote the dispersion relations for the 1D system derived from the 2D system. Each cutting line gives rise to a different energy subband. The energy extremum E_i for each cutting line at the wave vector k_i occurs at a van Hove singularity. The energies $E_i^{(v)}$ and $E_i^{(c)}$ for the valence and conduction bands and the corresponding wave vectors $k_i^{(v)}$ and $k_i^{(c)}$ at the van Hove singularities are indicated on the figure by the solid dots. (b) The 1D density of states (DOS) for the conduction and valence bands in (b) corresponding to the $E(k)$ dispersion relations for the 1D subbands shown in (a) as thick curves. The DOS shown in (b) is for a metallic 1D system, because one of the cutting lines in (a) crosses the degenerate Dirac point (the K point in the graphite Brillouin Zone (BZ)). For a semiconducting 1D system, no cutting line crosses the degenerate point, thus resulting in a band gap opening up in the DOS between the van Hove singularities $E_1^{(v)}$ and $E_1^{(c)}$ [135].

energy band extremum, $g(E)$ is given by $g \propto (E - E_0)^{(D/2)-1}$, where D is an integer, denoting the spatial dimension and D assumes the values 1, 2, and 3, respectively, for 1D, 2D, and 3D systems [137]. The parameter E_0 appearing in the density of states $g(E)$ denotes the energy band minimum (or maximum) for the conduction (valence) energy bands. For a 1D system, E_0 would correspond to the energy of a vHS in the DOS occurring at each subband edge, where the magnitude of the DOS becomes very large. One can see from Figure 8 that 1D systems exhibit DOS profiles which have some similarity to the case of 0D systems, with both 0D and 1D systems having very sharp maxima at certain energies, in contrast to the DOS profiles for 2D and 3D systems, which show a more monotonic increase with energy (see Figure 8). However, the 1D DOS is different from the 0D DOS (δ function at each discrete energy level) in that the 1D DOS has a sharp threshold and a decaying tail for each cutting line, so that the 1D DOS does not go to zero between the sharp maxima, as the 0D DOS does (see Figure 8). This is even true for semiconducting nanotubes which have a finite band gap and no occupied states between the first cutting lines in the valence and conduction bands. The extremely high values of the DOS at the vHSs allow us to observe physical phenomena for individual 1D nanostructures in various experiments, as discussed in Section 1.1.6.

1.5.3. Coherence time and length in Raman processes

It is not trivial to define whether a real system is large enough to be considered as being effectively infinite and therefore to exhibit a quasi-continuous phonon (or electron) energy dispersion relation. Whether or not an explicit dispersion relation can be defined indeed depends on the process that is under evaluation and the characteristics of this process. In the Raman process, we ask how long does it take for an electron excited by the incident photon to decay? Considering this Raman scattering time, what is the distance probed by an electron wave function? These issues are discussed in condensed matter physics textbooks [119] under the concept of *coherence*. The coherence time is the time the electron takes to experience an event such as a scattering process that changes its state. Thus, the coherence length is the distance over which the electron maintains its quantum state identity and its phase coherence. The coherence length is defined by the electron speed and the coherence time, both of which can be measured experimentally. The Raman process is an extremely fast process, and is in the range of femto-seconds (10^{-15} s). Considering the speed of electrons in graphite and graphene (10^6 m/s), this electron speed gives a coherence length of the order of nm. Interestingly, this number is much smaller than the wavelength of visible light. On the other hand, this is a particle picture for the scattering process and consideration of both the particle and wave aspects of electrons and phonons (as well as excitonic effects) are important for carbon sp^2 nanostructures. The study of such concepts is actually very interesting and important when dealing with local processes induced by defects, as discussed later (Section 4.3) in this article.

2. Experimental progress of Raman spectroscopy and related optics

As shown in Figure 10, the use of photo-physical techniques has contributed a great deal to our understanding of carbon nanostructures because of the large amount of information photo-physical techniques have provided and the relative simplicity of many of these experimental techniques. The resonance Raman effect and the strong el-ph coupling of carbon nanotubes and graphene, together with the simplicity of sample preparation required for Raman experiments when compared with many other techniques, elevate Raman spectroscopy to a special position. Raman spectrometers are broadly available and generally easy to use. For this reason, Raman spectroscopy is the most common sample characterization tool used by groups working with carbon nanotubes and graphene.

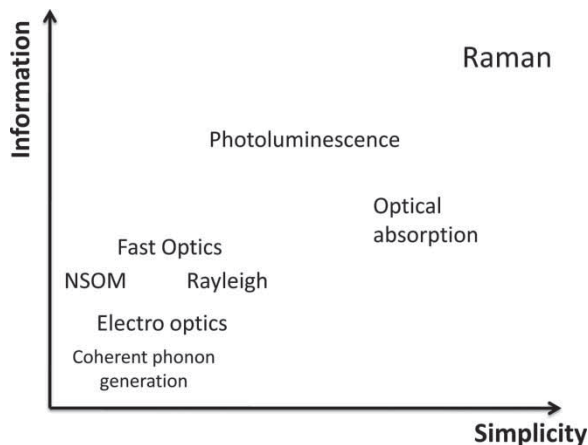


Figure 10. Qualitative comparative evaluation of the amount of information vs. the simplicity of performing an optical experiment in SWNTs based on the experience of the authors. The position of each technique in the plot is defined both by physical limitations (e.g. photoluminescence is not available from metallic SWNTs) and by aspects of practical implementation.

In Section 2, we review a number of optical and spectroscopic techniques that are used for characterizing materials and especially focusing on sp^2 carbon materials, carbon nanotubes and graphene. We start this section with a brief introduction to the special properties of electrons and phonons in graphene.

2.1. *Electrons and phonons in graphene*

In order to analyze optical phenomena and Raman spectra of sp^2 carbons, we focus on the electronic and vibrational structure of graphene, the mother material of sp^2 carbons. In this section, we review the geometrical structure, the electronic structure and the phonon structure of graphene.

2.1.1. *The hexagonal crystal structure of graphene*

Mono-layer graphene (1-LG) is a single atomic layer of graphite in which carbon atoms crystallize into a hexagonal lattice (see Figure 2). The unit cell of the hexagonal lattice is a rhombus which consists of two distinct carbon atoms A and B (see Figure 2(a)). The first BZ of graphene shown in Figure 2(e) also has a hexagonal periodicity in k space.

2.1.2. *The electronic structure and optical transitions*

The carbon valence electrons of graphene have $2p_z$ orbitals. This orbital is elongated in the direction perpendicular to the C–C bond and therefore is called a π orbital.⁸ A simple tight-binding calculation for the two π orbitals for the A and B atoms in the unit cell gives two π energy bands. The electron-occupied band is called the π band and the electron-unoccupied band is called the π^* band. Of particular interest is the fact that the two π energy bands touch each other at the K and K' points which are the two non-equivalent hexagonal corners of the BZ where the Fermi energy for undoped graphene is located. What is special about the π bands in graphene is that the energy dispersion of both π bands near the K and K' points have the same linear $E(k)$ relation. Thus, the corresponding electron and hole effective masses at the K and K' points become zero,

and increase as we move away from the K and K' points. The anomalous and symmetric behavior of the electrons and holes in graphene mainly originates from this unusual linear $E(k)$ energy dispersion relation of graphene near the Fermi energy, E_F .

Electronic transitions occur from the electron-occupied π band to the electron-unoccupied π^* energy band. Selection rules forbid intra-atomic transitions from $2p$ to $2p$ states. However, inter-atomic transitions from $2p$ to $2p$ states are allowed both for the nearest-neighbor pairs of carbon atoms and for further neighbors as well. Since the energy dispersion is linear near the K and K' points, the electronic dispersion in graphene forms Dirac cones. Optical transitions for a given laser excitation energy E_{laser} occur on the equi-energy lines around the K and K' points. Because of the three-fold symmetry of $E(k)$ around the K or K' points, the equi-energy lines are distorted into a triangle with increasing energy [32,138]. This trigonal warping effect of the energy dispersion and of the Fermi surface dominate the electronic properties.

2.1.3. Phonons and the el-ph interaction in graphene

The two carbon atoms in the graphene unit cell result in six phonon modes and six energy dispersions in the unit cell [1]. Three of the six phonon modes are acoustic (A) phonon modes whose phonon energy is zero at the zone center of the BZ (the Γ point). The other three phonon energy bands correspond to optical (O) phonon modes in which the vibration directions of the A and B atoms are anti-symmetric with respect to each other. The three A (or O) phonon modes consist of one longitudinal (LA or LO) mode and two tangential (TA or TO) phonon modes. The two tangential phonon modes (TA or TO) consist of one in-plane (i TA and i TO) and one out-of-plane (o TA and o TO) phonon mode. Since the L phonon modes of graphene are always in-plane phonon modes, the i label for the LA and LO phonon modes is generally suppressed. Hexagonal symmetry requires a degeneracy for the LO and i TO phonon modes at the Γ point and for the LA and LO modes at the K points.

The electron motion of the A and B carbon atoms is perturbed by the atomic vibrations which cause an electron to scatter from a k state to a $k + q$ state by emitting a $-q$ phonon. In Raman spectroscopy, we generally consider the el-ph interaction for a photo-excited electron within a π^* energy band. There is thus a restriction imposed on the scattering event that the final state must be unoccupied. Energy and momentum conservation applies to the scattering of electrons by emitting a phonon, resulting in a maximum energy for $E(k) - E(k + q)$ which corresponds to the maximum phonon energy (0.2 eV for graphene). The scattering of electrons only occurs within circles of equi-energy which specify the allowed optical transitions. Since we have two Dirac cones which are near the K and K' points, this restriction does not mean that the momentum transfer q is restricted to lie within the equi-energy circle. Electron scattering from the K to K' (or from the K' to K) regions is possible, for energy differences between the incident and scattered photons up to 0.2 eV, and we call these processes inter-valley scattering processes [139]. On the other hand, scattering within each of the K or the K' regions can also occur and this type of scattering is called an intra-valley scattering event. Another important concept for electron and phonon scattering is the distinction between forward and backward scattering. The velocity of the electron can change its sign upon scattering, since its group velocity is given by $\partial E(k)/\partial k$. If the scattered states are on the same (another) side of a Dirac cone, then the scattering event is classified as forward (backward) scattering. Considering the six phonon modes, the two types of valley scattering processes, and both forward and backward scattering processes, there are 24 different possible types of scattering processes that are relevant to the el-ph interaction and all of these 24 scattering processes are discussed below.

2.2. *Electrons and phonons in 1D carbon nanostructures*

2.2.1. *1D carbon structures*

Carbon nanotubes [32] and graphene nanoribbons [140] are 1D sp^2 carbon nanostructures based on graphene and their physical properties can be discussed by zone-folding the 2D dispersion relations of graphene onto the 1D BZs of carbon nanotubes and graphene nanoribbons both of which have discrete wave vectors which are specified in the quantum confined direction. Both carbon nanotubes and graphene nanoribbons have a 1D unit cell for which translational symmetry exists, respectively, along the direction of the nanotube axis and the ribbon axis. The quantum confinement of electrons and phonons in the circumferential direction of nanotubes or along the ribbon width direction of nanoribbons applies to their discrete wavelengths and discrete wavevectors, which are expressed by the cutting lines discussed in Section 1.5. The symmetries of the 1D unit cells are given by point group theory which specifies the possible Raman-active modes and the possible dipole-allowed optical transitions [141,142].

2.2.2. *π bands and phonons in carbon nanotubes and nanoribbons*

The electronic dispersion relations for the π (π^*) bands of carbon nanotubes and graphene ribbons consists of $2N$ energy subbands, where $2N$ denotes the number of carbon atoms in the 1D unit cell. Each energy subband is obtained from the 2D energy bands of graphene by combining the pertinent allowed 1D wave vectors on a cutting line in the 2D BZ of graphene. For zigzag graphene ribbons, special electronic states, called edge states appear for which the amplitude of the wavefunction is localized at one zigzag edge and on one sublattice (A or B) of graphene [140], and these zigzag edge states have a very high density of electronic states at the Fermi level [143]. The density of states for zigzag nanotubes including the spin-orbit interaction was calculated by Son and Louie [143,144].

The phonon dispersion of carbon nanotubes and graphene nanoribbons similarly contain $2N$ energy subbands. Most phonon subbands are also obtained by combining the zone-folding of the 2D phonon dispersion relations and using appropriate cutting lines. However, in the case of carbon nanotubes, special phonon modes which do not appear in graphene must be introduced to describe carbon nanotubes. These additional phonon modes are the RBM and the twist modes (TM), in which the carbon atoms are vibrating along the radial direction and along specific directions with respect to the nanotube axis [32].

2.2.3. *Optical transitions*

Special to 1D systems is the quantum confinement of discrete k vectors associated with the van Hove singularities in the 1D DOS for the top and bottom of each energy subband of the π bands (see Figure 9). When the light is polarized along the nanotube axis or along the graphene ribbon axis, optical transitions occur between π and π^* energy bands at the same cutting line for the initial and final state and a strong absorption occurs from the top of the π bands to the bottom of the π^* band at the wavevector k_{ii} . For 1D systems, the k_{ii} vector is special because the joint density of states (JDOS) for the i th π band and the i th π^* band become singular at the energy separation of E_{ii} . For light perpendicular to the nanotube axis, optical transitions occur between nearest-neighbor cutting lines with energies $E_{i,i+1}$ because the polarized light in this case has an additional quantum unit of angular momentum. Thus, different selection rules apply to light polarized parallel (E_{ii}) or perpendicular ($E_{i,i+1}, E_{i,i-1}$) to the nanotube or graphene ribbon axes.

2.2.4. *Type I and II semiconductor nanotubes*

In discussing optical transitions, it is important to classify (n, m) semiconducting nanotubes into two categories depending on whether $\text{mod}(2n + m, 3) = 1$ or 2, which we call Types I or II

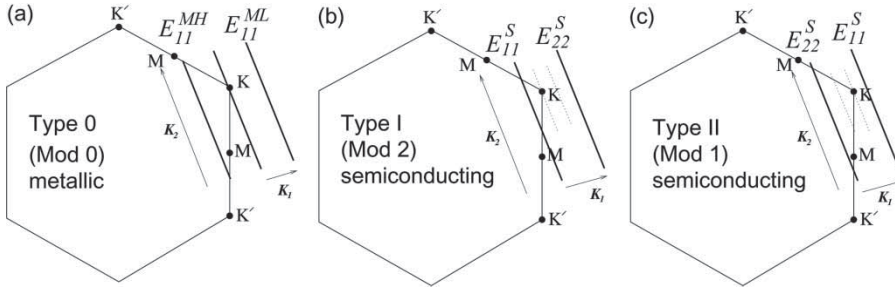


Figure 11. Cutting lines near the K point in the 2D BZ of graphene for (a) Type 0 (or Mod 0) metallic SWNTs, (b) Type I (Mod 2) and (c) Type II (Mod 1) semiconducting SWNTs.

semiconducting nanotubes (S-SWNTs), respectively.⁹ In Figure 11, we show the geometry of the cutting lines near the K point in the 2D BZ of graphene. In the case of type I (II) semiconducting nanotubes, the K point lies at the one-third (two-thirds) position between two cutting lines, since the distance of the K point from the cutting line at the Γ point is given by $(2n + m)/3$ times K_1 , where K_1 is a reciprocal lattice vector in the direction of the chiral vector [32]. In Figure 11(a), we see that $\text{mod}(2n + m, 3) = 0$ corresponding to metallic nanotubes. Each cutting line results in an optical transition for its E_{ii} value. Further discussion of this classification is given in [107,135, 136,141,145,146]. Because of the anisotropy of the effective mass tensor around the K point, the optical properties of S-SWNTs depend on their Type I or II classification (see Figure 11(b) and (c)). We call this classification the semiconductor type-dependence.¹

2.2.5. 1D exciton, exciton–photon and exciton–phonon interactions

For a pure 1D electron and hole pair, such as that occurs for a carbon nanotube or a graphene ribbon, the exciton binding energy becomes singular (∞ energy) for the lowest energy state. For a nanotube or a nano-ribbon, however, the binding energy of these nanostructures is also finite, since the nanotube circumference or nanoribbon width is finite. Though finite, the binding energy is still very large for a 1 nm diameter nanotube or a nanoribbon of 1 nm width, compared with the room temperature thermal energy of 25 meV. Thus, understanding excitonic electron and hole binding is essential for understanding the optical properties of nanotubes at room temperature.

Since the exciton is localized in real space, the exciton wavefunction is given by a linear combination of many wave vector states near the k_{ii} points, whose mixing coefficients are given by the Coulomb interaction between the photo-excited electron and the valence electrons (electron self-energy) or between a photo-excited electron and hole (exciton-binding energy). These exciton wavefunctions for graphene ribbons or nanotubes are calculated by the Bethe–Salpeter equation [120,147,148]. Because of the highly localized wavefunction of an exciton, the intensity of the excitonic optical transition (absorption and emission) intensity is enhanced significantly (10,000 times) relative to ordinary optical excitations between conventional band states. On the other hand, since the el–ph interaction strongly depends on the wavevectors k near the Fermi energy, the exciton–photon interaction energy (which is given by the integration of the el–ph interaction over k weighted by the exciton wavefunctions) shows a strong (n, m) dependence. In fact, the value of the exciton–phonon interaction is of the same order of magnitude as the el–ph interaction in these 1D systems. The observation of excitons in carbon nanotubes was first reported by the Heinz group at Columbia [44,121] and by the Reich–Thomsen group in Berlin [122].

2.3. The optical measurement techniques

In this section, we mention the various measurement techniques which have been used to study the photophysics of carbon nanotubes, graphene and graphene nanoribbons. In general, the studies on carbon nanotubes are more developed, while graphene and graphene nanoribbons are still in an early stage. Some techniques are found to be more sensitive for certain systems and others may be more sensitive for the specific applications that a particular system might be used for. It is also important to know which photophysical techniques have been or could be used for spectroscopic studies and for making related measurements on graphene, graphene nanoribbons, carbon nanotubes and related sp^2 nano-carbon systems. These various techniques are briefly reviewed in this section.

2.3.1. Light absorption

Light absorption is one of the most fundamental photophysical measurement techniques. A typical absorption spectrum is shown in Figure 12(a). This spectrum compares the optical absorption spectra in 1D SWNTs to that in colloidal 3D graphite. Above 2.0 eV, the spectrum of the two carbon forms is similar. At lower energies, however, the SWNT sample shows three broad peaks, A, B and C in Figure 12(a), associated with the two lowest allowed transitions in semiconducting SWNTs (A, E_{11}^S and B, E_{22}^S shown in Figure 12(b)) and the first peak in the joint density of states (JDOS) of the metallic nanotubes (C, E_{11}^M shown in Figure 12(b)). Measurements on isolated SWNTs show sharper transitions than for SWNT bundles, and each sharp transition is related to specific van Hove singularities, relevant to each SWNT. These transitions become merged and broadened in samples of nanotube bundles.

Graphene, being a 2D system, has no such van Hove singularities¹⁰ and the optical absorption of 2D graphene looks more similar to that of 3D graphite [42,149]. However, for a given optical frequency, the optical absorption of graphene depends on the number of graphene layers. The amount of light transmitted through an N -layer graphene sample only depends on N and on fundamental constants. Experiments have confirmed the theoretically expected universal value $\pi e^2/hc$ for the optical conductivity of graphene [74] (or a 2.3% optical absorption per graphene layer). Such experiments have also revealed departures of the quasi-particle dynamics from the

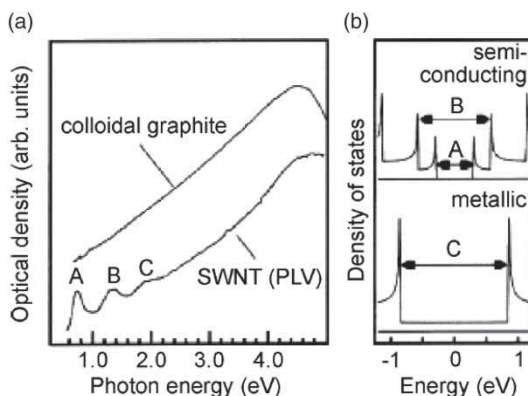


Figure 12. (a) The optical absorption spectra from SWNTs and from colloidal graphite shown comparatively. (b) Illustration of interband processes giving rise to the optical absorption peaks in semiconducting and metallic SWNTs [42].

simple predictions for Dirac Fermions in idealized graphene as we move sufficiently far from the Dirac point in k space.

2.3.2. Resonance Rayleigh scattering

Rayleigh scattering refers to the elastic scattering of light and the intensity of the Rayleigh scattered light intensity in graphene depends on the number of graphene layers and this technique can be used for determining the number of layers in a given few layer graphene sample. The Rayleigh scattering intensity is stronger when the laser is in resonance with an optical transition energy in which case the process is called resonance Rayleigh scattering. An important use of resonance Rayleigh scattering is to directly measure the E_{ii} values of SWNTs when using the laser light source whose frequency can be tuned. Figure 13(a) shows a schematic representation of the dark-field configuration which is used for this type of Rayleigh scattering spectroscopy. This geometry is used to efficiently reject the incident laser light so that the nearby Rayleigh signal can be clearly seen. One main challenge of Rayleigh scattering experiments comes from sample preparation. In this application, isolated SWNTs are prepared by chemical vapor deposition (CVD) and a substrate with a slit etched in it is used, allowing exploitation of the dark-field configuration shown in Figure 13(b). In the experiment of Figure 13(a), typical slit widths are tens of micrometers and slit lengths are up to 1 mm [44,150].

Since the pioneering work of the Heinz group [150], Rayleigh scattering is becoming increasingly popular as a method for the rapid identification of the (n, m) indices of individual SWNTs. Figure 14 shows the Rayleigh spectrum of different (n, m) SWNTs for the type of sample shown in Figure 13(b). The (n, m) of individual SWNTs are identified by comparing the observed resonance peak frequencies with the expected theoretical values, anchored on some geometrical constraints that are discussed in more detail from a theoretical standpoint in Section 3. For example, in Figure 14(a) the (16,11) type I S-SWNT has a similar electronic structure to the (15,10) type I SWNT, and the resonance Rayleigh spectra of both are displayed together in Figure 14(a). The diameter of the (16,11) nanotube is 1.83 nm, which is 0.12 nm greater than the 1.71 nm diameter

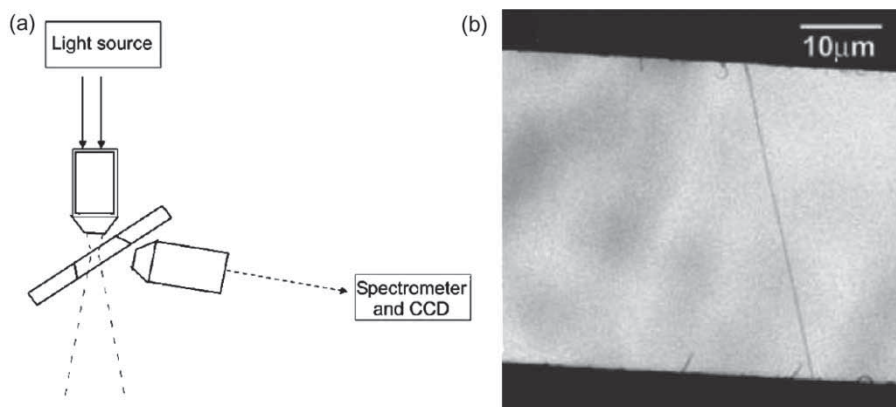


Figure 13. (a) Schematic diagram for a Rayleigh scattering measurement. Microscope objectives focus the incident light on a suspended nanotube and collect the radiation of the scattered light. Using a super-continuum source, different wavelengths can be detected simultaneously using a spectrometer and a multichannel (CCD) camera. (b) Electron micrograph of an individual suspended SWNT in a geometry used for Rayleigh scattering spectroscopy. Adapted from Carbon Nanotubes: Advanced Topics in the Synthesis, Structure, Properties and Applications, T.F. Heinz [44]. Copyright (2008) from Springer.

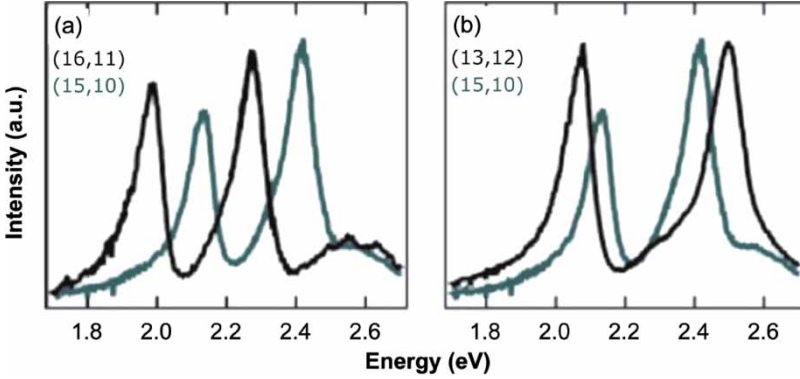


Figure 14. The Rayleigh scattering spectra of two different (n, m) semiconducting SWNTs shown comparatively for type I(a), type II(b) semiconducting SWNTs. The peaks in both cases correspond to the E_{33}^S and E_{44}^S interband transitions. The comparison in (a) corresponds to two nanotubes of the same $(2n + m) \bmod 3$ type, but having different diameters; the comparison in (b) corresponds to two nanotubes of different type, but with similar SWNT diameters. Adapted from M.Y. Sfeir *et al.* *Science*, 312, pp. 554–556, 2006, [150]. Adapted with permission from AAAS.

of the (15,10) SWNT. As a result, a downshift of about 150 meV in the E_{33}^S and E_{44}^S transitions of the larger diameter nanotube is observed. The ratio of the E_{44}^S to E_{33}^S transition energies is similar for these two nanotubes which are both of type I S-SWNT. However, a comparison of the (13,12) type II S-SWNT with the (15,10) type I S-SWNT (Figure 14(b)) shows a different behavior for the two different types of S-SWNTs. In this case, the average energies of the two transitions of the (15,10) and (13,12) nanotubes are very similar due to their nearly identical diameters (1.71 nm and 1.70 nm, respectively). However, the difference in behavior is manifested in the dissimilar intensity ratios for their E_{44}^S to E_{33}^S transitions. Rayleigh scattering measurements have been especially useful for advancing the theory related to optical transition energies in SWNTs and how environmental effects influence these values [44]. Rayleigh scattering experiments have also been carried out in graphene by Casiraghi [151].

2.3.3. Photoluminescence excitation spectra

The photoluminescence technique has become an especially popular method for characterizing semiconducting SWNTs [152,153]. The photoluminescence excitation (PLE) spectra conveniently characterize S-SWNTs by measuring their emission spectra and the technique is limited to semiconducting nanotubes. The PLE spectrum thus plots the light emission as a function of the laser excitation energy of the light and most experiments focus on measuring E_{11}^S rather than higher E_{ii}^S with PLE [152,153]. Here, we show a PLE spectrum for a semiconducting-(6,5)-enriched SWNT sample, illustrated in Figure 15 [154], in order to show several light scattering peaks (highlighted by circles in Figure 15(b)), which also include Raman scattering events in addition to PLE. The vertical gray band in Figure 15(a) denotes photoluminescence emission at the band gap $E_{PL} = E_{11} = 1.26$ eV. The horizontal gray bands denote nearly continuous-luminescence emission bands associated with thermally excited processes involving different phonon branches for the (6,5) SWNT. The cutoff energy at 1.06 eV is marked in Figure 15(b) by a vertical dotted line which corresponds to the maximum phonon energy ($1.26 - 1.06 = 0.20$ eV) in the first-order phonon spectra. Slanted dotted lines, which correspond to $E_{ex} - E_{em} = \text{constant}$, denote emission from resonance Raman spectra (RRS) for G-band, M-band and G'-band phonons. Note that the strong

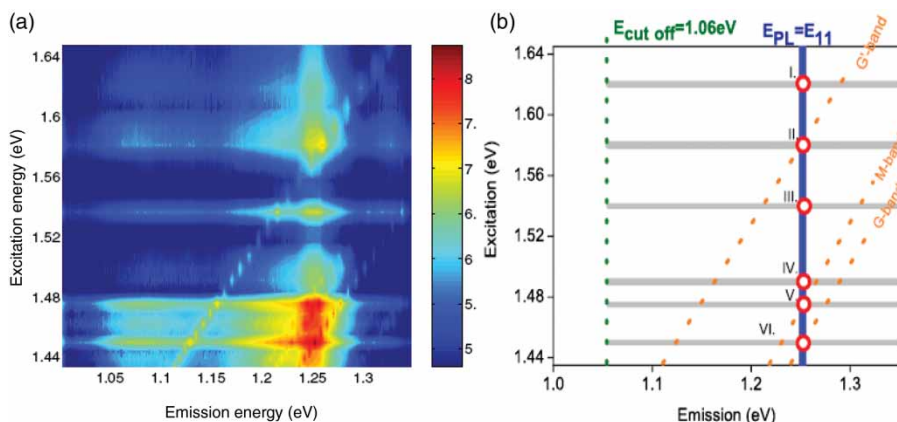


Figure 15. (a) A 2D excitation vs. emission contour map for a dried (6,5)-enriched DNA-CNT sample on a sapphire substrate. The spectral intensity is plotted using the log scale shown on the right. (b) A schematic view of the various observed light emissions plotted as the laser excitation energy vs. photon emission energy. Reproduced figure with permission from S.G. Chou *et al.* *Physical Review Letters* 94, p. 127402, 2005 [154]. Copyright © (2005) by the American Physical Society.

emission spots, appearing in Figure 15(a) at E_{11} and denoted by circles, correspond to energies where these bands cross the E_{11} transition energy. These intersection points are associated with a mixture of PL and RRS processes involving one-phonon (VI) and two-phonon (I–V) processes, following the labels in Figure 15(b). The various features in Figure 15 differ in linewidth. The Raman peaks are much sharper (tens of cm^{-1}) than the PL peaks which have linewidths of hundreds of cm^{-1} . The various peaks also differ by the fact that, when changing the excitation laser energy, the PL emission is fixed at E_{11} , while the Raman peaks change in frequency, keeping fixed the energy shift from E_{laser} . With light emission occurring at the same energy, the PL and RRS processes are sometimes confused in the literature, and the major reason is that RRS in solids often has a much greater (typically 10^3 times larger) intensity than the non-resonance Raman spectra [155]. To differentiate between the RRS and PL processes, one can just look at what happens to the spectral output when changing E_{laser} .

The difference in linewidth between RRS and PL arises because in Raman scattering the intermediate states that are excited between the RRS the initial state (incident photon plus the energy of the system before light absorption) and the final state (emitted photon plus the energy of the system after light emission) are “virtual” states.¹¹ These virtual states do not have to correspond to real states (and do not have to be eigenstates of the physical “system”) – any optical excitation frequency will, in principle, suffice in RRS. In photoluminescence, on the other hand, the optically excited state must be a real state of the system, and PL involves a real absorption of light at one frequency, followed by a real emission of light at a different frequency.¹² Photoluminescence is a technique commonly used to study graphene samples engineered for an energy gap opening but studies of energy gap opening are still at an early stage.

2.3.4. Electro-luminescence

Light emission by excited carriers can also be obtained by means other than photo-excitation, such as electro-luminescence (EL). In EL the electrically induced excitation is followed by ambipolar e–h recombination which comes from electrons and holes that are injected independently by using doped semiconductor electrodes and impact excitation occurs by hot carriers. These effects have

largely been studied in SWNTs [47,156,157], where both radiative decay of photo-excited and electron-excited emission occur, as well as the non-radiative decay to create free carriers which can then be studied by their photoconductivity spectra. EL processes could lead to the technological use of carbon nanotubes as nanometer scale light sources and as photo-current or photo-voltage detectors. EL has also been observed in graphene [157].

2.3.5. Infrared absorption spectroscopy

IR absorption spectroscopy has especially been useful for characterizing nanotubes [158–160]. In the case of graphene the IR absorption per layer of graphene is 2.3% and is given by the simple formula [74]

$$\pi\alpha = \pi \left(\frac{e^2}{\hbar c} \right) = 2.293\% \quad (10)$$

and for this reason can be used to determine the number of graphene layers in a few-layer graphene sample. IR spectroscopy typically is useful for studying the symmetry of the optical phonon modes.

When a particular phonon amplitude has the same symmetry as a vector, the corresponding phonon can directly absorb (or emit) a photon. Such phonon modes are called IR-active phonon modes. If the unit cell of a solid (or a molecule) has inversion symmetry, then the phonon modes can further be classified as either even and odd functions of the inversion operator, corresponding to Raman and IR-active phonon modes, respectively.¹³ Thus, by using polarized IR absorption spectroscopy for such materials, we can get independent information on the symmetry of specific phonons. For example, achiral nanotubes (armchair or zigzag nanotubes) have inversion symmetry along the nanotube axis. Since carbon materials tend to absorb light readily, IR absorption is typically measured by using reflected light in the back-scattered geometry. Complementary IR and Raman studies on sp^2 carbon materials have been performed [159,160] and used to study the symmetry of specific phonons in these materials.

2.3.6. Coherent phonon spectroscopy

In this section, we first describe the generation and measurement of coherent phonons (CPs) in general and then illustrate the use of this measurement technique in the case of carbon nanotubes [45,161–165]. When the duration of a light pulse is of the order of 10 fs which is smaller than the period of vibrational modes, then atomic vibrations start at the same time as the el-ph interaction starts to act on all involved atoms. This means that the amplitude of each phonon vibration has the same phase for all atoms, and we call this effect the coherent motion of a vibration. When we now send a second light pulse, we can then observe the vibrations of the atoms by a time-dependent transparency of the light, for which the mean frequency values correspond to the experimentally determined phonon frequencies. When we make a Fourier transform of the time-dependent transparency of materials, sharp peaks appear at the frequencies of the phonon modes which have strong el-ph matrix elements. The observed results are then similar to those obtained in Raman spectra. From the observation of the phase of the time-dependent transparency vibration, we can obtain information on the coupling constant of the el-ph interaction. For example, in the case of nanotubes, the nanotube can start a RBM phonon vibration by either increasing or decreasing its diameter, depending on the $\text{mod}(2n + m, 3)$ type of the nanotube. With ultra-fast laser spectroscopy, it is possible to monitor the photo-induced electronic and vibrational dynamics on a femto-second timescale. In general, time-domain observations of the phonon dynamics require the generation of CPs, corresponding to in-phase lattice vibrations of an ensemble of the same species that add up constructively to generate a detectable signal [45,161,164,165]. CPs have been

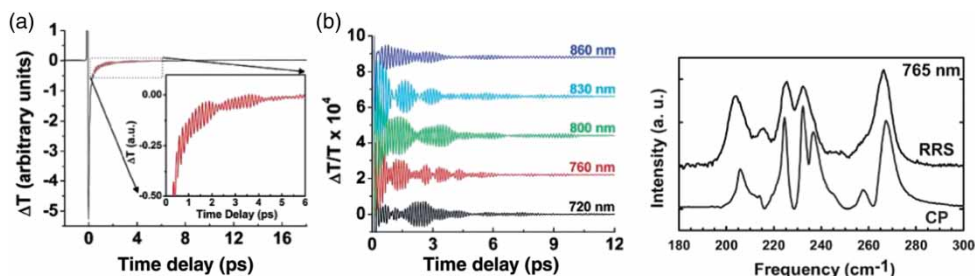


Figure 16. (a) Pump–probe time-delay data taken on a nanotube sample at a central wavelength of 800 nm in (b). The decay of the pump–probe signal within several picoseconds reflects the decay of the excited-state population. The inset in (a) is a zoom-in of the data between 0.3 and 6 ps, highlighting the coherent phonon contribution to the signal. (b) CP oscillations excited and measured at five different E_{laser} excitations (expressed in terms of their wavelengths). The individual traces for each wavelength are offset for clarity. The slower decay of the excited-state population has been subtracted in each case. (c) Phonon spectrum detected at a center wavelength of 765 nm obtained from both resonant Raman scattering (RRS) and from CP measurements in the frequency range of the RBM [45]. Adapted from carbon Nanotubes: Advanced Topics in the Synthesis, Structure, Properties and Applications, A. Hartschuh [45]. Copyright (2008) from Springer.

observed in a variety of different systems including thin films, semiconducting nanostructures, fullerenes and other carbon nanostructures.

Figure 16 shows results from coherent oscillations of the RBM coordinate, namely the diameter of the nanotubes [45]. Upon short-pulse laser excitation, all nanotubes of a certain (n, m) species within the sample will breathe in phase. By Fourier transforming this signal, the resulting response is similar to what is obtained in the frequency domain of resonance Raman spectroscopy. Upon close examination, however, noticeable differences are observed between CP and resonance Raman spectroscopy (RRS) data that were obtained from the same sample. For example, the spectral width of the phonon bands in the CP spectra is sharper, while the chirality dependencies of the CP and RRS signal intensities are different. Namely, in Raman scattering, the signal strength decreases as $(2n + m)$ increases, whereas the CP signal increases with increasing $(2n + m)$. These different types of behaviors can be used to distinguish one type of mechanism from the other in fast optics studies. Furthermore, pump–probe coherent phonon experiments on nanotubes (such as in Figure 16) also are very useful for finding the lifetime of photo-excited electrons in excited states.

2.4. Raman spectroscopy of sp^2 carbons

In this section, a brief introduction to Raman spectroscopy in sp^2 carbons is presented, starting with some historical background and then very briefly mentioning a number of different types of Raman spectroscopy that are being used to study sp^2 carbon materials.

2.4.1. Historical background

Raman spectroscopy has historically played an important role in the study and characterization of sp^2 carbon materials [19,166,167], which are being widely used in the last four decades to characterize pyrolytic graphite, carbon fibers [19], glassy carbon, pitch-based graphitic foams [101,168], nanographite ribbons [59], fullerenes [23], carbon nanotubes [32,167] and graphene [5,97,112]. For sp^2 nanocarbons, Raman spectroscopy can give information about crystalline size, clustering of the sp^2 phase within a given sample, the presence of sp^3 hybridization and chemical impurities, its mass density, optical energy gap, elastic constants, doping, defects and

other crystal disorder, edge structure, strain, the number of graphene layers, nanotube diameter, nanotube chirality and nanotube metallic vs. semiconductor behavior [169]. Another important area where much work has been done is on disordered, amorphous and diamond-like carbons [19,131,169], as well as graphite and graphene edges [151,170].

2.4.2. Raman spectra of graphite and graphene: G^- and G^+ -bands

Figure 4 shows the Raman spectra from different crystalline and disordered sp^2 carbon nanostructures and emphasizes the difference in these spectra from one sp^2 carbon material to another. The first spectrum shown is that for mono-layer graphene – the building block of many sp^2 nanocarbons. A clear message derived from Figure 4 is that every different sp^2 carbon material in this figure shows a distinct Raman spectrum, which can be used to understand the different properties that accompany each of these different sp^2 carbon structures. For example, 3D highly oriented pyrolytic graphite (labeled HOPG in Figure 4) shows a distinctly different spectrum from that of mono-layer graphene (1-LG), which in turn is distinct from the Raman spectra characteristic of the various few layer-graphene materials, such as for 2-LG and 3-LG (see sect. 4.2) [112].

2.4.3. First-order RBM, G^+ and G^- Raman spectra of SWNTs

The Raman spectrum for SWNTs is also shown in Figure 4. These spectra show a variety of features, such as the RBM and the splitting of the G-band into G^+ and G^- bands. These first-order Raman features distinguish a SWNT from all other sp^2 carbon nanostructures. Carbon nanotubes are unique materials in many ways. For example, SWNTs exhibit transport properties that are either metallic (where their valence band and conduction bands touch each other at the K and K' points in the graphene BZ) or semiconducting (where a band gap, typically of several hundred meV, separates their valence and conduction bands). The Raman G^- spectral feature differs in lineshape, linewidth and frequency, according to whether the resonant nanotubes are semiconducting or metallic, as shown in Figure 17 [171] regarding their G^- and G^+ frequencies.

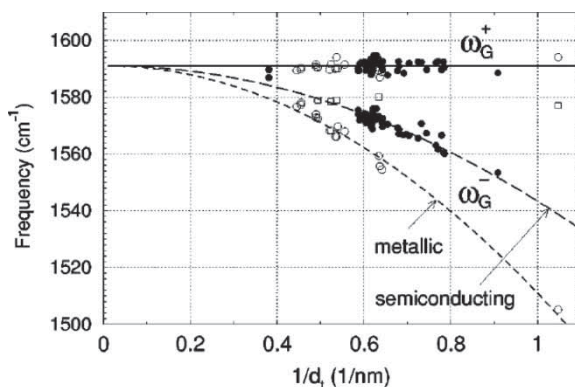


Figure 17. ω_G^- and ω_G^+ for semiconducting (filled circles) and metallic (open circles) SWNTs are plotted as a function of $1/d_i$. The flat solid line shows $\omega_G^+ = 1591 \text{ cm}^{-1}$. The curves are given by the function $\omega_G^- = 1591 - C/d_i^2$, where $C = C_S = 47.7 \text{ cm}^{-1} \text{ nm}^2$ for semiconducting SWNTs (long dashed curve) and $C = C_M = 79.5 \text{ cm}^{-1} \text{ nm}^2$ for metallic SWNTs (short dashed curve). Also plotted (open squares) are the data for the $\sim 1580 \text{ cm}^{-1}$ Lorentzian peak sometimes observed in metallic SWNTs. Adapted with permission from A. Jorio *et al.*, *Physical Review B* 65, p. 75414, 2001 [171]. Copyright © (2001) by the American Physical Society.

2.4.4. *The defect-induced Raman spectral features: D- and D'-bands*

The introduction of disorder breaks the crystal symmetry of graphene, 3D graphite and carbon nanotubes. The presence of disorder activates certain vibrational modes that would otherwise be silent, such as the D-band and the D'-band features and the combination D + G mode, shown in the spectrum-labeled damaged graphene in Figure [1,3,96,102,130,131,169,174]. The different types of defects do in fact show their own characteristic Raman spectra, as illustrated in Figure 4 by comparing the spectra-labeled damaged graphene and SWNH (denoting single wall carbon nanohorns, another nanostructured form of sp^2 carbon which may include pentagons with a small content of sp^3 bonding [37]). The topic of distinguishing between the Raman spectra of one and another type of defective sp^2 carbon remains an area for future study. When the disorder is so dominant that only nearest-neighbor structural correlations are present (labeled amorphous carbon in Figure 4), broad one-phonon ($< 1600 \text{ cm}^{-1}$) and two-phonon ($1600\text{--}3200 \text{ cm}^{-1}$) Raman features are seen [3,130]. At larger disorder limits, both sp^2 and sp^3 bonding might be seen. Some hydrogen uptake can also occur for such materials to satisfy their dangling bonds [131].

2.5. *Laser Raman scattering measurements*

In this section, we discuss the various types of Raman scattering studies that are generally carried out and we briefly describe in more detail how the measurements are done and the information that is provided by these measurements.

2.5.1. *The Raman setup*

In order to get a sharp and strong Raman signal, we generally use a laser light source. In the back-scattering geometry, the scattered light is collected at the same side of the laser spectrum relative to the position of the sample. Typical observation times to collect the scattered photons are from 1 s to 10 min. The incident and Rayleigh scattered light is filtered from the scattered light by a notch filter or some other method. The frequency shift of the Raman scattered light is measured by a monochromator which splits the observed scattered light as a function of the shift in the wavenumber of the scattered light relative to that of the incident light. The Raman intensity of each spectral line is measured by counting the number of photons recorded for that line and by considering the instrument function of the monochromator and the CCD detector to get a properly calibrated Raman signal. A typical resolution of a high-quality Raman system is 1 cm^{-1} . Splittings of the Raman spectra caused by experimental perturbations (such as due to external fields or applied stress) are directly measured by a CCD camera which counts photons, measuring frequency shifts, intensities and lineshapes of each pertinent Raman line.

2.5.2. *Polarized and micro Raman measurements*

Polarization is used to get additional information about crystal symmetry and selection rules. Symmetry information can be obtained by changing the polarization of the electric field of the light through use of suitable polarizers. The polarized incident light beam is focused on the sample and the scattered light is filtered by one polarizer and detected by a second polarizer. By selecting the propagating direction of the incident and the scattering light relative to the aligned sample and by selecting the polarization angles of the incident and scattering light beams, the optical dipole selection rules can be studied. This is the most common method that is used to determine the symmetry of the relevant phonons.

Micro Raman spectroscopy is a measurement technique in which the laser light of a given wavelength (or photon energy) is focused on the sample by an optical microscope. Such a system

is called a micro-Raman set up since the spatial resolution of the Raman signal is of the order of one micron. Not only is the incident light focused on the sample, but also the scattered light is collected by the same optical lens and is split by a half mirror [173]. An isolated graphene flake or SWNT on a Si substrate is located by putting the substrate on a mobile stage that moves the sample horizontally, and the mobile stage is controlled by stepping motors.

2.5.3. Confocal Raman spectroscopy and Raman imaging

Confocal Raman spectroscopy makes use of spatial filtering by means of pinholes in the optical paths, and it can generate spatially resolved Raman emission with a resolution on the order of $\lambda_{\text{laser}}/2m$, where λ_{laser} is the laser wavelength. By scanning the substrate on which an isolated nanotube or a graphene sample is located, we can get a Raman signal as a function of the position on the sample, which is generally called Raman imaging (see Figure 18). In the case of nanotubes, a micro-Raman imaging scan of a substrate can find the location of the nanotubes resonant with a given laser line. If we instead use near-field spectroscopy (see Sections 2.6.3 and 2.6.4), we can even get information on the Raman signal as a function of the position of an individual isolated nanotube with a resolution on the order of 10 to 20 nm. In the case of graphene or graphite, the D-band imaging technique is also important for determining the distribution and specific location of defects over the sample, since the D-band feature is not symmetry allowed, but is instead induced by a symmetry-breaking mechanism such as a defect or an edge [174].

2.5.4. Characterization of the sample edges and the imaging of defects

Since the D-band in sp^2 carbons is a feature that is only observed when the crystal symmetry is broken by a defect or a sample boundary, the D-band intensity can be used to characterize the disorder in graphene and carbon nanotubes. This effect is clearly observed in Figure 18 which shows two confocal Raman images of a $6\ \mu\text{m}$ highly oriented pyrolytic graphite crystallite deposited on a glass substrate. Figure 18(a) shows a Raman image of the crystalline regions of the sample, obtained by plotting the spatial dependence of the G-band intensity. In Figure 18(b) a map of the intensity of the disorder-induced D-band is shown, while Figure 18(c) shows two Raman spectra, one taken at the interior location of the crystalline region, and the other is taken at the edge. It is clear from Figure 18(a–c) that the G-band intensity is uniform over the whole graphite surface, while the D-band intensity is localized where the crystalline structure is not perfect, which

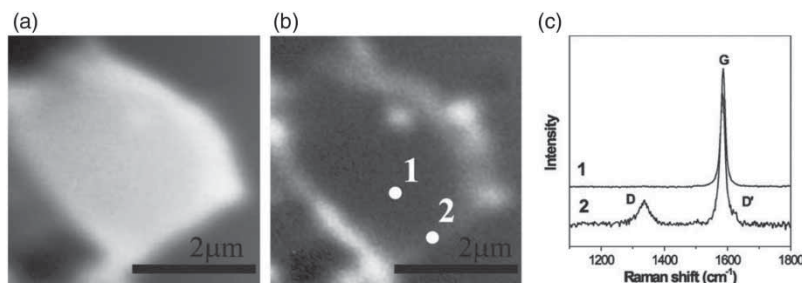


Figure 18. Raman spectra imaging of an HOPG micro-crystallite. In (a) the G-band intensity is plotted. In (b) the D-band intensity is plotted. (c) Spectra 1 and 2 are the spectra at locations 1 and 2 in (b) [174]. This experiment was performed in the laboratory of Prof. Achim Hartschuh and represent, to our knowledge, the first Raman imaging of localized defect modes in graphitic materials. M.A. Pimenta *et al.*, *Physical Chemistry Chemical Physics* 9, pp.1276–1290, 2007 [174]. Reprinted by permission of the PCCP Owner Societies.

occurs mainly at the edges of the crystalline region where symmetry-breaking occurs and D-band intensity due to the edge discontinuity is also seen.

The intensity of the D-band can also be used to assign the atomic structure of the edge in graphite and graphene [170], so that it can provide a useful tool to probe the edge chirality of graphene. In particular, armchair edges have a large matrix element for D-band scattering while for zigzag edges the matrix element for D-band scattering should vanish, and chiral edges show an intermediate amount of D-band edge scattering. However, imperfect graphene edges produced by the mechanical cleavage of graphite can produce ambiguous results that do not clearly discriminate the armchair and zigzag edges from one another.

2.5.5. Resonance Raman spectroscopy

In the Raman measurement, the resonance Raman effect strongly enhances the Raman intensity when the energy of either the incident or the scattered light matches the optical transition energy of a carbon nanotube or of a graphene ribbon. In the case of carbon nanotubes, since the JDOS becomes singular for an excitonic transition, the resonance Raman effect is especially strong. This is a major reason why we can get a strong Raman signal even from one nanotube [111]. On the other hand, if the resonance condition is not satisfied, we cannot get a measurable Raman signal even if a nanotube intersects with the light beam. This situation makes the search for isolated nanotubes in a sample very time consuming. Here, Rayleigh scattering is helpful for locating an individual SWNT and in providing its (n, m) assignment because all the nanotubes in a sample can thus be identified. However, with Raman spectroscopy we can always get a resonance Raman signal for bundle samples, but in this case we see only those nanotubes that are in resonance with E_{laser} . In the case of graphene which is a 2D system, the DOS is continuous near the Fermi energy and is not singular, so that any laser energy satisfies the condition for observing Raman spectra.

2.5.6. The Raman excitation profile

Using a continuous laser excitation energy light source, the Raman excitation profile (or resonance window) of a carbon nanotube is a plot of the Raman intensity measured at the same location on a sample as a function of laser energy. To determine the resonance energies of a carbon nanotube, denoted by E_{ii} , it is necessary to find the frequency of the peak in the Raman spectra taken as a function of the laser excitation frequency (E_{laser}), as shown in Figure 19(a). The FWHM intensity of the Raman excitation profile is defined as the resonance window width (typically 10 meV) which is inversely proportional to the lifetime of the photo-excited carriers (0.1 ps). The lifetime is defined as the time for the photo-excited electron to emit a phonon when it is in the excited state. In the case of the G-band, when we scan the laser excitation energy we can see two peaks satisfying the incoming and outgoing resonance conditions for the incident and the scattered light, while in the case of the RBM the two peaks for the incident and scattered light normally overlap with each other, since the resonance window width is larger than the RBM energy.

2.5.7. The Kataura plot

From the E_{ii} energy measured by the Raman excitation profile, we can plot E_{ii} for each (n, m) SWNTs as a function of the SWNT diameter, which we call the Kataura plot (Figure 19(b)) [176,177]. From the Kataura plot, we can determine the resonance conditions for all (n, m) SWNTs which is useful for assigning the (n, m) value to specific SWNTs from actual Raman measurements [178]. Since the radial breathing mode frequency ω_{RBM} depends on the SWNT diameter [111], we can plot the E_{ii} energy which is obtained by the resonance Raman excitation profile as a function of

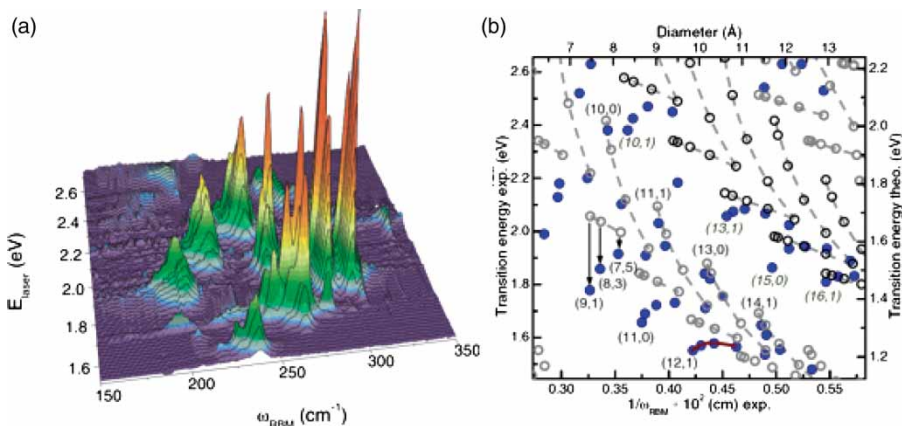


Figure 19. (a) RBM Raman measurements of HiPCO SWNTs dispersed in an SDS aqueous solution [152], measured with 76 different laser lines E_{laser} [175]. The non-resonance Raman spectrum from a separated CCl_4 solution is acquired after each RBM measurement, and this spectrum is used to calibrate the spectral intensities of each nanotube and to check its frequency calibration. (b) Filled circles are experimental E_{ii} vs. ω_{RBM} data points obtained by Telg *et al.* [107] from analysis of an experiment very similar to the one shown in (a). The label “Transition energy exp” actually indicates the excitation laser energy (E_{laser}) for each data point. Open circles come from third-neighbor tight-binding calculations, showing that even the addition of interactions with more neighbors in the π -band based tight-binding model is not enough to accurately describe the experimental results. Gray and black circles indicate the calculated optical transition energies from semiconducting (E_{22}^S and E_{33}^S) and from metallic (E_{11}^M) tubes, respectively. (a) Adapted from M.J. O’Connell *et al.*, *Science*, 297, p. 593, 2002 [152]. with permission from AAAS. And adapted with permission from C. Fatini *et al.*, *Physical Review Letters* 93, p. 147406, 2005 [175]. Copyright © (2005) by the American Physical Society. (b) Reprinted with permission from H. Telg, *et al.*, *Physical Review Letters* 93, p. 177401, 2004 [107]. Copyright © (2004) by the American Physical Society.

ω_{RBM} , and we call this plot an experimental Kataura plot. Figure 19(a) shows a 2D RBM map for the HiPCO nanotube sample in aqueous solution wrapped by the SDS (sodium dodecyl sulfate) surfactant [175]. For the construction of the plot in Figure 19(a), 76 different laser lines were used. By fitting each of the spectra with Lorentzians, (n, m) indices were assigned to the different SWNTs. Solid circles in Figure 19(b) denote the E_{ii} values obtained experimentally by fitting the resonance windows extracted from similar data to that shown in Figure 19(a), as compared with the E_{ii} obtained from tight-binding calculations (open circles) shown in Figure 19(b) [107].

2.6. Other measurement techniques related to Raman spectroscopy

In this section, we briefly describe several experimental techniques that have grown out of Raman spectroscopy or are related to Raman spectroscopy and are sensitively employed for specific types of optical studies used to gain unique and detailed information about nanostructures.

2.6.1. Surface-enhanced Raman spectroscopy

When light is incident on a small (nm in diameter) metallic particle, such as a gold or silver particle, the electric field near the metallic nano-particle is enhanced by several orders of magnitude, due to the surface plasmon excitation of the particle. The enhancement of the electric field

near the metallic nano-particle is given by the boundary condition for the transmitted electromagnetic wave on the metallic surface. When the light beam on the sample is located at the metallic nano-particle, the corresponding Raman signal becomes significantly enhanced (sometimes up to 10^{10} times that of the normal Raman signal). The surface-enhanced Raman spectroscopy (SERS) technique was utilized initially to obtain a large enough signal to observe the spectra from an isolated individual SWNT [128,179–181]. Changes in the symmetry selection rules are observed due to local symmetry breaking [182]. SERS measurements were carried out on SWNTs before researchers realized that there was a strong resonance effect occurring in the π -related states in carbon nanotubes and that this resonant effect was large enough to generate a measurable signal, without any SERS enhancement effect. In fact the observation of strong SERS spectra stimulated the first effort to observe the spectrum from one individual carbon nanotube [111]. Recently, the use of the SERS technique has been applied to graphene [183–186].

2.6.2. *Surface and interference enhanced Raman spectroscopy*

When we place a multi-layered sample on the top of a substrate, we can enhance the electric field of the light at the substrate by the interference of the incident light and the multi-reflecting light. This technique is called interference enhanced Raman spectroscopy and this technique can be used to get a large Raman signal from a graphene or a graphene nano-ribbon sample. Interference-enhanced Raman spectroscopy can also be combined with SERS and RRS, in which case the effect is called surface and interference co-enhanced Raman spectroscopy (SICERS) [184,187].

2.6.3. *Near-field enhanced Raman spectroscopy*

In order to get higher spatial resolution, an apex with a small aperture and a sharp tip at the end of an optical fiber is used to focus the light [45,188]. Since the diameter of the small aperture is smaller than the wavelength of the light, the light cannot get out from the aperture as a electromagnetic wave, but instead emerges as an exponentially decaying electric field which follows from a solution to Maxwell's equations. This decaying electric field of the light is called the near field while the conventional electromagnetic wave is called the far field. The amplitude of the near field can be much larger than that of the far field, and thus if the optical set up is sufficiently close to the sample, then we can get a much stronger signal with high spatial resolution using the near-field Raman technique, especially when tip enhancement techniques are used (Section 2.6.4). As discussed above, confocal Raman spectroscopy exhibits a limited resolution due to the Rayleigh criterion where the light cannot be spatially focused to better than $\sim \lambda/2$. This limitation can be overcome using near-field optical spectroscopy. We elaborate on this technique below in discussing the enhancement produced by using a metal tip and then by applying a combination of near field Raman and photoluminescence imaging to enhance atomic force microscopy imaging.

2.6.4. *Tip enhanced Raman spectroscopy*

Recently, laser-illuminated metal probes have largely been utilized to locally enhance electromagnetic fields, thereby generating a near-field effect [45]. So far, this so-called tip-enhanced microscopy (TERS, in comparison with more usual surface-enhanced techniques) has been applied to both Raman scattering and photoluminescence studies of SWNTs, and it is based on the local field enhancement at a laser-illuminated metal probe (see Figure 20). The highest spatial resolution achieved up to now is about 10 nm, which is limited by the tip size [45]. Near-field optical microscopy also provides significant signal enhancement by several orders of magnitude, which is crucial for efficient nanotube and graphene ribbon detection. The combination of nanoscale resolution and signal amplification makes the near-field optical techniques ideally suited

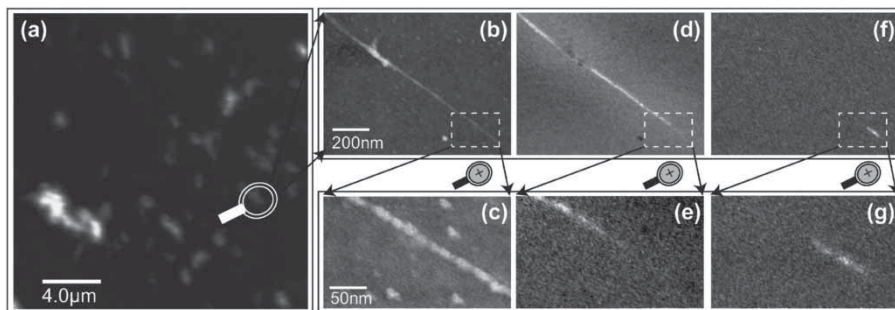


Figure 20. Imaging of DNA-wrapped SWNTs at different magnifications: (a) A confocal Raman image of a DNA-wrapped SWNT using an excitation wavelength of 632.8 nm. Topographic images in (b) and (c) indicate a periodic height modulation expected for wrapping with short DNA segments. Near-field Raman images (d) and (e) show the G-band intensity around 700 nm, and in (f) and (g) the intensity of photoluminescence images at around 950 nm corresponding to the emission wavelength of an (8,3) nanotube are shown. PL occurs only in the lower section of the nanotube where the Raman intensity is significantly weaker. The abrupt transition from strong to weak Raman scattering combined with the appearance of PL is interpreted as a local change in the nanotube (n,m) chirality [45]. Here, we see the power of near-field spectroscopy to show images with spectroscopic information at high spatial resolution. Adapted from *Carbon Nanotubes: Advanced Topics in the Synthesis, Structure, Properties and Applications*, A. Hartschuh [45]. Copyright (2008) from Springer.

for the investigation of nano-materials or localized perturbations caused by defects or nonuniform environments. The use of the TERS technique is time consuming and requires great care in its execution.

2.6.5. Simultaneous atomic force microscopy, near-field Raman and PL imaging

Figure 20 shows simultaneous near-field Raman and photoluminescence (PL) imaging for SWNTs grown on glass by the arc discharge method [45], where highly confined PL imaging from short 20 nm long segments of about 20 nm in length has been observed from SWNTs. The PL from micelle-encapsulated SWNTs on mica typically comes from much longer (more than 100 nm long) SWNT segments of up to several hundreds of nanometers. Figure 20 shows PL emission in images coming from a DNA-wrapped nanotube at different magnifications, starting with about 75 nm in the lower part of the nanotube (Figure 20g). The intensity of the Raman signal is seen to decrease sharply at the position where PL starts to occur and the results obtained in this particular image indicate a change in nanotube chirality (Figure 20e).

2.6.6. Coherent anti-Stokes Raman spectroscopy (CARS)

The CARS technique [189,190] consists of a pump–probe experiment using laser light. The electrons in the ground state are excited by the pump laser light and the electron excitation is transferred to a phonon via a Stokes Raman process. Then by the second probe light pulse, the phonon excitation is transferred to another electron by an anti-Stokes Raman process. In this subsequent process, we can observe the anti-Stokes Raman signal. An important concept in CARS is the coherence of the Raman processes. Since the amplitude of the anti-Stokes Raman scattered light has the same phase as the pump laser light, the CARS amplitude (intensity) is proportional to the square of the number of molecules or atoms in the sample. In order to obtain this coherence, a non-resonance condition is selected for both the first Stokes and the second anti-Stokes processes.

Since CARS observes a blue-shifted signal, the signal is well separated from the related red-shifted photoluminescence signal.

2.7. Kohn anomaly in graphene and carbon nanotubes

The use of the gate voltage to vary the electrochemical potential of a nanostructure has provided a very sensitive tool to probe many different phenomena that are sensitive to the carrier density, such as the Kohn anomaly (KA) [127,191–194]. We discuss the dependence of the Kohn anomaly on the frequency and linewidth of the G-band phonon for mono-layer graphene in Section 2.7.1, and for bi-layer graphene in Section 2.7.2, and for metallic SWNTs in Section 2.7.3. A theoretical approach to the KA of carbon nanotubes is later discussed in Section 3.6.5 and 5.4.4.

2.7.1. Kohn-anomaly of the G-band of graphene

In Figure 21, the G-band Raman spectra of graphene is shown as a function of applying a gate voltage to the substrate on which the graphene sample is positioned [195]. Here, the G-band is observed to upshift in frequency with both negative and positive applied potentials (see Figure 21(a) and (b)) and this frequency upshift is accompanied by a decrease in its linewidth (see Figure 21(c)) which is observed for both electron or hole doping. These effects are known as the Kohn anomaly [194,196–199]. These observations are explained as follows.

In the presence of the el-ph interaction of free electrons near the Fermi energy E_F , the phonon frequency and spectra become, respectively, down-shifted and broad, which is given by second-order, time-independent perturbation theory for the phonon energy and the phonon self-energy [194,196–199]. When the Fermi energy shifts from the Dirac point by more than 0.1 eV ($\pm\hbar\omega_G/2$), the virtual absorption of an electron by a G-band phonon with an energy of 0.2 eV is suppressed and thus a phonon hardening occurs. Furthermore, since the el-ph interaction is suppressed, the lifetime of a phonon becomes large, which corresponds to the decrease in linewidth shown in Figure 21(c).

2.7.2. Kohn anomaly of bi-layer graphene

In bi-layer graphene, the unit cell has four C atoms rather than two, and as a result there are two π bands and two π^* bands at the K point. In this case, there will be more than two Kohn anomalies in the G-band gate-dependent frequency renormalization [200]. When the Fermi energy reaches $\pm\hbar\omega_G/2$, the π - π^* transition from the valence band to the lower conduction band shown in Figure 22(I) is no longer allowed, as it is in mono-layer graphene. However, the transition from the now filled lowest energy π^* band to the higher energy π^* band, shown by the dashed arrow in Figure 22(II), is possible. Therefore, when the gate voltage rises further and the Fermi energy reaches the second band, then the π^* - π^* transitions shown in Figure 22(III) are suppressed. These effects are seen in the G-band frequency and linewidth of bi-layer graphene (see Figure 22)[191, 200], where a distinctly different behavior with respect to the mono-layer case (see Figure 21) is clearly observed for both the G-band frequency and linewidth.

Furthermore the interlayer interaction between phonons in bi-layer graphene gives rise to even and odd functions for the G-band vibrational modes in which only the even function mode is Raman active. However, if an interaction with the substrate exists, this symmetry-imposed effect is relaxed and both even and odd types of G-band spectra can be observed [5].

2.7.3. Kohn anomalies of SWNTs

Similar Kohn anomalies of the G-band for SWNTs when compared with mono-layer graphene are observed [193], but for SWNTs there is also a dependence on both the diameter and chiral angle [196,199,201–203]. In this case, the RBM mode also shows a weak phonon softening effect [170,204,205], which is further discussed in Section 5.

The Raman spectra of the G-band of sp^2 carbons have an asymmetric lineshape if there are free electrons at the Fermi energy. The asymmetric lineshape is expressed by Breit–Wigner–Fano lineshapes (BWF), whose origin is generally understood by an interference of discrete energy levels with a continuum energy spectrum (Fano resonance [129]). The second-order perturbation theory expression for the el–ph interaction for the KA only gives a symmetric broadening of the phonon spectra and thus the el–ph interaction by itself is not sufficient to account for the observed BWF lineshapes. There is, however, another continuum spectra for the electron excitations involving the Coulomb interaction in which there is an electron–electron interaction between photo-excited electrons and the free electrons associated with the SWNTs that is relevant to accounting for the BWF lineshapes. Recent measurements of the electronic Raman spectra of SWNTs clearly show a BWF asymmetric shape depending on the energy position of E_{ii} [202,206].

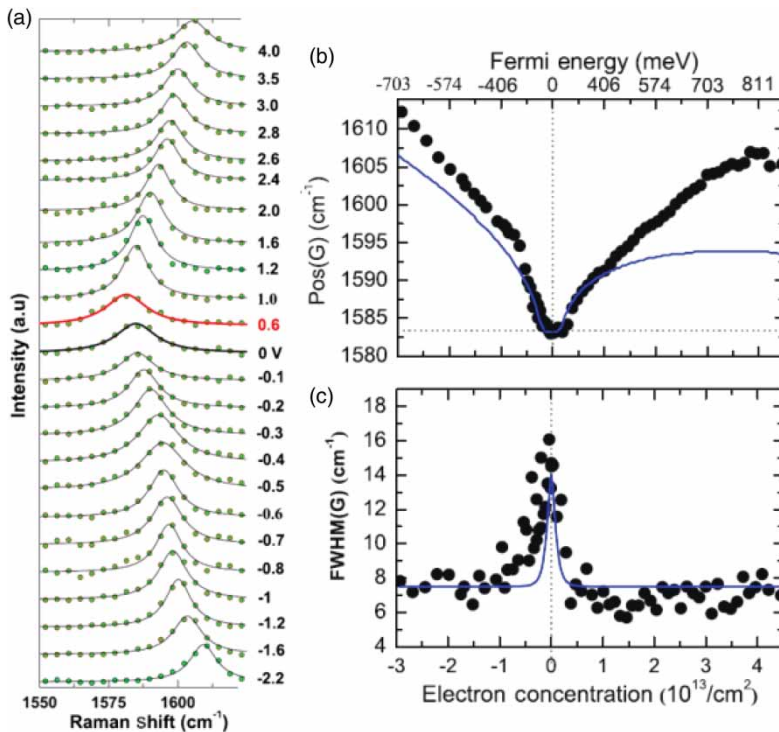


Figure 21. The dependence of the Raman G peak frequency of mono-layer graphene on doping using a gate voltage to provide positive and negative potentials. (A) The G-band spectra at 295 K for many values of the gate voltage V_g are shown. The darker line spectrum is at $V = 0$ but the spectrum at $V = 0.6$ V corresponds to the undoped case, which occurs at $V \neq 0$ due to the natural doping of graphene by the environment. (B) The G peak position (frequency) and (C) the G peak FWHM linewidth as a function of electron concentration as deduced from the applied gate voltage data are shown. Black circles show the measurements and the solid lines show results from a finite-temperature non-adiabatic calculation. Adapted with permission from Macmillan Publishes Ltd. Nature Nanotechnology [195], Copyright © (2008).

2.8. Classification of Raman processes

In this section, we classify the Raman spectra of sp^2 carbon materials from the point of view of Raman processes.

2.8.1. First-order Raman process

After photo-absorption, if one phonon is emitted by the el-ph interaction, we can observe the inelastically scattered light coming from the electron, whereby a phonon is emitted through the el-ph interaction in the first-order Raman spectra. Through the recombination of a photo-excited electron with the hole that was left behind, the scattered electron should have the same k value as the hole, which requires that the phonon q vector should be zero. The phonon thus produced is called a zone-centered (or a Γ point) phonon [104,207,208]. In the case of graphene, the degenerate LO and iTO phonon modes at the Γ point are Raman-active and are known as the E_{2g} symmetry phonon modes. These modes occur around 1585 cm^{-1} , while the oTO phonon mode occurs around 850 cm^{-1} and is an IR-active phonon mode, which does not contribute to the Raman spectra for either defect-free graphene or SWNTs. The remaining three modes are acoustic modes and have zero phonon energy at the Γ point. In the case of SWNTs, the RBM and G-band phonons correspond to first-order Raman processes.

2.8.2. Two-phonon second-order Raman process

After photo-absorption, if two-phonons are emitted by the el-ph interaction, then we can observe inelastically scattered light as a two-phonon second-order Raman process. In this case, there are two possibilities for the actual Raman processes. One process involves the harmonic formed by two

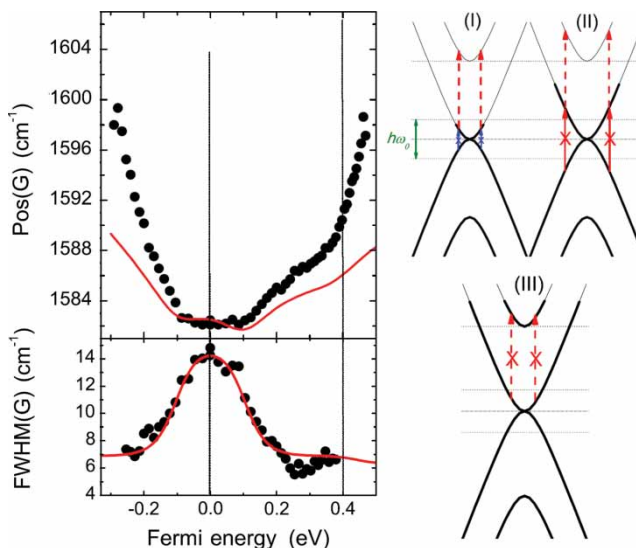


Figure 22. On the left, the peak frequency (Pos(G)) and linewidth (FWHM(G)) for the Raman G-band feature of doped bi-layer graphene vs. Fermi energy are shown. The black circles show the measurements and the solid line shows the finite-temperature non-adiabatic calculation. On the right, schematics of the el-ph coupling at three different doping levels, as indicated by the thicker lines on the electronic bands, are shown. Adapted figure with permission from A. Das *et al.*, *Physical Review B* 79, p. 155417, 2009 [191]. Copyright © (2009) by the American Physical Society.

Γ point phonons, which is an over-tone phonon mode and the overtone mode of the G-band appears at around 3170 cm^{-1} (twice the G-band mode frequency at 1585 cm^{-1}). A feature associated with the harmonic of the D'-band also appears at 3240 cm^{-1} .

The other process is given by emitting two K point phonons with q and $-q$ wavevectors by an inter-valley scattering process. By emitting two phonons with opposite q and $-q$ vectors, the photo-excited electron can go back to its original position and recombine with a hole. Because of the many possible $q \neq 0$ vectors, the spectral width for two-phonon Raman processes is broad compared with the linewidths typically found in the first-order Raman spectra. The G' -band around 2700 cm^{-1} arises from a two-phonon Raman process occurring near the K point iTO phonon mode. For both cases of two-phonon scattering processes, there is no restriction on $q = 0$ for either of these processes. Furthermore, the two phonons are not always the same types of phonon modes and can have the same wavevector but different frequencies. If two different phonon modes are involved in the two-phonon process, the Raman shift becomes the sum of the two phonon mode frequencies, which we call a combination mode. It is important to emphasize that combination modes which combine via an intra-valley scattering process together with an inter-valley scattering process are not possible since the corresponding q vectors would be completely different from each other¹⁴ and conservation of momentum would be violated.

2.8.3. One-phonon and one-elastic second-order Raman process

In a real crystal lattice, there are many defect structures by which a photo-excited electron can be scattered by defects, such as the edges of graphene or point defects in both graphene and carbon nanotubes. As far as there is no elementary excitation creation or annihilation at the defect site, the scattering is elastic and only the momentum of the electron k can be changed to $k + q$ by the q component of the defect potential $V(q)$. There is also the possibility of a second-order Raman scattering process in which one of the two phonon scattering processes can be changed from an inelastic scattering process to an elastic scattering process. Here, we still call this scattering process a second-order Raman process, since the number of the order is defined by the number of scattering events that occur. For this process, the corresponding Raman shift involves only one phonon energy. What is different here from the first-order process is that the restriction on $q = 0$ is relaxed and many different phonon modes with $q \neq 0$ can contribute to the Raman spectra. The D-band around 1350 cm^{-1} is near the K point iTO phonon mode and the D-band intensity come from a Raman process involving one-phonon and one-elastic inter-valley scattering process. The D'-band around 1620 cm^{-1} is near the Γ point LO phonon mode which consists of one-phonon and one-elastic intra-valley scattering process. Since many q vectors are possible in this Raman process, defect-related Raman peaks are generally broad compared with typical first-order Raman features. The optical process which consists of only elastic scattering processes is the Rayleigh scattering process.

In Figure 23, we show the schematics for (a1,a2) first-order and (b1-b4) one-phonon second-order and finally (c1,c2) two-phonon second-order, resonance Raman spectral processes [209]. In Figure 23, we also show the incident and the scattered resonance conditions. For second-order Raman processes, a DR Raman condition is satisfied [104,209,210], which is clarified in Section 2.8.4. Although not shown in Figure 23, the Raman process for inter-valley phonons which connects the K and K' points in the BZ is a second-order process.

2.8.4. Double resonance Raman spectra

Referring to Figure 23 [104,208], there are three intermediate electronic states in second-order Raman processes: (1) excited states at k , (2) the intermediate state at $k + q$, and (3) the second

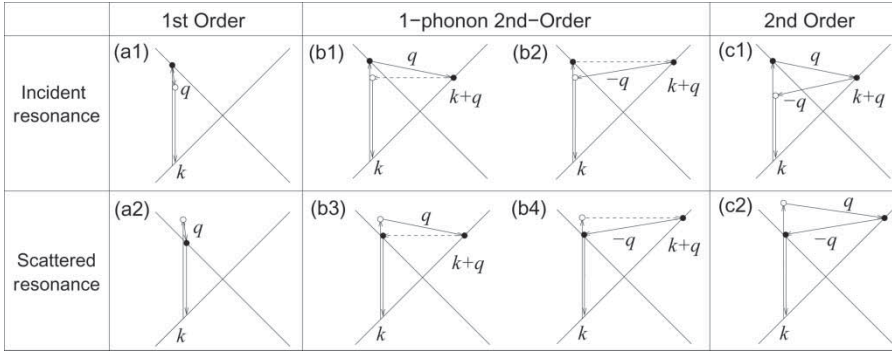


Figure 23. Schematic diagrams for (a1,a2) first-order and (b1–b4) one-phonon second-order, (c1,c2) two-phonon second-order, resonance Raman spectral processes for which the top diagrams refer to incident photon resonance conditions and the bottom diagrams refer to the scattered resonance conditions. For one-phonon, second-order transitions, one of the two scattering events is an elastic scattering event (dashed line). Resonance points are shown as solid circles [104,207–209]. Adapted with permission from R. Saito *et al.*, *New Journal of Physics* 5, p. 157, 2003 [209]. Copyright © (2003) by the Institute of Physics.

intermediate state back to k (see Figure 23(b) and (c)) [209]. This two-scattering amplitude process is expressed by perturbation theory in which the numerator of the resulting term consist of four scattering matrix elements (two for photon absorption and emission, and two for phonon emission or absorption), while the denominator of this term consists of three energy difference factors. If two of the three energy difference factors becomes zero, the scattering intensity becomes strongly enhanced by each of these factors. We call a process containing two resonance denominators double resonance (DR) Raman scattering [104,174,207,210,211]. The G' -band of mono-layer graphene represents a resonance Raman spectral feature for an iTO phonon mode near the K point which is resonant for each of the three scattering processes.

2.8.5. Dispersive behavior of the phonon energy in DR Raman processes

An important aspect of the DR Raman spectra is that the observed phonon energy changes by changing the laser excitation energy, which gives rise to a dispersive behavior of the scattered phonon. Since the electronic energy dispersion of the π and π^* bands is linear in k as measured from the K (K') point in the 2D BZ of graphene, a special k value is selected on an equi-energy line for a given laser energy (E_{laser}). In order to satisfy energy–momentum conservation for the DR scattering from k to $k - q$ and from $k - q$ to k , the phonon momentum q is selected by the circles near the K point shown in Fig. 23(c). When we calculate the phonon density of states for this DR process, the DR wave vector $q_{\text{DR}} \approx 2k$ for a phonon frequency $\omega(q)$ is selected [104,207]. Thus by changing the photon energy, we can probe the phonon energy along the phonon energy dispersion [174,210,212]. The D- (G' -) band frequency is 1350 (2700) cm^{-1} for $E_{\text{laser}} = 2.41$ eV and the D- (G' -) band frequency increases by 53 (106) cm^{-1} by changing E_{laser} by 1 eV [213]. In the case of SWNTs, the selection of q_{DR} becomes more selective because of the 1D character of q_{DR} , which is the reason why a sharp D-band spectral feature occurs in the case of SWNTs [210,211]. The pioneering work on the variation of the G' -band peak frequency with laser excitation energy was first studied by Vidano *et al.* [214,215] and by Baranov *et al.* [207].

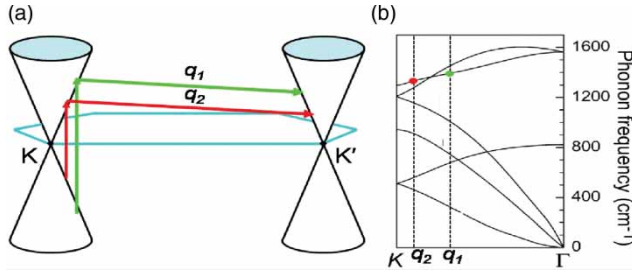


Figure 24. (a) The schematic diagram shows the light-induced e–h formation and the one electron–one phonon scattering event taking place in the DR process with two different excitation laser energies (associated with phonon wave vectors q_1 and q_2 , respectively), which are indicated by the gray and black arrows, respectively. The two events in the DR process can occur in either order in time. (b) The phonon dispersion in graphene is shown where the phonon wavevector q that fulfills the DR requirements for each E_{laser} value in (a) is also indicated in terms of the phonon wavevectors q_1 and q_2 (see text). Reprinted figure with permission from A. Jorio *et al.* Spectroscopy in Graphene Related Systems, 2010 [1]. Copyright © Wiley–VCH Verlag GmbH & Co. KGaA.

2.8.6. The inter-valley double resonance Raman scattering processes

When a photon with a given energy is incident on mono-layer graphene, it will excite an electron from the valence band to the conduction band vertically in momentum space (vertical arrows in Figure 24(a)). Since the graphene energy band does not have an energy gap, we always have an electron with wavevector k for any E_{laser} value which satisfies energy conservation $E_{\text{laser}} = E^c(k) - E^v(k)$. In the single-resonance Raman process, a zone center ($q = 0$) phonon is created or destroyed by coupling with the excited electron or hole, and the e–h recombination generates the Raman shifted photon.

In contrast, the photo-excited electron at k can be scattered by emitting a phonon with wave vector q to a state at $k - q$, as shown by the quasi-horizontal arrows in Figure 24(a). The phonon emission in Figure 24(a) corresponds to an inter-valley scattering process in which the phonon q vector connects two energy bands at the K and K' points of the BZ. If there is a phonon in the vibrational structure of graphene with the wavevector q and phonon energy E_q so that this photon can connect the two conduction electronic states, then this phonon scattering process will be resonant. The DR process (involving both electron–photon and el–ph scattering, shown in Figure 24(a)) will then take place.

2.8.7. Forward and backward scattering

The slope of the energy dispersion $\partial E/\partial k$ is called the *group velocity*. When we consider only the direction of the group velocity for the initial k , there are two possibilities for the scattered $k - q$ states, as shown in Figure 25, where each of the inter-valley (a,b) and intra-valley (c,d) scattering processes correspond to backward (a,c) and forward (b,d) scattering. Here the backward (forward) scattering means that the direction of the group velocity does (does not) change after scattering. The corresponding q vectors for inter-valley scattering are given by (see Figure 26)

$$q = K + q_{\text{DR}} = K + k + k' \approx K + 2k \quad (\text{backward scattering}), \tag{11}$$

$$q = K + q_{\text{DR}} = K + k - k' \approx K \quad (\text{forward scattering}), \tag{12}$$

where K is the magnitude of the reciprocal lattice vector that connects K and K' , and k (k') here is measured from the K (K') point, which means that the double resonance wave vector q_{DR} is the

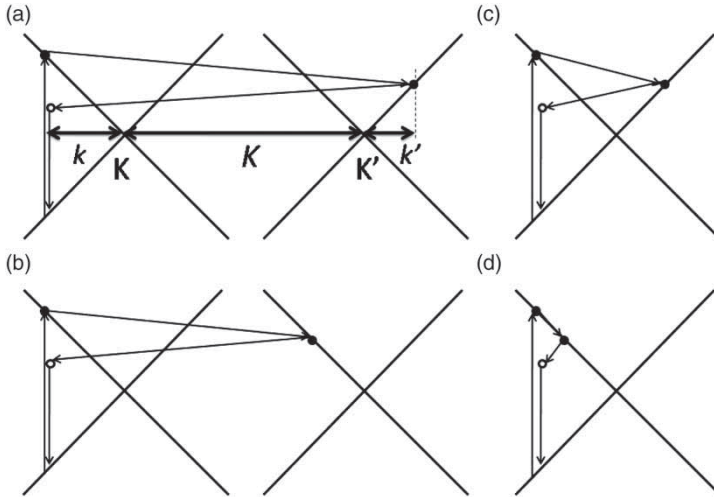


Figure 25. The full DR Stokes Raman processes for inter-valley (a,b) and intra-valley (c,d) scattering. Here (a,c) relates to the backward scattering process with $q_{\text{DR}} = k + k'$ and (b,d) relates to the forward scattering process with $q_{\text{DR}} = k - k'$, with k and k' measured from the K point. The reciprocal lattice vector K is the distance between the K and K' points, k (k') is the distance of the resonant states from K (K'), as defined in (a). Reprinted figure with permission from A. Jorio *et al.* Spectroscopy in Graphene Related Systems, 2010 [1]. Copyright © Wiley–VCH Verlag GombH & Co. KGaA.

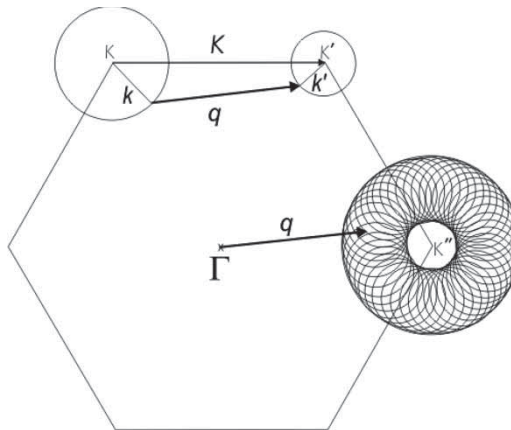


Figure 26. One of the possible DR Stokes Raman processes involving the emission of a phonon with wavevector $-\mathbf{q}$. The set of all phonon wavevectors \mathbf{q} which are related to transitions from points on the two circles around K and K' gives rise to the collection of small circles around the K'' point obeying the vector sum rule $\mathbf{q} = \mathbf{K} - \mathbf{k} + \mathbf{k}'$ (here we neglect the trigonal warping effect). Note that this collection of circles is confined to a region between the two circles with radii $q_{\text{DR}} = k + k' \approx 2k$ and $q_{\text{DR}} = k - k' \approx 0$. The differences between the radii of the circles around K and K' and thus the radius of the inner circle around K'' are actually small in magnitude and are here artificially enlarged for clarity in presenting the concepts of the double resonance process. Adapted with permission from L.G. Cançado *et al.*, *Physical Review B* 66, p. 35415, 2002 [216]. Copyright © (2002) by the American Physical Society.

phonon wavevector distance linking the K and K' points. In the case of intra-valley scattering, we just put $K = 0$ into Equations (11) and (12). Since the phonon energy is usually small compared to the excited electronic energy levels, $k \approx k'$, these two double resonance conditions approach $q_{\text{DR}} = 2k$ and $q_{\text{DR}} = 0$ (as is commonly used in the literature [114,172,210]).

2.8.8. DR q circles in 2D graphene

The picture discussed up to now is not the full story because graphene is a 2D material. For a given laser energy, not only is the e–h excitation process shown in Figure 24 resonant, but any similar process on a circle in these cones defined by E_{laser} (see Figure 26) is also resonant. Furthermore, the mechanism of DR is actually satisfied by any phonon whose wavevector connects two points on two circles around the K and K' points, as shown in Figure 26 [216]. (In constructing this figure, we neglect the trigonal warping effect of the constant energy surface of graphene for simplicity). A phonon with wavevector q connects two points along the circles with radii k and k' around the K and K' points, respectively, where the difference between k and k' (for $k \neq k'$) comes from the energy loss from the electron to the phonon.¹⁵ By translating the vector q to the Γ point, and considering all possible initial and final states around the K and K' points, the doughnut-like figure shown in Figure 26 is generated [216]. Therefore, there is a large set of q vectors fulfilling the DR condition. However, there is also a high density of phonon wavevectors \mathbf{q} satisfying the DR mechanism for which the end points of the wavevectors measured from the Γ point are on the inner and outer circles of the “doughnut” in Figure 26. Therefore, the radii of the inner and outer circles around K'' (see Figure 26) are, respectively, $k - k'$ and $k + k'$. Exactly as given by the 1D model (Equations (11) and (12)), these wavevectors correspond to the phonons associated with the singularities in the density of \mathbf{q} vectors that fulfill the DR requirements, and these special wavevectors in Figure 26 are expected to make a significantly larger contribution to the second-order Raman scattering process. However, for a full description and lineshape analysis, it is important to consider the 2D model, which seems to generate the asymmetric lineshape that is observed for the 2450 cm^{-1} G' -band feature.

Finally, Figure 24 shows that, if E_{laser} is changed, then the specific wavevector q and phonon energy E_q that will fulfill the DR conditions will also change. This effect gives rise to the dispersive nature of the G' -band, which comes from an *inter-valley* DR Raman process involving an electron with wave vector k in the vicinity of the K point and two iTO phonons with wave vectors $q_{\text{DR}} \approx 2k$, where both k and q_{DR} are measured from the K point.

To analyze experimental data for graphene in Figure 27 one has to consider the electron and phonon dispersion of a graphene mono-layer. Near the K point, the electron and phonon dispersions can be approximated by the linear relations $E(k) = \hbar v_{\text{F}} k$ and $E(q_{\text{DR}}) = \hbar v_{\text{ph}} q_{\text{DR}}$, respectively, where $v_{\text{F}} = \partial E(k)/\partial k$ and $v_{\text{ph}} = \partial E(q)/\partial q$ are the electron and phonon velocities near the K point, respectively (in which v_{F} is usually called the Fermi velocity, $v_{\text{F}} \sim 10^6 \text{ m/s}$) for graphene. We denote the electron (phonon) wave vector by k (q_{DR}) which is measured with respect to the K point, so that the conditions for the DR Raman effect are given by [1]

$$\begin{aligned} E_{\text{laser}} &= 2v_{\text{F}}k, \\ E_{\text{ph}} &= v_{\text{ph}}q_{\text{DR}}, \\ q_{\text{DR}} &= k \pm k', \end{aligned} \tag{13}$$

where E_{laser} and E_{ph} are, respectively, the laser and phonon energies, and k' is the scattered electron wave vector near the K' point in the graphene BZ. It is important to remember that we are dealing here with combination modes, so that the observed E_{ph} has to reflect this combination. For example, for the G' -band, the observed G' -band energy is given by $E_{G'} = 2E_{\text{ph}}$, where E_{ph} is the energy for

the iTO phonon mode at q_{DR} .¹⁶ Making another commonly used approximation in Equation (13), i.e., $q_{\text{DR}} = k + k' \approx 2k$, then $E_{G'}$ can be written as [1]

$$E_{G'} = 2 \frac{v_{\text{ph}}}{v_{\text{F}}} E_{\text{laser}}. \quad (14)$$

A drawback in using the DR Raman features to define the electron and phonon dispersion relations is that the measured values depend on both v_{ph} and v_{F} , and one has to be known in order to obtain the other. In addition to this problem, the physics of the phonon dispersion for graphene near the K point is rather complex due to the Kohn anomaly, and the KA also occurs for phonons at $q \rightarrow K$ (see Section 2.7). The high frequency of the iTO phonon when combined with the KA near the K point are together responsible for the strong dispersive behavior observed for $\omega_{G'}$. The exact values for v_{ph} and v_{F} are still under debate since they also depend on the complex physics of many-body effects [112,194,217–220]. This is one area where more work for future research is needed.

2.8.9. Dispersive behavior of the G' - and G^* -band

Since both G^* and G' features in Figure 27 are due to double resonance processes, both Raman features show dispersion with E_{laser} , but with quite different characteristics. So far, we explained that there are two possibilities for selecting q while satisfying the double resonance condition: $q_{\text{DR}} \approx 2k$ and 0. The condition for $q_{\text{DR}} \approx 0$ will or no select a phonon frequency at $q = 0$ measured from the K point, and these q_{DR} show weak dispersion even though the signal is due to a DR Raman spectra. Figure 27(a) shows the Raman spectra in the region of both the G^* ($\sim 2450 \text{ cm}^{-1}$) and G' ($\sim 2700 \text{ cm}^{-1}$) bands for different laser excitation energies. Also the G^* -band can either be explained by the $q \approx 0$ DR relation [221] or by the $q \approx 2k$ relation applied to an *inter-valley* process [213], but involving two different phonons in each case. Figure 27(b) shows the G' and G^*

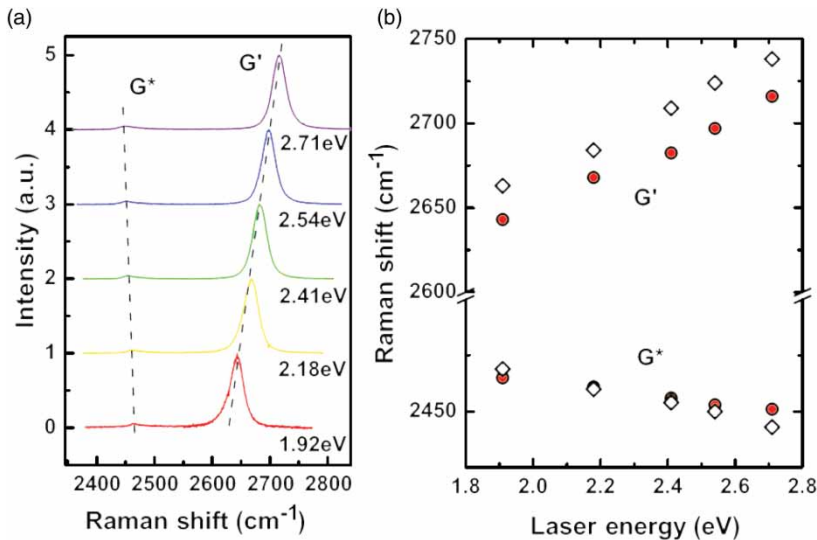


Figure 27. (a) Raman spectra of the G' and the G^* -bands of mono-layer graphene for 1.92, 2.18, 2.41, 2.54 and 2.71 eV laser excitation energy. (b) Dependence of $\omega_{G'}$ and ω_{G^*} on E_{laser} . The circles correspond to the graphene data and the lozenges correspond to data for turbostratic graphite. Adapted with permission from D. Mafra *et al.*, *Physical Review B*, 76, p. 233407, 2007 [213]. Copyright © (2007) by the American Physical Society.

frequencies $\omega_{G'}$ and ω_{G^*} as a function of E_{laser} for graphene and turbostratic graphite (for which the stacking between graphene layers is random). The G' -band in Figure 27 exhibits a highly dispersive behavior with $(\partial\omega_{G'}/\partial E_{\text{laser}}) \simeq 88 \text{ cm}^{-1}/\text{eV}$ for mono-layer graphene, $95 \text{ cm}^{-1}/\text{eV}$ for turbostratic graphite [213] and $106 \text{ cm}^{-1}/\text{eV}$ for carbon nanotubes (see Figure 27 and [222]). The G^* -band feature exhibits a much less pronounced dispersion than the G' -band, and of opposite sign, with $(\partial\omega_{G^*}/\partial E_{\text{laser}}) \simeq -10$ to $-20 \text{ cm}^{-1}/\text{eV}$ for both mono-layer and turbostratic graphite [208,213], and no dispersion is reported for carbon nanotubes [221]. It should be noted that a different interpretation to the origin of the G^* -band is given in [131,223], which together with [221] identified the origin of the 2450 cm^{-1} peak with the overtone of the 1225 cm^{-1} feature which has a peak in the phonon density of states for two phonons [223], while [224,225] assigned this feature to the combination modes $iTA + iTO$. As already stated, the $q_{\text{DR}} \approx 2k$ wavevector gives rise to the G' -band, while the $q_{\text{DR}} \approx 0$ wavevector gives rise to a DR feature coming from the iTO phonon very close to the K point. The $q_{\text{DR}} \approx 0$ processes are expected to be less intense than the $q_{\text{DR}} \approx 2k$ processes because the destructive interference condition is exactly satisfied for $q_{\text{DR}} = 0$ [208].

2.8.10. Double resonance, overtone and combination modes

The sp^2 carbons exhibit several combination modes and overtones, which are shown in Figure 28 for graphite whiskers as a function of frequency up to 7000 cm^{-1} [226]. Basically all the branches in the phonon dispersion can be seen to have a combination and overtone Raman features which obey the DR condition [104,210]. Many of the peaks observed in the spectra of Figure 28 below 1650 cm^{-1} are actually one-phonon bands activated by defects (see Section 4.3). Above 1650 cm^{-1} , the observed Raman features are all multiple-order combination modes and overtones, and here too some of the features in Figure 28 are also activated by defects.

As shown in Figure 28, the DR peaks change frequency with changing E_{laser} , and they can be fitted onto the phonon dispersion diagram shown in Figure 29 using DR theory. The data points displayed in Figure 29 all stand for the $q_{\text{DR}} \approx 2k$ DR backward resonance condition, those near Γ and K coming from intra-valley and inter-valley scattering processes, respectively. Actually, in the Raman spectra there are no characteristic features distinguishing peaks associated with the intra-valley scattering process from those associated with inter-valley scattering processes, or even features that distinguish between the $q_{\text{DR}} \approx 2k$ or $q_{\text{DR}} \approx 0$ resonance conditions. All we have in hand in analyzing actual Raman spectra is the E_{laser} dependence of each peak. Here, each peak has to fulfill one of the DR processes and to fit the predicted phonon dispersion relations. For example, the data points near the K point in Figure 29 that are assigned as the $iTO+LA$ combination mode (TO+LA) could alternatively be assigned to a $q_{\text{DR}} \approx 0$ process, since this combination mode is weakly dispersive [221]. Supporting this assignment is the asymmetric (DR phonon-density-of-states-like shape) observed for this peak, and against this identification is the destructive interference working towards DR Raman processes at exactly $q = K$ [208]. The debate about the $iTO + LA$ combination mode assignment near the K point remains for future clarification. Near the Γ point, the dispersive behavior is more clear and the assignment of the observed Raman features is on a more solid foundation [227].

2.9. Summary

The power of Raman spectroscopy for studying carbon nanotubes is in particular revealed through exploitation of the resonance Raman effect, which is greatly enhanced by the singular density of electronic states of SWNTs and the resonant effect comes from the 1D confinement of the electronic states due to the small diameters of carbon nanotubes. Soon after the discovery of the

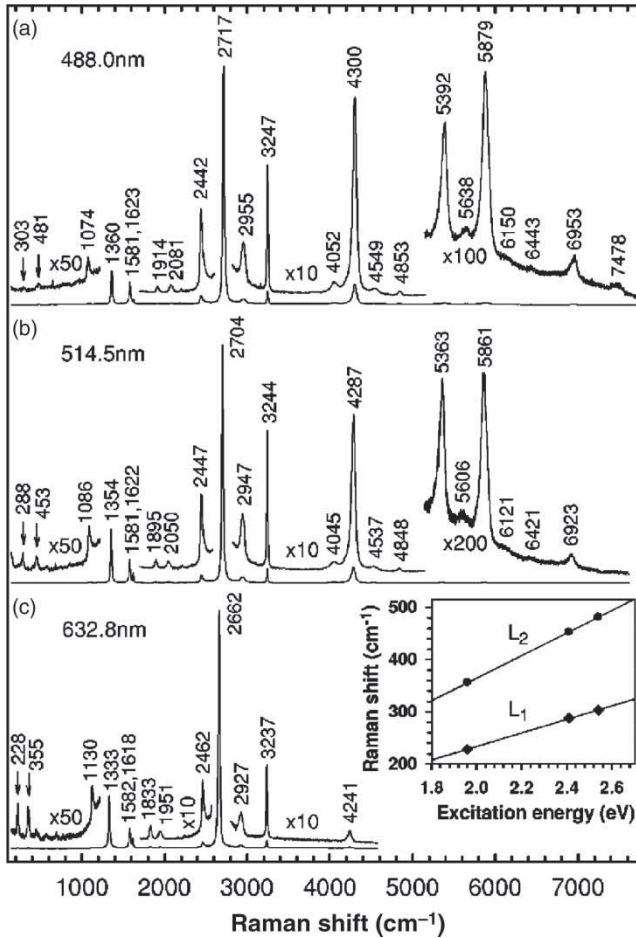


Figure 28. Raman spectra of graphite whiskers obtained at three different laser wavelengths (excitation energies) [226]. Note that some phonon frequencies vary with E_{laser} and some do not. Above 1650 cm^{-1} the observed Raman features are all multiple-order combination modes and overtones (see Figure 29), though some of the peaks observed below 1650 cm^{-1} are actually one-phonon bands activated by defects. The inset to (c) shows details of the peaks labeled by L_1 and L_2 . The L_1 and L_2 peaks, which are dispersive, are explained theoretically by the defect activation of double-resonance one-phonon processes (see Section 2.8.10) involving the acoustic iTA and LA branches, respectively, as discussed in Ref. [210]. Adapted figure with permission from P.H. Tan *et al.*, *Physical Review B* 64, p. 214301, 2001 [226]. Copyright © (2001) by the American Physical Society.

resonance Raman effect in SWNTs [103], it was found that the resonance lineshape could be used to identify the nanotube structure, i.e., the chiral indices (n, m) [111], and to distinguish metallic from semiconducting SWNTs [128,228]. It is clear that most of the results achieved up to now have been developed for SWNTs, while the optics of graphene and nanoribbons is still at an early stage. This is the way it happened historically, and the knowledge developed in carbon nanotube science is now fostering an amazingly fast development of graphene photo-physics. It is expected that graphene photo-physics will follow a similar path of development that will reveal much new physics as this very fundamental field develops such as the understanding of the KA which helped to elucidate the phonon dispersion relation of graphite and all related sp^2 carbons.

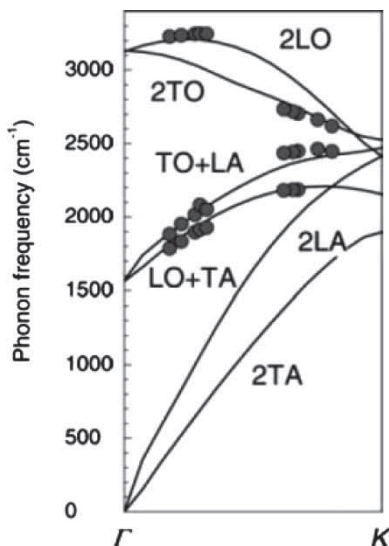


Figure 29. Two-phonon dispersion of graphite based on second-order double-resonance peaks in the Raman spectra (dark circles). Solid lines are dispersion curves from *ab initio* calculations considering combination modes and overtones associated with totally symmetric irreducible representations. Adapted figure with permission from J. Maultzsch *et al.*, *Physical Review B* 70, p. 155403, 2004 [208]. Copyright © (2004) by the American Physical Society.

3. Calculation method of resonance Raman spectra

Within the tight-binding approximation methods, we can calculate the Raman spectra and the Raman excitation profile of an (n, m) nanotube by considering the electron–photon, el–ph, exciton–photon and exciton–phonon interactions. In this section, the (n, m) dependence of the RBM and G-band intensities, spectral width and resonance window are directly compared with experiment. The exciton energy calculations can reproduce the E_{ii} energy within high accuracy. In Section 3, however, we do not mention the environmental effects (see Section 5.2.1) which are here comparatively considered here by experiment [229,230] and theory [231,232]. The electron–electron interaction and elastic scattering matrix elements [233] need to be developed further for obtaining the asymmetric shape of the BWF lines and the D- (G' -) band spectra, respectively. Using the established computer library, we can extend these calculations to consideration of the coherent phonon response of a nanotube [165]. In this section, we do not mention the polarization dependence of the Raman spectra, in which the screening effect (the so-called depolarization effect [234]) is important.

3.1. Overview of calculations reviewed in this section

In Section 3, we review the theoretical calculation of the resonance Raman spectra and exciton energy states for carbon nanotubes. The method used here for carbon nanotube calculations can also be applied to graphene Raman spectra, though we do not need to consider exciton states for graphene. Most of the quantitative comparisons are made in Section 3 with regard to resonance energy, Raman frequencies and spectral linewidths. In order to obtain the Raman intensity, we review the calculations of the excitonic (electronic) interaction matrix element for nanotubes (graphene). Since the derivations consist of many topics, each topic is first briefly mentioned in this subsection and is then described in more detail in the following subsections.

3.1.1. Raman scattering and phonon energy dispersion

In Raman spectroscopy studies of solids, we generally observe the phonon frequency at the center of the BZ (zone-center phonon). Other inelastic scattering techniques, such as inelastic neutron scattering [235,236], or inelastic X-ray scattering [208] or electron energy loss spectroscopy [237,238] provide measurements of the phonon dispersion inside the BZ, which we can reproduce theoretically [235,239] either by fitting force-constant calculations to experimental data or by first-principles calculations [32,240,241]. Graphene-related systems have a special electronic structure which allows the observation of phonons in the interior of the BZ by DR Raman spectroscopy. In Section 3.2, we mention how to obtain the phonon dispersion relations by force-constant models.

3.1.2. Electronic energy bands

Optical processes can be studied by Raman spectroscopy as well as by other techniques. If there is either a photo-absorption or a photo-emission process that couples the ground state to an excited state of an electron, then the amplitude of the phonon scattering process is greatly enhanced if the excited state is a real electronic state. This resonant process is known as resonance Raman spectroscopy. In order to obtain the resonance condition by which a given laser energy E_{laser} matches the transition energy of the actual electronic states, the electronic energy bands are calculated by a simple tight-binding method in Section 3.3 or by an extension of this method as given in Section 3.3.1 using the so-called extended tight-binding model. Angle-resolved photo-electron spectroscopy (ARPES) experiments [123–126] are especially relevant for providing information about the occupied electronic energy bands in graphene.

3.1.3. The double resonance process

While the most usual first-order Raman processes measure only zone center phonon modes, excited electron scattering processes may also take place involving phonons in the interior of the BZ. Such processes can become Raman allowed either by two phonon scattering processes, thus conserving momentum, or in the presence of a lattice defect, where the momentum conservation requirement can be broken. However, these are generally low probability processes. In graphene-related systems, however, such DR scattering processes become highly probable because of the so-called DR phenomena in graphene [104,207,210]. One resonant phenomenon is light absorption or emission, and the other resonant phenomenon is the scattering of the excited electron (or hole) by phonons. Here “resonant” means that the phonon brings the electron from one real state to another real state, which matches the energy and momentum transfer required for momentum and energy conservation.

3.1.4. Electron–photon and electron–phonon interactions

To obtain good agreement with experiment, it is necessary to include el–ph and electron–photon interactions in such calculations of the Raman intensity as a function of E_{laser} . In this connection, we here discuss the calculation of the electron–photon matrix elements (Sections 3.4 and 3.4.1) and of the el–ph matrix elements (Section 3.4.3), which are the matrix elements that appear in the numerator of the perturbation calculation of the Raman scattering amplitude (Section 3.6). Calculation of the Raman excitation profile (Section 3.6.3) in which the Raman intensity is observed as a function of E_{laser} is of great interest for obtaining the Raman intensity at resonance which is the quantity of greatest interest for experimental studies. Many experimental Raman studies that are found in the literature are actually not carried out under fully resonance conditions, but only

within the resonance window, so care must be exercised in making proper comparisons between experiment and theory.

3.1.5. Excitons

In the case of carbon nanotubes, the exciton binding energy is much larger (up to 1 eV [120–122,147,242]) than that for Si (which is in the meV range). The exciton, which is formed from a photo-excited electron and the hole that is left behind, is especially important and dominates the observed optical processes in carbon nanotubes which are 1D systems where excitonic effects are exceedingly strong. Even at room temperature, the excitonically mixed electronic states are specified by a wavevector \mathbf{k} so as to form a spatially localized state. In order to obtain excitonic states and their corresponding wavefunctions, the Bethe–Salpeter equation for π electrons is used here within the tight-binding method (Section 3.5). Using excitonic wavefunctions, we can calculate the relevant exciton–photon (Section 3.6) and exciton–phonon (Section 3.6.3) matrix elements. Two-photon absorption or time-dependent Raman spectroscopy have also been used to observe many specific exciton-related phenomena.

3.1.6. Resonance window and the Kohn Anomaly

Since the photo-excited electron (or hole) has a finite lifetime (less than 1 ps), the transition energy of an exciton has an energy uncertainty which is observed as an energy width in the measurement of the Raman excitation profile, which we also call the resonance window. A typical value for the experimentally reported resonance windows is 100 meV and the origin of the finite lifetime of the photo-excited carriers lies in the exciton–phonon scattering process, which depends on the metallicity, chiral angle and diameter of the SWNT. In the case of metallic nanotubes, phonons typically couple to an e–h pair excitation by the el–ph (or more precisely the exciton–phonon) interaction. **Second-order perturbation theory for the phonon energy gives values for the energy shifts and spectral broadening that arise through the el–ph interaction, and we call these energy shifts and broadening effects the KA [127,194,197–199,243].** This topic is discussed in Section 3.6.5. The KA is observed experimentally in the G-band of graphene (Section 2.7.1) and in both the G-band and the RBM features for metallic nanotubes in gating or electro-chemical doping experiments Section 2.7.3 [196,203–205].

3.2. Tight-binding calculation for phonons

The phonon energy dispersion can be calculated by using a force constant tensor which connects the relevant motion of nearest-neighbor atoms through these theoretical calculations. The equations of motion are given by

$$M_i \ddot{\mathbf{u}}_i = \sum_j K^{(ij)} (\mathbf{u}_j - \mathbf{u}_i), \quad (i = 1, \dots, N), \quad (15)$$

where M_i and \mathbf{u}_i are, respectively, the mass and the vibrational amplitude of the i th atom and $K^{(ij)}$ represents a 3×3 force constant tensor which connects i th and j th atoms. The summation on j is taken over the j th nearest neighbor atoms so as to reproduce the phonon energy dispersion relation (see Figure 30). The $K^{(ij)}$ terms are obtained by fitting to experimentally obtained phonon dispersion relations, such as are determined from neutron or X-ray inelastic scattering measurements [208,235,239]. The fitting procedure to the experimental phonon dispersion is possible even if the KA effect is included. However, the broadening of the phonon dispersion due to the finite lifetime

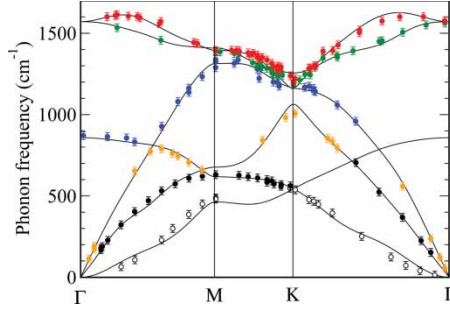


Figure 30. Phonon dispersion of graphene in the 2D BZ. The symbols are experimental data obtained by inelastic X-ray scattering [244] and the lines are fitted to the experimental phonon data using up to 14th nearest-neighbor interactions [245].

of phonon cannot be expressed by the present method and the self-energy for the phonon should then be calculated as discussed below [196,205,219,220,246].

Since the lattice is periodic, each displacement \mathbf{u}_i in the unit cell can be expressed by a wave with a phonon wavevector \mathbf{k} and frequency ω as follows:

$$\mathbf{u}_{\mathbf{k}}^{(i)} = \frac{1}{\sqrt{N_u}} \sum_{\mathbf{R}_i} e^{i(\mathbf{k}\cdot\mathbf{R}_i - \omega t)} \mathbf{u}_i, \quad (16)$$

where the sum is taken over all N_u lattice vectors \mathbf{R}_i in the crystal for the i th atom in the unit cell. The equation for $\mathbf{u}_{\mathbf{k}}^{(i)}$ ($i = 1, \dots, N$), where N is the number of atoms in the unit cell, is given by [32]

$$\left[\sum_j K^{(ij)} - M_i \omega^2(\mathbf{k}) I \right] \mathbf{u}_{\mathbf{k}}^{(i)} - \sum_j K^{(ij)} e^{i\mathbf{k}\cdot\Delta\mathbf{R}_{ij}} \mathbf{u}_{\mathbf{k}}^{(j)} = 0 \quad (17)$$

in which I is a 3×3 unit matrix and $\Delta\mathbf{R}_{ij} = \mathbf{R}_i - \mathbf{R}_j$ denotes the relative coordinate of the i th atom with respect to the j th atom. The simultaneous equations implied by Equation (17) with $3N$ unknown variables $\mathbf{u}_{\mathbf{k}} \equiv {}^t(\mathbf{u}_{\mathbf{k}}^{(1)}, \mathbf{u}_{\mathbf{k}}^{(2)}, \dots, \mathbf{u}_{\mathbf{k}}^{(N)})$, for a given \mathbf{k} vector, can be solved by a diagonalization of the $3N \times 3N$ matrix in brackets, which we call the dynamical matrix. By diagonalizing the dynamical matrix for each \mathbf{k} , we get the phonon frequencies and corresponding amplitudes as a function of \mathbf{k} , $\omega(\mathbf{k})$ and $\mathbf{u}_{\mathbf{k}}$, respectively, which are the eigenvalues and eigenfunctions of the dynamical matrix.

In Figure 30, the phonon dispersion relations of graphene are plotted in the 2D BZ. Lines are fitted for the calculated phonon energy dispersion to the experimental data for inelastic X-ray scattering (symbols) by a set of force constants that includes force constants up to 14th nearest neighbors [245]. This force constant set is obtained by minimizing the square of the difference between experiment and theory for each experimental data point. In order to get good convergence for the nonlinear fitting, we must start with a small number of nearest neighbors and we then increase the number of neighbors one by one. Further, in order to get the required zero value for the acoustic phonon modes at the Γ point, we should consider the relationships between the force constant set, known as the force constant set sum rule [217]. Degenerate in-plane optical phonon modes around 1600 cm^{-1} at the Γ point are known by symmetry requirements to correspond to the Raman-active phonon mode (G-band), while the out-of-plane optical (oTO) phonon mode around 860 cm^{-1} at the Γ point is an infrared-active phonon mode. The acoustic modes are discussed in [247].

The phonon modes near the K point and Γ point can be observed by defect-induced or two-phonon derived features in the Raman spectra. The phonon modes along the phonon dispersion relation can be observed by studying phonon modes arising from DR Raman processes (see Section 2.8.6) [210]. The LO phonon mode (the highest frequency mode) of graphene has a local minimum at the Γ point and the phonon energy increases with increasing k by a process which we call “over-bending”. The “over-bending” can be reproduced using force constants going beyond the fifth nearest neighbor. Both the in-plane optic phonon modes near the Γ point and the iTO phonon mode near the K point show phonon softening phenomena for graphene and metallic SWNTs and the resulting phonon frequency down-shifts are known as the KA effect [127,194,196–199,205,219,220,243,246] (see Section 3.6.5). When we calculate phonon dispersion by first principles [248–250], the effect of the Kohn anomalies should be taken into account when calculating a force constant set, while in the simple tight-binding method, we just obtain a force constant set either by fitting to the experimental results [208,244,251,252] or by first-principles calculation in which the Kohn anomalies are taken into account. When we obtain a force constant set by the atomic potential as a function of the C–C bond distance, such as by the extended tight-binding method [253,254], we should consider the additional effect of the KA in the calculation.

Interlayer force constants of multi-layer graphene are much weaker than the intralayer force constant set. Each phonon mode of a graphene sheet is split into symmetric and anti-symmetric vibrational modes with respect to the inversion or mirror symmetry of multi-layers, depending on whether the multilayer graphene consists of an even or odd number of graphene layers, respectively. It is important that some phonon modes (oTO, oTA, LO) become Raman active (or inactive) by the interlayer interaction [4].

3.3. Simple tight-binding calculation for the electronic structure

Tight-binding calculations of the electronic energy bands for sp^2 carbons are useful for understanding the physics of sp^2 carbons and for saving computational time. The tight-binding wavefunction $\Psi_j(\vec{k})$, where j denotes the energy band index, is given by a linear combination of a small number of tight-binding Bloch wave functions Φ_j

$$\Psi_j(\vec{k}, \vec{r}) = \sum_{j'=1}^N C_{jj'}(\vec{k}) \Phi_{j'}(\vec{k}, \vec{r}) \quad (j = 1, \dots, N), \quad (18)$$

where $C_{jj'}(\vec{k})$ are coefficients to be determined and N the number of atomic orbitals in the unit cell. When we consider π orbitals for n -layer graphene, then $N = 2n$. Here Φ_j denotes the Bloch function for an atomic orbital φ_j which is given by

$$\Phi_j(\vec{k}, \vec{r}) = \frac{1}{\sqrt{N_u}} \sum_{\vec{R}} e^{i\vec{k} \cdot \vec{R}} \varphi_j(\vec{r} - \vec{R}) \quad (j = 1, \dots, N), \quad (19)$$

where the summation takes place over N_u lattice vectors \vec{R} in the crystals. When we put Equation (18) into the Schrödinger equation $\mathcal{H}\Psi_j = E\Psi_j$ for a Hamiltonian \mathcal{H} , we get

$$\sum_{j'=1}^N \mathcal{H}_{ij'}(\vec{k}) C_{ij'} = E_i(\vec{k}) \sum_{j'=1}^N S_{ij'}(\vec{k}) C_{ij'} \quad (i = 1, \dots, N). \quad (20)$$

Here $\mathcal{H}_{jj'}(\vec{k})$ and $\mathcal{S}_{jj'}(\vec{k})$ are the Hamiltonian, and the overlap matrices are defined by

$$\mathcal{H}_{jj'}(\vec{k}) = \langle \Phi_j | \mathcal{H} | \Phi_{j'} \rangle, \quad \mathcal{S}_{jj'}(\vec{k}) = \langle \Phi_j | \Phi_{j'} \rangle \quad (j, j' = 1, \dots, N). \quad (21)$$

By defining a column vector \mathbf{C}_i as

$$\mathbf{C}_i = \begin{pmatrix} C_{i1} \\ \vdots \\ C_{iN} \end{pmatrix}, \quad (22)$$

then Equation (20) is expressed by the eigenvalue equation

$$\mathcal{H}\mathbf{C}_i = E_i(\vec{k})\mathcal{S}\mathbf{C}_i. \quad (23)$$

By diagonalization of a given \mathcal{H} and \mathcal{S} for each \vec{k} vector, we get the energy eigenvalues $E_i(\vec{k})$ and eigenfunctions $\mathbf{C}_i(\vec{k})$.

The ij matrix element of \mathcal{H} is given by

$$\begin{aligned} \mathcal{H}_{ij}(\vec{k}) &= \frac{1}{N_u} \sum_{R, R'} e^{ik(R-R')} \langle \varphi_i(r-R') | \mathcal{H} | \varphi_j(r-R) \rangle \\ &= \sum_{\Delta R} e^{ik(\Delta R)} \langle \varphi_i(r-\Delta R) | \mathcal{H} | \varphi_j(r) \rangle, \end{aligned} \quad (24)$$

where $\Delta R \equiv R - R'$ and in the second of line of Equation (24), we use the fact that the tight-binding parameter $\langle \varphi_i(r-R') | \mathcal{H} | \varphi_j(r-R) \rangle$ only depends on ΔR . Similarly, the matrix elements of \mathcal{S} are given by

$$\mathcal{S}_{ij}(\vec{k}) = \sum_{\Delta R} e^{ik(\Delta R)} \langle \varphi_i(r-\Delta R) | \varphi_j(r) \rangle. \quad (25)$$

The tight-binding parameters $\langle \varphi_i(r-\Delta R) | \mathcal{H} | \varphi_j(r) \rangle$ and $\langle \varphi_i(r-\Delta R) | \varphi_j(r) \rangle$ are obtained by: (1) integrating the matrix elements using the atomic orbitals $\varphi_j(r)$ [247] or (2) fitting them so as to reproduce experimentally obtained energy dispersion measurements. Values for a typical fitted parameter set (TBP) are listed in Table 1.

As seen in Table 1, tight-binding parameters are listed for up to the third nearest neighbor (3NN) within a layer (upper half) and for interlayer interactions between graphene layers (lower half) [255]. In Figure 31, we show a definition of the tight-binding parameters listed in Table 1 for the Hamiltonian for pairs of carbon atoms separated by their corresponding distances ΔR [255]. The notation used for the parameters γ_i follows that of Slonczewski and Weiss [257], while γ_0^j and s_j ($j = 1, 2, 3$) denote the in-plane parameters with the j th nearest neighbors up to the 3rd nearest neighbor (3NN). As far as we consider transport properties near the K point of the first BZ, the in-plane nearest-neighbor parameter γ_0^1 is sufficient. However, when we consider optical transition phenomena around the K point, it is necessary to include the parameters γ_0^2 and γ_0^3 which are indicated explicitly in Figure 31 [256]. The parameters γ_1 , γ_3 and γ_4 denote interactions between carbon atoms in the nearest-neighbor layers, while the parameters γ_2 and γ_5 couple carbon atoms in next nearest-neighbor layers. The parameters γ_3 and γ_4 introduce a \mathbf{k} -dependent interlayer interaction and γ_2 sensitively determines a small energy dispersion along the KH direction in the 3D BZ for energy bands near the Fermi energy of graphite (see [5, Fig. 1f]) which gives rise to the semi-metallic nature of 3D graphite.

The overlap tight-binding parameters, s_0 , s_1 and s_2 , are essential for describing the asymmetry between the valence and conduction energy bands relative to the Fermi energy. The energy band

Table 1. Third nearest-neighbor tight-binding (3NN TB) parameters for few-layer graphene and graphite.

TBP	3NN TB-GW ^a	3NN TB-LDA ^a	EXP ^b	3NN TB-LDA ^c	ΔR , pair ^d
γ_0^1	-3.4416	-3.0121	-5.13	-2.79	$a/\sqrt{3}$, AB
γ_0^2	-0.7544	-0.6346	1.70	-0.68	a , AA and BB
γ_0^3	-0.4246	-0.3628	-0.418	-0.30	$2a/\sqrt{3}$, AB
s_0	0.2671	0.2499	-0.148	0.30	$a/\sqrt{3}$, AB
s_1	0.0494	0.0390	-0.0948	0.046	a , AA and BB
s_2	0.0345	0.0322	0.0743	0.039	$2a/\sqrt{3}$, AB
γ_1	0.3513	0.3077	-	-	c , AA
γ_2	-0.0105	-0.0077	-	-	$2c$, BB
γ_3	0.2973	0.2583	-	-	$(a/\sqrt{3}, c)$, BB
γ_4	0.1954	0.1735	-	-	$(a/\sqrt{3}, c)$, AA
γ_5	0.0187	0.0147	-	-	$2c$, AA
E_0^e	-2.2624	-1.9037	-	-2.03	
Δ^f	0.0540 ^g	0.0214	-	-	

^aFits to LDA and GW calculations [255].

^bFit to ARPES experiments by Rotenberg *et al.* [124].

^cFit to LDA calculations by Reich *et al.* [256].

^dIn-plane and out-of-plane distances between a pair of A and B atoms.

^eThe energy position of π orbitals relative to the vacuum level.

^fDifference of the diagonal term between A and B atoms for multi-layer graphene.

^gThe impurity doping level is adjusted in order to reproduce the experimental value of Δ in graphite.

All values are in eV except the dimensionless overlap parameters of s_0 - s_2 . The parameters of fits to LDA and GW calculations are shown. The 3NN Hamiltonian is valid over the whole 2-D (3-D) BZ of graphite (graphene layers) [255]. Mopac93 and Gaussian 9 software packages were used for implementing Gaussian and other software applications.

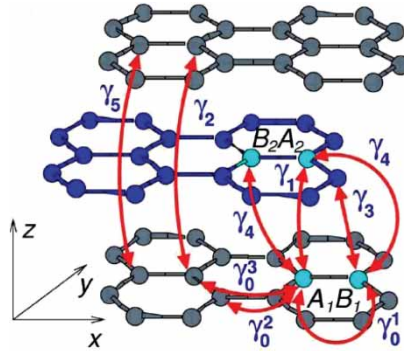


Figure 31. Identification of the various Slonczewski–Weiss parameters for the tight-binding parameters for a pair of carbon atoms separated by a distance ΔR . Adapted figure with permission from A. Grüneis *et al.*, *Physical Review B* 78, p. 205425, 2008 [255]. Copyright © (2008) by the American Physical Society.

width of the conduction band is larger than that of the valence band when using this set of tight-binding parameters [32], thereby inducing asymmetry between the electrons and holes in few layer graphene. Further, depending on whether the number of graphene layers is odd (even), the linear (quadratic) k energy dispersion behavior appears near the K point. Koshino and Ando [258] have explained analytically the reason for the odd-even dependence of the electronic structure of few layer graphene on the number of graphene layers by the tight-binding method.

3.3.1. Extended tight-binding calculation for the graphene electronic structure

The simple tight-binding parameters obtained in Section 3.3 are only for π orbitals in graphene. When we consider SWNTs, the curvature of the cylindrical tube surface should be considered. The curvature effect mixes π orbitals with σ orbitals ($2p_x$, $2p_y$ and $2s$). Furthermore, when we consider the geometrical optimization of the lattice, we need to calculate tight-binding parameters as a function of the actual C–C bonds.

The extended tight-binding (ETB) calculation is a tight-binding calculation for π , σ and $2s$ orbitals, in which the tight-binding parameters for a pair of orbitals are given as a function of the C–C bond lengths and bond angles. The basic treatment of the mixing between π and σ orbitals uses a formalism known as the Slater–Koster method in which p orbitals can be projected on to a chemical bond [259]. Values for the ETB parameters as a function of the C–C bond length are given by first-principles calculations for several sp^2 molecules or solids. For carbon systems, the tight-binding parameters as a function of the C–C bond length have been calculated by Porezag [253], and the optimized structure of SWNTs using ETB parameters reproduced well the transition energy separation E_{ii} especially for SWNTs with diameters smaller than 1 nm [254].

In quantum chemistry calculations, great effort has been given to ETB-like calculations for reproducing the energy levels for many different molecules, which are known as semi-empirical methods. MNDO, MINDO, AM3 and PM5 are names of the parameter sets for popular semi-empirical methods, which are used in many chemistry molecular level calculations, such as MOPAC [260] and Gaussian [261], etc. An advantage of the ETB or the semi-empirical methods is that the calculation is fast and small in size. This calculational approach is suitable for the calculation of SWNTs since a SWNT has a large number of carbon atoms in the unit cell.

3.4. Calculations of matrix elements

Using the electronic and phonon eigenfunctions, we can calculate the matrix elements for the electron–photon and el–ph interactions.

3.4.1. The electron–photon matrix element

Using the simple tight-binding wavefunction, the electron–photon matrix element is calculated within the dipole approximation. The perturbation Hamiltonian of the optical dipole transition is given by

$$H_{\text{opt}} = \frac{ie\hbar}{m} \mathbf{A}(t) \cdot \nabla, \quad (26)$$

where \mathbf{A} is the vector potential. When we adopt the Coulomb gauge $\nabla \cdot \mathbf{A}(t) = 0$, the electric field of the light is given by $\mathbf{E} = i\omega\mathbf{A}$. Hereafter, we consider only a linear polarization of the light, and thus the vector potential \mathbf{A} is given by

$$\mathbf{A} = \frac{-i}{\omega} \sqrt{\frac{I}{c\epsilon_0}} \exp(\pm i\omega t) \mathbf{P}, \quad (27)$$

where \mathbf{P} is the unit vector (polarization vector) which specifies the direction of \mathbf{E} , I the intensity of the light in W/m^2 and ϵ_0 the dielectric constant for the vacuum in SI units. The “ \pm ” sign corresponds to the emission (“+”) or absorption (“−”) of a photon with frequency ω . Here, we can assume that the wavevector \mathbf{k} of an electron does not change during the transition (vertical transition). Then the matrix element for optical transitions from an initial state $\Psi'(\mathbf{k})$ to a final

state $\Psi^f(\mathbf{k})$ at \mathbf{k} is defined by

$$\mathbf{M}_{\text{opt}}^{f_i}(\mathbf{k}) = \langle \Psi^f(\mathbf{k}) | H_{\text{opt}} | \Psi^i(\mathbf{k}) \rangle. \quad (28)$$

The electron–photon matrix element between initial and final states in Equation (28) is calculated by

$$\mathbf{M}_{\text{opt}}^{f_i}(\mathbf{k}) = \frac{e\hbar}{m\omega_\rho} \sqrt{\frac{I_\rho}{c\epsilon_0}} e^{i(\omega_F - \omega_i \pm \omega)t} \mathbf{D}^{f_i}(\mathbf{k}) \cdot \mathbf{P} \quad (29)$$

where the weak spatial dependence of the vector potential A is neglected and $\mathbf{D}^{f_i}(\mathbf{k})$ is the dipole vector defined by the matrix element

$$\mathbf{D}^{f_i}(\mathbf{k}) = \langle \Psi^f(\mathbf{k}) | \nabla | \Psi^i(\mathbf{k}) \rangle. \quad (30)$$

For a given polarization, \mathbf{P} , the optical absorption (or stimulated emission) becomes large (absent) when \mathbf{D} is parallel (perpendicular) to \mathbf{P} .

3.4.2. Electric dipole vector for graphene

When we expand Ψ in Equation (30) into atomic orbitals $\varphi_j(\vec{r} - \vec{R})$ (Equation (19)), the dipole vector \mathbf{D} can be expressed by the atomic dipole vector $\langle \varphi_j(\vec{r} - \vec{R}') | \nabla | \varphi_j(\vec{r} - \vec{R}) \rangle$. The optical dipole transition of an electron from a π ($2p_z$) band to an unoccupied π^* band within an atom ($\vec{R}' = \vec{R}$) is forbidden in the case of graphene, which is understood by the mirror symmetry occurring at $z = 0$. However, the optical transition between a π and a π^* energy band is possible when the optical transition between nearest-neighbor interaction is allowed, as shown below.

Here, we consider the electric dipole vector for graphene [262]. The wavefunction in Equation (18) with $N = 2$ is given by $\Psi(\mathbf{k}) = C_A \Phi_A(\mathbf{k}, \mathbf{r}) + C_B \Phi_B(\mathbf{k}, \mathbf{r})$, in which Φ is the Bloch wavefunction for $2p_z$ atomic orbitals for the A and B sites of graphene. If we neglect the next nearest-neighbor interaction between the A and A atoms (or the B and B atoms), the electric dipole vector $\mathbf{D}^{f_i}(\mathbf{k}_F, \mathbf{k}_i)$ for graphene is given by,

$$\begin{aligned} \mathbf{D}^{f_i}(\mathbf{k}_F, \mathbf{k}_i) &= C_B^{f*}(\mathbf{k}_F) C_A^i(\mathbf{k}_i) \langle \Phi_B(\mathbf{k}_F, \mathbf{r}) | \nabla | \Phi_A(\mathbf{k}_i, \mathbf{r}) \rangle \\ &+ C_A^{f*}(\mathbf{k}_F) C_B^i(\mathbf{k}_i) \langle \Phi_A(\mathbf{k}_F, \mathbf{r}) | \nabla | \Phi_B(\mathbf{k}_i, \mathbf{r}) \rangle. \end{aligned} \quad (31)$$

Since both the $2p_z$ orbital and the $\partial/\partial z$ component of ∇ have odd symmetry with respect to the z mirror plane, the z component of \mathbf{D} becomes zero. Thus, we conclude that the dipole vector lies in the xy plane.

When we expand Ψ into atomic orbitals, the leading term of $\langle \Phi_A(\mathbf{k}_F, \mathbf{r}) | \nabla | \Phi_B(\mathbf{k}_i, \mathbf{r}) \rangle$ is the atomic matrix element m_{opt} between nearest neighbor atoms given by

$$m_{\text{opt}} = \left\langle \phi(\mathbf{r} - \mathbf{R}_{\text{nn}}) \left| \frac{\partial}{\partial x} \right| \phi(\mathbf{r}) \right\rangle, \quad (32)$$

where \mathbf{R}_{nn} is the lattice vector between nearest-neighbor C atoms along the x -axis.

When we use a linear approximation for the coefficients C_A and C_B for a \mathbf{k} point around the corner point of the 2D BZ $\mathbf{K} = (0, -4\pi/(3a))$ for the valence (v) and conduction (c) bands, we

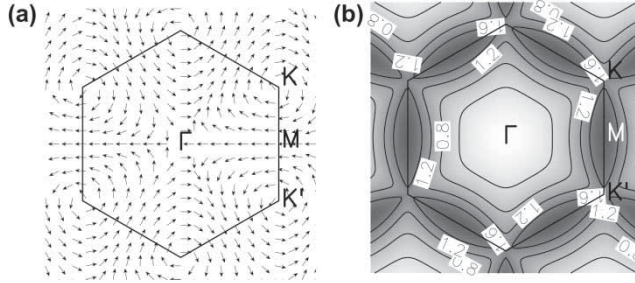


Figure 32. (a) The normalized dipole vector $\mathbf{D}^{cv}(\mathbf{k})$ is plotted as a function of \mathbf{k} over the 2D BZ. (b) The oscillator strength in units of the atomic matrix element m_{opt} is plotted as a function of \mathbf{k} over the 2D BZ. The separation between two adjacent contour lines is $0.4 m_{opt}$. The darker areas have a larger value for the oscillator strength. Reprinted figure with permission from A. Grüneis *et al.*, *Physical Review B* 67, pp. 165402–165407, 2003 [262]. Copyright © (2003) by the American Physical Society.

write [32]

$$\begin{aligned}
 C_A^v(\mathbf{K} + \mathbf{k}) &= \frac{1}{\sqrt{2}}, & C_B^v(\mathbf{K} + \mathbf{k}) &= \frac{k_y - ik_x}{\sqrt{2}k}. \\
 C_A^c(\mathbf{K} + \mathbf{k}) &= \frac{1}{\sqrt{2}}, & C_B^c(\mathbf{K} + \mathbf{k}) &= \frac{-k_y + ik_x}{\sqrt{2}k},
 \end{aligned}
 \tag{33}$$

The electric dipole vector coupling the valence and conduction bands is then given by

$$\mathbf{D}^{cv}(\mathbf{K} + \mathbf{k}) \equiv \langle \Psi^c(\mathbf{K} + \mathbf{k}) | \vec{\nabla} | \Psi^v(\mathbf{K} + \mathbf{k}) \rangle = \frac{3m_{opt}}{2k} (k_y, -k_x, 0).
 \tag{34}$$

In Figure 32(a) we plot the normalized directions of the normalized dipole vector $\mathbf{D}^{cv}(\mathbf{k})$ as arrows over the 2D BZ of graphene [262]. Around the K points, the arrows show a vortex behavior. Note also that the rotational directions of $\mathbf{D}^{cv}(\mathbf{k})$ around the K and K' points are opposite to each other in Figure 32(a). In Figure 32(b) we plot the values of the magnitude of the oscillator strength $O(\mathbf{k})$ in units of m_{opt} on a contour plot. Here $O^{cv}(\mathbf{k})$ is defined by

$$O^{cv}(\mathbf{k}) = \sqrt{\mathbf{D}^{cv*}(\mathbf{k}) \cdot \mathbf{D}^{cv}(\mathbf{k})}.
 \tag{35}$$

As shown in Figure 32(b), the oscillator strength $O^{cv}(\mathbf{k})$ has a maximum at the M points and a minimum at the Γ point in the 2D BZ. The \mathbf{k} dependent $O^{cv}(\mathbf{k})$ will be relevant to the calculation for the type-dependent photoluminescence (PL) intensity of a single wall S-SWNT [263] in which the PL of type I ($\text{mod}(2n + m, 3) = 1$) is stronger than for type II ($\text{mod}(2n + m, 3) = 2$) S-SWNTs, though we need to consider the electric dipole vector for each carbon nanotube individually in terms of its diameter and chiral angle [262,264,265].

The optical absorption intensity is given by the inner product $\mathbf{D}^{cv}(\mathbf{k}) \cdot \mathbf{P}$ up to linear terms in k_x and k_y for a given polarization vector $\mathbf{P} = (p_x, p_y, p_z)$

$$\mathbf{P} \cdot \mathbf{D}^{cv}(\mathbf{K} + \mathbf{k}) = \pm \frac{3m_{opt}}{2k} (p_y k_x - p_x k_y).
 \tag{36}$$

Equation (36) shows that the line $p_y k_x - p_x k_y = 0$ in the 2D BZ denotes the conditions for the occurrence of a node in the optical absorption for a given polarization vector $\mathbf{P} = (p_x, p_y)$. In the case of graphene, however, the optical transition events take place along equi-energy contours

around the K points, and we cannot see the nodes. This phenomena might be observed in graphene nanoribbons in which a 1D k value is specially selected. The polarization dependence of the optical absorption relative to the edge of graphene nanoribbon is now an interesting problem. In the case of a normal semiconductor, since the dipole vector is not a linear function of k , we cannot get a node in such cases.

3.4.3. Calculation of the electron–phonon interaction

The el–ph interaction which is the focus of this section is expressed by a modification to the tight-binding parameters that are pertinent to describing the lattice vibrations. In most theoretical works on the el–ph interaction, modification to the electron transfer energy as a function of the C–C bond length is considered for only the nearest neighbor C–C bonds as a parameter [219,220,266]. Here we calculated the el–ph interaction not only for long distance C–C bonds, but also for the so-called on-site el–ph interaction in which the site energy is modified by the vibration [267,268]. Their values are obtained by using the wavefunction and atomic potential as a function of the C–C distance [253].

Here, we rewrite the wavefunctions appearing in Equations (18) and (19) using a different notation, which is suitable for calculating the el–ph matrix elements [268]. We then write the Bloch functions

$$\Psi_{a,\mathbf{k}}(\mathbf{r}) = \frac{1}{\sqrt{N_u}} \sum_{s,o} C_{s,o}(a, \mathbf{k}) \sum_{\mathbf{R}_t} e^{i\mathbf{k}\cdot\mathbf{R}_t} \phi_{t,o}(\mathbf{r} - \mathbf{R}_t), \quad (37)$$

where $s = A$ and B is an index denoting the two carbon atoms in the unit cell, and \mathbf{R}_t denotes the equilibrium atom positions relative to the origin. $\phi_{t,o}$ denotes the atomic wave functions for the orbitals $o = 2s, 2p_x, 2p_y$ and $2p_z$ at \mathbf{R}_t , which are real functions (with no imaginary components).

The potential energy of the lattice V can be expressed by the atomic potentials $v(\mathbf{r} - \mathbf{R}_t)$ at \mathbf{R}_t ,

$$V = \sum_{\mathbf{R}_t} v(\mathbf{r} - \mathbf{R}_t), \quad (38)$$

where v in Equation (38) is given by the first-principles calculation for the Kohn–Sham potential of a neutral pseudo-atom [253]. The matrix element for the potential energy between the two different states $\Psi_i = \Psi_{a,\mathbf{k}}$ and $\Psi_f = \Psi_{a',\mathbf{k}'}$ is then written as

$$\begin{aligned} \langle \Psi_{a',\mathbf{k}'}(\mathbf{r}) | V | \Psi_{a,\mathbf{k}}(\mathbf{r}) \rangle &= \frac{1}{N_u} \sum_{s',o'} \sum_{s,o} C_{s',o'}^*(a', \mathbf{k}') C_{s,o}(a, \mathbf{k}) \\ &\times \sum_{u'} \sum_u e^{i(-\mathbf{k}'\cdot\mathbf{R}_{u',s'} + \mathbf{k}\cdot\mathbf{R}_{u,s})} m(t', o', t, o), \end{aligned} \quad (39)$$

with the matrix element m for the atomic potential given by

$$m = \int \phi_{s',o'}(\mathbf{r} - \mathbf{R}_{t'}) \left\{ \sum_{\mathbf{R}_{t''}} v(\mathbf{r} - \mathbf{R}_{t''}) \right\} \phi_{s,o}(\mathbf{r} - \mathbf{R}_t) d\mathbf{r}. \quad (40)$$

The atomic matrix element m thus comes from an integration over three centers of atoms, \mathbf{R}_t , $\mathbf{R}_{t'}$ and $\mathbf{R}_{t''}$. We neglect m for the cases for which the three centers t , t' and t'' are different from one another. When we consider only two center integrals, m consists, respectively, of off-site and

on-site matrix elements m_α and m_λ as follows:

$$\begin{aligned}
 m_\alpha &= \int \phi_{s',o'}(\mathbf{r} - \mathbf{R}_{t'}) \{v(\mathbf{r} - \mathbf{R}_{t'}) + v(\mathbf{r} - \mathbf{R}_t)\} \phi_{s,o}(\mathbf{r} - \mathbf{R}_t) \, d\mathbf{r}, \\
 m_\lambda &= \int \phi_{s',o'}(\mathbf{r} - \mathbf{R}_t) \left\{ \sum_{\mathbf{R}_{t'} \neq \mathbf{R}_t} v(\mathbf{r} - \mathbf{R}_{t'}) \right\} \phi_{s',o}(\mathbf{r} - \mathbf{R}_t) \, d\mathbf{r}.
 \end{aligned}
 \tag{41}$$

The potential $v(\mathbf{r} - \mathbf{R}_t)$ is vibrating within an adiabatic approximation with a phonon amplitude $\mathbf{S}(\mathbf{R}_t)$. Then the potential modification δV due to a lattice vibration is given by

$$\begin{aligned}
 \delta V &= \sum_{\mathbf{R}_t} v[\mathbf{r} - \mathbf{R}_t - \mathbf{S}(\mathbf{R}_t)] - v(\mathbf{r} - \mathbf{R}_t) \\
 &\approx - \sum_{\mathbf{R}_t} \nabla v(\mathbf{r} - \mathbf{R}_t) \cdot \mathbf{S}(\mathbf{R}_t).
 \end{aligned}
 \tag{42}$$

Since the potential modification δV breaks the periodicity of the lattice, the wavevector for an electron is no longer a good quantum number and thus the scattering of an electron by the el-ph interaction occurs. If we consider δV as a perturbation, then the el-ph matrix element is defined on the basis of perturbation theory: as [139,267–270]

$$\begin{aligned}
 M_{a,\mathbf{k} \rightarrow a',\mathbf{k}'} &\equiv \langle \Psi_{a',\mathbf{k}'}(\mathbf{r}) | \delta V | \Psi_{a,\mathbf{k}}(\mathbf{r}) \rangle \\
 &= -\frac{1}{N_u} \sum_{s',o'} \sum_{s,o} C_{s',o'}^* (a', \mathbf{k}') C_{s,o} (a, \mathbf{k}) \sum_{u',u} e^{i(-\mathbf{k}' \cdot \mathbf{R}_{u',s'} + \mathbf{k} \cdot \mathbf{R}_{u,s})} \delta m(t', o', t, o),
 \end{aligned}
 \tag{43}$$

where $\delta m(t', o', t, o)$ is the atomic deformation potential which consists of the off-site and on-site deformation potentials δm_α and δm_λ given by

$$\begin{aligned}
 \delta m_\alpha &= \int \phi_{s',o'}(\mathbf{r} - \mathbf{R}_{t'}) \{ \nabla v(\mathbf{r} - \mathbf{R}_{t'}) \cdot \mathbf{S}(\mathbf{R}_{t'}) + \nabla v(\mathbf{r} - \mathbf{R}_t) \cdot \mathbf{S}(\mathbf{R}_t) \} \times \phi_{s,o}(\mathbf{r} - \mathbf{R}_t) \, d\mathbf{r}, \\
 \delta m_\lambda &= \delta_{\mathbf{R}_t, \mathbf{R}_{t'}} \int \phi_{s',o'}(\mathbf{r} - \mathbf{R}_{t'}) \left\{ \sum_{\mathbf{R}_{t''} \neq \mathbf{R}_{t'}} \nabla v(\mathbf{r} - \mathbf{R}_{t''}) \cdot \mathbf{S}(\mathbf{R}_{t''}) \right\} \phi_{s',o}(\mathbf{r} - \mathbf{R}_{t'}) \, d\mathbf{r}.
 \end{aligned}
 \tag{44}$$

It is noted that both terms δm_α and δm_λ are of the same order of magnitude and that they work in a different way for each phonon mode [271].

The atomic deformation potential for any orbitals and for any vibration can be expressed by a small number of terms which are defined by the bonding or force constants between atoms along or perpendicular to the two atoms by using the Slater–Koster scheme [32,253]. The atomic el-ph matrix elements $\langle \phi | \nabla v | \phi \rangle$ are thus defined for four fundamental hopping and overlap integrals denoted by (ss) , $(s\sigma)$, $(\sigma\sigma)$ and $(\pi\pi)$, which are defined as a function of the C–C distance [253, 268] as follows:

$$\begin{aligned}
 \vec{\alpha}_p(\tau) &= \int \phi_\mu(\mathbf{r}) \nabla v(\mathbf{r}) \phi_\nu(\mathbf{r} - \boldsymbol{\tau}) \, d\mathbf{r} = \alpha_p(\tau) \hat{I}(\alpha_p), \\
 \vec{\lambda}_p(\tau) &= \int \phi_\mu(\mathbf{r}) \nabla v(\mathbf{r} - \boldsymbol{\tau}) \phi_\nu(\mathbf{r}) \, d\mathbf{r} = \lambda_p(\tau) \hat{I}(\lambda_p),
 \end{aligned}
 \tag{45}$$

which are, respectively, denoted by $\vec{\alpha}_p(\tau)$ and $\vec{\lambda}_p(\tau)$ for the off-site and on-site deformation potentials. Here $\hat{I}(\alpha_p)$ and $\hat{I}(\lambda_p)$ are unit vectors describing the direction of the off-site and on-site

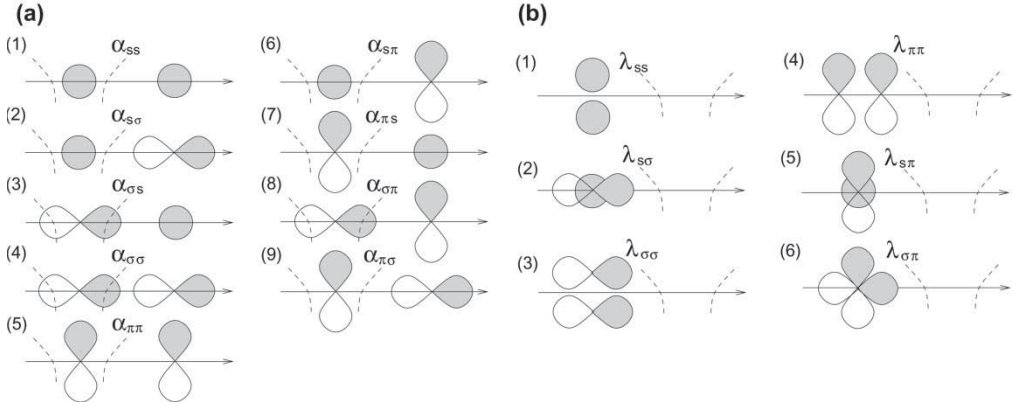


Figure 33. (a) The nine non-zero off-site deformation potential vectors $\vec{\alpha}_p$. The dashed curves represent the atomic potentials. (b) The six non-zero on-site deformation potential vectors $\vec{\lambda}_p$. The dashed curves represent the atomic potentials. For λ_{ss} , $\lambda_{\sigma\sigma}$ and $\lambda_{\pi\pi}$, the two same orbitals are illustrated by shifting them with respect to each other. Reprinted figure with permission from J. Jiang *et al.*, *Physical Review B* 72, pp. 235408–235411, 2005 [268]. Copyright © (2005) by the American Physical Society.

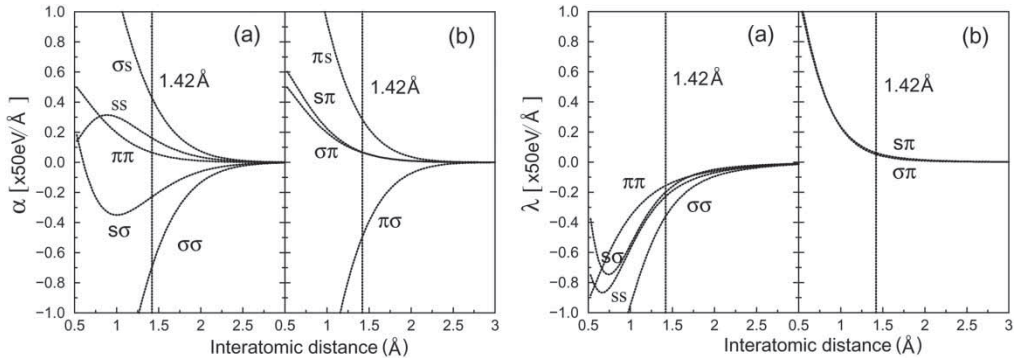


Figure 34. (a) The off-site deformation potential $\vec{\alpha}_p$ and (b) the on-site deformation potential $\vec{\lambda}_p$ as a function of inter-atomic distance. The vertical line corresponds to 1.42 Å which is the C–C distance in graphite. Reprinted figure with permission from J. Jiang *et al.*, *Physical Review B* 72, pp. 235408–235411, 2005 [268]. Copyright © (2005) by the American Physical Society.

deformation potential vectors $\vec{\alpha}_p$ and $\vec{\lambda}_p$, respectively [271], and $p = \mu\nu$ as given in Equation (45). The 2p orbital ϕ_μ (ϕ_ν) is along or perpendicular to the bond connecting the two carbon atoms and τ is the distance between the two atoms.¹⁷ In Figure 33, we show the non-zero matrix elements for the (a) off-site $\vec{\alpha}_p$ and (b) on-site $\vec{\lambda}_p$ atomic deformation potentials for 2s, σ and π atomic orbitals.

In Figure 34, the calculated values of $\vec{\alpha}_p$ and $\vec{\lambda}_p$ are plotted as a function of inter-atomic distance between two carbon atoms [268]. At $r = 1.42$ Å, which is the bond length between a carbon atom and one of its nearest neighbors, we have $\alpha_{\pi\pi} \approx 3.2$ eV/Å, and $|\lambda_{\pi\pi}| \approx 7.8$ eV/Å, and $|\alpha_{\pi\sigma}| \approx 24.9$ eV/Å. In order to calculate the el–ph matrix element of Equation (43) for each phonon mode, the amplitude of the atomic vibration $\mathbf{S}(\mathbf{R}_l)$ for the phonon mode (ν, \mathbf{q}) is calculated by

$$\mathbf{S}(\mathbf{R}_l) = A_\nu(\mathbf{q})\sqrt{\bar{n}_\nu(\mathbf{q})}\mathbf{e}^\nu(\mathbf{R}_l)e^{\pm i\omega_\nu(\mathbf{q})t}. \quad (46)$$

Here \pm is for phonon emission (+) and absorption (−), respectively, and A , \bar{n} , \mathbf{e} and ω are the zero-point phonon amplitude, number, eigenvector, and frequency, respectively. At equilibrium, the phonon number in Equation (46) is determined by the Bose–Einstein distribution function $n_\nu(\mathbf{q})$ for phonon ν :

$$n_\nu(\mathbf{q}) = \frac{1}{e^{\hbar\omega/k_B T} - 1}. \tag{47}$$

Here, $T = 300$ K is the lattice temperature at room temperature and k_B is the Boltzmann constant. For phonon emission, the phonon number is $\bar{n} = n + 1$, while for phonon absorption, $\bar{n} = n$. The amplitude of the zero-point phonon vibration is

$$A_\nu(\mathbf{q}) = \sqrt{\frac{\hbar}{N_u M_C \omega_\nu(\mathbf{q})}}, \tag{48}$$

where M_C is the mass of a carbon atom and the phonon eigenvector $\mathbf{e}^\nu(\mathbf{R}_i)$ is given by diagonalizing the dynamical matrix Eq. (17)¹⁸.

3.5. Calculation of excitonic states

In order to calculate the excitonic states, we first introduce in section 3.5.1 the Bethe–Salpeter equation Equation (49) which makes a localized wavefunction in real space. Using the exciton wavefunction, we show how to obtain the exciton–photon matrix element in Section 3.5.2 and the exciton–phonon matrix element in Section 3.5.3 within the tight-binding method.

3.5.1. The Bethe–Salpeter equation for exciton states

The exciton is a photo-excited electron and hole pair that is bonded by an attractive Coulomb interaction. In a SWNT, because of its 1D properties, the e–h binding energy becomes as large as 1 eV, so that exciton effects can be observed even at room temperature. Thus excitons are essential for explaining optical processes in SWNTs, such as optical absorption, photoluminescence and resonance Raman spectroscopy. The localization of the wavefunction can be obtained by mixing different k states with one another. The equation for making localized wavefunctions is called the Bethe–Salpeter equation.

Here, we show the Bethe–Salpeter equation for the tight-binding method in order to calculate the exciton energy Ω_n and the corresponding wavefunction Ψ^n [120,147,148,272,273]. Since the exciton wavefunction is localized in real space by a Coulomb interaction, the wavevector of an electron (\mathbf{k}_c) or a hole (\mathbf{k}_v) is not a good quantum number any more, and thus the exciton wavefunction Ψ_n for the n th exciton energy Ω_n is given by a linear combination of Bloch functions at many \mathbf{k}_c and \mathbf{k}_v wavevectors. In the case of carbon nanotubes, since the range of the Coulomb interaction is larger than the nanotube diameter, the mixed k 's are selected near the k_{ii} point on one cutting line of the 1D BZ [148]. The mixing of different wavevectors by the Coulomb interaction is obtained by the Bethe–Salpeter equation [147]

$$\sum_{\mathbf{k}_c, \mathbf{k}_v} \{ [E(\mathbf{k}_c) - E(\mathbf{k}_v)] \delta_{\mathbf{k}'_c, \mathbf{k}_c} \delta_{\mathbf{k}'_v, \mathbf{k}_v} + K(\mathbf{k}'_c, \mathbf{k}'_v, \mathbf{k}_c, \mathbf{k}_v) \} \Psi^n(\mathbf{k}_c, \mathbf{k}_v) = \Omega_n \Psi^n(\mathbf{k}'_c, \mathbf{k}'_v), \tag{49}$$

where $E(\mathbf{k}_c)$ and $E(\mathbf{k}_v)$ are the quasi-electron and quasi-hole energies, respectively (see Equation (52)). Here “quasi-particle” means that the particle has a finite lifetime in an excited state because of the Coulomb interaction. Equation (49) is solved by a matrix that includes many

\mathbf{k}'_c and \mathbf{k}'_v points. The mixing term of Equation (49) which we call the kernel, $K(\mathbf{k}'_c\mathbf{k}'_v, \mathbf{k}_c\mathbf{k}_v)$, is given by

$$K(\mathbf{k}'_c\mathbf{k}'_v, \mathbf{k}_c\mathbf{k}_v) = -K^d(\mathbf{k}'_c\mathbf{k}'_v, \mathbf{k}_c\mathbf{k}_v) + 2\delta_S K^x(\mathbf{k}'_c\mathbf{k}'_v, \mathbf{k}_c\mathbf{k}_v) \quad (50)$$

with $\delta_S = 1$ for spin singlet states and 0 for spin triplet states [167]. The direct and exchange interaction kernels K^d and K^x are, respectively, given by [274]

$$\begin{aligned} K^d(\mathbf{k}'_c\mathbf{k}'_v, \mathbf{k}_c\mathbf{k}_v) &\equiv W(\mathbf{k}'_c\mathbf{k}_c, \mathbf{k}'_v\mathbf{k}_v) \\ &= \int d\mathbf{r}' d\mathbf{r} \psi_{\mathbf{k}'_c}^*(\mathbf{r}') \psi_{\mathbf{k}_c}(\mathbf{r}') w(\mathbf{r}', \mathbf{r}) \psi_{\mathbf{k}'_v}(\mathbf{r}) \psi_{\mathbf{k}_v}^*(\mathbf{r}), \\ K^x(\mathbf{k}'_c\mathbf{k}'_v, \mathbf{k}_c\mathbf{k}_v) &= \int d\mathbf{r}' d\mathbf{r} \psi_{\mathbf{k}'_c}^*(\mathbf{r}') \psi_{\mathbf{k}'_v}(\mathbf{r}') v(\mathbf{r}', \mathbf{r}) \psi_{\mathbf{k}_c}(\mathbf{r}) \psi_{\mathbf{k}_v}^*(\mathbf{r}), \end{aligned} \quad (51)$$

where the functions w and v are the screened and bare Coulomb potentials, respectively, and ψ denotes the quasi-particle wavefunction. The quasi-particle energies are the sum of the single particle energy ($\epsilon(\mathbf{k})$) and the self-energy ($\Sigma(\mathbf{k})$),

$$E(\mathbf{k}_i) = \epsilon(\mathbf{k}_i) + \Sigma(\mathbf{k}_i) \quad (i = c, v), \quad (52)$$

where the self-energy $\Sigma(\mathbf{k})$ is expressed by

$$\begin{aligned} \Sigma(\mathbf{k}_c) &= - \sum_{\mathbf{q}} W(\mathbf{k}_c(\mathbf{k} + \mathbf{q})_v, (\mathbf{k} + \mathbf{q})_v \mathbf{k}_c), \\ \Sigma(\mathbf{k}_v) &= - \sum_{\mathbf{q}} W(\mathbf{k}_v(\mathbf{k} + \mathbf{q})_v, (\mathbf{k} + \mathbf{q})_v \mathbf{k}_v). \end{aligned} \quad (53)$$

In order to determine the kernel and self-energy, the single particle Bloch wavefunction $\psi_{\mathbf{k}}(\mathbf{r})$ and the screening potential W are evaluated by either a first-principles calculation [147] or by using an extended tight-binding wavefunction within a random phase approximation (RPA) calculation [148]. In the RPA, the static screened Coulomb interaction for π electrons is expressed by

$$W = \frac{V}{\kappa \epsilon(\mathbf{q})}, \quad (54)$$

with a static dielectric constant κ and a dielectric function $\epsilon(\mathbf{q}) = 1 + v(\mathbf{q})\Pi(\mathbf{q})$. For describing the exciton energy and exciton wavefunction it is essential to select a reasonable function for the unscreened Coulomb potential $v(\mathbf{q})$ [120,148]. For 1D materials, the Ohno potential is commonly used for the unscreened Coulomb potential $v(q)$ for π orbitals [275] at two sites, $\mathbf{R}_{u's'}$ and \mathbf{R}_{0s} , (u : unit cell, s : atom position) with

$$v(|\mathbf{R}_{u's'} - \mathbf{R}_{0s}|) = \frac{U}{\sqrt{((4\pi\epsilon_0/e^2)U|\mathbf{R}_{us} - \mathbf{R}_{0s'}|)^2 + 1}}, \quad (55)$$

where U is the energy cost to place two electrons on a single site ($|\mathbf{R}_{us} - \mathbf{R}_{0s'}| = 0$) and this energy cost is taken as $U \equiv U_{\pi_a\pi_a\pi_a\pi_a} = 11.3$ eV for π orbitals [275]. The Ohno potential works well in reproducing the ground state and low-energy electronic excitations [276].

3.5.2. Exciton–photon matrix element

The exciton–photon matrix element $M_{\text{ex-op}}$ is given by a linear combination of the electron–photon matrix element $D_{\mathbf{k}}$ at \mathbf{k} , weighted by $Z_{\mathbf{k},\mathbf{k}\nu}^{n*}$

$$M_{\text{ex-op}} = \langle \Psi_0^n | H_{\text{el-op}} | 0 \rangle = \sum_{\mathbf{k}} D_{\mathbf{k}} Z_{\mathbf{k},\mathbf{k}\nu}^{n*}, \quad (56)$$

where Ψ_0^n is the exciton wavefunction with a $\mathbf{q} = 0$ center of mass momentum. Since the center of mass momentum is conserved before and after an optical transition, only $\mathbf{q} = 0$ excitons can be excited.

In the case of a SWNT, since the lattice structure is symmetric under a C_2 rotation around an axis which is perpendicular to the nanotube axis and goes through the center of a C–C bond, the C_2 exchange operation between A and B carbon atoms in the hexagonal lattice is equivalent to the exchange of \mathbf{k} and $-\mathbf{k}$ states. Since the exciton wavefunction of a carbon nanotube should transform as an irreducible representation of the C_2 symmetry operation, we can get A_1, A_2, E and E^* symmetry excitons [142]. For example, the A_1 and A_2 exciton wavefunctions which are, respectively, symmetric and antisymmetric under a C_2 rotation, are given by

$$|\Psi_0^n(A_{1,2})\rangle = \frac{1}{\sqrt{2}} \sum_{\mathbf{k}} Z_{\mathbf{k},\mathbf{k}\nu}^n (c_{\mathbf{k}c}^+ c_{\mathbf{k}\nu} \mp c_{-\mathbf{k}c}^+ c_{-\mathbf{k}\nu}) | 0 \rangle, \quad (57)$$

where \mathbf{k} and $-\mathbf{k}$ are located around the K and K' points, respectively, and $-(+)$ in \mp corresponds to an A_1 (A_2) exciton.¹⁹ When we use the relation $D_{\mathbf{k}} = D_{-\mathbf{k}}$, the excitonic-optical (ex-op) matrix elements for the A_1 and A_2 excitons are given by

$$\begin{aligned} M_{\text{ex-op}}(A_1^n) &= 0, \\ M_{\text{ex-op}}(A_2^n) &= \sqrt{2} \sum_{\mathbf{k}} D_{\mathbf{k}} Z_{\mathbf{k},\mathbf{k}\nu}^{n*}. \end{aligned} \quad (58)$$

Equation (58) directly indicates that A_1 excitons are dark and only A_2 excitons are bright, which is consistent with the predictions by group theory [277]. Because of the spatially localized exciton wavefunction, the exciton–photon matrix elements are greatly enhanced (on the order of 100 times) compared with the corresponding electron–photon matrix elements [273].

3.5.3. The exciton–phonon interaction

The exciton–phonon interaction is given by a linear combination of el–ph interactions weighted by the exciton wavefunction. Using creation and annihilation operators, the el–ph interaction for a phonon mode (\mathbf{q}, ν) is given by

$$H_{\text{el-ph}} = \sum_{\mathbf{k}\mathbf{q}\nu} [M_{\mathbf{k},\mathbf{k}+\mathbf{q}}^{\nu}(c) c_{(\mathbf{k}+\mathbf{q})c}^+ c_{\mathbf{k}c} - M_{\mathbf{k},\mathbf{k}+\mathbf{q}}^{\nu}(\nu) c_{(\mathbf{k}+\mathbf{q})\nu}^+ c_{\mathbf{k}\nu}] (b_{\mathbf{q}\nu} + b_{\mathbf{q}\nu}^+), \quad (59)$$

where $M(c)$ ($M(\nu)$) denotes the el–ph matrix element for the conduction (valence) band, and $b_{\mathbf{q}\nu}^+$ ($b_{\mathbf{q}\nu}$) is a phonon creation (annihilation) operator for the ν th phonon mode at \mathbf{q} . From Equation (59), we obtain the exciton–phonon matrix element between the initial state $|\Psi_{\mathbf{q}1}^{n1}\rangle$ and a final state $|\Psi_{\mathbf{q}2}^{n2}\rangle$,

by writing

$$\begin{aligned} M_{\text{ex-ph}} &= \langle \Psi_{\mathbf{q}_2}^{n2} | H_{\text{el-ph}} | \Psi_{\mathbf{q}_1}^{n1} \rangle \\ &= \sum_{\mathbf{k}} [M_{\mathbf{k},\mathbf{k}+\mathbf{q}}^v(c) Z_{\mathbf{k}+\mathbf{q},\mathbf{k}-\mathbf{q}_1}^{n2*} Z_{\mathbf{k},\mathbf{k}-\mathbf{q}_1}^{n1} - M_{\mathbf{k},\mathbf{k}+\mathbf{q}}^v(v) Z_{\mathbf{k}+\mathbf{q},\mathbf{k}}^{n2*} Z_{\mathbf{k}+\mathbf{q}_2,\mathbf{k}+\mathbf{q}}^{n1}], \end{aligned} \quad (60)$$

with $\mathbf{q} = \mathbf{q}_2 - \mathbf{q}_1$ accounting for momentum conservation. Since the electron–phonon interaction smoothly changes as a function of \mathbf{k} for the region of the exciton wavefunction, the value of the exciton–phonon interaction is similar to the electron–phonon interaction [273].

3.6. The resonance Raman process

3.6.1. Matrix elements for the resonance Raman process

Combining all the matrix elements discussed above, we can formulate the first-order Stokes Raman intensity of graphene by time dependent perturbation theory as

$$I_{\text{el}} = \left| \frac{1}{L} \sum_{\mathbf{k}} \frac{D_{\mathbf{k}}^2 [M_{\text{el-ph}}(\mathbf{k} \rightarrow \mathbf{k}, c) - M_{\text{el-ph}}(\mathbf{k} \rightarrow \mathbf{k}, v)]}{[E - E_{\text{cv}}(\mathbf{k}) + i\gamma][E - E_{\text{cv}}(\mathbf{k}) - E_{\text{ph}} + i\gamma]} \right|^2, \quad (61)$$

where γ is the width of the resonance Raman window (Section 3.6.3) [278]. The γ value is essential in determining I_{el} as a function of laser excitation energy (Raman excitation profile). When we use the exciton–photon and exciton–phonon interactions, we apply the formula to the Raman intensity of SWNTs as follows:

$$\begin{aligned} I_{\text{ex}} &= \left| \frac{1}{L} \sum_a \frac{M_{\text{ex-op}}(a) M_{\text{ex-ph}}(a \rightarrow b) M_{\text{ex-op}}(b)}{(E - E_a + i\gamma)(E - E_a - E_{\text{ph}} + i\gamma)} \right|^2 \\ &= \left| \frac{1}{L} \sum_a \frac{M_{\text{ex-op}}(a)^2 M_{\text{ex-ph}}(a \rightarrow a)}{(E - E_a + i\gamma)(E - E_a - E_{\text{ph}} + i\gamma)} \right|^2. \end{aligned} \quad (62)$$

In the second line of Equation (62), we assume that the virtual state b can be approximated by the real state a .²⁰ In the case of a first-order Raman process, since $\mathbf{q} = 0$, the matrix element of Equation (60) is simplified as

$$M_{\text{ex-ph}} = \sum_{\mathbf{k}} [M_{\mathbf{k},\mathbf{k}}^v(c) - M_{\mathbf{k},\mathbf{k}}^v(v)] |Z_{\mathbf{k},\mathbf{k}}|^2. \quad (63)$$

When we consider the second-order Raman intensity, we should consider $\mathbf{q} \neq 0$ phonon scattering. In this case, the exciton–phonon interaction between an A_2 exciton state and an E exciton state is important, in particular, for the case where the E exciton state consists of an electron near the K point and a hole near the K' point and vice versa. Here the inter-valley exciton–phonon interaction is generally large.

3.6.2. Matrix elements for double resonance Raman scattering

The two-phonon process is described in quantum mechanical terms by using fourth-order, time-dependent perturbation theory and the scattering intensity can be calculated using:

$$I(\omega, E_{\text{laser}}) \propto \sum_i \left| \sum_{m', m'', \omega_1, \omega_2} J_{m', m''}(\omega_1, \omega_2) \right|^2, \quad (64)$$

in which the summation is taken over two intermediate electronic states m and m' and the corresponding phonon frequencies ω_1 and ω_2 with phonon wavevectors $-q_1$ and $-q_2$, respectively, and for the initial states i , after taking the square of the scattering amplitude, $J_{m,m'}$ that is given by

$$J_{m',m''}(\omega_1, \omega_2) = \frac{M_{\text{ex-op}}(im'')M_{\text{ex-ph}}(m''m')M_{\text{ex-ph}}(m'm)M_{\text{ex-op}}(mi)}{(\Delta E_{m''i} - \hbar\omega_1 - \hbar\omega_2 - i\gamma)(\Delta E_{m'i} - \hbar\omega_1 - i\gamma)(\Delta E_{mi} - i\gamma)}, \quad (65)$$

where $\Delta E_{m'i} \equiv E_{\text{laser}} - (E_m - E_i)$ and $M_{\text{ex-op}}(mi)$ denote the optical transition from i to m states, etc. In general, energy and momentum conservation for the incident (i) and scattered (s) electrons requires:

$$E_s = E_i \pm E_{q_1} \pm E_{q_2}, \quad (66)$$

$$k_s = k_i \mp q_1 \mp q_2, \quad (67)$$

where $+$ ($-$) in Equation (66) and $-$ ($+$) in Equation (67) correspond to phonon absorption and emission with the wavevectors q_1 and q_2 . By considering $k_s \approx k_i$ (see Section 1.5), momentum conservation requires $q_2 \approx -q_1$ for satisfying the DR condition for two of the three energy denominators in Equation (65).

3.6.3. Resonance window width

The resonance width, or γ in eV, of the Raman excitation profile is related by the uncertainty relation in quantum mechanics and to the lifetime of the photo-excited carriers. Usually, the dominant contribution to the lifetime of the carriers in the Raman spectra is in an inelastic scattering process by the emission or absorption of phonons. The Raman spectral width, Γ in cm^{-1} , in the Raman spectra, on the other hand, which has a different physical value from γ , is related to the phonon lifetime. Γ is determined by the elastic (or inelastic) scattering of a phonon due to defects, anharmonicity or by the electron-phonon interaction. The carrier transition rate τ ($=\hbar/\gamma$), [139,263,267,278] is estimated by the Fermi Golden rule for the electron-phonon matrix elements [268,269]. For metallic systems (graphene and M-SWNTs), an additional interaction of phonons with free electrons can shorten the lifetime (broaden the γ values) significantly, and this additional interaction is known as the Kohn anomaly (KA) (Section 3.6.5).

The transition rate $1/\tau$ or the scattering rate per unit time of an excited electron from an initial state \mathbf{k} to all possible final states \mathbf{k}' by the ν th phonon mode is given by [263]

$$\begin{aligned} \frac{1}{\tau_\nu} &= W_{\mathbf{k}}^\nu \\ &= \frac{S}{8\pi M d_t} \sum_{\mu', k'} \frac{|D_\nu(\mathbf{k}, \mathbf{k}')|^2}{\omega_\nu(\mathbf{k}' - \mathbf{k})} \left[\frac{dE(\mu', k')}{dk'} \right]^{-1} \\ &\quad \times \left\{ \frac{\delta(\omega(\mathbf{k}') - \omega(\mathbf{k}) - \omega_\nu(\mathbf{k}' - \mathbf{k}))}{e^{\beta\hbar\omega_\nu(\mathbf{k}' - \mathbf{k})} - 1} + \frac{\delta(\omega(\mathbf{k}') - \omega(\mathbf{k}) + \omega_\nu(\mathbf{k}' - \mathbf{k}))}{1 - e^{-\beta\hbar\omega_\nu(\mathbf{k}' - \mathbf{k})}} \right\}, \end{aligned} \quad (68)$$

where S, M, d_t, β and μ' , respectively, denote the area of the graphene unit cell, the mass of a carbon atom, the diameter of a SWNT, $1/k_B T$ (where k_B is the Boltzmann constant), and the cutting line indices of the final state. Here $D_\nu(\mathbf{k}, \mathbf{k}')$ denotes a matrix for scattering an electron from \mathbf{k} to \mathbf{k}' by the ν th phonon mode. The relaxation process is restricted to 24 possible phonon scattering processes satisfying energy-momentum conservation [267]. The two terms in braces in Equation (68), respectively, represent the absorption and emission processes of the ν th phonon

mode with energy $\hbar\omega_v(\mathbf{k}' - \mathbf{k})$. The calculation of the transition rates as in Equation (68) have been considered by the Ferrari group using another approach [151,219].

For the result, in the case of S-SWNTs, we can obtain calculated γ values in agreement with experiments by just considering the electron–phonon coupling model [278]. The calculated γ value shows a strong dependence on chirality and diameter for S-SWNTs. However, the calculated γ value for M-SWNTs is much smaller than the experimental γ value which shows the presence of

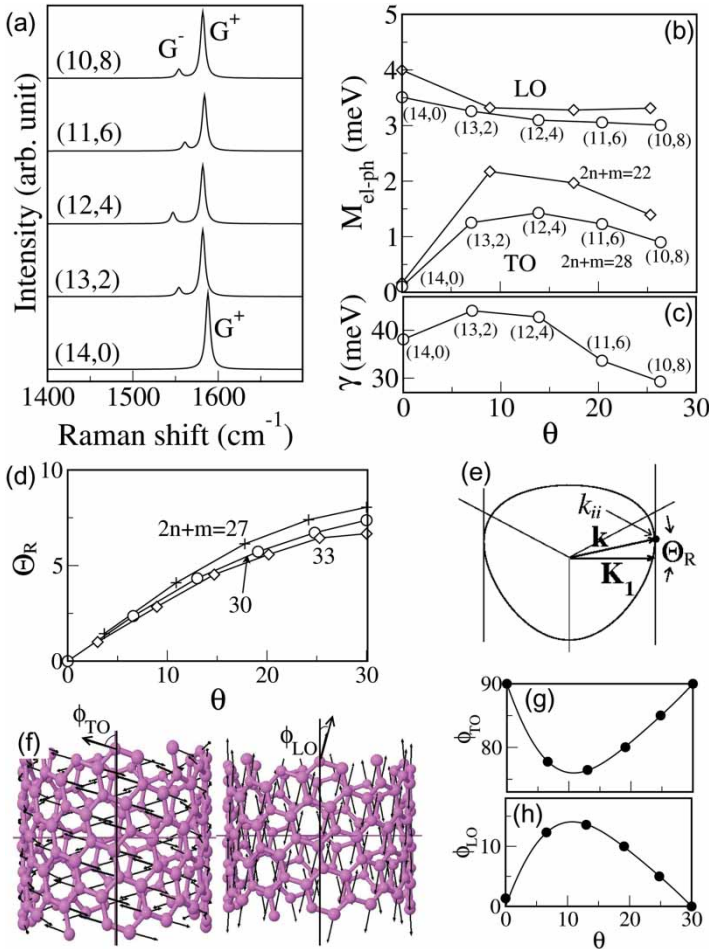


Figure 35. (a) The calculated G-band spectra for S-SWNTs with the same family number $p = 2n + m = 28$. (b) The calculated electron–phonon matrix elements vs. chiral angle θ for the LO and TO phonons and for two different $2n + m$ family numbers (22 and 28). (c) Plot of γ vs. θ for members of $p = 28$. (d) Plot of Θ_R vs. θ for three $2n + m$ families of M-SWNTs. (e) The angle Θ_R between the circumferential vector K_1 and the cutting line for the polar coordinate of a \mathbf{k} vector at the van Hove singular point. (f) The angle ϕ between the tube axis and the phonon eigenvector direction for a (12,6) SWNT. The calculated angles ϕ vs. θ for the TO phonons (g) and the LO phonons. (h) For the results for the LO phonons as a function of θ (fitted by the function of Equation (70) (see text)). Reprinted with permission from J.S. Park *et al.*, *Physical Review B* 80, p. 81402, 2009 [86]. Copyright © (2009) by the American Physical Society.

an additional scattering path associated with the charge carriers in M-SWNTs. Such a scattering path might come from the electron–electron interaction, but this theory is not yet well described.

3.6.4. G-band intensity for semiconducting SWNTs

Next, we consider the G-band Raman intensity as a function of (n, m) [86]. Figure 35(a) shows the calculated resonance Raman spectra for the G-band for type I S-SWNTs [86] with family number $p = 2n + m = 28$. The (n, m) SWNTs with the same family number p have a similar diameter and E_{ii} value to one another. In this figure, values for E_L and γ (see Figure 35(c)) are taken from E_{22}^S for each (n, m) SWNT. The chiral angle can vary from $\theta = 0^\circ$ to $\theta \sim 30^\circ$. The intensity of the G^- peak (TO) is always smaller than that of the G^+ peak (LO), because $\mathcal{M}_{ep}^{R,LO} > \mathcal{M}_{ep}^{R,TO}$ for the electron–phonon matrix elements, as shown in Figure 35(b), in which the above notation R indicates Raman scattering. In particular, the intensity of the G^- peak vanishes for a (14,0) SWNT, since $\mathcal{M}_{ep}^{R,TO}$ for zigzag SWNTs is zero, as shown in Figure 35(b). Here \mathcal{M}_{ep}^R is calculated for the phonon amplitude at 300 K. These calculated G-band Raman spectra can be compared with previous experimental results which show only one peak in the G-band spectra of (n, m) SWNTs with smaller chiral angles [193,279].

In order to explain the chiral angle dependence of the el–ph matrix elements for the LO and TO phonons, we obtain the analytical formulae for the el–ph matrix element within the effective mass approximation [196]

$$\begin{aligned} \mathcal{M}_{ep}^{R,LO} &\equiv \langle e(\mathbf{k}), \omega_{LO} | \mathcal{H}_{ep} | e(\mathbf{k}) \rangle = gu \cos \Theta_R(\mathbf{k}), \\ \mathcal{M}_{ep}^{R,TO} &\equiv \langle e(\mathbf{k}), \omega_{TO} | \mathcal{H}_{ep} | e(\mathbf{k}) \rangle = -gu \sin \Theta_R(\mathbf{k}), \end{aligned} \tag{69}$$

respectively, where g is the el–ph coupling constant, u the phonon amplitude and $\Theta_R(\mathbf{k})$ is defined by an angle between the \mathbf{k} vector from the K point of the 2D BZ to the van Hove singular point, k_{ii} , and the circumferential direction vector, \mathbf{K}_1 , [32,136,177] as shown in Figure 35(d). The values of g are consistent with the work by Basko *et al.* [151,219]. Since $\Theta_R(\mathbf{k})$ is zero for all zigzag SWNTs ($\mathbf{k} \parallel \mathbf{K}_1$), we obtain $\mathcal{M}_{ep}^{R,TO} = 0$, while $\mathcal{M}_{ep}^{R,LO}$ has a maximum value [196]. The meaning of Θ_R vs. θ for SWNTs with the same family number p is shown in Figure 35(e). For the TO phonon mode, the magnitude of the matrix element \mathcal{M}_{ep}^R for SWNTs with a similar θ value increases with decreasing d_t because of the diameter dependence in the circumferential direction [86] as shown in Figure 35(b). The angle ϕ between the SWNT- axis and the phonon eigenvector for the LO and TO phonons [280] is essential for determining the value of the el–ph matrix element. In fact, when we consider ϕ , then Equation (69) is modified and becomes

$$\begin{aligned} \langle e(\mathbf{k}), \omega_{LO} | \mathcal{H}_{ep} | e(\mathbf{k}) \rangle &= gu \cos(\Theta_R(\mathbf{k}) + \phi), \\ \langle e(\mathbf{k}), \omega_{TO} | \mathcal{H}_{ep} | e(\mathbf{k}) \rangle &= -gu \sin(\Theta_R(\mathbf{k}) + \phi). \end{aligned} \tag{70}$$

Figure 35(g) and (h) show that the calculated angle ϕ here changes smoothly as a function of θ [86]. The sum $\phi_{LO} + \phi_{TO}$ for a general chiral angle θ always becomes $\pi/2$, because of symmetry. The angle ϕ vs. θ for the LO and TO phonons can be fitted by the chiral angle dependence $(A + B\theta + C\theta^2) \sin(6\theta)$, where A, B and C are fitting parameters and θ is the chiral angle in units of degrees ($^\circ$). Values obtained for A, B and C for ϕ_{LO} , are $A = 26.9, B = -76.3$ and $C = 84.5$, respectively, and for ϕ_{TO} , the corresponding values are $A = -26.7, B = 75.4$, and $C = -83.2$. The units for the fitting parameters are degree ($^\circ$). This ϕ dependence of ϕ_{LO} and ϕ_{TO} should be taken into account when carrying out Raman spectral calculations.

3.6.5. G-band intensity for metallic SWNTs: The Kohn Anomaly

In the case of metallic SWNTs, the G-band spectra become soft and broad and they are represented by the Breit–Wigner–Fano (BWF) lineshape [128]. The BWF lineshape has been widely observed for graphite intercalation compounds as a function of doping concentration and also as a function of carrier density [281]. The phonon softening phenomena for metallic SWNTs is understood by the electron–phonon interaction between phonons and free electrons at the Fermi energy, (E_F), and these phenomena are known as the KA effect [127] which has been widely discussed [151,193,194,197–199,243]

The phonon frequency ω of the LO and TO phonon modes at the Γ point for M-SWNTs is modified by the KA effect, which we understand by second-order perturbation theory. The phonon energy $\hbar\omega$ becomes $\hbar\omega = \hbar\omega^{(0)} + \hbar\omega^{(2)}$, where $\omega^{(0)}$ is the original phonon frequency without the el–ph interaction, and $\omega^{(2)}$ is the quantum correction to $\omega^{(0)}$ which is given by [196]

$$\hbar\omega^{(2)} = 2 \sum_{\mathbf{k}} \frac{| \langle eh(\mathbf{k}) | \mathcal{H}_{ep} | \omega^{(0)} \rangle |^2}{\hbar\omega^{(0)} - [E_e(\mathbf{k}) - E_h(\mathbf{k})] + i\Gamma} \times \{ f[E_e(\mathbf{k}) - E_F] - f[E_h(\mathbf{k}) - E_F] \}, \tag{71}$$

in which the factor 2 comes from spin degeneracy, and $E_e(\mathbf{k})$ [$E_h(\mathbf{k})$] denotes the electron (hole) energy as a function of wave vector \mathbf{k} , while $\langle eh(\mathbf{k}) | \mathcal{H}_{ep} | \omega^{(0)} \rangle$ represents the el–ph matrix element for creating an e–h pair with wave number \mathbf{k} by the el–ph interaction \mathcal{H}_{ep} and $f(E)$ is the Fermi distribution function. The G-band spectral width is given by the decay width Γ in Equation (71), which is calculated self-consistently by evaluating $\Gamma = -\text{Im}(\hbar\omega^{(2)})$ [196,205]. The electron–phonon interaction is used, too, for defining the $\omega^{(0)}$ and thus we should be careful about not double counting the constituents of this interaction [198].

Figure 36(a) shows the calculated Raman spectra for the G-band of M-SWNTs with family number $p = 30$ and $E_F=0$. The E_L and γ values (see Figure 36(c)) are taken from E_{11}^M for each (n, m) SWNT. The G^- peak intensity is larger than that of the G^+ peak, because the G^- (G^+) peak corresponds to the LO (TO) phonon due to the LO phonon softening, in which $\mathcal{M}_{ep}^{R,LO} > \mathcal{M}_{ep}^{R,TO}$ for any θ value, as shown in Figure 36(b). The relative intensities of the two peaks, G^+ and G^- , are affected by the Raman spectral width which relates to the phonon lifetime, Γ . For the (10,10) armchair SWNT, the G^+ (TO) peak width is significantly smaller than those for the G^- (LO) peak

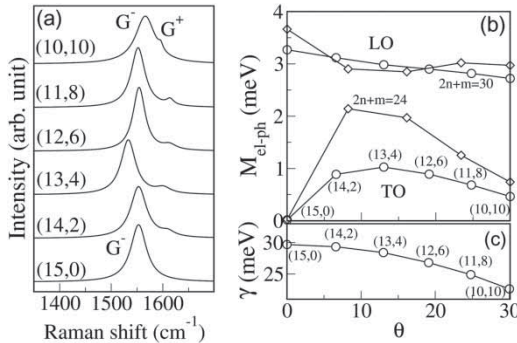


Figure 36. (a) The calculated G-band spectra of M-SWNTs with the same family number $p = 30$ and $E_F=0$. (b) el–ph matrix elements vs. θ for the LO and TO phonons and for two different $2n + m$ family numbers. Open-circles indicate the \mathcal{M}_{ep} values for the family number $p = 30$. (c) γ vs. θ for members of $p = 30$. Reprinted with permission from J.S. Park et al., Physical Review B 80, p. 81402, 2009 [86]. Copyright © (2009) by the American Physical Society.

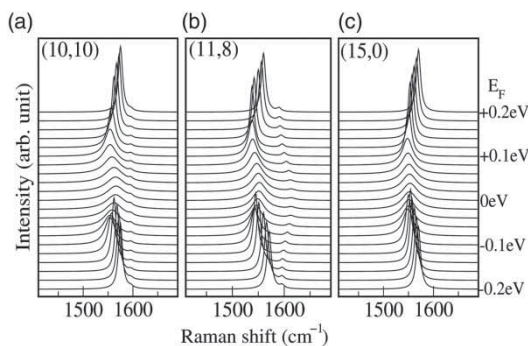


Figure 37. The calculated G-band spectra for three M-SWNTs with different chiral angles taken by changing the Fermi energy from $E_F = -0.2$ eV to 0.2 eV. (a) (10,10). (b) (11,8) and (c) (15,0). Reprinted with permission from J.S. Park *et al.*, *Physical Review B* 80, p. 81402, 2009 [86]. Copyright © (2009) by the American Physical Society.

and of the G^+ peaks for the other chiral tubes. Therefore, the G^+ peak intensity of the (10,10) tube becomes large compared with the other chiral SWNTs, even though the $\mathcal{M}_{ep}^{R,TO}$ for the armchair tube has a smaller value than that for the other chiral tubes. Since the Raman peak intensity is large for large \mathcal{M}_{ep} and small Γ values, the chiral angle dependence of these values gives an irregular behavior to the G^+/G^- spectra as a function of (n, m) , as seen in Figure 36.

For a zigzag SWNT ((15, 0)), only the G^+ peak appears, because $\mathcal{M}_{ep}^{R,TO}$ vanishes for zigzag nanotubes as seen in Equation (69). The other chiral tubes in this $p = 2n + m > 30$ family, (11,8), (12,6), (13,4) and (14,2), show various intermediate intensity ratios. In Figure 36(c), we show that γ decreases monotonically with increasing θ . Because of the small difference between the γ and the el-ph coupling for the LO phonon as compared to that for the TO phonon as a function of θ , the G^- peak intensity does not show a large change for the different chiral SWNTs. These results show that the G-band intensity for both the G^+ and G^- components depends on θ , but the Raman intensity is more sensitive to the E_F position, especially for M-SWNTs.

This effect is shown more clearly by varying the Fermi Level, as shown in Figure 37(a), where the calculated G-band spectra is plotted vs. E_F at 300 K for a (10,10) armchair SWNT. Here neither are the changes in the C-C bond nor the changes in the E_{ii} transition energy by doping with electrons or holes considered [86].

In Figure 37, the positive (negative) Fermi energy $+E_F$ ($-E_F$) corresponds to electron (hole) doping. When E_F is changed from $E_F = 0$, the G^- peak shows a frequency shift and a sharpening of the spectral width, while the G^+ peak does not show any change in intensity or width. The el-ph interaction for the photo-excited electron does not couple to the TO phonon for armchair SWNTs [196]. For the chiral M-SWNT (11,8) as shown in Figure 37(b), both the LO and TO phonons couple to the intermediate e-h pair state, which is excited by a lower energy phonon. The TO phonon becomes harder for $E_F = 0$ eV, since the intermediate state of an e-h pair for $E < \hbar\omega_{TO}$ contributes to a TO phonon hardening [196]. In the case of the (15,0) SWNT, the G^+ peak always vanishes because of a vanishing $\mathcal{M}_{ep}^{R,TO}$ (See Figure 36(b)).

The matrix element \mathcal{M}_{ep}^{KA} for the KA effect in Equation (71) is given by [196]

$$\begin{aligned} \mathcal{M}_{ep}^{KA,LO} &\equiv \langle eh(\mathbf{k}) | \mathcal{H}_{ep} | \omega_{LO} \rangle = igu \sin \Theta_{KA}(\mathbf{k}), \\ \mathcal{M}_{ep}^{KA,TO} &\equiv \langle eh(\mathbf{k}) | \mathcal{H}_{ep} | \omega_{TO} \rangle = -igu \cos \Theta_{KA}(\mathbf{k}), \end{aligned} \quad (72)$$

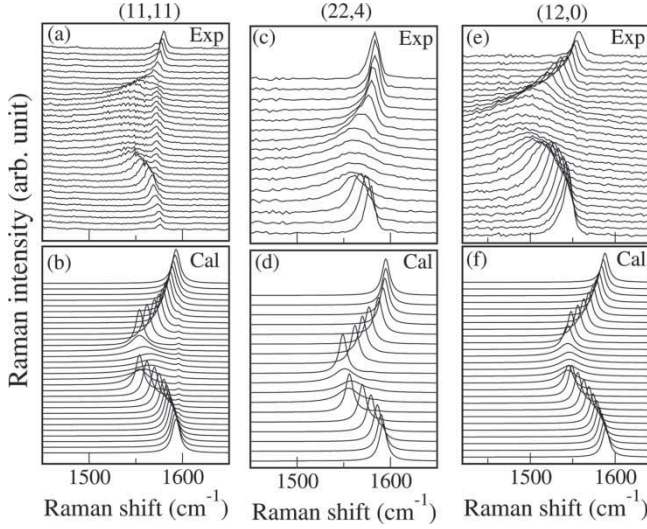


Figure 38. (a,c,e) Experimental G-band Raman spectra which are given by the electro-chemical doping effect. (a) $V_g = 1.5$ to -1.5 V. (c) $V_g = 1.9$ to -1.3 V. (e) $V_g = 1.3$ to -1.3 V with the traces taken at uniform changes in V_g . (b,d,f) Calculated G-band Raman spectra taken by changing the Fermi energy E_F in equal steps (b) 0.45 to -0.45 eV, (d) 0.60 to -0.42 eV and (f) 0.39 to -0.39 eV. The tube chiralities are: (a,b) (11,11), (c,d) (24,4) and (e,f) (12,0). Reprinted with permission from J.S. Park *et al.*, *Physical Review B* 80, p. 81402, 2009 [86]. Copyright © (2009) by the American Physical Society.

where $\Theta_{KA}(\mathbf{k})$ is defined as the angle between the \mathbf{k} point taken on a cutting line²¹ for two-linear metallic sub-bands and the nanotube circumferential direction of a unit vector, \mathbf{K}_1 . For the armchair nanotube, the cutting line for the two-linear metallic bands lies on the nanotube axis direction unit vector, and then Θ_{KA} is $\pi/2$ ($-\pi/2$), which gives a vanishing $\mathcal{M}_{ep}^{KA,TO}$. For a chiral nanotube, Θ_{KA} is not zero, since the cutting line for the two-linear metallic bands deviates from the K point due to the curvature effect, and then the KA effect appears in both the LO and TO modes. For the zigzag M-SWNT (15,0), only the G^- peak that is related to the LO phonon appears, since the el-ph matrix element for the Raman scattering process for iTO phonon has a zero value for a zigzag tube, as shown in Figure 36(b). Thus, only an LO phonon softening is measured experimentally, even though a TO phonon hardening was expected theoretically.

The calculated G-band Raman spectra vs. E_F can be directly compared with the experimental G-band Raman spectra which are obtained for electro-chemically doped individual SWNTs, as seen in Figure 38 [86]. Here, we assume $\Delta E_F = 0.3 \Delta V_g$ according to Sasaki *et al.* [196]. The experimental Raman spectra are shown in Figure 38(a,c,e), and the corresponding calculated Raman spectra are shown in Figure 38(b,d,f). In Figure 38(a), the experimental Raman spectra show only a LO phonon softening, and a TO phonon frequency shift does not occur. As mentioned above, for the armchair SWNT, the TO phonon frequency shift does not appear and only LO phonon softening appears. Therefore, we can predict that Figure 38(a) shows an armchair-type behavior by changing the gate voltage. The RBM peak for these experimental Raman spectra appears at 161 cm^{-1} with $E_L = 1.72$ eV. Then we can select possible (n, m) values for a tube by using a simple tight-binding (STB) model with $\gamma_0 = 2.9$ eV for simplicity and by using the relation between the RBM frequency and diameter, $\omega_{RBM}(\text{cm}^{-1}) = 248/d_t(\text{nm})^{22}$, the possible for identifying the possible (n, m) values for SWNTs we obtain these (n, m) values as (19,1), (18,3), (14,8) and (11,11). If our prediction is correct, Figure 38(a) can be assigned as an (11,11) armchair SWNT. Figure 38(c) and (e) are assigned as chiral (24,4) and zigzag (12,0) SWNTs, respectively, from the possible (n, m) values,

$\{(21, 6), (22, 4), (23, 2)\}$ and $\{(10, 4), (11, 2), (12, 0)\}$. For the chiral M-SWNTs, not only is there a LO phonon softening, but there is also a TO phonon hardening that appears in the calculation of the G-band Raman spectra vs. E_F . However, in Figure 38, the TO peak is too small to see on the intensity scale of the figure. Figure 38(e) shows that the zigzag SWNT has only a G^- peak and thus only the LO phonon softening appears by changing E_F , experimentally. Brown *et al.* [128] and others [282,283] pointed out that asymmetric line shapes appear in the G^- band Raman spectrum for metallic tubes, which is related to the Fano resonance (Breit–Wigner–Fano, BWF line shape) lines. Recently, Farhat *et al.* showed that this asymmetry is sensitive to the relative position of the scattered light energy relative to $E_{ii}^{(M)}$, suggesting that the electron–electron interaction is important for understanding BWF lineshapes [206].

4. Raman spectra of graphene

In the family of sp^2 carbon systems, mono-layer graphene is the simplest crystal structure (see Figure 2), having the highest symmetry and, consequently, the simplest Raman spectra (see Figure 39). The big rush into graphene research started in 2004 [7,55,61]. The large research community that had become knowledgeable about the Raman spectroscopy associated with other nano-carbon systems was ready for a quick appreciation of the Raman spectra in mono-layer graphene as a perfect prototype spectra for the study and characterization of sp^2 carbons more generally [112,114,250]. For example, the detailed study of effects of inter-layer coupling on the *electronic* structure was carried out using the dispersion of the G' -band when changing the excitation laser energy in bi-layer graphene [284]. Strain[285–287], charge transfer and disorder effects due to doping, top gates and different types of substrates were addressed using the G and G' -bands of graphene [151,191,192,195,284–291]. Actually, graphene provides an ideal system to study defects using light as a probe because there are no aspects related to the penetration depth [3,65,292]. Interestingly, most of these findings in graphene are helping our basic understanding of long standing experimental results on carbon nanotubes and other nanocarbon systems [151,191,192,195,288,289,293]. Another important aspect that is peculiar to graphene is the fact that the G-band phonons (energy of 0.2 eV) can promote electrons from the valence band to the conduction band. This happens because graphene is a zero gap semiconductor, and the linear $E(k)$ dispersion relation centered around the Dirac cones for the valence and conduction bands (see Figure 9(a)) near the Fermi level makes the effect especially interesting, and it gives rise to a

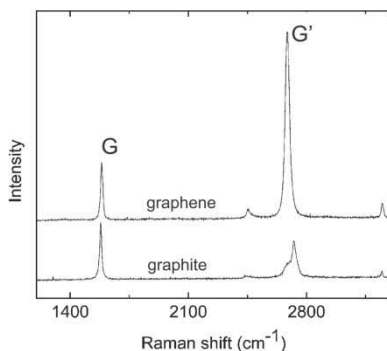


Figure 39. Raman spectrum of single-layer graphene in comparison to graphite measured with a $E_{\text{laser}} = 2.41$ eV (514 nm) laser. The two most intense features are named the G and G' -bands. The Raman spectrum of pristine mono-layer graphene is unique among sp^2 carbons, i.e., the second-order G' feature is very intense when compared to the first-order G-band feature (see discussion in Section 4.1) [112,250].

renormalization of the electronic and phonon energies, including a sensitive dependence of the electronic structure on electron or hole doping [195]. Raman imaging can be used to define the number of layers in different locations of a given graphene flake by measuring the dependence of the Raman spectra (e.g., for the G-band intensity) on the number of scattering graphene layers [294]. It is true that such information has to be analyzed with care since doping and other physical phenomena perturb the graphene Raman spectra. The effect of environmental interactions on few-layer graphene samples have also been studied using Raman spectroscopy, including the epitaxial growth of graphene on a substrate [295]. In this brief survey a number of important topics are reviewed, including the spectra of mono-layer graphene, the layer number dependence in few layer graphene, disorder-related phenomena, edge phonon phenomena, polarization effects and the effects of doping.

4.1. *The G-band and G'-band intensity ratio*

The first intriguing result that was observed when the Raman spectrum from single layers of graphene was measured was the unusual G' to G intensity ratio $I_{G'}/I_G$. While the second-order G' Raman band in 3D graphite has a much smaller intensity than the first-order Raman-allowed G-band, in single-layer graphene the G' -band intensity is much stronger, reaching 4 times the G-band intensity. In principle, the G' to G intensity ratio can be used to determine the number of layers in a few layer graphene sample, since $I_{G'}/I_G$ is reduced by increasing the number of layers. However, it is also true that this ratio is sensitive to doping [220,291] and disorder [130], and the intermixing of information (doping vs. number of layers) makes it complicated to use Raman spectroscopy to determine the number of layers in few-layer graphene samples accurately, unless the parameters for the environmental effects are clearly delineated.

Basko [219,296] argues that the special Raman spectrum of mono-layer graphene (1-LG) is an indication that the very strong G' -band comes from a fully resonant scattering process where both the el-ph absorption and emission are resonant, as well as the el-ph and hole-phonon scattering processes, so that the absorption and recombination occur at different Dirac cones. The very strong G' -band intensity could also be related to different el-ph matrix elements near the K point (for the G' -band) and near the Γ point (for the G-band) phonons [218–220]. The fully resonant process should, in principle, be much more probable than the other processes which exhibit a virtual (non-resonant) state. However, this can only happen if the electron and hole electronic dispersion relations are symmetric within the phonon uncertainty and if the electron and hole scattering by phonons is equally probable. Since the electron wave function overlap in graphene results in a different normalization for the valence and conduction bands, an e-h dispersion asymmetry is introduced, and for this reason the two processes could select double resonance phonons with somewhat different q vectors. This asymmetry is relatively small and is generally neglected in common descriptions of the electronic structure of graphene in terms of mirror band cones. More theoretical and experimental work is required to fully understand the differences in the el-ph vs. hole-phonon scattering, including the differences in the matrix elements for these two processes.

4.2. *Layer number dependence of G'-band*

4.2.1. *The number of graphene layers with AB stacking*

Because of its dependence on the layer number, the Raman G' -band has been used to characterize the number of layers in few layer graphene samples and the stacking order between these layers, as shown in Figure 40. The Raman spectra for highly ordered pyrolytic graphite (HOPG) and for turbostratic graphite (which has random inter-layer stacking) are also shown in Figure 40 for comparison. To explain this observed behavior, we first remind the reader about the dispersive

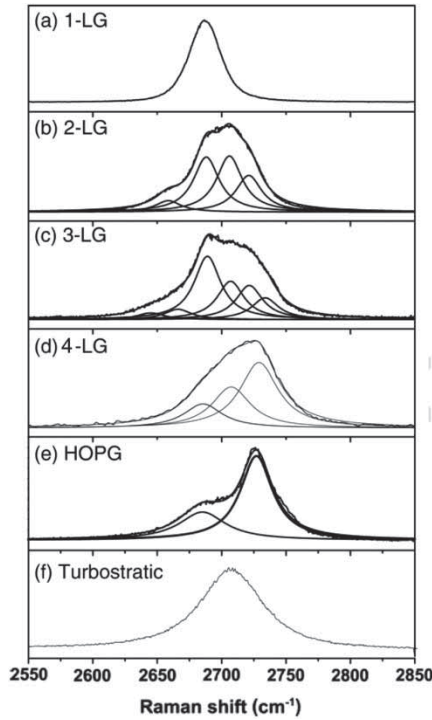


Figure 40. The differences in the G' Raman band for (a) 1-LG, (b) 2-LG, (c) 3-LG, (d) 4-LG, (e) HOPG and (f) turbostratic graphite. All spectra are measured with $E_{\text{laser}} = 2.41$ eV. The original work was done by Ferrari *et al.* [112] and is summarized in the review article of Malard *et al.* [5].

behavior discussed in connection with Figures 24 and 27. Then we turn to a discussion of the electronic properties of bi-layer graphene with AB Bernal layer stacking (as also occurs in graphite), since the band structure change from mono-layer to bi-layer graphene is the most striking and both mono-layer and bi-layer graphene have been probed by Raman scattering [284]. The change in the electronic structure of graphene due to layer stacking can be probed in some detail by the DR Raman features (see Section 3.1.3), and most sensitively by the detailed lineshape of the G' -band [112]. Bi-layer graphene has a 4-peak G' -band spectrum (Figure 40(b)) while mono-layer has a 1-peak G' -band (Figure 40(a)), and this fact is explained by the special electronic structure of bi-layer graphene, which consists of two conduction and two valence bands [112], as discussed below.

Figure 41(a) shows the dispersion (peak frequency as a function of E_{laser}) of each one of the four peaks in Figure 40(b), which comprises the G' -band for bi-layer graphene with AB stacking. The double Raman resonance processes for bi-layer graphene are shown in Figure 41(b)–(e), where the diagrams show the possible DR Raman processes that give rise to the four G' peaks in Figure 41(a). The processes are labeled by P_{ij} ($i, j = 1, 2$) [284], where the states with energy E_i in the valence band and E_j in the conduction band are connected in the photon absorption process using laser energy E_{laser} . The highest frequency G' peak for a given E_{laser} energy is associated with the P_{11} process, since the P_{11} process has the largest wave vector (q_{11}) and the i TO phonon along the KM direction in the BZ increases its frequency with increasing wave vector q (see Figure 40(b) and Figure 41). The lowest frequency G' -band peak is associated with the process P_{22} , which gives rise to the smallest phonon wave vector q_{22} . Processes P_{12} and P_{21} shown in Figure 41(b) give rise to the two intermediate frequency peaks of the G' -band [112,284,297]. This DR Raman

model has been used to relate the electronic and phonon dispersion of bi-layer graphene with the experimental dependence of $\omega_{G'}$ on E_{laser} [284].

Tri-layer graphene has 15 possible DR processes [1,4], but the frequency spacings between these peaks are not large enough to allow identification of each of the 15 scattering events (Figure 40(c)). Increasing the number of layers increases the number of possibilities for the G' -band DR scattering processes, and an in depth analysis would get more and more complicated for N -layer graphene ($N > 3$). However, experimentally the G' -band spectra at a typical E_{laser} energy (e.g., 2.41 eV) actually gets simpler in appearance when the number of layers increases (see, for example Figure 40(d) for 4-LG). The spectra of increasing N converge to the two-peak structure observed in HOPG, where $N \rightarrow \infty$, as shown in Figure 40(e). The two-peak structure of HOPG (Figure 40(e)) is the result of a 3D electron and phonon dispersion, as discussed in [298], which can be seen as a convolution of an infinite number of allowed DR processes along the third dimension of $N \rightarrow \infty$ graphite.

4.2.2. Characterization of the graphene stacking order by the G' spectra

The use of G' -band Raman spectroscopy to assign the number of layers has to be a cautious procedure, because the G' -band lineshape is related not only to the number of layers, but also to the stacking order of these layers. The G' -band has actually been used to quantify the structural ordering along the c - axis in graphite [299–301] much before the rise of the graphene field in 2004. The change from one peak to two peaks in the G' -band profile observed in the Raman spectra from polycrystalline to crystalline graphite was shown in the late 1970s [223,302]. Raman spectroscopy studies of carbon materials heat treated at different temperatures T_{htt} show that, by increasing T_{htt} , the G' -band changes from a one-peak to a two-peak structure (see Figure 40(e,f)) [299,300]. Lespade *et al.* [299] associated this evolution with the degree of graphitization of the samples, suggesting that the origin of the two-peak structure of the G' -band in crystalline graphite was related to the stacking order occurring along the c - axis. Finally, the evolution from the 2D to 3D aspect (from one to two peaks [303]) has been quantitatively systematized (see also Section 4.2.1). Barros *et al.* have used the G' -band to identify three G' -band peaks due to the coexistence of 2D

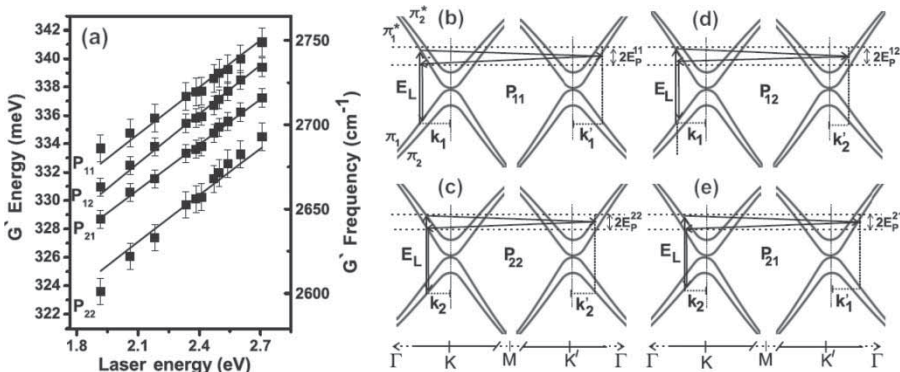


Figure 41. (a) Plot of the frequency of the four Raman G' -band peaks vs. E_{laser} observed in bi-layer graphene. These four peaks arise from the four processes shown in (b)–(e) which comprise the G' -band scattering processes that are expected for the phonon frequencies in bi-layer (2-LG) graphene plotted in (a) as a function of laser energy E_{laser} . Reprinted with permission from L.M. Malard *et al.*, *Physical Review B* 76, p. 201401, 2007 [284]. Copyright © (2007) by the American Physical Society.

and 3D graphite phases in more complicated carbon-based materials, such as pitch-based graphitic foams [101].

The differences between stacked and non-stacked graphene layers became even more clear when the G-band Raman spectra of AB stacked and misoriented folded bi-layer graphene were compared [4,295,304]. While the AB stacked bi-layer graphene shows a four-peak structure, as illustrated in Figure 40(b), the G-band spectra of misoriented bi-layer graphene shows a one-peak profile, with an upshift of $\sim 14 \text{ cm}^{-1}$. This result is generally consistent with the observations for turbostratic graphite shown in Figure 40 and it was explained as due to changes in the Fermi velocity of graphene due to interlayer interactions in AB-stacked samples [295]. These aspects also explain why a broadened single G' peak is observed for regions of a sample that contains domains of mono-layer or bi-layer graphene. For example, CVD-grown graphene often shows such domains of mono-layer and bi-layer graphene and furthermore the stacking of the layers is often not AB Bernal stacking [85,305,306]. Using a similar path of reasoning as was followed to understand the difference in the G' -band lineshape between mono-layer graphene and bi-layer graphene with AB stacking, it is easy to understand that the G' lineshape will be different for ABC and ABA trilayer graphene stacking. Recently, Liu *et al.* [307] showed that the G' -band can indeed be used to distinguish between ABC versus ABA stacking in trilayer graphene samples. The G' -band for ABC stacked samples is generally broader than that for ABA, and by mapping the G' width, Liu *et al.* showed that these two types of stacking order coexist in trilayer graphene samples. By mapping several samples, they showed that about 15% of the samples generated by the mechanical exfoliation of HOPG are ABC-stacking-like, and this value for the mixed stacking order is in very good agreement with X-ray studies on HOPG [9].

4.3. D-band and G-band intensity ratio and other disorder effects

Graphene provides an ideal structure to study the effect of disorder on a Raman spectrum, because in a mono-layer 2D structure one does not have to worry about cascade effects and the penetration depth of the light [3,65,292]. Here we discuss the effect of disorder caused by low energy Ar^+ bombardment [3].

4.3.1. Ar^+ ion bombardment on graphene

Raman spectroscopy is one of the most sensitive techniques that can be used to characterize disorder in the sp^2 network of carbon materials [308]. It is widely used to identify disorder in diamond-like carbon, amorphous carbon, nanostructured carbon, carbon nanofibers, carbon nanotubes and carbon nanohorns [2,174]. Just as Raman spectroscopy has been used for the characterization of defects through the observation of symmetry-breaking features in the Raman spectra, point defects have been used as a characteristic defect that can be readily reproduced [308] and the uses of ion implantation to create these point defects has been widely adopted.

The first-order Raman spectra of crystalline graphene is shown in Figure 42(a), where the presence of the Raman-allowed G-band is observed. When graphene is bombarded by Ar^+ ions (starting with a low dose, $10^{11} \text{ Ar}^+/\text{cm}^2$ in Figure 42(b)), point defects are formed and the Raman spectra of the disordered graphene exhibit two new sharp features, named by D and D' , appearing at 1345 cm^{-1} and 1626 cm^{-1} , respectively, for $E_{\text{laser}} = 2.41 \text{ eV}$ (Figure 42(b)). The D and D' labels indicate that these Raman bands are induced by disorder [102]. Both of these bands are dispersive and change frequency when changing $E_{\text{laser}} = 2.41 \text{ eV}$. Actually, the DR process discussed for the symmetry-allowed G' -band was developed to explain the dispersive behavior of the D-band [104]. Instead of electron scattering by two phonons with momentum q and $-q$, the breaking of the translational symmetry of crystals can be activated by introducing defects into the

lattice. Introducing disorder breaks down the momentum conservation requirement, and phonons at interior k points of the BZ can contribute to the Raman scattering process. Similar to the case of the G' -band, those scattering processes due to point defects which fulfill the DR process are privileged in the disorder-induced Raman scattering process discussed in this section.

Finally, if the periodic structure of graphene is largely disordered, for example from a high defect density caused by applying a large ion dose bombardment, such as 10^{15} Ar^+/cm^2 , the Raman spectrum evolves into a phonon DOS-like profile, where most of the higher-energy optical phonon branch would be contributing to the spectra, rather than solely the special phonons fulfilling the DR process (see Figure 42(c)) [3]. Of course in a fully disordered material, not only are all phonons activated, but also changes in the structure, bonding and strain fields change the vibrational frequencies and lineshapes.

4.3.2. The D to G intensity ratio and the L_D dependence

Mono-layer graphene samples were bombarded with Ar^+ ions and consecutive Raman spectra were performed to study the evolution of the disorder-induced Raman peaks [3]. Figure 43 shows the Raman spectra of a graphene mono-layer sample subjected to the ion bombardment procedure that is described in the beginning of Section 4.3.5. From the pristine sample (bottom spectrum in Figure 43) to the lowest bombardment dose in Figure 43 (10^{11} Ar^+/cm^2), the D-band process is activated, showing a very small D-band intensity relative to the G peak which is symmetry-allowed. Within the bombardment dose range 10^{11} - 10^{13} Ar^+/cm^2 , the intensities of the disorder induced peaks increase. A second disorder-induced peak around ~ 1620 cm^{-1} (the D' -band) also becomes clearly evident at a dose of 10^{12} Ar^+/cm^2 , but we do not focus on this feature here. The Raman spectra start to broaden significantly above 10^{13} Ar^+/cm^2 , and the spectra end up exhibiting the graphene phonon density of states-like spectrum, corresponding to Figure 42(c)). From 10^{14} Ar^+/cm^2 (top spectrum in Figure 43) and above, the Raman scattering shows a lineshape broadening with no measurable change in the peak frequencies of these broad features.

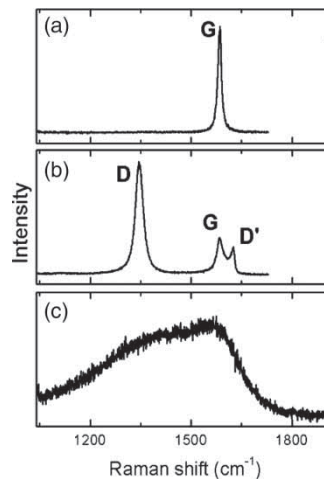


Figure 42. The Raman spectrum of (a) crystalline graphene, (b) defective graphene, (c) and fully disordered single-layer graphene. These spectra were obtained with $E_{\text{laser}} = 2.41$ eV and the graphenes are deposited on a SiO_2 substrate using the mechanical exfoliation method (scotch-tape). Reprinted with permission from A. Jorio *et al.*, Journal of Physics: Condensed Matter 22, p. 334204, 2010 [309]. Copyright © (2010) by the Institute of Physics.

The development of disorder in sp^2 carbon nano-crystallites is conveniently described by plotting the I_D/I_G ratio as a function of crystallite size [102]. Here we perform a similar analysis, but plotting the I_D/I_G ratio as a function of the average distance L_D between defects, as shown in Figure 44. Note that the I_D/I_G ratio has a non-monotonic dependence on L_D . The I_D/I_G ratio is here seen to increase initially with increasing L_D , up to $L_D \sim 3.5$ nm, and then it decreases for $L_D > 3.5$ nm, consistent with the proposed amorphization trajectory for sp^2 carbon nano-crystallites [131]. Such a behavior indicates the existence of two competing mechanisms that contribute to the Raman D-band, as described below.

4.3.3. The D to G intensity ratio: the “local activation” model

The impact of a single ion on a graphene sheet causes modifications on two length scales, which we denote here by r_A and r_S . These two length scales represent, respectively, the radii of two circular areas measured from the impact point, as shown in Figure 45. Structural disorder from the impact position occurs within the shorter radius r_S , where the subscript S stands for structurally disordered. For distances larger than r_S but shorter than r_A , the lattice structure is preserved but a break-down of the selection rule is caused by the proximity to the structurally disordered area (S-region), thus leading to a local enhancement of the Raman D-band. We call this the A-region, where A stands for activated. When the Raman scattering process occurs at distances larger than $\ell_\phi = r_A - r_S$ from the defective region, only the G-band is active. The I_D/I_G ratio is then given as a function of the average distance between two defects, L_D , by [3]:

$$\frac{I_D}{I_G}(L_D) \propto I_D(L_D) = C_A f_A(L_D) + C_S f_S(L_D). \quad (73)$$

The intensity I_G remains constant, independent of L_D , while f_A and f_S are the fractions of the A and S areas in the sheet, respectively, with respect to the total area. Both the A and S regions break momentum conservation and give rise to a D-band. However, the A-regions will contribute

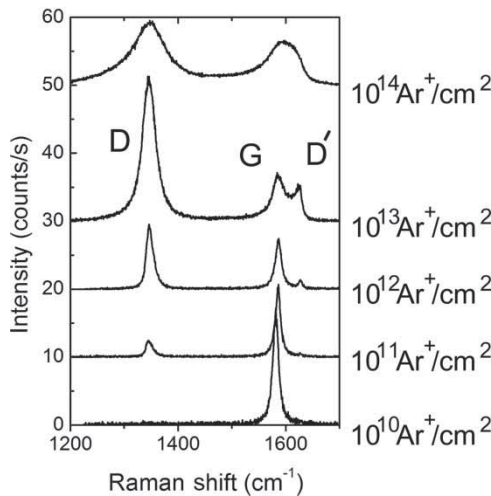


Figure 43. Evolution of the first-order Raman spectra using a $\lambda = 514$ nm laser ($E_{\text{laser}} = 2.41$ eV) to investigate a graphene mono-layer sample deposited on a SiO_2 substrate, and subjected to Ar^+ ion bombardment. The Ar^+ ion doses from the bottom trace to the top trace are: zero (pristine), 10^{11} , 10^{12} , 10^{13} and 10^{14} Ar^+/cm^2 for 90 eV ions. The spectra in this figure are also displaced vertically for clarity. Reprinted From Carbon 48(5), M.M. Lucchese *et al.*, pp. 1592–1597 [3]. Copyright © (2010) Elsevier.

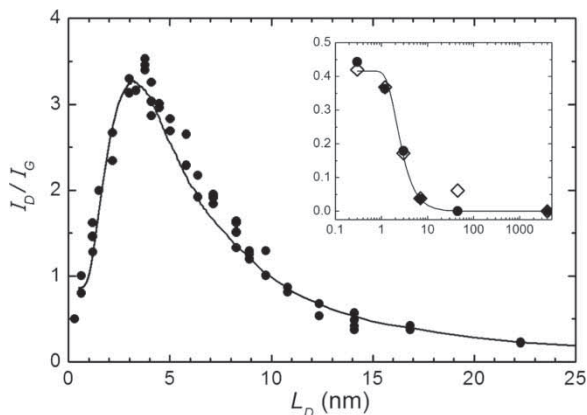


Figure 44. The I_D/I_G data points from three different mono-layer graphene samples as a function of the average distance L_D between defects, induced by the Ar^+ ion bombardment procedure described in Section 4.3.2. The solid line is a modeling of the experimental data with Equation (73). The inset shows a plot of I_D/I_G vs. L_D on a log scale for two samples: (i) a ~ 50 -layer graphene sample; (ii) a 2 mm-thick HOPG sample, whose measured values are here scaled by $(I_D/I_G) \times 3.5$. Reprinted From Carbon 48(5), M.M. Lucchese *et al.*, pp. 1592–1597 [3]. Copyright © (2010) Elsevier.

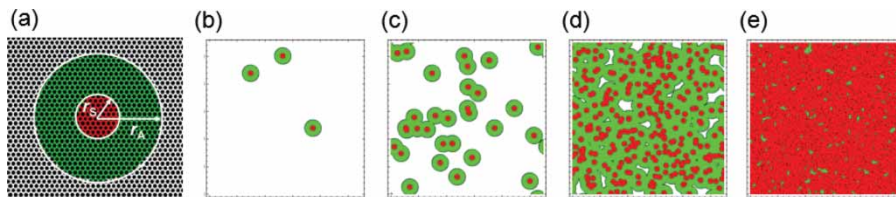


Figure 45. (a) Definition of the “activated” A-region (darkest gray) and “structurally disordered” S-region (dark gray). The radii r_S and r_A are measured from the impact point which is chosen randomly in this simulation. (b–e) show 55 nm \times 55 nm portions of the graphene simulation cell, with snapshots of the structural evolution of the graphene sheet for different defect concentrations: (b) $10^{11} \text{ Ar}^+/\text{cm}^2$; (c) $10^{12} \text{ Ar}^+/\text{cm}^2$; (d) $10^{13} \text{ Ar}^+/\text{cm}^2$ and (e) $10^{14} \text{ Ar}^+/\text{cm}^2$, as in Figure 43. Reprinted From Carbon 48(5), M.M. Lucchese *et al.*, pp. 1592–1597 [3]. Copyright © (2010) Elsevier.

most strongly to the D-band, while the S-regions will make less contribution to the D-band due to the break-down of the lattice structure itself. These two different scattering cross sections for the disorder-induced processes will give rise to the non-monotonic behavior observed in the L_D dependence of the I_D/I_G ratio, as shown in Figure 44.

The structurally disordered (S) region and the activated (A) region are shown in Figure 45(a) by light and dark gray regions, respectively. The evolution of the S and A regions for a graphene sheet under ion bombardment was simulated by randomly choosing a sequence of impact positions on a graphene sheet. As the number of impacts increase, the activated A-region increases, leading to a decrease in L_D and an increase of the D-band intensity I_D . When the graphene is fully covered with A-regions, an increase in ion bombardment fluence causes the structurally disordered S-regions to take over from the A-regions, thus leading to a decrease of the D-band intensity I_D (see Figure 45(b–e)). This model is the basis for the evolution of I_D/I_G based on Equation (73) which, with the parameters $C_A = 4.56$, $C_S = 0.86$, $r_A = 3 \text{ nm}$ and $r_S = 1 \text{ nm}$, give the line curve

in Figure 44 that fully describes the experimental evolution of I_D/I_G , shown by the black bullets in Figure 44 [3].

For low defect concentrations (large L_D values), $I_D/I_G = (102 \pm 2)/L_D^2$, which means the total area contributing to scattering is proportional to the number of defects. This regime is valid for $L_D > 2r_A$, while below this limit for L_D , the activated regions start to overlap (see Figure 45(e)), thus changing the simple $I_D/I_G \propto L_D^{-2}$ dependence. The D-band intensity then reaches a maximum and a further increase in the defect concentration decreases the D-band intensity because the graphene sheet starts to be dominated by the structurally disordered areas (S-region).

The $r_S = 1$ nm value is in agreement with the average size of the disordered structures seen in the STM images [3,130]. This is not a universal parameter, but is a parameter that is actually specific to the ion bombardment process. The $\ell_\phi = r_A - r_S = 2$ nm value represents the Raman relaxation length for the defect-induced resonant Raman scattering in graphene. This value is valid for the laser excitation energy 2.41 eV and room temperature, and may change with changing E_{laser} and temperature. Be aware that this is the relaxation length for the excited electrons, which should not be confused with the relaxation length for the phonons. The value $C_A = 4.56$ is in rough agreement with the ratio between the electron–phonon coupling for the iTO phonons evaluated between the Γ and the K points in the BZ [218–220], which is consistent with the expectation that the C_A parameter should be related to the electron–phonon matrix elements. The C_S parameter is related to the size of the highly disordered area, and there is no theoretical work yet available on this matter.

It is important to have an equation relating I_D/I_G to L_D that can be used by researchers looking for a Raman characterization of the defect density present in a specific graphene sample. The entire regime ($0 \rightarrow L_D \rightarrow \infty$) can be fitted using [3]:

$$\frac{I_D}{I_G} = C_A \frac{r_A^2 - r_S^2}{r_A^2 - 2r_S^2} \left[\exp\left(\frac{-\pi r_S^2}{L_D^2}\right) - \exp\left(\frac{-\pi(r_A^2 - r_S^2)}{L_D^2}\right) \right] + C_S \left[1 - \left(\frac{-\pi r_S^2}{L_D^2}\right) \right], \quad (74)$$

which comes from solving rate equations for the bombardment process. Fitting the data in Figure 44 with Equation (74) gives $C_A = (4.2 \pm 0.1)$, $C_S = (0.87 \pm 0.05)$, $r_A = (3.00 \pm 0.03)$ nm and $r_S = (1.00 \pm 0.04)$ nm. This equation represent the results very well, since the fitting obtained with Equation (74) is also in very good agreement with experiment and the fitting parameters are fully consistent with the parameters obtained by computational modeling using Equation (73) [3].

4.3.4. The Local Activation Model and the Raman Integrated Areas

The dependence of the intensity ratio I_D/I_G on L_D was found to accurately follow an analytical formula (Equation (74)), as described above, and this result is useful for practical applications and for inter-laboratory comparisons. However, the physics behind this effect has to take into account that both I_D and I_G vary when L_D is changed. As discussed in Section 1.4.5, the evolution of the Raman profile can be discussed as related to the peak intensity or to the integrated peak area. In this section, we choose to use the same model as was used to derive Equation (74) when we analyze the evolution of the intensity and integrated area of the many Raman peaks that vary with increasing structural disorder, by normalizing each of them to the G-band integrated area (see Figure 46). As shown in the inset to Figure 46 (top-right panel), the integrated area of the G-band does not show any simple evolution with disorder [130].

The lower-left panels of Figure 46 show that this analytical expression fits the quantities A_D/A_G and $A_{D'}/A_G$ nearly perfectly, where A refers to the integrated area. For the D-band, the fitting parameters are $r_S = 2.6$ nm, $r_A = 4.1$ nm, $C_S = 2.4$ and $C_A = 3.6$, whereas for the D'-band the fitting parameters are $r_S = 2.6$ nm, $r_A = 3.8$ nm, $C_S = 0.28$ and $C_A = 0.19$. Note that we obtain close to the same value of r_S for both the D and D' modes, indicating that indeed r_S

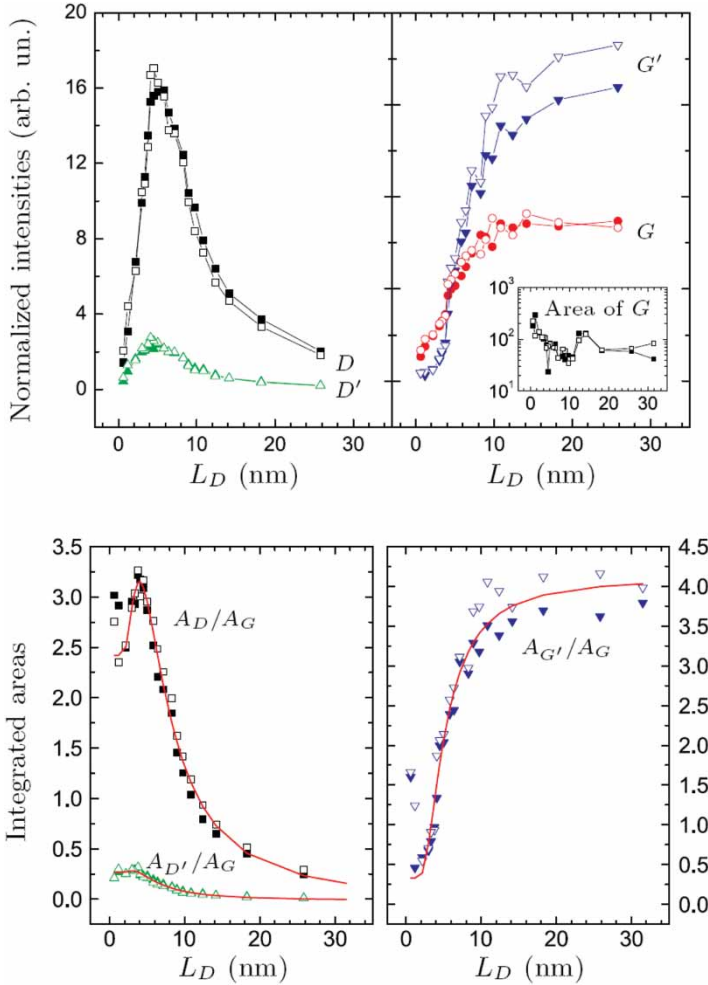


Figure 46. Normalized intensities (upper panel) and areas (lower panel) of the Raman D-, D'-, G- and G'-bands as a function of L_D . All quantities are normalized by the area of the G-band (see the as-measured A_G in the inset to the upper-right panel). The solid lines in the lower panel are theoretical results based on the model described in Section 4.3.4. Reprinted figure with permission from E.H. Martins Ferreira *et al.*, *Physical Review B* 82, p. 125429, 2010 [130]. Copyright © (2010) by the American Physical Society.

is a geometrical, structure-related length. Also, we find 1.5 and 1.3 nm for the spatial extent of the Raman processes $r_A - r_S$, which is of the same order of magnitude as the rough estimates $v_F/\omega_D = 4.3$ nm and $v_F/\omega_{D'} = 3.6$ nm. We remind the reader that the distance $r_A - r_S$ is a rough measure of the length traveled over the lifetime of the e-h pair, v_F/ω_X , where v_F is the graphene Fermi velocity of the electron and hole carriers and ω_X is the frequency of any X phonon mode [130]. More interestingly, the ratio between $r_A - r_S$ for the D- and D'-bands matches very closely to the ratio of the inverse frequencies $\omega_{D'}/\omega_D \approx 1.2$.

Similar ideas can be applied to a discussion of the $A_{G'}/A_G$ ratio, but in this case, since the G'-band is already active for pristine graphene, the intensity ratio is only affected by the disruption of the hexagonal network, leading to a decrease in the $A_{G'}/A_G$ ratio as a function of increasing

disorder described by the simple formula [130]

$$\frac{A_{G'}}{A_G}(L_D) = \frac{A_{G'}}{A_G}(\infty) - B \left[1 - \exp\left(-\frac{\pi r_S^2}{L_D^2}\right) \right], \quad (75)$$

where $A_{G'}/A_G(\infty)$ is the area ratio for pristine graphene while $A_{G'}/A_G(L_D)$ is the area ratio for an actual sample characterized by its L_D value. The fitting of the experimental data, shown in the lower-right panel of Figure 46, gives in this case $r_S = 2.5$ nm, which is also similar to the structural damage length obtained for the D- and D'-band spectra. This result is in accordance with the typical defect-size estimates found independently from the STM analysis [3,130]. In Section 4.3.5, we describe what happens to the frequency and linewidth of the Raman peaks as a result of ion implantation-induced structural damage.

4.3.5. Modeling disorder effects in the Raman linewidths and frequency shifts: the spatial correlation model for defects

Disorder introduced by a random distribution of defects causes a broadening and a shifting of the Raman mode frequencies and increases in the asymmetry of both the Raman-allowed and the newly disorder-activated Raman bands discussed in Section 4.3.4. Here, we use the so-called “spatial-correlation model” introduced by Capaz and Moutinho in [130] to describe these effects in graphene. Other work on this topic that should also be referred to is in Refs. [65,292],

As described in Section 1.4.6, a random distribution of point defects will scatter phonons and it will also add a contribution to the FWHM by an el-ph coupling of phonons with wave vectors \mathbf{q}_0 and $\mathbf{q}_0 + \delta\mathbf{q}$. In the limit of low levels of disorder, the Raman intensity for the disordered graphene $I(\omega)$ can be calculated by Equation (7). With this model, we can calculate the full lineshape of $I(\omega)$ and from that we can extract the disorder-induced peak shifts $\Delta\omega_{\mathbf{q}_0}$ (Figure 47, lower panel) and the increases in the FWHM $\Delta\Gamma_{\mathbf{q}_0}$ (Figure 48, lower panel). Since we use experimentally available dispersion relations $\omega(\mathbf{q})$, the only fitting elements in this model are: (1) the relationship between the coherence length L and the typical inter-defect distance L_D , and (2) the weighting function $W(\mathbf{q})$ in Equation (7).

We now describe in more detail the application of the above model to the different Raman bands considered in graphene, including the G-band, the D'-band, the D-band and the G'-band [130].

A. G-band—The G-band in perfect graphene is associated with phonons at the Γ -point, i.e., $\mathbf{q}_0 = 0$ phonons. We consider that disorder mixes equally the Γ -point phonons with nearby phonons in both the LO and iTO phonon branches. We find that the best agreement with experiment is obtained by using a constant weighting function (which is equivalent to not use a weighting function at all). For the LO and TO phonon dispersions, we take

$$\begin{aligned} \omega_{\text{LO}}(q) &= \omega_G + 181q - 230.29q^2, \\ \omega_{\text{iTO}}(q) &= \omega_G - 135.42q, \end{aligned} \quad (76)$$

where $\omega_n(q)$ is in cm^{-1} ($n = \text{LO}$ or iTO) and $\omega_G = 1580 \text{ cm}^{-1}$ is the experimental G-band frequency for pristine graphene used in this work. Here q is measured from the Γ -point in units of \AA^{-1} . These dispersions are taken from the work of Maultzsch *et al.* [208] by interpolating the frequencies at high-symmetry points and by averaging the dispersions between the Γ - K and Γ - M directions. Also, since the main contribution to the integral in Equation (7) will come from q vectors near the Γ point, the BZ can be safely approximated by a circular disk and the integral will be considered explicitly in the radial coordinate only. Taking all these considerations into account, Equation (7)

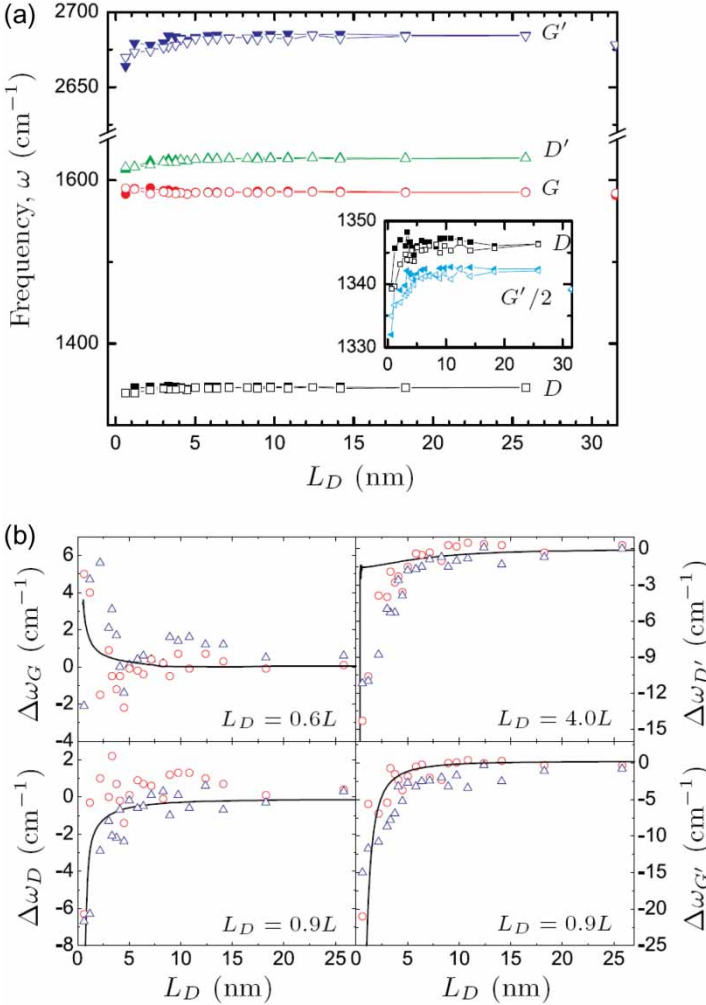


Figure 47. The upper panel shows peak frequencies of the D, G, D' and G'-bands as a function of L_D denoting a typical distance between defects. The inset compares the frequency of the D-band and the G'-band divided by two, showing that we always have $\omega_{G'}/2 < \omega_D$, in agreement with Ref. [216]. The lower panel shows frequency shifts with respect to the zero-disorder limit. Dots are experimental points and solid lines are theoretical results based on the model described in the text. Experimental error bars are 2 cm^{-1} . Reprinted figure with permission from E.H. Martins Ferreira *et al.*, *Physical Review B* 82, p. 125429, 2010 [130]. Copyright © (2010) by the American Physical Society.

becomes [130]

$$I_G(\omega) \propto \sum_n \int 2\pi q dq \frac{\exp[-q^2 L^2/4]}{[\omega - \omega_n(q)]^2 + [\Gamma_0/2]^2} \quad (77)$$

in which the sum is over the two (LO and iTO) phonon branches.

B. D'-band – The D'-band arises from intra-valley phonons with a linear wavevector intensity dependence with respect to the laser energy. Since the D'-band has been assigned to LO phonons, only this branch is considered in calculations of the D'-band intensity using Equation (7). We

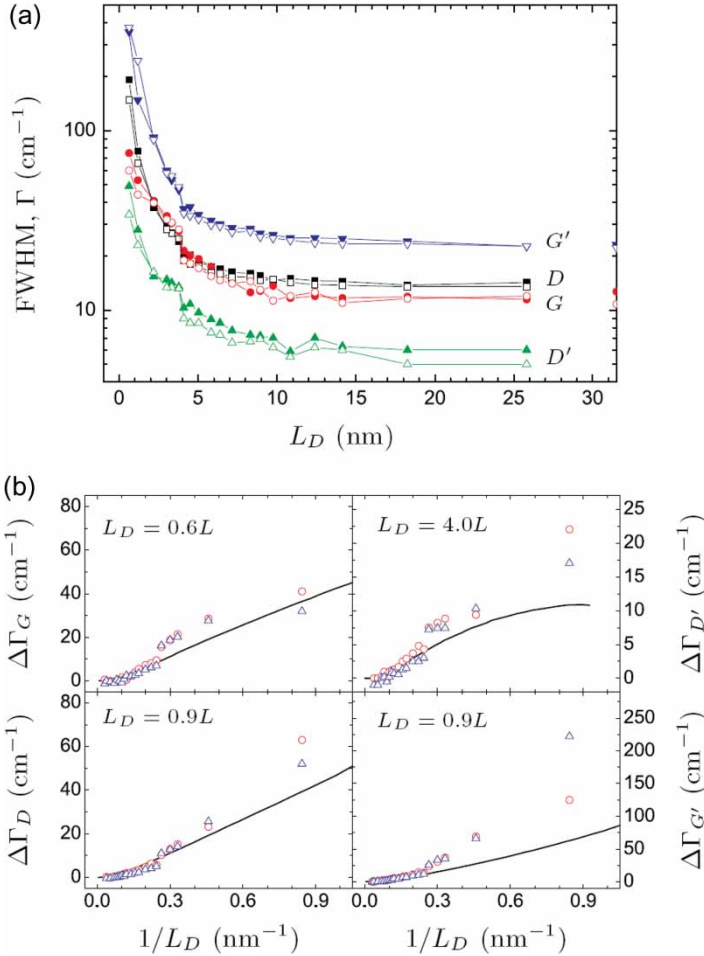


Figure 48. (a) FWHM intensity of the D-, G-, D'- and G'-bands as a function of L_D , denoting the typical distance between defects. (b) Disorder contribution to the peak widths, $\Delta\Gamma$, for the D, G, D' and G'-bands. Points denote are experiments and solid lines are theoretical results based on the model described in the text. Reprinted figure with permission from E.H. Martins Ferreira *et al.*, *Physical Review B* 82, p. 125429, 2010 [130]. Copyright © (2010) by the American Physical Society.

average over all possible directions θ of the wavevector \mathbf{q}_0 and, similarly to the case of the G-band, there is no need to introduce a q -dependent weighing function $W(\mathbf{q})$. Then, the D'-band intensity becomes [130]:

$$I_{D'}(\omega) \propto \int q dq d\theta \frac{\exp[-(\mathbf{q} - \mathbf{q}_0)^2 L^2 / 4]}{[\omega - \omega_{LO}(q)]^2 + [\Gamma_0 / 2]^2}. \quad (78)$$

For the laser energy of 2.41 eV, the value for $|\mathbf{q}_0|$ in Equation (78) is found to be $|\mathbf{q}_0| = 0.42 \text{ \AA}^{-1}$ measured from the Γ point.

C. D-band– The D-band arises from inter-valley phonons which also show a linear wavevector dependence with respect to the laser energy. In fact, for the laser energy of 2.41 eV, we also find $|\mathbf{q}_0| = 0.42 \text{ \AA}^{-1}$ for the D-band, but now \mathbf{q}_0 is measured from the K point. Since the D-band has been assigned to iTO phonons along the K – M direction in the BZ, we choose \mathbf{q}_0 along this

direction and the weighting function $W(\mathbf{q})$ is also restricted to be non-zero only along the same direction. Mathematically, $W(\mathbf{q}) = \delta(\theta - \theta_{K-M})f(q)$, where θ_{K-M} indicates the K - M direction and $f(q) = 1 + a(q_0 - q)$ is a function that linearizes the radial dependence of the electron-phonon coupling along the K - M direction near q_0 . With these conditions, the D-band intensity becomes [130]

$$I_D(\omega) \propto \int dq \frac{f(q) \exp[-(q - q_0)^2 L^2 / 4]}{[\omega - \omega_{\text{iTO}}(q)]^2 + [\Gamma_0 / 2]^2}. \quad (79)$$

For the iTO phonon dispersion along the K - M direction, we use [244]:

$$\omega_{\text{iTO}}(q) = \omega_K + 589.35q - 485.46q^2, \quad (80)$$

where ω_{iTO} is in cm^{-1} and q is measured from the K point in units of \AA^{-1} .

D. G' -band – The G' -band is related to a DR process associated with the same inter-valley phonons as the D-band. For this reason, the expression for the intensity becomes more complicated and it involves a double integral over the forward (q) and backward (q') phonon wavevectors. Using the same considerations for the el-ph matrix elements, which essentially select phonons in the K - M direction, we have

$$I_{G'}(\omega) \propto \int dq dq' \frac{f(q)f(q') \exp[-(-(q - q_0)^2 + (q' - q_0)^2)L^2/4]}{[\omega - \omega_{\text{iTO}}(q) - \omega_{\text{iTO}}(q')]^2 + [\Gamma_0/2]^2} \quad (81)$$

where $f(q)$ is the same linear function as in the D-band case and q_0 is also the same. We also impose the condition that the same relation between L (the disorder-induced phonon coherence length) and L_D (the average distance between defects) must be valid for the D and G' -bands.

In Figures 47 and 48, we see the results for the frequency and linewidth as a function of the typical distance L_D between defects for the data fitting of the frequency shifts and widths, respectively, as described above. Note that the general agreement is good, especially for large values of L_D . Indeed, this spatial correlation model, because of its perturbation character, is not expected to be valid in the highly disordered regime. In Figures 47 and 48, the best relationships between L and L_D in each case are shown (as obtained by the fits between the model and the experimental data). It is physically reasonable to see that L and L_D are similar to each other. This condition was not imposed, but it comes automatically from the fitting procedure. This means that the disorder-induced phonon coherence length L is of the same order of magnitude as the typical inter-defect distance L_D , which is physically reasonable. There is no reason to expect that the same relation between L and L_D should be found for the different phonon modes, since different modes should have different defect scattering cross-sections. From the results shown here, it seems that the D' modes are the most affected by point defect disorder, showing a smaller coherence length than the other modes for the same amount of disorder. Finally, the model allows us to explain the greater increase in the FWHM for each of the modes near the K point relative to the modes near the Γ point as being simply a consequence of the larger magnitude of the phonon dispersions near the K point.

4.3.6. Evolution of overtone and combination modes

In Figure 49, we present the spectral evolution of the G' -band and other second-order processes in mono-layer graphene for three different ion dose levels. The G' and G'' -band intensities decrease as the line widths increase for increasing ion dose. The defect-related combination modes $D + G$ at 2930 cm^{-1} and $G + D'$ at 3190 cm^{-1} can be observed at higher ion bombardment doses ($10^{13} \text{ Ar}^+/\text{cm}^2$), but the G'' -band is too weak to be seen in these measurements. At a dose of

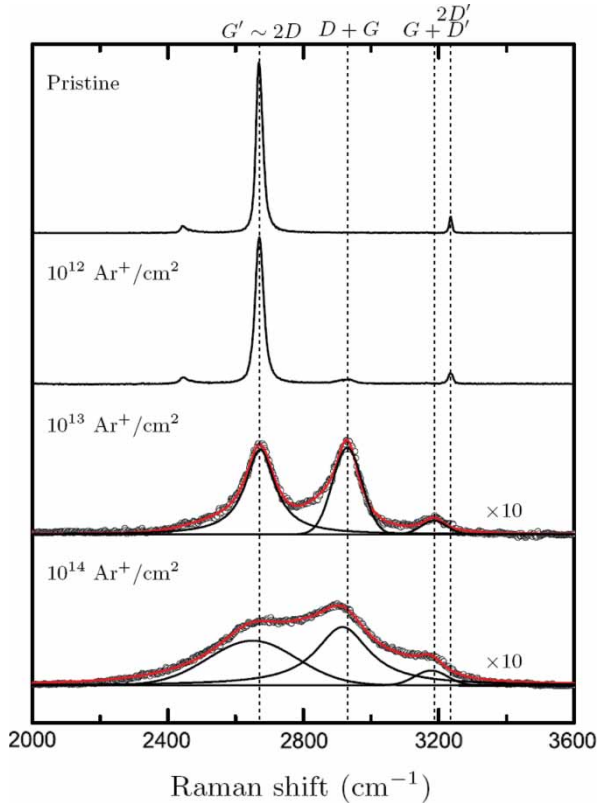


Figure 49. Evolution of the G' -band (at 2670 cm^{-1}) and other second-order peaks, the $(D + G)$ at 2930 cm^{-1} , the $(D' + G)$ at 3190 cm^{-1} , and the G'' ($2D'$ in the figure) at 3220 cm^{-1} with increasing ion doses. The intensities of the two lower graphs are multiplied by a factor of 10 for the sake of readability [130]. Here the notation $2D'$ is used instead of G'' , as has also been used in the literature by other authors. Reprinted figure with permission from E.H. Martins Ferreira *et al.*, *Physical Review B* 82, p. 125429, 2010 [130]. Copyright © (2010) by the American Physical Society.

$10^{14}\text{ Ar}^+/\text{cm}^2$ the results show a frequency downshift for all DR features, in agreement with the results of Section 4.3.5.

4.3.7. Disorder and the number of layers

The I_D/I_G results for ion bombarded graphene depend on the number of graphene layers N [130] in the case of low energy ions (90 eV). Because of the low ion energy, the ion bombardment process is limited generally to one defect per bombarding ion, so that the I_D/I_G scales with N . For many-layer graphene (~ 50 and higher), a monotonic evolution of I_D/I_G with increasing ion fluence is seen because in this case there are always more unperturbed graphene layers available to be bombarded.

4.4. Edge phonon Raman spectroscopy

The disorder-induced Raman bands should also depend on the type of defect structure, and not only on the number of defects. This dependence has been demonstrated for graphene and graphite edges, where the orientation of the carbon hexagons with respect to the edge axis was determined

experimentally, thereby distinguishing the so-called zigzag edge from the armchair or random atomic edge structures [170]. The armchair/random vs. zigzag edge structure can be identified spectroscopically by the presence vs. absence of the D-band, and this effect results from the momentum requirements of the DR model, as discussed below.

The defect associated with a step edge has a 1D character, which means that it is able to transfer momentum solely in the direction perpendicular to the edge. In this sense, the wave vectors of the defects associated with zigzag and armchair edges are represented in Figure 50(a) by \vec{d}_a (a for armchair) and \vec{d}_z (z for zigzag) edges. When we translate these vectors into reciprocal space, we see that different selection rules apply for the electron scattering by phonons for each of these edge types. This is illustrated in Figure 50(b), where the first BZ of 2D graphite (graphene) is shown, oriented in accordance with the real space directions shown in Figure 50(a).

Light-induced e-h pairs will be created on an equi-energy circle around points K' and K (here neglecting the trigonal warping effect for simplicity), which has a radius that is defined by E_{laser} , as shown in Figure 50(b). Note that for inter-valley electron-defect scattering, which connects K to K' points, only the \vec{d}_a vector for armchair edges can connect points belonging to circles centered at two inequivalent K and K' points. In contrast the zigzag \vec{d}_z vector to connect inequivalent points, which means that inter-valley scattering is not allowed for zigzag edges. This therefore means that the inter-valley DR process, which is the process responsible for the observation of the D-band in graphitic materials, is not allowed for a perfect zigzag edge [170]. The D-band phonon connects two inequivalent K and K' points, and along the zigzag edge there will be no defect able to connect those points to achieve momentum conservation in the final process.

On the other hand, intra-valley electron-defect scattering can occur for both zigzag and armchair edges (see Figure 50(b)). Therefore, intra-valley scattering processes induced by phonons can achieve final momentum conservation using both \vec{d}_a and \vec{d}_z vectors. Another well-known defect-induced band is the so-called the D'-band, which appears at around 1620 cm^{-1} , and it is related to intra-valley el-ph processes. For this reason, the D'-band observation should be independent of the zigzag vs. armchair structure of the edges, in agreement with experimental observation.

Another selection rule aspect refers to the D-band intensity dependence on the polarization direction of the light with respect to the edge orientation. The D-band intensity has a maximum value when the light is polarized along the edge, and should give a null value when the light is polarized perpendicular to the edge. The physics behind this selection rule is the optical absorption (emission) anisotropy around the $K(K')$ point in 2D graphite, which can be represented by [262]

$$W_{\text{abs,ems}} \propto |\vec{P} \times \vec{k}|^2. \quad (82)$$

Here the polarization of the incident (scattered) light for the absorption (emission) process is represented by \vec{P} , while the wave vector of the electron measured from the K point is given by \vec{k} .

These selection rules were first observed for graphite edges, as reported in [170], and similar results have been observed later in mono-layer graphene [151,311]. However, only edge-dependent variations in the D-band intensity consistent with the selection rules have been reported. Raman-based indications for the high crystallinity of zigzag edges have indeed been observed by Krauss *et al.* [312], although the complete absence of the D-band together with the observation of the D'-band, which is expected for a zigzag edge structure, has never been reported, which might imply that, up to now, no perfect zigzag structure has been measured by Raman spectroscopy. In general, the polarization direction dependence for the D-band intensity, as given by Equation (82), together with the zigzag vs. armchair dependence, can be used for an identification of the edge orientation and structure. Raman spectroscopy is, therefore, a valuable tool for the development of our understanding of edge structures, important for the science of graphene ribbons, and more. The results reported here represent an effort to improve our understanding of the influence of

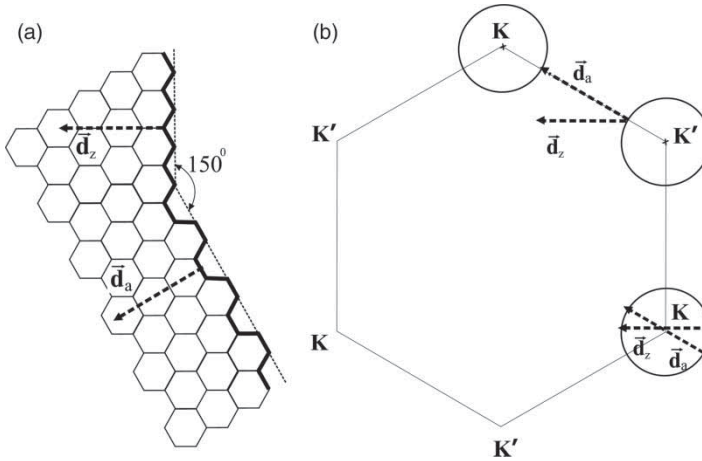


Figure 50. (a) Schematic illustration of the atomic structure of edges with the zigzag and armchair orientations. The boundaries can scatter electrons with momentum transfer along \vec{d}_z for the zigzag edge, and along \vec{d}_a for the armchair edge. (b) First BZ of 2D graphite (graphene), showing defect-induced inter-valley and intra-valley scattering processes. Since \vec{d}_z is too short to connect the K and K' points, the defect-induced DR inter-valley process is forbidden at zigzag edges. Reprinted figure with permission from L.G. Cancado *et al.*, *Physical Review B* 93, p. 47403, 2004 [59]. Copyright © (2004) by the American Physical Society.

the specific defect structure on the Raman spectra of sp^2 carbon systems. Other defect-dependent effects are expected, which may be very useful to characterize defects in nanographite-based devices, but both theory and experiment have to be developed along these lines.

4.5. Polarization effects in graphene nanoribbons

Polarization effects have also been observed in the G-band of graphene nanoribbons, as shown in Figure 51 [59]. Again, this development came before the graphene rush, and the experimental results were actually obtained on a one-layer thick ribbon grown by CVD on top of HOPG. The lower frequency G_1 band in Figure 51 comes from the nano-ribbon, while the higher frequency G_2 band comes from the HOPG substrate. The reason why the frequencies are distinct is actually related to the different heat dissipation, whereby the nano-ribbon and the substrate get into equilibrium at different temperatures when heated independently by the laser (see Figure 51). Thus the nanoribbon is heated to a higher temperature by the laser heating than the substrate, and therefore ω_{G_1} for the nanoribbon decreases more than ω_{G_2} for the substrate. This happens because the thermal conductivity of the substrate is much higher than that of the graphene ribbon, as shown in Figure 51(c).

Finally, the nanoribbon G_1 band shows a clear dependence on the excitation laser light polarization with respect to its axis, as illustrated in Figure 51(b). The Raman signal for the ribbon disappears when the light polarization direction is perpendicular to the ribbon axis. This result is related to both the anisotropy of the optical absorption (emission), according to Equation (82), and the quantum confinement perpendicular to the ribbon axis.

5. Raman spectra of carbon nanotubes

Since the Raman spectra of carbon nanotubes have additional unique spectral features that are not found in other carbon nano-structured materials, Raman spectroscopy has provided an especially important tool for developing characterization techniques for nanocarbon materials [313]. In particular the RBM, which is unique to carbon nanotubes (see Figure 4), provides a highly sensitive tool for determining the presence of carbon nanotubes in a particular carbon-based sample and for characterizing the (n, m) chirality of the carbon nanotubes present in the sample. The KA effect provides a mechanism for study of the el-ph interaction through its effect on both the G-band and the RBM mode features in the Raman spectra. The DR effect provides a mechanism for studying aspects of the 1D quantum confined electronic energy band structure through the el-ph interaction. Since the electronic transitions in carbon nanotubes are dominated by excitonic effects, study of the Raman spectra of carbon nanotubes provides important insights into excitonic phenomena in 1D systems. Near-field Raman spectroscopy has been especially sensitive for revealing new and important spatial information about specific defects in carbon nanotubes. These topics are discussed in this Section.

5.1. The radial breathing mode and the Kataura plot

The RBM is the nanotube normal mode vibration where all the C atoms vibrate in phase in the radial direction, as if the tube is breathing. Since the atomic vibrational motion does not break the tube symmetry, the RBM is a totally symmetric mode according to group theory, belonging to the A_1 symmetry irreducible representation (IR) [1,141,142]. The RBM only occurs in carbon

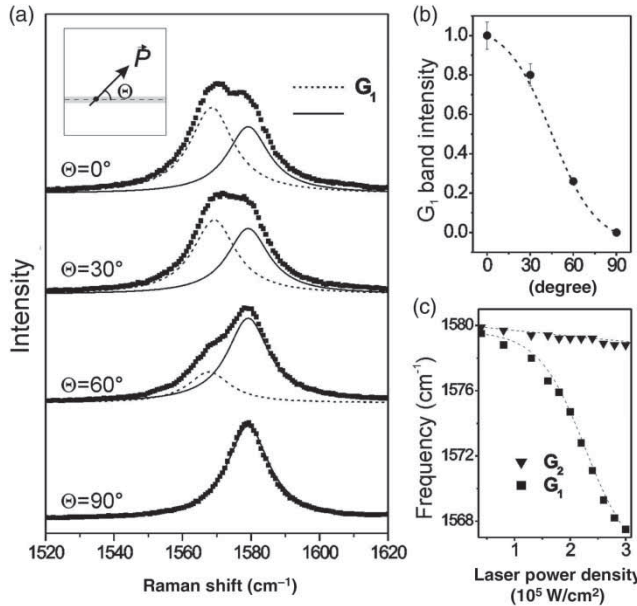


Figure 51. (a) The G-band Raman spectra from a graphene nano-ribbon (G₁) and from the HOPG substrate (G₂) on which the nano-ribbon was grown. (b) The dependence of the G₁ frequency on the light polarization direction, with respect to the ribbon axis. Points are experimental results and the dashed curve is the theoretical expectation. (c) Frequency of the G₁ and G₂ peaks as a function of the incident laser power density. Reprinted figure with permission from L.G. Cancado *et al.*, *Physical Review B* 93, p. 47403, 2004 [59]. Copyright © (2004) by the American Physical Society.

nanotubes and, therefore, it can be used to distinguish SWNTs from other sp^2 carbon structures in the samples. In general the intensity of the RBM is unusually strong when compared with other non-resonant spectral features coming from other carbonaceous materials or from the substrate on which the tubes are sitting [111]. Furthermore, the RBM frequency ω_{RBM} depends on the tube diameter, following the proportionality relation $\omega_{\text{RBM}} \propto 1/d_t$. This dependence was predicted initially using force constant calculation models (e.g. [100]), but a rather simple and instructive analytical derivation can be made using elasticity theory, and we present this approach in sequence.

5.1.1. The RBM frequency

The RBM frequency of a SWNT is given by $\omega_{\text{RBM}} = A/d_t$, with the value $A = 227 \text{ cm}^{-1}\text{nm}$ being expected by elasticity theory, thereby directly connecting 1D carbon nanotubes to their 2D counterpart graphene from which nanotubes are conceptually derived [314,315]. The experimental values for A and the expected value for A coming from elasticity theory agree perfectly for one specific type of SWNT [314,315], that is, for SWNTs which are ultra-long, vertically aligned, and grown by the water-assisted CVD method [316]. This sp^2 carbon material is used here as a standard reference material from a metrology standpoint. Most of the RBM experimental results in the literature have been fitted to the relation $\omega_{\text{RBM}}=A/d_t+B$, with values for the parameters A and B varying widely from paper to paper [107,109,111,153,175,188,314,317–321]. In the limit of the tube diameter going to infinity, we ideally expect $\omega_{\text{RBM}} \rightarrow 0$, suggesting that B is associated with an environmental effect, and the environmental conditions differ from one experimental system to another.

A simple model that has been used to model the RBM is a simple harmonic oscillator equation for a cylindrical shell subjected to an inwards pressure ($p(x)$) given by [314,315]

$$\frac{\rho}{Y}(1 - \nu^2) \frac{\partial^2 x(t)}{\partial t^2} + \frac{2}{d_t} x(t) = -\frac{(1 - \nu^2)}{Yh} p(x), \quad (83)$$

where $x(t)$ is the displacement of the nanotube in the radial direction, $p(x) = (24K/s_0^2)x(t)$, and K (in $\text{eV}/\text{\AA}^2$) gives the van der Waals interaction strength, s_0 the equilibrium separation between the SWNT wall and the surrounding environmental shell, Y the Young's modulus ($69.74 \times 10^{11} \text{ g/cm}\cdot\text{s}^2$), ρ the mass density per unit volume (2.31 gm/cm^3), $\nu = 0.5849$ is the Poisson's ratio and h represents the thickness of the environmental shell [315]. If there are no environmental effects, the term $p(x)$ vanishes and Equation (83) will become the fundamental frequency ω_{RBM}^0 for a pristine SWNT in units of cm^{-1} ,

$$\omega_{\text{RBM}}^0 = \left\{ \frac{1}{\pi c} \left[\frac{Y}{\rho(1 - \nu^2)} \right]^{1/2} \right\} \frac{1}{d_t}. \quad (84)$$

The term inside the curly bracket above gives the fundamental value of $A = 227.0 \text{ cm}^{-1}\text{nm}$. However, for a non-vanishing inward pressure $p(x)$, the result is

$$\omega'_{\text{RBM}} = 227.0 \left[\frac{1}{d_t^2} + \frac{6(1 - \nu^2) K}{Yh s_0^2} \right]^{1/2}. \quad (85)$$

Here $[6(1 - \nu^2)/Yh] = 26.3 \text{ \AA}^2/\text{eV}$. The shift in ω'_{RBM} due to the nanotube environment is given by $\Delta\omega_{\text{RBM}} = \omega'_{\text{RBM}} - \omega_{\text{RBM}}^0$. We fit the value K/s_0^2 in Equation (3) to the RBM frequency as a function of d_t . The fitted value for the environmental term for the “super-growth” sample is sufficiently small, since $K/s_0^2 = (2.2 \pm 0.1) \text{ meV}/\text{\AA}^4$, that it can be neglected. The d_t dependent

Table 2. Environmental effects on the RBM frequency of different samples, as measured by the C_e factor in Equation (86) [323].

C_e	Sample	Reference
0	Water-assisted CVD	Araujo [314]
0.05	HiPCO@SDS	Bachilo [153]
0.059	Alcohol-assisted CVD	Araujo [321]
0.065	SWNT@SiO ₂	Jorio [111]
0.067	Free-standing	Paillet [320]

behavior of the environmental effect in ω_{RBM} reproduces well the experimental result for d_t up to $d_t = 3$ nm [314]. A similar environmental effect is obtained for SWNTs surrounded by different surfactants [107,175,188,317,319], in bundles [109,321], sitting on a SiO₂ substrate [111], and even for tubes suspended in air by posts [320]. This environmental effect is almost absent in “super-growth” SWNTs, but the reason why this sample is special is not presently understood, and the pristine-like ω_{RBM} behavior is lost if this sample is dispersed in solution [322].

A simple relation can be proposed for all the ω_{RBM} results in the literature, which are generally upshifted from the pristine values observed for the “super-growth” samples due to the van der Waals interaction with the environment. This simple relation is [314]

$$\omega_{\text{RBM}}^{\text{Lit.}} = \frac{227}{d_t} \sqrt{1 + C_e * d_t^2}, \quad (86)$$

where C_e in Equation (86) represents the effect of the environment on ω_{RBM} , i.e. $C_e = [6(1 - \nu^2)/Eh][K/s_0^2] \text{ nm}^{-2}$. The several C_e values that are obtained by fitting the RBM results for different commonly found samples in the literature are given in Table 2. The curvature effects become important for $d_t < 1.2$ nm, and in this case the environmental effect depends more critically on the specific sample. For example, the C_e for SWNT samples sitting on a SiO₂ substrate may differ from sample to sample. The observed environmentally induced upshifts for the RBM from small diameter tubes, either within bundles or wrapped by different surfactants (e.g., SDS (sodium dodecyl sulfate) or single stranded DNA), range from 1 to 10 cm^{-1} . This environmental effect gets richer in a double wall carbon nanotube (DWNT), as discussed in Section 5.1.2.

Finally, all the ω_{RBM} dependence on the carbon nanotube structure discussed here addresses the importance of the diameter dependence. The chiral angle has a weaker dependence on the RBM frequency, but to fully discuss this topic, the KA has to be introduced [193,324]. This topic is discussed in Section 5.4.

5.1.2. The RBM for double wall carbon nanotubes

Spectroscopic experiments on DWNTs have been largely performed on solution-based samples or in bundles [325–329]. For this reason, it has been difficult to identify and learn about the Raman spectroscopic signatures that are specific to the inner (n, m) tube of a DWNT, which can be contained inside different possible outer (n', m') tubes (see Figure 52(a)). The DWNTs are formed by an inner and an outer tube, and they can be either metallic (M) or semiconducting (S). There are four different possible configurations, namely M@M, M@S, S@S and S@M. Here S@M denotes a DWNT with an S inner tube inside an M outer tube, following a similar notation introduced for fullerenes [330,331]. Interesting aspects are related to the DWNT electronic properties, e.g. the S@M configuration can be regarded as a good approximation for an isolated semiconducting SWNT, since it is electrostatically shielded by the outer metallic tube [330]. In order to determine

which specific inner and outer tubes form a given DWNT, one has to perform Raman experiments on individual DWNTs (see Figure 52(c)).

For a well-defined experiment, the combination of electron-beam lithography, atomic force microscopy (AFM) and Raman spectral mapping have been developed to measure the Raman spectra from the inner and the outer tubes of an individual DWNT (see Figure 52) [330,331]. The Raman spectra of 11 isolated DWNTs grown from annealing C_{60} filled SWNTs were measured using a single laser excitation energy ($E_{\text{laser}} = 2.10 \text{ eV}$ [330]). Specific E_{laser} values were used to select all DWNTs with (6,5) semiconducting inner tubes that were in resonance, and all with the S@M configuration so that the RBMs from both the inner and outer tubes of individual DWNTs could be observed. The RBM frequencies $\omega_{\text{RBM},o}$ for the outer tube measured for such a DWNT as a function of $\omega_{\text{RBM},i}$ for the inner tube are shown in Figure 53(a). For these 11 individual isolated DWNTs, $\omega_{\text{RBM},o}$ for the outer tubes varies along with $\omega_{\text{RBM},i}$, thus showing that the inner and outer tubes impose considerable stress on one another. Actually, the nominal wall-to-wall distances $\Delta d_{t,io}$ between the inner (i) and outer (o) tubes of the DWNTs are less than the 0.335 nm interlayer c-axis distance in graphite. Figure 53(b) shows $\Delta d_{t,io}$ values as small as 0.29 nm, with a decrease of up to 13% in the wall to wall distance [330]. Because of the differences in the Coulomb interaction

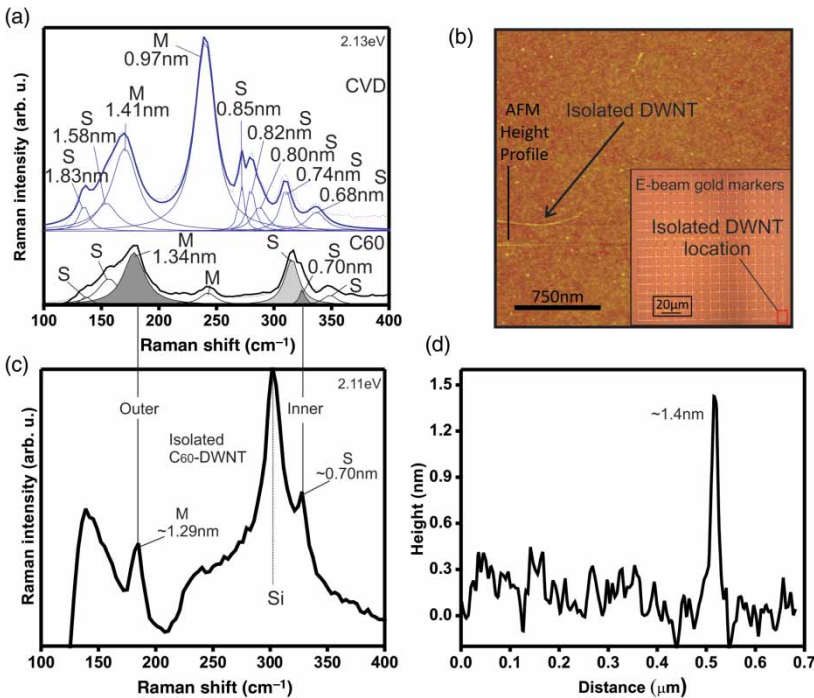


Figure 52. (a) Raman spectra for the RBM region for two types of DWNTs, obtained with $E_{\text{laser}} = 2.13 \text{ eV}$. (b) AFM image of one individual DWNT. The inset shows the silicon substrate with gold markers showing the location of an individual DWNT. (c) RBM Raman spectra obtained with $E_{\text{laser}} = 2.11 \text{ eV}$ for an isolated individual DWNT grown from a C_{60} filled SWNT-bundle. (d) AFM height profile of the individual, isolated DWNT shown in (b), with the RBM spectrum shown in (c). The vertical lines connecting (a) and (c) show that the ω_{RBM} of the prominent tube diameters observed in the C_{60} -DWNT bundles coincide with the ω_{RBM} of the inner and outer tubes of the isolated C_{60} -DWNT. F. Villalpando-Paez *et al.*, *Nanoscale* 2, pp. 406–411, 2010 [330]. Adapted by permission of the Royal Society of Chemistry.

expected for the four different DWNT metallicity configurations, S@M, M@S, S@S and M@M, the detailed relation between ω_{RBM} and $1/d_t$ will depend on the metallicity configuration.

By adding walls to form MWNTs, the RBM signal from inner tubes with small enough diameters ($d_t \lesssim 2$ nm) can be observed experimentally [332]. However, most of the usually made MWNT samples are composed of inner tubes with diameters too large to exhibit observable RBM features.

5.1.3. The Raman excitation profile for the RBM

In the Raman scattering experiment, when the energy of the incident or scattered light matches an optical transition in the scattering system, resonance effects occur, and the Raman signal is strongly enhanced [103,109,111]. Using the resonance Raman effect, it is possible to study the electronic structure of individual SWNTs [111,336,338]. In this section, we review observations of the Raman excitation profile for the RBM feature for an individual SWNT.

Isolated SWNTs were grown on top of a Si/SiO₂ substrate by a CVD method [111,339]. Figure 54(a) shows an AFM image of the substrate with lithographic markers that were used to locate an individual SWNT. The dashed circles in Figure 54(a,b) display the position where the laser spot is placed. Figure 54(c,d) show anti-Stokes/Stokes Raman spectra of the sample, measured in the excitation wavelength (energy) range $1.585 \text{ eV} \leq E_{\text{laser}} \leq 1.722 \text{ eV}$. The Stokes/anti-Stokes ratio are calibrated by $[n(\omega) + 1]/n(\omega)$, where $n(\omega) = 1/[\exp(\hbar\omega/k_B T) - 1]$, ω is the RBM frequency, k_B is the Boltzmann constant, and T is the temperature, which was found not to be higher than 325 K [338].

An RBM Raman feature appears in the spectra in Figure 54(c,d) at 173.6 cm^{-1} , with a clear resonance behavior. The RBM peak appears and disappears over the tunable energy range of E_{laser} , meaning that E_{laser} is tuned over the whole resonance window of one optical transition energy (E_{ii}) for the SWNT which is sitting under the laser spot. The linewidth for the RBM peak is sharp, ($\Gamma_{\text{RBM}} = 5 \text{ cm}^{-1}$), showing a typical value measured for isolated SWNTs deposited on substrates [111,340]. Figure 55 shows the 173.6 cm^{-1} RBM peak intensity vs. E_{laser} for (a) the anti-Stokes and (b) Stokes processes for the individual SWNT measured in Figure 54.

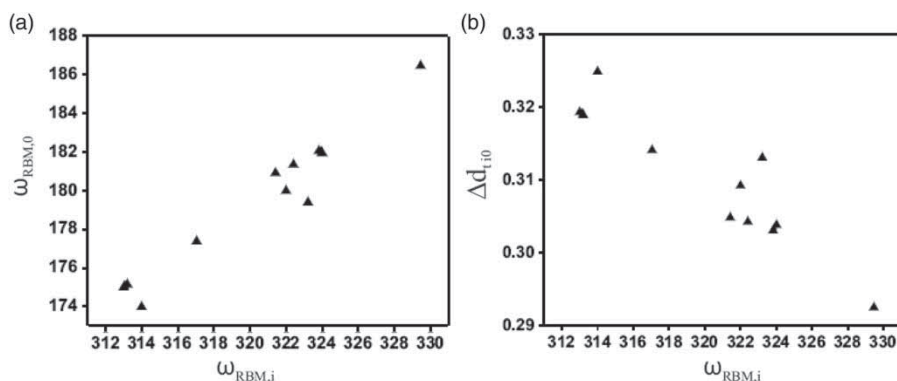


Figure 53. All the inner tubes for the 11 peapod-DWNTs in this figure are (6,5) semiconducting tubes. (a) Plot of the $\omega_{\text{RBM},i}$ for the inner tube vs. $\omega_{\text{RBM},o}$ for the outer tubes which pair to form eleven different isolated DWNTs. (b) Plot of the nominal wall-to-wall distance $\Delta d_{t,i,o}$ for each of the 11 isolated DWNTs vs. $\omega_{\text{RBM},i}$ shown in (a). An increase in the $\omega_{\text{RBM},i}$ of the (6,5) inner tubes shown here is accompanied by a decrease in the measured nominal wall-to-wall $d_{t,i,o}$ distance for these peapod-derived DWNTs. F. Villalpando-Paez *et al.*, *Nanoscale* 2, pp. 406–411, 2010 [330]. Adapted by permission of the Royal Society of Chemistry.

The Stokes RBM peak intensity I is a function of E_{laser} and can be evaluated from Equation (62) [269]. The two factors in the denominator of Equation (62) describe the resonance effect with the incident and scattered light, respectively. A \pm sign before E_{ph} applies to Stokes/anti-Stokes processes, while γ_{RBM} is related to the inverse lifetime for the resonant scattering process [278]. The matrix elements in the numerator are most usually considered to be independent of energy because of the small energy range. The theory for these matrix elements is discussed in Section 3.6.1. The lines in Figure 55 show the fits to the experimental data for the Stokes (dashed) and anti-Stokes (solid) resonance windows, using $E_{\text{ph}} = 21.5$ meV, obtained from $\omega_{\text{RBM}} = 173.6$ cm^{-1} [338]. The asymmetric lineshape in the resonance windows in Figure 55 was obtained in [338] by considering not a coherent Raman process, but an incoherent scattering process, where the sum over the internal states (\sum_a in Equation (62)) was taken outside the square modulus. This procedure is indeed controversial because this asymmetry could be also generated by different γ_r values for the incident and scattered resonance windows or by other resonance levels lying close in energy.

Disregarding the asymmetry aspect, $E_{\text{ii}} = 1.655 \pm 0.003$ eV and $\gamma_{\text{RBM}} = 8$ meV is obtained for the spectra shown in Figure 55. A shift in the Stokes (S) and anti-Stokes (aS) resonant windows is expected due to the resonant condition for the scattered photon, $E_s = E_{\text{ii}} \pm E_{\text{ph}}$, with (+) for the Stokes and (−) for the anti-Stokes processes, and this effect is shown in the upper inset to Figure 55. For this reason, under sharp resonance conditions the $I_{\text{aS}}/I_{\text{S}}$ intensity ratio depends sensitively on $E_{\text{ii}} - E_{\text{laser}}$, and the $I_{\text{aS}}/I_{\text{S}}$ ratio can be used to determine E_{ii} experimentally and to determine whether the resonance is with the *incident* or the *scattered* photon [141,338].

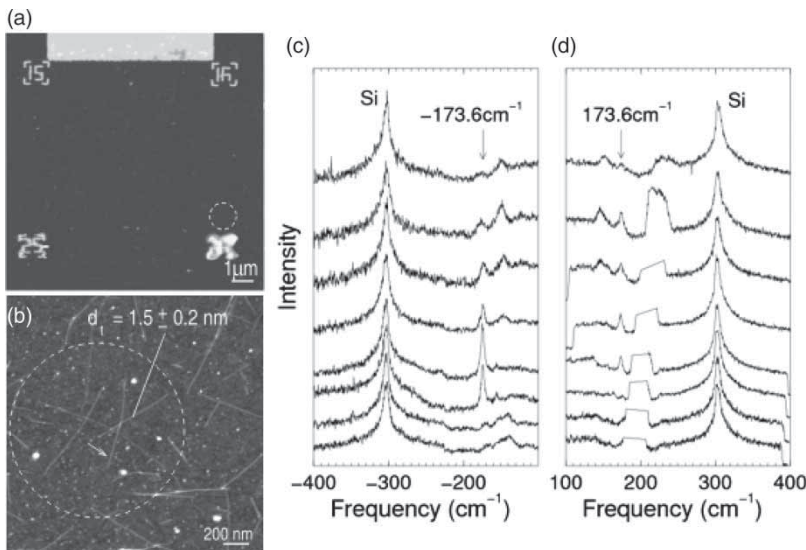


Figure 54. (a) AFM image of a SWNT sample showing markers that were used to localize the spot position (dashed circle) on the substrate during the Raman experiment and for further AFM characterization of the SWNTs that are located within the light spot indicated by the dashed circle in (b). (c) anti-Stokes and (d) Stokes Raman spectra from isolated SWNTs on a Si/SiO₂ substrate for several different laser excitation energies. For more details, see Ref. [338]. Adapted with permission from A. Jorio *et al.*, *Physical Review B* 63, p. 245416, 2001 [338]. Copyright © (2001) by the American Physical Society.

5.1.4. The RBM spectra of SWNT bundles

Figure 56(a) show a RBM Raman spectrum obtained from SWNT bundles [321]. The solid line shows the fit obtained using a sum of Lorentzians. Each Lorentzian gives the RBM from one specific (n, m) SWNT species. The red Lorentzians represent the RBM from metallic SWNTs

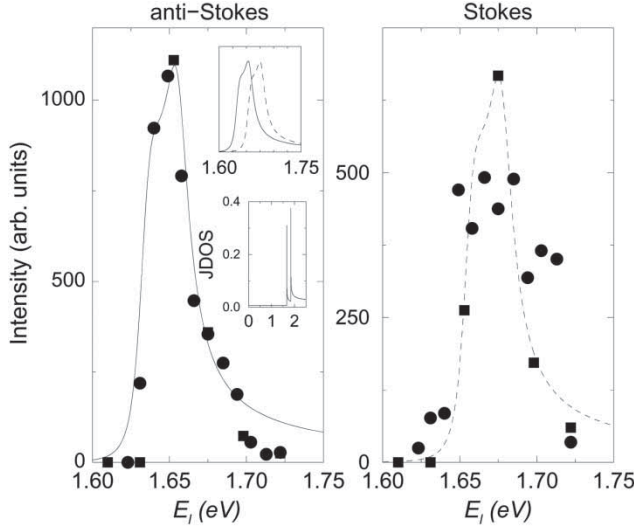


Figure 55. Raman intensity vs. laser excitation energy E_l for the $\omega_{RBM} = 173.6 \text{ cm}^{-1}$ peak in Figure 54, for both anti-Stokes and Stokes processes. Circles and squares indicate two different runs on the same sample. The line curves indicate the resonant Raman window predicted from Equation (1), with $E_{ii} = 1.655 \text{ eV}$, $\gamma_r = 8 \text{ meV}$, but taking the sum over internal states ($\sum_{m,m'}$) outside the square modulus. The upper inset compares the theoretically predicted Stokes and anti-Stokes resonant windows on an energy scale in eV, and the lower insert shows the joint density of states (JDOS) vs. E_{laser} for this SWNT. Adapted with permission from A. Jorio *et al.*, *Physical Review B* 63, p. 245416, 2001 [338]. Copyright © (2001) by the American Physical Society.

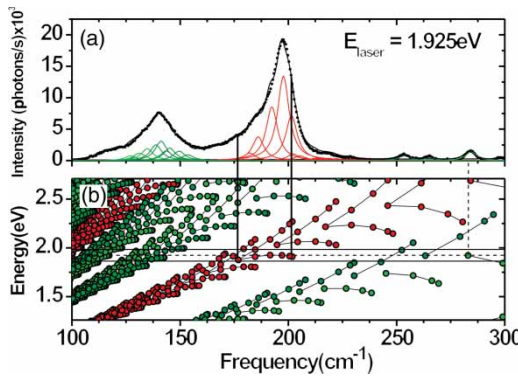


Figure 56. (a) Raman spectrum (bullets) of SWNT bundles obtained with a 644 nm laser line ($E_{laser} = 1.925 \text{ eV}$). This spectrum was fitted by using 34 Lorentzians (curves under the spectra) and the solid line is the fitting result. (b) The Kataura plot used as a guide for the fitting procedure. Adapted with permission from P.T. Araujo *et al.*, *Physical Review Letters* 98, p. 67401, 2007 [321]. Copyright © (2007) by the American Physical Society.

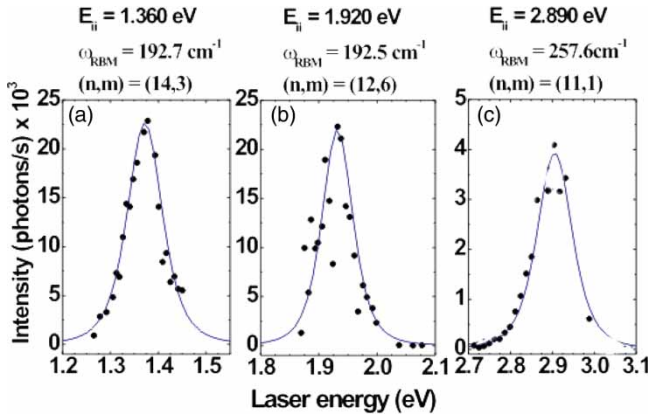


Figure 57. Resonance windows for specific (n, m) SWNTs within a bundle. (a) Resonance profile (black dots) in the near-infrared range for $\omega_{\text{RBM}} = 192.7 \text{ cm}^{-1}$. The data for tube $(14, 3)$ were fitted (solid line) using Equation (87) with $\gamma = 0.065 \text{ eV}$ and $E_{\text{ii}} = 1.360 \text{ eV}$. (b) Resonance profile in the visible range is shown for $\omega_{\text{RBM}} = 192.5 \text{ cm}^{-1}$ (tube $(12, 6)$), with $\gamma = 0.045 \text{ eV}$ and $E_{\text{ii}} = 1.920 \text{ eV}$. (c) Resonance profile in the near-ultraviolet range is shown for $\omega_{\text{RBM}} = 257.6 \text{ cm}^{-1}$ (tube $(11, 1)$), with $\gamma = 0.073 \text{ eV}$ and $E_{\text{ii}} = 2.890 \text{ eV}$. Adapted with permission from P.T. Araujo *et al.*, *Physical Review Letters* 98, p. 67401, 2007 [321]. Copyright © (2007) by the American Physical Society.

and the green Lorentzians represent the RBMs from semiconducting SWNTs. The number of Lorentzians used to fit each resonance spectrum can be defined by the Kataura plot [177,342,343] (see Figure 56(b)), which plots the E_{ii} for all possible (n, m) SWNTs. The ω_{RBM} values obey the relation $\omega_{\text{RBM}} = (227/d_t)\sqrt{1 + C_e/d_t^2}$, which correctly describes environmental effects by the proper choice of C_e , and this relation is discussed in detail in Section 5.1.1. For lack of information, we assume that all the Lorentzian peaks in one experimental spectrum share the same FWHM value.

The RBM peak intensity $I(E_{\text{laser}})$ for each Lorentzian peak in the RBM spectra from an individual SWNT can be evaluated by

$$I(E_{\text{laser}}) \propto \left| \frac{1}{(E_{\text{laser}} - E_{\text{ii}} - i\gamma)(E_{\text{laser}} - E_{\text{ii}} \pm E_{\text{ph}} - i\gamma)} \right|^2, \quad (87)$$

which is a simplification of Equation (62). Figure 57 shows the resonance profiles for three different (n, m) SWNTs [321,335]. The resonance window widths γ_r for SWNTs in bundles are usually within the 40–160 meV range, which are much broader than for isolated SWNTs (see Figure 55) and γ_r also depends on (n, m) [321].

5.1.5. (n, m) dependence of RBM intensity – experimental analysis

In experiments using a nearly continuous set of laser energies E_L , we compare the RBM intensity for different (n, m) SWNTs at a resonance condition (i.e., $E_L = E_{\text{ii}}$). The RBM spectra from the “super-growth” water-assisted SWNTs obey the relation $\omega_{\text{RBM}} = 227/d_t \text{ cm}^{-1} \text{ nm}$ and these spectra have been used for (n, m) -dependent intensity analysis [344].

The d_t distribution of a given super-growth sample was established by high resolution transmission electron microscopy (HRTEM) [344], to calibrate the RRS (resonance Raman scattering) intensities. For the (n, m) analysis, it was assumed that SWNTs of different chiral angles are

equally abundant in the growth process. Actually, chiral SWNTs are twice as populous as achiral ones because there are right-handed and left-handed isomers present in a typical sample. The intensity calibrated experimental RRS map is shown in Figure 58(a). The (n, m) nanotubes in the $(2n + m) = \text{constant}$ family have similar diameters and E_{ii} values to one another, and the Raman intensity within a given $(2n + m) = p = \text{constant}$ family has a chiral angle dependence. From the spectral map it is clear that the RBM intensity is stronger for smaller chiral angles (near zigzag nanotubes) as compared to those with larger chiral angles. Each spectrum $(S_{(\omega, E_L)})$ is the sum of the individual contributions of all SWNTs present in the light beam, and we can write [344]

$$S_{(\omega, E_L)} = \sum_{n,m} \left[\text{Pop}(n, m) I(n, m)^{E_L} \frac{\Gamma/2}{(\omega - \omega_{\text{RBM}})^2 + (\Gamma/2)^2} \right], \quad (88)$$

where $\text{Pop}(n, m)$ is the relative population of the (n, m) nanotube species, $\Gamma = 3 \text{ cm}^{-1}$ is the experimental average value for the FWHM intensity of the Raman spectra (Lorentzian), ω_{RBM} is the RBM frequency and ω is the corresponding Raman shift variable. The total integrated area $(I(n, m)^{E_L})$ for the Stokes process at a given excitation laser energy (E_L) is given by

$$I(n, m)^{E_L} = \left| \frac{\mathcal{M}}{(E_L - E_{ii} + i\gamma)(E_L - E_{ii} - E_{ph} + i\gamma)} \right|^2, \quad (89)$$

where the superscript E_L denotes the laser excitation energy, $E_{ph} = \hbar\omega_{\text{RBM}}$ is the energy of the RBM phonon, E_{ii} is the energy corresponding to the i th excitonic transition, γ is the resonance window width and \mathcal{M} represents the matrix elements for the Raman scattering by one RBM phonon of the (n, m) nanotube. The values for E_{ii} and ω_{RBM} have to be determined experimentally. The effective matrix element square term \mathcal{M} and the effective resonance window width γ for each (n, m) tube were found by fitting the experimental RBM component of the RRS map with Equation (88) using the functions:

$$\mathcal{M} = \left[\mathcal{M}_A + \frac{\mathcal{M}_B}{d_r} + \frac{\mathcal{M}_C \cos(3\theta)}{d_r^2} \right]^2 \quad \text{and} \quad \gamma = \gamma_A + \frac{\gamma_B}{d_r} + \frac{\gamma_C \cos(3\theta)}{d_r^2}. \quad (90)$$

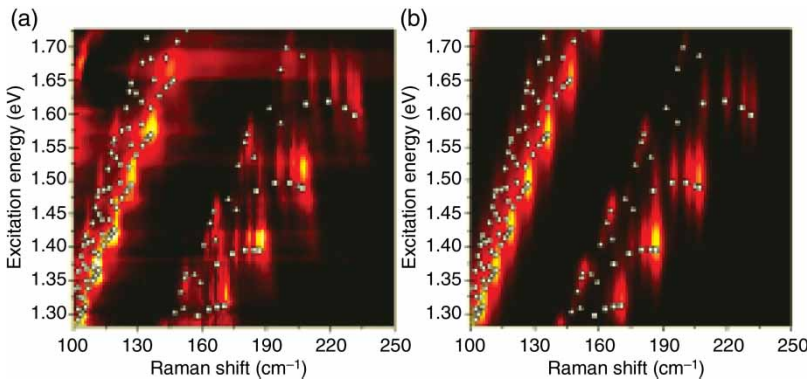


Figure 58. (a) Experimental RRS map for the RBM feature. The intensity calibration was made by measuring a standard tylenol sample. (b) Modeled map obtained by using Equation (88) in the same laser excitation energy range as (a). Adapted with permission from P.B.C. Pesce *et al.*, Applied Physical Letters 96, p. 51910, 2010 [344]. Copyright © (2010) by the American Institute of Physics.

Here \mathcal{M}_i and γ_i ($i = A, B, C$) are fitting parameters. The best values for \mathcal{M}_i and γ_i , considering the excitonic transitions E_{22}^S and the lower branch of E_{11}^M , are listed in Table 3. Here d_t is given in nm, γ in meV and \mathcal{M} in arbitrary units.

The modeled RRS map shown in Figure 58(b) was obtained using the values thus obtained in Equation (88). Note that the model represents the experimentally observed results in Figure 58(a) very well.

5.1.6. The experimental Kataura plot

The resonance window analysis can be extended to all (n, m) SWNTs, from which we can study the E_{ii} dependence on (d_t, θ) . Figure 59(a) shows a 2D RBM map for the “super-growth” (S.G.) SWNT sample [316]. The experimental Kataura plot in Figure 59(a) was constructed using 125 different laser excitation lines [314,335]. By applying the fitting procedure described in Section 5.1.4, the (n, m) indices have been assigned to 197 different SWNTs.

By fitting the resonance windows extracted from the data in Figure 59(a) as a function of $\omega_{\text{RBM}}^{S.G.}$, all $E_{ii}^{S.G.}$ excitonic transition energies have been obtained experimentally, as shown in Figure 59(b). These $E_{ii}^{S.G.}$ values displayed in Figure 59(b) have been fitted using the empirical equation [321,345]:

$$E_{ii}(p, d_t) = \alpha_p \frac{p}{d_t} \left[1 + 0.467 \log \frac{0.812}{p/d_t} \right] + \frac{\beta_p \cos 3\theta}{d_t^2}. \quad (91)$$

Here p is defined as $1, 2, 3, \dots, 8$ for $E_{11}^S, E_{22}^S, E_{11}^M, \dots, E_{66}^S$, and is a measure of the distance of each cutting line from the K point in the zone-folding procedure [135,177,343]. The fitting gives $\alpha_p = 1.074$ for $p = 1, 2, 3$ and $\alpha_p = 1.133$ for $p \geq 4$. The β_p values found for the lower (upper) E_{ii} branches are: $-0.07(0.09), -0.18(0.14), -0.19(0.29), -0.33(0.49), -0.43(0.59), -0.6(0.57), -0.6(0.73)$ and -0.65 (unknown) for $p = 1, 2, 3, \dots, 8$, respectively [335,345]. Equation (91) carries a linear dependence of E_{ii} on p/d_t , which is expected from tight-binding theory. It also includes a logarithmic correction term in p/d_t that comes from many-body interactions, plus a chiral angle θ dependence related to electronic trigonal warping and chirality-dependent curvature effects due to $\sigma - \pi$ hybridization [321]. The theoretical background for all these factors is discussed in Section 3.

5.2. Exciton environmental effect

The E_{ii} values are now understood in terms of the bright exciton energy within the framework of a tight binding calculation which includes curvature optimization [254,346] and many-body effects [39–41,148,342]. The assignments of E_{ii} for SWNTs over a large region of both diameter ($0.7 < d_t < 3.8$ nm) and E_{ii} (1.2–2.7 eV) values and for a variety of surrounding materials are now available [21,230,335], thus making it possible to accurately determine the effect of the

Table 3. Adjusted parameters \mathcal{M}_i and γ_i for metallic (M), semiconductor type 1 (S_1) and type 2 (S_2) tubes.

Type	\mathcal{M}_A	\mathcal{M}_B	\mathcal{M}_C	γ_A	γ_B	γ_C
M	1.68	0.52	5.54	23.03	28.84	1.03
S_1	-19.62	29.35	4.23	-3.45	65.10	7.22
S_2	-1.83	3.72	1.61	-10.12	42.56	-6.84

These parameters are to be used in Equation (90) with d_t in nm, yielding \mathcal{M} in arbitrary units and γ in meV [344].

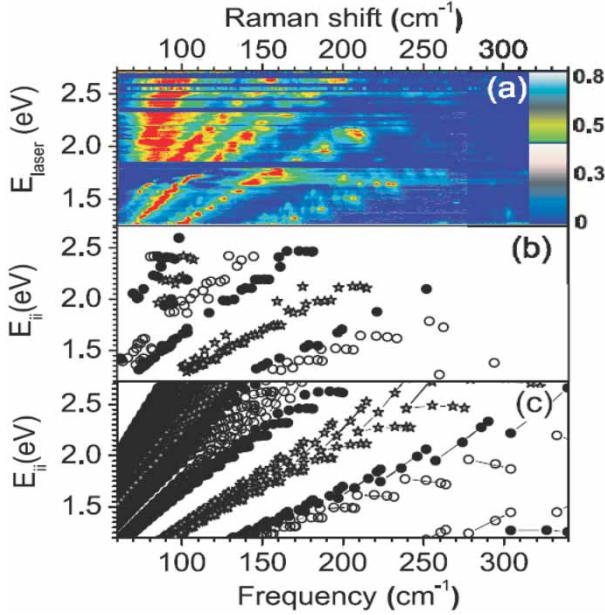


Figure 59. (a) RBM resonance Raman map for the “super-growth” (S.G.) SWNT sample [314,335,345]. (b) Kataura plot of all transition energies ($E_{ii}^{S.G.}$) that could be experimentally obtained from the resonance windows extracted from (a) as a function of ω_{RBM} . (c) Kataura plot obtained from Equation (91) with the parameters that best fit the data in (b). The stars stand for M-SWNTs, the open bullets stand for type I S-SWNTs and the filled bullets stand for type II S-SWNTs. Reprinted figure with permission from P.T. Araujo and A. Jorio, *Physical Status Solidi B*, 2008, 245, pp. 2201–2204 [335]. Copyright © Wiley–VCH Verlag GmbH & Co. KGaA.

general dielectric constant κ on E_{ii} . By “general” we mean that κ comprises the screening from both the tube core electrons and from the tube environment.²⁴ A d_t -dependent effective κ value for the exciton calculation is needed to reproduce the experimental E_{ii} values consistently. This dependence is important for the physics of quasi-1D and truly 1D materials generally and can be used in interpreting optical experiments and environment effects for such materials. Environmental effects are therefore considered further in Sections 5.2.1 to 5.2.3.

5.2.1. The effect of the dielectric constant κ on E_{ii}

Figure 60 shows a map of experimental E_{ii} values (black dots) [314,335] from a SWNT sample grown by the water-assisted (“super-growth”) CVD method [34,316]. The resulting data for the E_{ii} transition energies are plotted as a function of the RBM frequencies ω_{RBM} , as obtained by RRS [314,335,345]. In Figure 60, the experimental values of E_{ii} vs. ω_{RBM} for the “super-growth” sample E_{ii}^{exp} are compared with the calculated bright exciton energies E_{ii}^{cal} (open circles and stars), obtained with the dielectric screening constant $\kappa = 1$. Although E_{ii}^{cal} includes SWNT curvature and many-body effects [148], clearly the E_{ii}^{exp} values are red shifted when compared with theory, and this red shift depends on both ω_{RBM} (*i.e.*, on d_t) and on the optical energy levels (i in E_{ii}). Figure 63 shows a comparison between the E_{ii}^{exp} from the “super-growth” SWNT sample (bullets) [335] and E_{ii}^{exp} from the “alcohol-assisted” SWNT sample (open circles) [321]. From Figure 63, we see that besides the changes in ω_{RBM} , the E_{ii}^{exp} values from the “alcohol-assisted” SWNTs are generally red shifted with respect to those from the “super-growth” SWNTs. Assuming that κ_{tube} does not change from sample

to sample for a particular type of SWNT sample, since the electronic structure of a given (n, m) tube should be the same, these results indicate that the “alcohol-assisted” SWNTs are surrounded by an environment with a larger κ_{env} value than the “super growth” sample, thus increasing the effective κ and decreasing E_{ii} [229], which is consistent with Figure 61, discussed below.

5.2.2. Screening effect: a general κ function

The E_{ii} values can be renormalized in the calculation by explicitly considering the dielectric constant κ in the Coulomb potential energy given by Equation (54) [231]. Here, κ represents the screening of the e-h (e-h) pair by core (1s) and σ electrons (κ_{tube}) and by the surrounding materials (κ_{env}), while $\varepsilon(q)$ explicitly gives the polarization function for π -electrons calculated within the RPA [120,148,275]. To fully account for the observed energy-dependent E_{ii} redshift, the total κ values ($1/\kappa = C_{\text{env}}/\kappa_{\text{env}} + C_{\text{tube}}/\kappa_{\text{tube}}$) are fitted to minimize $E_{ii}^{\text{exp}} - E_{ii}^{\text{cal}}$ in Figure 60.

The κ values are found to depend on the following three parameters: (1) the subband index p where $p = 1, 2, 3, 4$ and 5 stands for $E_{11}^S, E_{22}^S, E_{11}^M, E_{33}^S$ and E_{44}^S , respectively [177,229], (2) the diameter of the nanotube d_t and (3) the exciton size l_k in reciprocal space [232]. Using the optimized κ values which are fitted to the calculated E_{ii} values as a function of κ and to the experimental E_{ii} values, a general κ function is modeled to have the following functional form [232]:

$$\kappa \approx C_\kappa \left[p^a \left(\frac{1}{d_t} \right)^b \left(\frac{1}{l_k} \right)^c \right]. \tag{92}$$

The parameters (a, b, c) thus determined are common for all different samples $(a, b, c) = (0.8 \pm 0.1, 1.6 \pm 0.1, 0.4 \pm 0.05)$ so as to both optimize the correlation between κ and (p, d_t, l_k) , and to minimize differences between theory and experiment. Here, it should be mentioned that the variable l_k is involved in the κ function because of the screening by the different environments

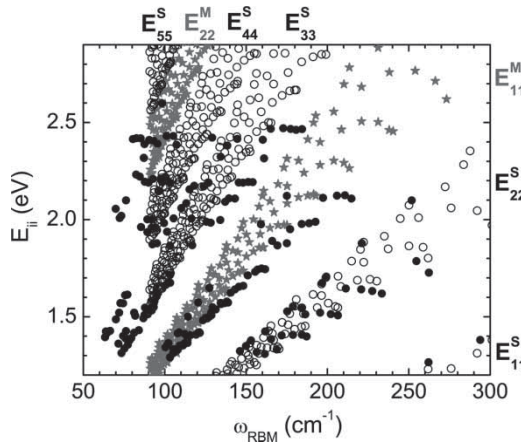


Figure 60. Black dots show E_{ii}^{exp} vs. ω_{RBM} results obtained from resonance Raman spectra taken from a super-growth SWNT sample. The black open circles (semiconducting; S-SWNTs) and the dark-gray stars (metallic; M-SWNTs) give E_{ii}^{cal} calculated for the bright exciton with a dielectric constant $\kappa = 1$ [148]. Along the x axis, the E_{ii}^{cal} values are calculated using the relation $\omega_{\text{RBM}} = 227/d_t$. Due to computer time availability, only E_{ii} for tubes with $d_t < 2.5$ nm (i.e., $\omega_{\text{RBM}} > 91$ cm^{-1}) have been calculated. Transition energies E_{ii}^S ($i = 1$ to 5) denote semiconducting SWNTs and E_{ii}^M ($i = 1, 2$) denote metallic SWNTs. Reprinted figure with permission from P.T. Araujo *et al.*, *Physical Review Letters* 103, p. 146802, 2009 [229]. Copyright © (2009) by the American Physical Society.

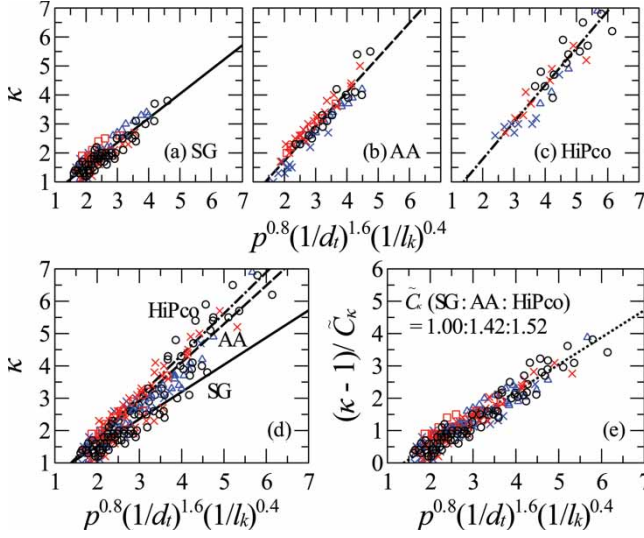


Figure 61. The κ function for: (a) SG, (b) AA, and (c) HiPco samples. (d) Data for the three different types of samples are plotted on the same figure with a fitted slope C_κ for each sample. (e) All the κ functions collapse on to a single line after dividing each function by the corresponding \tilde{C}_κ . The following symbols are used: E_{11} (\circ), E_{22} (\times), E_{33} (\triangle) and E_{44} (\square). Black, red, and blue colors, respectively, denote metallic ($\text{mod}(2n+m, 3) = 0$), semiconductor type I ($\text{mod}(2n+m, 3) = 1$), and type II ($\text{mod}(2n+m, 3) = 2$) SWNTs. Reprinted figure with permission from A.R.T. Nugraha *et al.*, Applied Physical Letters 97, p. 91905, 2010 [232]. Copyright © (2010) American Institute of Physics.

which modify the exciton size. However, we will show below that the selection of l_k as a variable for κ is essential for explaining the difference between metallic and semiconducting SWNTs. In fact, Equation (92) indicates another scaling relation for excitons, similar to the previously reported scaling law which relates E_{bd} with d_t , κ , and the “effective mass” μ [275]. However, it is found that the scaling relation involving μ works well only for S-SWNTs and another scaling function is needed for M-SWNTs. This is because E_{bd} for an M-SWNT is screened by free electrons even for a similar effective mass as that for the photo-excited carriers.

In Figure 61, we show a series of results for the κ function [232] for different samples grown by different methods: (a) super-growth [316], (b) alcohol-assisted CVD [347], and (c) the high pressure gas-phase decomposition of CO (HiPco) [348]. For each sample, the κ function is successfully unified for lower energy transitions ($E_{11}^S, E_{22}^S, E_{11}^M$) and for the higher energy transitions (E_{33}^S, E_{44}^S). Considering l_k explicitly is important for describing the environmental effect for both metallic and semiconducting SWNTs simultaneously, since l_k is very different between metallic and semiconducting SWNTs, even for similar effective mass values because of the screening of the π electrons. When we consider a SWNT, the κ values for the higher E_{ii} transitions which have larger l_k^{-1} values are smaller than those for lower E_{ii} (smaller l_k^{-1}). Thus, l_k^{-1} (the exciton size in real space) is also smaller for the higher E_{ii} because only a small amount of the electric field created by an e-h pair will influence the surrounding materials.²⁵

Qualitatively, the origin of the diameter dependence of κ consists of: (1) the diameter-dependent exciton size and (2) the amount of electric field which goes into the surrounding material. These two factors are connected to one another and Ando gave an analytic form for an expression connecting these two factors [349]. The development of an electromagnetic model is needed to fully rationalize Equation (92). Interestingly, the similarity between the κ values found for E_{22}^S and

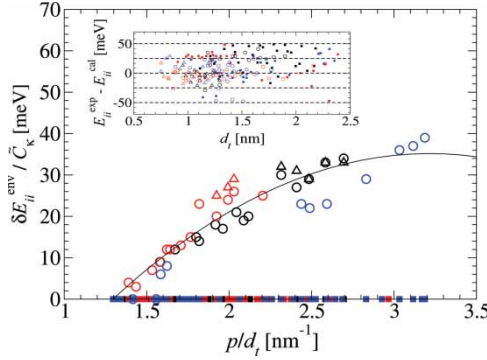


Figure 62. δE_{ii}^{env} versus d_t , scaled by \tilde{C}_κ . Circles and triangles, respectively, denote AA and HiPCO samples (see text). Many square symbols on the zero line denote the SG sample which is taken as the standard. The inset shows differences between experimental (exp) and calculated (cal) E_{ii} values for all samples, showing good agreement between experiment and the model calculations. Reprinted figure with permission from A.R.T. Nugraha *et al.*, Applied Physical Letters 97, p. 91905, 2010 [232]. Copyright © (2010) American Institute of Physics.

E_{11}^M shows that the difference between metallic and semiconducting tubes is satisfactorily taken into account by l_k using the random phase approximation (RPA) in calculating $\varepsilon(q)$ [148,342].

In Figure 61(d), three sets of data contained in Figure 61(a)–(c) are merged, from which we know that the three plots when taken together depend only on the difference of the slopes, that is C_κ of Equation (92). Values of C_κ for the SG, AA and HiPCO samples are 0.84, 1.19 and 1.28, respectively. We expect that such differences in the values for C_κ arise from the environmental effects on the exciton energies. Therefore, we assume that each C_κ value characterizes the environmental dielectric constant κ_{env} for that particular sample. The SG sample has the largest E_{ii} and hence the smallest dielectric constant relative to any of the other samples found in the literature [230], and so we normalize C_κ of the SG sample to be $\tilde{C}_\kappa(\text{SG}) = 1.00$ for simplicity. The values of \tilde{C}_κ for the other samples can then be determined by taking the ratio of their C_κ values to that for the SG sample. Thus, \tilde{C}_κ for the SG, AA, and HiPCO samples becomes 1.00, 1.42, and 1.52, respectively. When we use the normalized \tilde{C}_κ , all points collapse on to a single line, as shown in Figure 61(e), hence giving justification for the use of this assumption. It is interesting to see that all the lines shown in Figure 61 cross the horizontal axis at $\kappa = 1$ at the same point. This point corresponds to the large diameter limit beyond which the 1D exciton does not exist. The corresponding diameter is scaled by p and l_k .

In Figure 62, we plot the calculated energy shift δE_{ii}^{env} relative to the SG results as a function of p/d_t . The data on the horizontal axis are the data for the SG sample which should be zero from the definition of δE_{ii}^{env} . The δE_{ii}^{env} for the AA and HiPCO sample are fitted to a function:

$$\delta E_{ii}^{env} = E_{ii}^{\text{SG}} - E_{ii}^{env} \equiv \tilde{C}_\kappa \left[A + B \left(\frac{p}{d_t} \right) + C \left(\frac{p}{d_t} \right)^2 \right], \quad (93)$$

where A , B and C are parameters common to all types of environments and E_{ii}^{env} is calculated using the κ function obtained previously. The best fit is found for $A = -42.8$ meV, $B = 46.34$ meV \cdot nm and $C = -7.47$ meV \cdot nm². In the inset to Figure 62, we show the energy difference between experiment and theory that is obtained by using the κ function (Equation (92)) and we see all the data points are within 50 meV for a large range of SWNT diameters and energies.

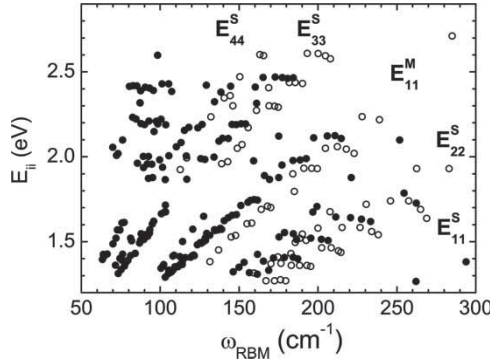


Figure 63. E_{ii}^{exp} vs. ω_{RBM} results obtained for the “super-growth” (bullets) and the “alcohol-assisted” (open circles) SWNT samples. Reprinted figure with permission from P.T. Araujo *et al.*, *Physical Review Letters* 103, p. 146802, 2009 [229]. Copyright © (2009) by the American Physical Society.

5.2.3. Effect of the environmental dielectric constant κ_{env} on E_{ii}

Looking at Figure 61, we can observe a difference in the κ values resulting from fitting the E_{ii}^{exp} to the “super-growth” (Figure 61(a)) sample in comparison to the “alcohol-assisted” (Figure 61(b)) SWNT sample. For E_{22}^{S} and E_{11}^{M} , we see in Figure 61(a) a clear difference for κ up to $p = 3$ when comparing the two samples. However, for E_{33}^{S} and E_{44}^{S} (Figure 61(d)), no difference in κ in the range $\kappa = 1-3$ can be seen between the two samples. This means that the electric field of the E_{33}^{S} and E_{44}^{S} excitons does not extend much outside the SWNT volume, in contrast to the E_{22}^{S} and E_{11}^{M} excitons for which the κ_{env} effect is significant. Since the effect of κ_{env} is relatively small for energies above E_{11}^{M} , it is still possible to assign the (n, m) values from E_{33}^{S} and E_{44}^{S} even if the dielectric constant of the environment is not known, and even though the E_{33}^{S} and E_{44}^{S} values are seen within a large density of dots in the Kataura plot of Figure 63.

5.3. Splitting of the G mode

The first-order Raman-allowed G-band mode in 2D graphene is a single peak feature ($\omega_{\text{G}} \approx 1584 \text{ cm}^{-1}$) [112]. In SWNT, the G-band appears as multiple peaks centered around ω_{G} [333, 350]. Two, four or six G-band phonons are allowed for the first-order G-band Raman feature in SWNTs, depending on the polarization scattering geometry. Two of these mode, named the totally symmetric A_1 modes (see Figure 64), usually dominate the spectra, although this depends both on the polarization geometry and on the resonance condition. Finally, the G-band profile depends strongly on the metal vs. semiconducting nature of the tube, as well as on changes in the Fermi level. In this section, we discuss the effects responsible for these dependencies, which are related to the effect of curvature and el-ph interaction on the G-band modes.

5.3.1. The G-band eigenvectors and curvature

Because of the curvature of the graphene sheet in carbon nanotubes, the longitudinal optical (LO) vs. in-plane transverse optical (iTO) phonons, which are degenerate in graphene, have different frequencies in carbon nanotubes. Actually, the definition of iTO and LO is different for graphene and nanotubes. For 2D systems, transverse and longitudinal are defined with respect to the phonon propagation direction. In the 1D SWNTs, the longitudinal vibration denotes atomic motion along the tube axis, where phonon momentum q can be defined, and the transverse vibration corresponds to atomic motion perpendicular to the tube axis [100,280].

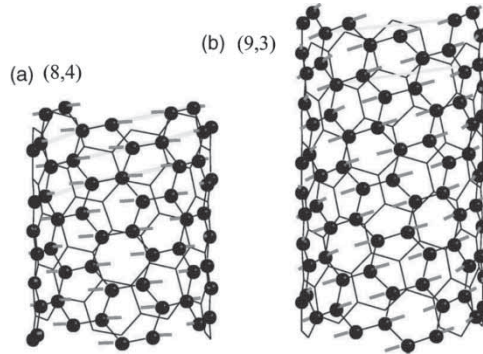


Figure 64. (a) The totally symmetric G-band eigenvectors for the (8,4) semiconducting SWNT. The atomic displacements are almost parallel to the circumference. (b) The totally symmetric G-band eigenvector for the (9,3) metallic SWNT. The atomic displacements are almost parallel to the carbon–carbon bonds. Reprinted figure with permission from S. Reich *et al.*, *Physical Review B* 64, p. 195416, 2001 [280]. Copyright © (2001) by the American Physical Society.

First-principles calculations have been performed for different SWNTs by Reich *et al.* [280]. They found that, while for armchair and zigzag SWNTs, which have higher symmetry than chiral tube structures, the LO and iTO vibrations of the G-band exist [280], such a definition is not strictly valid for chiral nanotubes, where the atomic vibrations actually depend on the chiral angle. In Figure 64(a and b) Reich *et al.* show the mode displacements for one totally symmetric (A_1) G-band mode in two different chiral SWNTs. For each case, another G-band mode is expected with the atomic vibrations perpendicular to those indicated in the figure. Note that the atomic displacements in Figure 64 are almost perfectly aligned along the circumference in the (8,4) S-SWNT (a), but mostly parallel to the C–C bonds in the (9,3) M-SWNT (b), and in neither case is the strict iTO definition applicable. These findings by Reich *et al.* [280] are qualitatively consistent with other calculations [86], but the quantitative definitions are model-dependent. There is still controversy about whether the many peaks within this G-band can be assigned to LO and iTO type mode behavior, as discussed by Piscanec *et al.* [193].

5.3.2. The six G-band phonons – confinement effect

While the doublet nature of the G-band discussed above is related to strain effects from the tube curvature, 1D confinement makes one, two or three of those doublets observable, each pair having either A_1 , E_1 or E_2 symmetry. This happens because, when rolling up the graphene sheet to form a nanotube, the zone folding along the circumferential direction generates a larger number of first-order Raman-allowed modes [32,99,100,167].

The difference between A_1 , E_1 and E_2 symmetry Raman modes is given by the number of nodes for the atomic motion along the tube circumference, where the number of nodes is zero, two and four, respectively. This zone-folding procedure is shown in Figure 65(b). Therefore, combined with the (quasi) LO and iTO vibrational nature, two, four or six G-band phonons can be Raman-allowed in the Raman spectra from SWNTs, and their observation depends on the polarization of the scattering geometry *and* on the resonance condition, as explained below.

Selecting the Z-axis as the SWNT axis direction, and the Y-axis as the photon propagation direction, light can be polarized parallel (Z) or perpendicular (X) to the nanotube axis. The possible scattering geometries are given by $p_i(\text{is})p_s$, using what is called the Porto notation in memory of S.P.S. Porto, where p_i and p_s give the propagation directions for the incident and scattered

Table 4. Selection rules for polarization dependent G-band features and the corresponding resonance conditions.

Symmetry of phonon	Scattering event	Resonance condition
A_1	(ZZ)	$E_{\text{laser}} = E_{ii}, E_{\text{laser}} \pm E_G = E_{ii}$
A_1	(XX)	$E_{\text{laser}} = E_{ii\pm 1}, E_{\text{laser}} \pm E_G = E_{ii\pm 1}$
E_1	(XZ)	$E_{\text{laser}} = E_{ii\pm 1}, E_{\text{laser}} \pm E_G = E_{ii}$
E_1	(ZX)	$E_{\text{laser}} = E_{ii}, E_{\text{laser}} \pm E_G = E_{ii\pm 1}$
E_2	(XX)	$E_{\text{laser}} = E_{ii\pm 1}, E_{\text{laser}} \pm E_G = E_{ii\pm 1}$

The Z- and Y- axes are the SWNT axis direction and the photon propagation direction, respectively. The polarization of the incident and scattered light is given as well as the resonance condition. E_G is the G-band phonon energy [1].

photons, respectively, while the incident polarization i and scattered polarization s appear inside the parenthesis (is). Since the SWNT experiments are usually made by using microscopes in the back-scattering configuration, p_i and p_s are usually Y and $-Y$, so that the simplified notation (is) can be applied. In this case, four different scattering geometries are possible, and these are labeled XX, XZ, ZX and ZZ .

The first-order Raman signal from isolated SWNTs can only be seen when the excitation laser energy is in resonance with a van Hove singularity (VHS) in the JDOS. Chiral SWNTs exhibit C_N symmetry [351,352] and, following the (is) notation introduced above, selection rules imply that: (1) totally symmetric A phonon modes are observed for the (ZZ) scattering geometry when either the incident or the scattered photon is in resonance with E_{ii} , and for the (XX) scattering geometry when either the incident or the scattered photon is in resonance with $E_{i,i\pm 1}$. (2) E_1 symmetry modes can be observed for the (ZX) scattering geometry for resonance of the incident photon with the E_{ii} VHSs, or for resonance of the scattered photon with the $E_{i,i\pm 1}$ VHSs, while for the (XZ) scattering geometry, for resonance of the incident photon with the $E_{i,i\pm 1}$ VHSs, or for resonance of the scattered photon with the E_{ii} VHSs; (3) E_2 symmetry phonon modes can only be observed for the (XX) scattering geometry for resonance with $E_{i,i\pm 1}$ VHSs. Therefore, it is possible to observe two, four or six G-band peaks, depending on the resonance conditions and on the polarization scattering geometry, as summarized in Table 4.

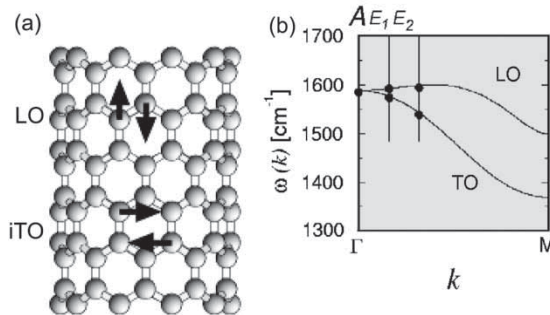


Figure 65. (a) Schematic picture of the G-band atomic vibrations along the nanotube circumference and along the nanotube axis of a zigzag nanotube. (b) The Raman-active modes with A, E_1 and E_2 symmetries and the corresponding cutting lines $\mu = 0, \mu = \pm 1$ and $\mu = \pm 2$ in the unfolded 2D BZ. The Γ points of the cutting lines are shown by solid dots. Reprinted from Raman Spectroscopy of Carbon Nanotubes, M.S. Dresselhaus *et al.* [167]. Copyright © (2005) with permission from Elsevier.

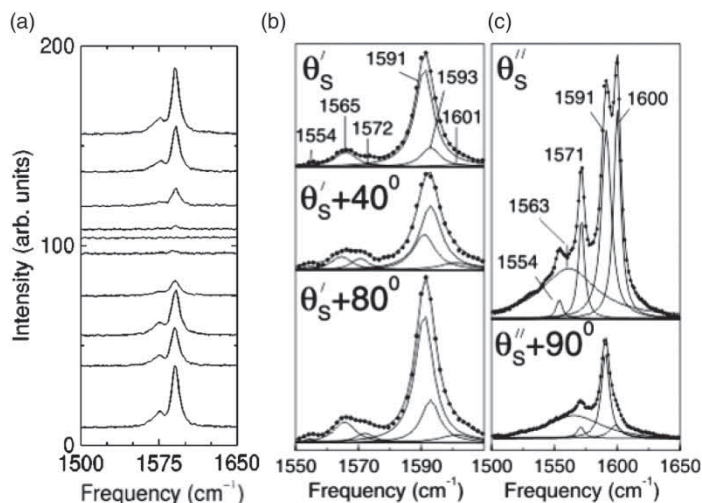


Figure 66. (a) G-band polarization dependence from one isolated semiconducting SWNT sitting on a Si/SiO₂ substrate [357]. Both incident and scattered light are polarized parallel to each other and vary from ZZ (bottom) to XX (middle) and back to ZZ (top). (b,c) G-band polarization scattering geometry dependence from two isolated SWNTs. The Lorentzian peak frequencies are given in cm⁻¹. The incident angles θ'_S and θ''_S between the light polarization and the SWNT axis directions are not known *a priori*, but have been assigned as $\theta'_S \sim 0^\circ$ and $\theta''_S \sim 90^\circ$ based on the relative intensities of the polarization behavior of the G-band modes and the expected selection rules and frequencies (see Section 5.3.3) for the A_1 , E_1 and E_2 modes [352]. Reprinted figure with permission from A. Jorio *et al.*, *Physical Review B* 65, p. R121402, 2002 [357]. Copyright © (2009) by the American Physical Society.

Before showing the experimental results related to the selection rules discussed above, we introduce a general polarization behavior that is not accounted for in these selection rules and is responsible for the totally symmetric A_1 modes in the G-band spectra which dominate these spectra. Carbon nanotubes are nano-antennas, and both the absorption and emission of light are suppressed when the light is polarized perpendicular to the nanotube axis. This phenomenon is called as the depolarization effect [353,354], where photo-excited carriers screen the electric field of the cross-polarized light inside the carbon nanotube [234,353,354]. Considering these effects, it is clear that the Raman intensity is generally largest for the (ZZ) scattering polarization geometry, while the signal will be suppressed for the (XX) scattering, as shown in Figure 66(a) [355–357]. In addition, remember that the resonance energies are different for light along Z (E_{ii}) and along X ($E_{ii\pm 1}$), as described in Table 4. This means that one rarely observes the Raman signals from parallel (ZZ) and perpendicular ((ZX), (XZ) or (XX)) polarization directions simultaneously.

Now we can discuss experimental results related to the symmetry selection rules for the different scattering geometries [351,357,358]. Figure 66(b) shows the G-band Raman spectra from a semiconducting SWNT with three different directions for the incident light polarization. Considering θ'_S the initial angle between light polarization and the nanotube axis, unknown *a priori*, the three spectra in Figure 66(b) were acquired with θ'_S , $\theta'_S + 40^\circ$ and $\theta'_S + 80^\circ$. Six well-defined G-band peaks are observed with different relative intensities for the different polarization geometries and, based on the selection rules and on their frequencies (see Section 5.3.3), they are assigned as follows: 1565 and 1591 cm⁻¹ are A_1 symmetry modes; 1572 and 1593 cm⁻¹ are E_1 symmetry modes; and 1554 and 1601 cm⁻¹ are E_2 symmetry modes. Figure 66(c) shows the G-band Raman spectra obtained from another semiconducting SWNT, the two spectra with θ''_S and $\theta''_S + 90^\circ$,

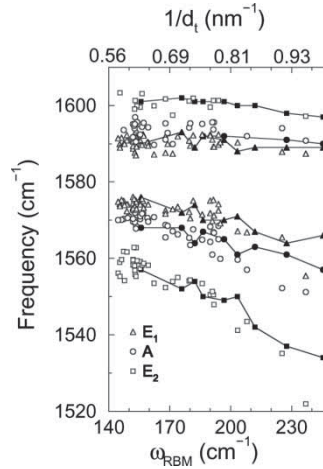


Figure 67. ω_G (open symbols) vs. ω_{RBM} (bottom axis) and vs. $1/d_t$ (top axis) for S-SWNTs. Explicit experimental G-band data obtained with $E_{\text{laser}} = 1.58, 2.41$ and 2.54 eV are presented. Solid symbols connected by solid lines give results obtained from *ab initio* calculations [249], downshifted by about 1% to fit the experimental data [352]. Reprinted figure with permission from O. Dubay and G. Kresse, *Physical Review B* 67, p. 35401, 2003 [249]. Copyright © (2003) by the American Physical Society.

where θ'_S is also unknown *a priori*. The spectra requires four sharp Lorentzians for a good line-shape fitting, plus a broad feature at about 1563 cm^{-1} . This broad feature (FWHM $\sim 50 \text{ cm}^{-1}$) is sometimes observed in weakly resonant G-band spectra from SWNTs, and is generated by defect-induced DR processes. For the sharp peaks, based on the polarization Raman studies and on their relative frequencies [351], the 1554 and 1600 cm^{-1} peaks are E_2 symmetry modes, while the 1571 and 1591 cm^{-1} peaks are unresolved ($A_1 + E_1$) symmetry modes, with their relative intensities depending on the incident light polarization direction [351].

Generally speaking, the intensity ratio between the two scattering geometries $ZZ : XX$ can assume values either larger or smaller than 1, depending on the resonance condition. Observation of the spectra with (XX) polarization in Figure 66(c) indicates resonance with a $E_{i,j\pm 1}$ optical transition. In samples with a large diameter distribution, e.g. d_t from 1.3 nm up to 2.5 nm in Ref. [351], both the E_{ii} and $E_{i,j\pm 1}$ transitions can occur within the resonance window of the same laser, and an average value of $ZZ : XX = 1.00 : 0.25$ was then observed. However, for most isolated SWNTs, the Raman intensities exhibit an intensity ratio $I_{ZZ} : I_{XX} \sim 1 : 0$. This “antenna effect” is observed for samples in resonance with only E_{ii} electronic transitions, as shown in [355–357].

Finally, the above discussion is related to phonon confinement within the first-order *single resonance* process [333,350,351]. There has been interesting discussion on whether the features in the multi-peak G-band could all be assigned to A_1 symmetry modes [355,359] originating from a defect-induced DR Raman scattering process [145]. It seems that both cases, i.e. a multi-peak feature from multi-symmetry scattering and from an A_1 symmetry feature induced by disorder are possible in very disordered samples [360].

5.3.3. The diameter dependence of the G band phonon frequencies

The G-band mode assignment proposed in Section 5.3.2 comes from a comparison between experimental results and *ab initio* calculations of the diameter dependence of ω_G [249], as shown

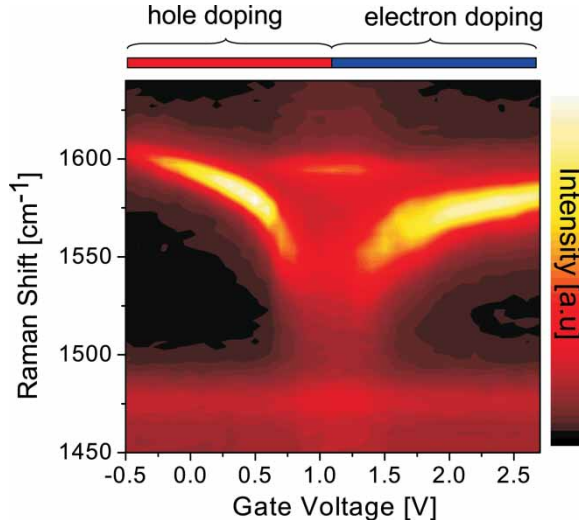


Figure 68. Experimental intensity plot of the G-band spectrum of a metallic SWNT as a function of electrochemical gate potential. For this nanotube the charge neutrality point, corresponding to the Dirac point, is 1.2 V. Adapted figure with permission from M. Farhat *et al.*, *Physical Review Letters* 99, p. 145506, 2009 [201]. Copyright © (2009) by the American Physical Society.

in Figure 67. The relation between ω_{RBM} (bottom axis – for experimental results) and inverse nanotube diameter (top axis – for theoretical results) were made in this figure considering $1/d_t = \omega_{\text{RBM}}/248$. This $\omega_{\text{RBM}} = 248/d_t$ relation [111] was broadly used in the early years of single nanotube spectroscopy (2001–2005). The present understanding uses Equation (86) with $C_e = 0.065$, which is applicable to a larger variety of samples.

The spectra in this work were fit using 2, 4 or 6 peaks with FWHM $\gamma_G \sim 5 \text{ cm}^{-1}$, which is the natural linewidth for the G-band modes [340]. The diameter dependent downshift in frequency comes from strain and from curvature-induced mixing of low frequency out-of-plane components. In the time-independent perturbation picture, the ω_G^{LO} mode frequency is expected to be independent of diameter, since the atomic vibrations are along the tube axis. In contrast, the ω_G^{TO} mode has atomic vibrations along the tube circumference, and increasing the curvature increases the out-of-plane component, thus decreasing the spring constant with a $1/d_t^2$ dependence. This picture holds for semiconducting SWNTs, where G^+ now stands for the LO mode, and G^- stands for the iTO mode [171]. However, for metallic SWNTs the picture is different: G^+ now stands for the iTO mode, and G^- stands for the LO mode [193,249]. The G-band profile in this case is very different and depends strongly on doping, as shown in Figure 68, and this behavior can only be understood within a time-dependent perturbation picture. In this section, we focus on the spectra from semiconducting SWNTs. Metallic SWNTs are discussed in Section 5.4.

The d_t dependence of the frequencies for each of the three higher frequency G^+ band modes (A_1 , E_1 and E_2) observed experimentally are in very good agreement with theory [249], showing basically no diameter dependence. For the lower frequency G^- band modes, both *ab initio* calculations and the experimental results show a considerable d_t dependence of the mode frequency. The experimental G-band frequencies from semiconducting SWNTs can be fit with [352]

$$\omega_G = 1592 - \frac{C}{d_t^\beta}, \quad (94)$$

where the values for the various parameters are: $\beta = 1.4$, $C_{A_1} = 41.4 \text{ cm}^{-1} \text{ nm}$, $C_{E_1} = 32.6 \text{ cm}^{-1} \text{ nm}$ and $C_{E_2} = 64.6 \text{ cm}^{-1} \text{ nm}$.

A simpler formula for the G-band intensities has also been proposed in Ref. [171], where the G-band fitting is not performed with six Lorentzians, but rather by considering just the peak value for the two most intense features. In this case, the higher frequency G^+ peak is diameter independent and the lower frequency G^- feature decreases in frequency with a $1/d^2$ dependence. In practice, the G band can be used for a diameter determination for both semiconducting and metallic SWNTs by using the formula from [171]. For more detailed studies, the more complete analysis discussed above and including dynamic effects [193] and environmental effects [232] should be used.

5.4. Kohn Anomaly effect on the G-band and the RBM mode

In this section, the first-order spectra for metallic SWNTs are discussed giving special attention to the dependence of these spectral features on the Fermi level position and the KA phenomena that account for the special properties of these spectral features for metallic SWNTs [193]. First, we discuss the characteristics of the KA for the G-band in Section 5.4.1 through Section 5.4.4, followed by an elaboration of the KA for the RBM feature in Section 5.4.5.

5.4.1. G-band Kohn anomaly

The Fermi-level dependencies of the LO and iTO modes on SWNT bundles have been measured [50,51,361,362], showing mainly changes in frequency and linewidth of the Breit–Wigner–Fano (BWF)-like feature in the G-band associated with metallic nanotubes, as E_F was varied. This effect is now understood within the framework of time-dependent perturbation theory including dynamic effects [193], and this effect has been shown more clearly with Fermi level variation experiments performed on individual metallic carbon nanotubes [193,201,283]. The G-band spectrum of an individual metallic nanotube changes as a function of an electrochemical gate potential as shown in Figure 68. The higher frequency peak does not change significantly as a function of gate voltage, but the broad lower frequency peak (BWF-like) upshifts and narrows in linewidth with both positive and negative changes in the Fermi level. Differently from semiconducting SWNTs, where the higher frequency peak is assigned to the LO vibration, metallic SWNTs have a lower frequency mode with a BWF-like lineshape that is assigned to the LO mode, which downshifts in energy significantly due to the KA effect [193].

The KA is predicted to occur in metallic carbon nanotubes [193], and to exhibit two characteristic signatures related to non-adiabatic effects: (1) within the energy window $E_F < |\hbar\omega_{LO}|$, the LO phonon peak is broadened due to the creation of real e–h pairs; (2) the LO frequency vs. E_F curve shows a characteristic “W” lineshape due to the two singularities located at $E_F = \pm\hbar\omega_{LO}$. This “W” lineshape is not resolved in Figure 68 because of inhomogeneous charging due to trapped charges on the substrate that result in a smearing of E_F . However, using pristine suspended nanotubes that are gated electrostatically, the “W” feature can be explicitly seen in the frequency dependence of the LO mode [363].

The intensities of the LO and iTO modes depend also on the chiral angle, with the iTO mode being symmetry forbidden for a zigzag nanotube [283,364]. A chiral angle dependence of the iTO mode softening has been predicted theoretically [365]. Future experiments on structurally identified and truly isolated individual (n, m) nanotubes are needed to further advance our understanding of these phenomena related to the KA.

Gate-dependent experiments on semiconducting nanotubes reveal that their G-band phonons also experience energy renormalization due to el–ph coupling [51,366]. However, $\hbar\omega_{LO/iTO} < E_{11}^S$

for semiconducting SWNTs, which means that the G-band phonons are unable to create real e–h excitations across a typical non-zero bandgap. Therefore, lifetime broadening of the phonon is not expected, and the G-band peak FWHM should not change significantly. Still, virtual e–h excitations contribute to the softening of the phonon energies [366]. Both the iTO and LO modes couple to intermediate e–h pairs, and the iTO mode is expected to show a greater E_F -dependent frequency shift, most significantly in larger diameter nanotubes, as the band gap energy approaches the phonon energy [366]. This behavior in semiconducting SWNTs is opposite to metallic SWNTs.

5.4.2. Chemical doping and the G band

The KA effect discussed in Section 5.4.1 is important at low doping levels. For higher doping levels, structural distortions dominate, and these distortions depend on the level of the p vs. n doping, which should cause upshift vs. downshift in the phonon frequencies, respectively. Such p vs. n doping behavior has been demonstrated for the G band of single-wall and multi-wall carbon nanotubes doped chemically with atomic species that are donors or acceptors to carbon [36,367]. For example, the doping with K, Rb and Cs (alkali metals) leads to a G-band mode softening of 35 cm^{-1} accompanied by significant changes in the G-band lineshape. For SWNT bundles doped with Br_2 (halogens), an upshift in the Raman-mode frequencies is observed. For more details on the effect of chemical doping on the Raman spectra of SWNTs, see, e.g. [36].

5.4.3. Substrate interaction and the G band

The confocal image shown in Figure 69(a) was obtained by integrating the G-band Raman signal from a SWNT serpentine sample, while raster scanning the sample [324]. These carbon serpentine nanotubes are SWNTs with parallel straight segments connected by alternating U-turns, as shown in Figure 69(a) [324]. These serpentine nanotubes were grown by catalytic CVD on miscut single-crystal quartz wafers [368]. The resulting vicinal SiO_2 (1 1 0 1) substrate is insulating, and is terminated by parallel atomic steps. At the temperature of nanotube growth, the surface contains exposed unpassivated Si atoms, thus enabling a strong tube–substrate interaction to occur, especially when the nanotube lies along a step. Alternatively, when the nanotube lies across the surface steps, the interaction is discontinuous and weaker. The orientation between the tube and crystalline quartz varies, which means that the tube–substrate interaction is modulated along the tube. The straight segments usually lie along the quartz steps, while the U-turns lie across the steps. Figure 69(b) shows the G-band Raman spectra obtained from all 41 points indicated by the pointers in Figure 69(a). Careful analysis of the individual G-band spectral features shows that the G-band spectra changes along the SWNT serpentine. These changes are related to strain and doping which varies along the tube due to the morphology of the tube–substrate interaction in these samples [324]. Such a strong interaction also has a strong effect on the RBM frequencies, leading to an environmental constant of $C_e = 0.085$ in Equation (86) which relates ω_{RBM} and d_t [323].

5.4.4. Theoretical approach to the Kohn Anomaly

The KA in metallic SWNTs was introduced firstly by Piscanec *et al.* [193]. As discussed in Section 3.6.5, the phonon softening phenomena is understood by second-order perturbation theory in which a phonon virtually excites an e–h pair across the metallic energy subband of a metallic SWNT (as shown in Figure 70(a)). The effective Hamiltonian in second-order perturbation theory is given by Equation (71) [196,205,246]. In Figure 70(b), we show the energy denominator of Equation (71), in which the real part of $h(E)$ is related to the frequency shift, while the imaginary part of $h(E)$ is related to the spectral broadening. From this figure, for the energy below (above) the phonon energy of the G-band, the virtual excitation contributes to the phonon hardening

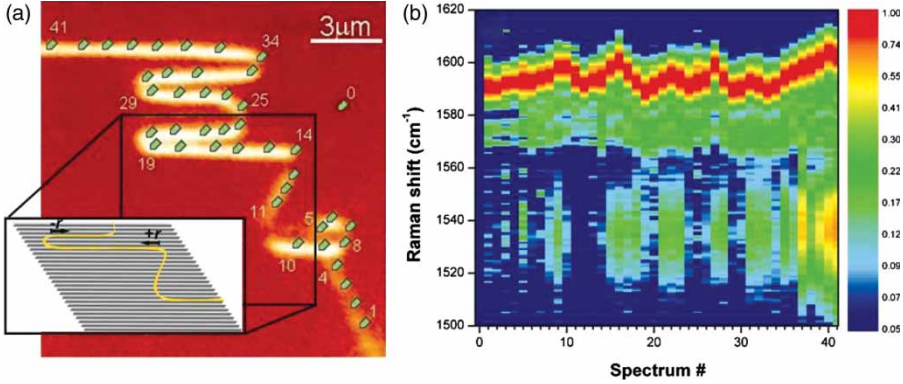


Figure 69. (a) Confocal image of the G-band integrated intensity using a laser wavelength $\lambda_{\text{laser}} = 632.8 \text{ nm}$ ($E_{\text{laser}} = 1.96 \text{ eV}$). The inset shows a schematic view of the SWNT (yellow) lying on top of the miscut quartz. (b) The G-band Raman spectra obtained at the 41 points indicated and numbered in (a). There is a modulation of the higher frequency G^+ feature ($\sim 1590\text{--}1605 \text{ cm}^{-1}$) along with the appearance and disappearance of the lower frequency G^- feature ($\sim 1540 \text{ cm}^{-1}$). This appearance and disappearance of the G^+ and G^- features are related to the tube-substrate morphology and interaction. Adapted with permission from J.S. Soares *et al.*, *Nano Letters* 10, pp. 5043–5048, 2010 [324]. Copyright © (2010) American Chemical Society.

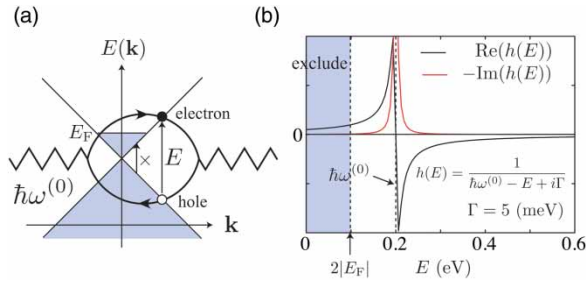


Figure 70. (a) An intermediate e-h pair state that contributes to the energy shift of the optical phonon modes is depicted. A phonon mode is denoted by a zigzag line and an e-h pair is represented by a loop. The low energy e-h pair satisfying $0 \leq E \leq 2|E_F|$ is forbidden at zero temperature by the Pauli principle. (b) The energy correction to the phonon energy by an intermediate e-h pair state, especially the sign of the correction, depends on the energy of the intermediate state as $h(E)$. Adapted figure with permission from K. Sasaki *et al.*, *Physical Review B* 78, pp. 235405–235411, 2008 [365]. Copyright © (2008) by the American Physical Society.

(softening). Thus, when the phonon hardening processes are suppressed by increasing the Fermi energy, we get a large phonon softening and broadening at $2E_F = \pm 0.2 \text{ eV}$. This is the origin of the observed W lineshape [196]. Recent measurements of the G-band spectra at $T = 12 \text{ K}$ show phonon anomalies at $E_F = \pm \hbar\omega_G/2$ that could be clearly distinguished experimentally [200]. Furthermore, the el-ph matrix element for this virtual excitation has a chiral angle dependence that acts differently for iTO and LO phonons [196]. For example, the el-ph interaction for the iTO phonon is absent (no KA effect) for armchair nanotube, while phonon hardening of the iTO mode occurs for zigzag nanotubes. Thus, a detailed analysis of the LO and iTO phonon modes as a function of the Fermi energy gives important information about the (n, m) assignment for metallic carbon nanotubes. For a detailed description of these phenomena, see [193,196,205,246].

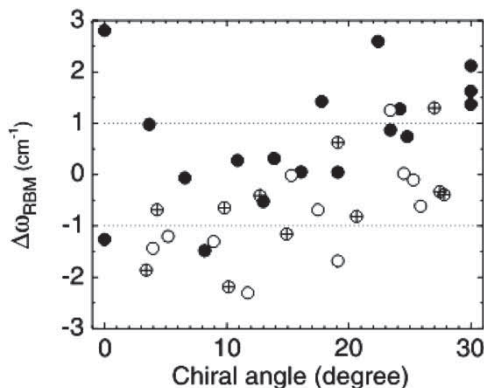


Figure 71. Deviation of the experimentally observed RBM frequency (ω_{RBM}) from the linear dependence given by $(218.3/d_t + 15.9)$, as a function of θ for a particular HiPCO nanotube sample. Filled, open and crossed circles denote M-SWNTs, type I and type II S-SWNTs, respectively. The dotted lines show an experimental accuracy of $\pm 1 \text{ cm}^{-1}$. Reprinted figure with permission from A. Jorio *et al.*, *Physical Review B* 71, p. 75401, 2005 [369]. Copyright © (2005) by the American Physical Society.

5.4.5. RBM band and G-band Kohn anomaly

The diameter dependence of the RBM frequency ω_{RBM} can be described by elasticity theory, as presented in Section 5.1.1. However, there are two effects that are not considered by elasticity theory when discussing the ω_{RBM} , the first related to the chirality-dependent distortion of the lattice, and the second related to the el-ph coupling occurring in metallic SWNTs. The first effect should be observable in SWNTs with $d_t \lesssim 1 \text{ nm}$ SWNTs, where the curvature-induced lattice distortion is important, while the second should be observable in metallic SWNTs.

Figure 71 shows a plot of the deviations of the observed ω_{RBM} values from the best linear $1/d_t$ dependence that fits all the experimental data [$\Delta\omega_{\text{RBM}} = \omega_{\text{RBM}} - (218.3/d_t + 15.9)$] as a function of chiral angle θ , for SWNTs grown by the HiPCO (high pressure CO CVD) method [369]. Deviations of the points from $\Delta\omega_{\text{RBM}} = 0$ are clearly seen, with interesting trends in the deviations: (i) metallic SWNTs (solid bullets) exhibit systematically larger $\Delta\omega_{\text{RBM}}$ when compared with semiconducting SWNTs (open bullets); (ii) $\Delta\omega_{\text{RBM}}$ depends on the chiral angle θ , showing an increase in $\Delta\omega_{\text{RBM}}$ with increasing θ from zigzag (0°) to armchair (30°) SWNTs.

Because of tube curvature, there is sp^2 - sp^3 mixing, and the RBM frequencies decrease with respect to their ideal values as the SWNT diameter decreases [254,370]. In armchair tubes, the circumferential strain is more evenly distributed between the bonds, leading to smaller bond elongations. This is a purely geometric effect, related to the directions of the three C-C bonds with respect to the circumferential direction. Since the RBM softening is directly related to the bond elongation along the nanotube circumference, a larger softening of ω_{RBM} for zigzag tubes relative to armchair tubes is expected, as is shown in Figure 71 [369].

Finally, similar to the effect discussed for the G-band, a phonon frequency shift of the RBM for metallic SWNTs was predicted [193,365] and observed experimentally [204] as a function of the Fermi energy, although a much smaller shift ($\sim 3 \text{ cm}^{-1}$) due to the KA effect is expected for ω_{RBM} than for ω_{G} . Furthermore, in the chiral and zigzag metallic SWNTs, a mini-gap exists and, when the gap is larger than $\hbar\omega_{\text{RBM}}$, then the KA effect disappears. There is a lower limit of d_t (1–1.8 nm depending on chiral angle) below which the KA effect for the RBM phonon cannot be observed, since the mini-gap is proportional to $1/d_t^2$ and $\hbar\omega_{\text{RBM}}$ is proportional to $1/d_t$ [365].

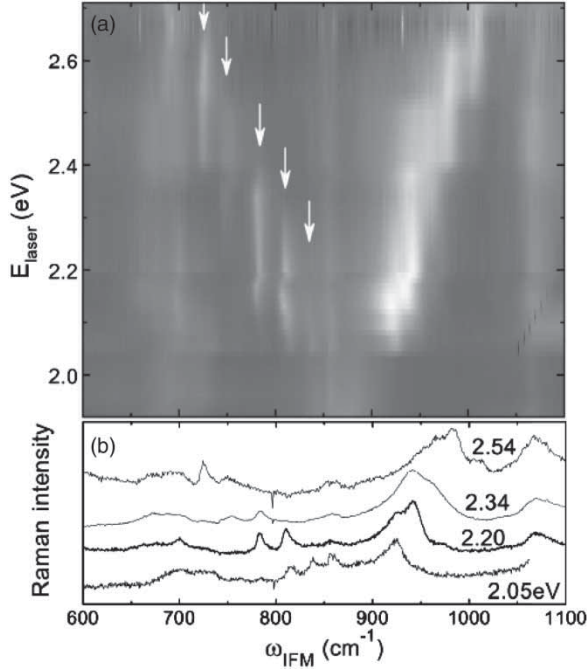


Figure 72. (a) 2D plot of the E_{laser} dependence for the Raman spectra of SWNT bundles in the intermediate frequency mode (IFM) range. The bright, light areas indicate high Raman scattering intensity. Arrows point to five well-defined ω_{IFM} features. (b) Raman spectra in the corresponding IFM range are taken at discrete laser excitation energies $E_{\text{laser}} = 2.05, 2.20, 2.34,$ and 2.54 eV. Reprinted figure with permission from C. Fatini *et al.*, *Physical Review Letters* 93, p. 87401, 2005 [371]. Copyright © (2003) by the American Physical Society.

5.5. Double resonance effect and quantum confinement

Like in graphene, SWNTs exhibit dispersive bands related to the DR effect. However, for SWNTs the Raman signal is dominated by resonance effects associated with van Hove singularities. The vertical stripes in Figure 72(a) define the resonance window for a given resonance band, for a given (n, m) SWNT within a SWNT-bundle sample. The modes appearing in the spectral region between 400 and 1200 cm^{-1} have been named intermediate frequency modes (IFMs), making reference to their frequencies being between the commonly studied RBM and G modes. The IFM features are related to combinations of out-of-plane transverse modes (σTO) and longitudinal acoustic modes (LA), more specifically $\sigma\text{TO} \pm \text{LA}$ [371,372] in the 2D-unfolded graphene system. Up to now, it is not yet clear whether or not these modes are activated by defects. Theory relates the observation of the IFMs to quantum confinement effects along the tube length [373], and some experimental evidence has been found to support such theory [374].

The G' peak [193,310,375] in the Raman spectra for SWNTs, shows a dispersive behavior with laser excitation energy, but some unique characteristics are observed due to the 1D structure of SWNTs. We will detail these results in the next two sections, where in Section 5.5.1 we show the G' behavior for SWNT bundles, and in Section 5.5.2 we discuss the G' -band behaviour in isolated SWNTs.

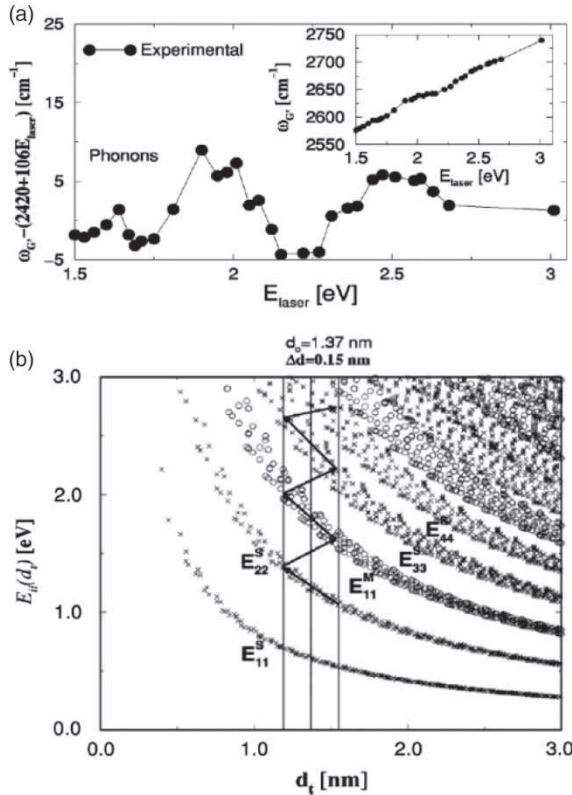


Figure 73. (a) G' -band data for $\omega_{G'}$ for a SWNT bundle sample taken from [222] after subtracting the linear dispersion $2420 + 1106E_{\text{laser}}$ from the $\omega_{G'}$ vs. E_{laser} data shown in the inset. (b) Optical transition energies E_{ij} as a function of diameter for SWNTs. The vertical lines denote the diameter range of the SWNT bundle used in the G' -band dispersion experiment shown in (a). Reprinted figure with permission from A.G. Souza Filho *et al.*, *Physical Review B* 65, p. 35404, 2001 [376]. Copyright © (2001) by the American Physical Society.

5.5.1. The G' -band in SWNT bundles

For SWNT bundles, most of the (n, m) dependent 1D-related effects are averaged out, and a close relation is observed experimentally between the G' -band in SWNTs and in graphene. However, anomalous effects are still observed, and these effects are related to the 1D structure of the material in the nanotube bundle. The inset to Figure 73(a) shows the dispersion of the $\omega_{G'}$ frequency in cm^{-1} in SWNT bundles. Fitting the observed linear dispersion of $\omega_{G'}$ for SWNTs [222] gives

$$\omega_{G'} = 2040 + 106E_{\text{laser}}, \tag{95}$$

which is consistent with observations in graphene and graphite. However, different from graphene and graphite, the G' -band dispersion in SWNTs exhibits a superimposed oscillatory behavior as a function of E_{laser} , as shown in Figure 73(a), where the linear dispersion effect was subtracted from the experimentally observed frequencies. The oscillatory behavior seen in Figure 73(a) is due to the $\omega_{G'}$ dependence on tube diameter, as discussed below.

The G' -band frequency ($\omega_{G'}$) depends on tube diameter (d_t) because of a force constant softening, which is associated with the curvature of the nanotube wall. Experiments on isolated tubes

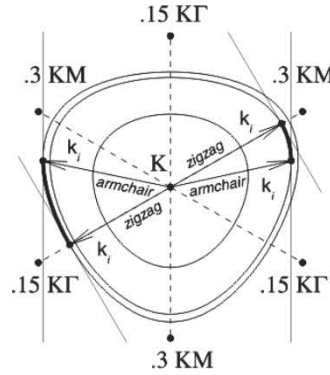


Figure 74. Cutting lines for two metallic SWNTs, one zigzag and one armchair, in the unfolded 2D BZ of graphene. The wavevectors k_i point with arrows to the locations where the van Hove singularities occur. Reprinted figure with permission from G.G. Samsonidze *et al.*, *Physical Review Letters* 90, p. 27403, 2003 [378]. Copyright © (2003) by the American Physical Society.

show that [377]

$$\omega_{G'} = \omega_{G'_0} - \frac{35.4}{d_t}, \tag{96}$$

where $\omega_{G'_0}$ is the laser energy-dependent value observed in graphene, which can be considered to be the limiting value of $\omega_{G'}$ for an infinite diameter tube. This diameter dependence of $\omega_{G'}$ is the critical factor behind the oscillatory behavior observed in Figure 73(a). The vertical lines in Figure 73(b) denote the diameter range of the SWNTs contained in the SWNT bundle used in the G' -band dispersion experiment illustrated in Figure 73. When moving along an arrow by increasing the excitation laser energy, for example, within the E_{22}^S subband by changing the E_{laser} value, just above 1 eV, different SWNTs with different diameters enter and leave the resonance window for a given E_{ii} optical transition. By increasing the laser energy, the diameters of the tubes that are in resonance decrease, thus increasing the expected energy due to the DR process. When the resonance condition with E_{laser} jumps from one interband transition to another, e.g., from E_{22}^S to E_{11}^M , which occurs at around $E_{laser} = 1.5$ eV, the nanotube diameter jumps to higher values. This process modulates the $\omega_{G'}$ dispersion, as observed by the oscillatory behavior shown in Figure 73(a).

The “continuous” frequency dispersion observed in Figure 73(b) is a result observed in SWNT bundles where different tubes enter and leave resonance, thus probing the whole unfolded 2D BZ. This result is clearer for the IFMs as shown in Figure 72. The 1D confinement effects on the G' spectra can only be clearly seen in experiments at the individual isolated SWNT level, discussed further in Section 5.5.2.

5.5.2. *The (n, m) dependence of the G'-band; phonon trigonal warping*

This section gives an appreciation of the effect of 1D confinement on the G' feature in SWNTs at the individual SWNT level. In the case of SWNTs, the resonance condition is restricted to $E_{laser} \approx E_{ii}, E_{ii} \pm E_{ph}$ (the resonant transition energy between van Hove singular energies). This fact gives rise to a $\omega_{G'}$ dependence on the SWNT diameter (see Section 5.5.1) and on the chiral angle.

Figure 74 shows the cutting lines for two metallic SWNTs, one zigzag and one armchair, in the unfolded 2D BZ of graphene. The van Hove singularities occur where a cutting line is tangent to

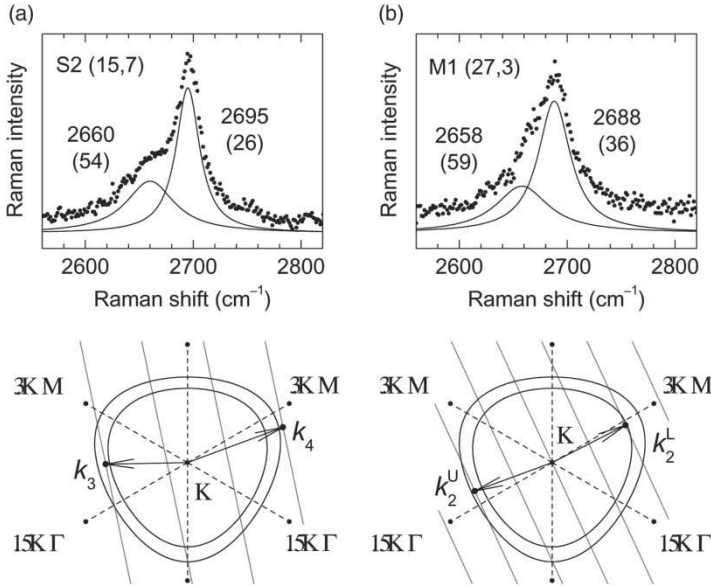


Figure 75. The G' -band Raman spectra for (a) a semiconducting (15, 7) and (b) a metallic (27, 3) SWNT, showing two-peak structures [375,378,379], respectively. The vicinity of the K point in the unfolded BZ is shown in the lower part of the figure, where the equi-energy contours for the incident $E_{\text{laser}} = 2.41$ eV and the scattered $E_{\text{laser}} - E_{G'} = 2.08$ eV photons, together with the cutting lines and wave vectors for the resonant van Hove singularities ($E_{33}^S = 2.19$ eV, $E_{44}^S = 2.51$ eV, $E_{22}^{M(L)} = 2.04$ eV, $E_{22}^{M(U)} = 2.31$ eV) are shown. Reprinted figures from A.G. Souza Filho *et al.*, *Physical Review B* 65, p. 85417, 2002 [375]. Copyright © (2002) by the American Physical Society and A.G. Souza Filho *et al.*, *Chemical Physics Letters* 354, pp. 62–68, Copyright © (2002) with permission from Elsevier.

an equi-energy contour, thus causing a chiral angle dependence on the k_i value where a particular excited state k_i occurs. The states at k_i are those responsible for the dominant optical spectra observed in SWNTs, including the DR features. The presence of cutting lines in carbon nanotubes is expected to affect all the dispersive Raman features [376], but here we focus on the G' -band, because the G' -band dispersion is very large and is an interesting effect.

The two-peak G' -band Raman features in the Raman spectra observed from semiconducting and metallic isolated nanotubes are shown in Figure 75(a) and (b), respectively. The presence of two peaks in the G' -band Raman feature indicates the resonance with both the incident E_{laser} and scattered $E_{\text{laser}} - E_{G'}$ photons, respectively, with two different van Hove singularities (VHSs) for the same nanotube. E_{laser} and $E_{\text{laser}} - E_{G'}$ are defined in Figure 75(a) and (b) below the G' -band spectra, by the outer and inner equi-energy contours near the 2D BZ boundary, in which the cutting lines are shown and the trigonal warping of these constant energy contours can be seen [380]. The two peaks in Figure 75(a) and (b) can be associated with the phonon modes of the wave vectors $\vec{q}_i = -2\vec{k}_i$, where $i = 3, 4, 2L, 2U$ relate to $E_{33}^S, E_{44}^S, E_{22}^{ML}$ and E_{22}^{MU} , respectively, and the electronic wave vectors \vec{k}_i are shown in the lower part of Figure 75. For the semiconducting SWNT shown in Figure 75(a), the resonant wave vectors \vec{k}_3 and \vec{k}_4 have different magnitudes, $k_4 - k_3 \simeq K_1/3$, resulting in twice the difference for the phonon wave vectors, $q_4 - q_3 \simeq 2K_1/3 = 4d_t/3$, so that the splitting of the G' -band Raman feature arises from the *phonon dispersion* $\omega_{\text{ph}}(q)$ around the K point. In contrast, for the metallic nanotube (M-SWNT) shown in Figure 75(b), the resonant wave vectors \vec{k}_2^L and \vec{k}_2^U have roughly equal magnitudes and opposite directions away from the K

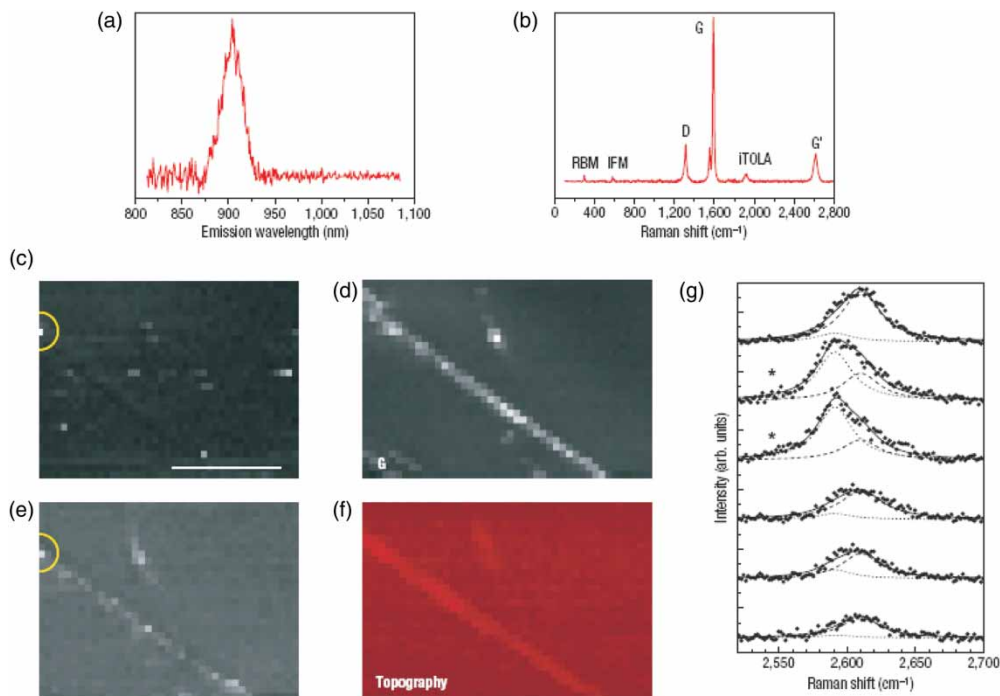


Figure 76. Localized excitonic emission in a semiconducting SWNT. (a) Photoluminescence emission at $\lambda_{\text{em}} = 900$ nm from a single SWNT. (b) Raman spectrum recorded from the same SWNT. The spectral position of the RBM, $\omega_{\text{RBM}} = 302$ cm^{-1} , together with the $\lambda_{\text{em}} = 900$ nm information, leads to the (9,1) assignment for this tube. (c) Near-field photoluminescence image of the SWNT revealing localized excitonic emission. (d)–(e) Near-field Raman imaging of the same SWNT, where the image contrast is provided by spectral integration over the G and D bands, respectively. (f) Corresponding topography image. The circles indicate localized photoluminescence (c) and defect-induced (D band) Raman scattering (e). The scale bar in (c) denotes 250 nm. (g) Evolution of the G'-band spectra near the defective segment of the (9,1) SWNT. The spectra were taken in steps of 25 nm along the nanotube, showing the defect-induced G' peak (dotted Lorentzian). The asterisks denote the spatial locations where localized photoluminescence and defect-induced D-band Raman scattering were measured (see circles in (c) and (e), respectively). Reprinted with permission from I.O. Maciel *et al.*, *Nature Materials* 7, pp. 878–883, 2008 [293]. Copyright © (2008) American Institute of Physics.

point, so that the splitting of the G'-band Raman feature for metallic nanotubes arises from the *anisotropy* of the phonon dispersion $\omega_{\text{ph}}(q)$ around the *K* point [378], which we identify with the phonon trigonal warping effect. Overall, the presence of two peaks in the DR Raman features of isolated carbon nanotubes is associated with quantum confinement effects expressed in terms of cutting lines.

Of course the G'-band is not the only feature to exhibit an (n, m) dependence for SWNT systems. Actually, all the DR features are expected to exhibit such a chirality dependence. The stronger the dispersive behavior, the larger is the (n, m) chirality dependence. For this reason, SWNTs with smaller d_t show larger frequency splittings and larger G'-band shift effects. The (n, m) dependence of other combination modes, such as the iTO+LA combination mode near the Γ point, have also been studied in some detail (see e.g. Ref. [227]).

5.6. Near-field Raman spectroscopy

The near-field technique can generate optical information with spatial resolution Δx below the diffraction limit ($\Delta x \sim \lambda_{\text{laser}}/2$) [381,382]. The near-field Raman spectroscopy and imaging of individual isolated SWNTs with a record spatial resolution of 25 nm was first measured by Hartschuh *et al.* [382]. In sequence, this group performed several studies of local variations in the Raman spectrum along a single SWNT [45]. Figure 76 shows near-field spectra and imaging for an individual SWNT [293]. In particular, Figure 76(a) and (b) show the photoluminescence and Raman spectra, respectively, with $\Delta x \sim 30$ nm. The near-field microscopy maps from the same SWNT are shown in Figure 76(c)–(f). Figure 76(c) represents the near-field photoluminescence image of this same SWNT, where the image contrast is provided by spectral integration over the photoluminescence peak centered at $\lambda_{\text{em}} = 900$ nm (see Figure 76(a)). The most striking feature in this image is the high degree of spatial localization of the photoluminescence emission along the SWNT. This is evident by inspection of the extended topography image of the nanotube shown in Figure 76(f), and also of the near-field Raman image of the G-band, with a peak intensity near 1590 cm^{-1} shown in Figure 76(d). While from Figure 76(d) we observe that the G band Raman scattering is present along the entire length of the nanotube, from Figure 76(e) we observe an increased defect-induced D band occurring at 1300 cm^{-1}). The strong Raman scattering intensity appears to be localized in the *same* spectral region where exciton emission (i.e., exciton emission), thereby providing insights into the correlations observed between Figure 76(c) and (a).

Interestingly, when measuring the Raman spectra across the defective spot, sudden changes in many Raman features are observed. Maciel *et al.* [293] have shown that substitutional doping in SWNTs causes changes in the G'-band spectra due to charge-induced renormalization of the electronic and vibrational energies. Figure 76(g) shows six G'-band spectra measured on the same SWNT, and these spectra were taken by moving along the SWNT to the position where the local D band and photoluminescence emission is observed (circle in Figure 76(e)). The two spectra marked by “*” in Figure 76(g) were obtained at this defect location, and a new peak is here observed in the G'-band. The frequency and intensity of this new peak depend on the dopant species and the level of doping, respectively [383–385]. This makes the G'-band a sensitive probe for studying and quantifying doping, which is more accurate than the D band, since the D-band can also be related to amorphous carbon and to any other symmetry-breaking defective sp^2 structure [193,293,383–385]. Tip-enhanced Raman spectra can show changes in chirality along a given tube [388], due to a large increase in the local signal intensity [389].

6. Challenges of Raman spectroscopy in graphene and carbon nanotubes

We identify in this concluding section current research opportunities where graphene and carbon nanotubes can have special impact. New research areas can be related to new structures, such as nanoribbons, and also to still poorly developed but promising experimental techniques. For example, near-field and time-dependent phenomena have thus far received little attention and show promise for future in-depth development. All these developments have been the basis for the nanometrology field, which is at an early stage of development, and carbon nanotubes have been a focal point for nanometrological protocol development. Although much progress has been made in the use of Raman spectroscopy to study graphene and carbon nanotubes, many research opportunities remain, especially in the applications area. In identifying future directions we look for both novelty and areas of special opportunity, as discussed below.

6.1. *The novelties of graphene*

As already pointed out in this article, graphene appears as the simplest prototype material for solid state physics, let alone the simplest in the family of sp^2 carbons. We still expect a lot more to come with the advance of all kinds of technologies for processing multi-layer graphene samples with different stacking orders, and for generating new kinds of ribbons, edges and defects in general. Here, the technology for producing new kinds of samples is the key issue.

When thinking about the future of graphene nanoribbons, we can now give attention to the past developments of the nanotube field. The great rush into carbon nanotube photophysics arrived when nanotubes with diameters close to 1 nm in diameter and smaller were first produced. Lots of interesting many-body and quantum confinement effects could then be studied in depth, while for larger diameter nanotubes such effects were not so evident. The new physics learned here was then extended to larger diameter tubes. A 1 nm diameter nanotube corresponds to a nanoribbon of about 3–4 nm in width. Since this size is still very small for present technology, we can expect, by analogy, that the most interesting effects are yet to come from nanoribbons smaller than 10 nm in width.

Of course this is not considering edges, which are very interesting by themselves. New and important physics and chemistry related to edges may also come, and these are also dependent on developing more control over the geometry and quality of the edges. For example, the scattering at the edge becomes very important for optics and spin (or charge) transport. Progress has been made, but not enough to lay a strong foundation for the full development of this new research area.

The study of defects in general is a very open field that might generate important new results, both from the study of isolated defects using Raman spectroscopy, as well as through the use of multiple characterization tools that complement Raman spectroscopy. No one has ever measured the characteristic spectral response from a single 7-5-5-7 defect, or from a single vacancy, or even a double vacancy, etc. It is only recently that L_ϕ , the spatial extent of a point-defect induced Raman scattering process ($L_\phi \sim 2$ nm), was measured as is discussed in Section 4.3.3. Furthermore, L_ϕ is expected to exhibit an important dependence on sample temperature. The study of Raman spectroscopy in the transition from a low defect concentration to a high defect concentration may provide important information on the transition from weak to strong localization. These topics are mainly largely discussed for disordered materials, thus providing experimental information for the development of theories linking these limits in 2D materials to studies in few-layer graphene. Defect physics is certainly one of the most open solid state physics sub-fields and this topic can profit greatly from studies made on nearly perfect and highly controlled 2D graphene systems.

However, the rush into studying graphene is not only because it is a prototype material, but also because of the many fundamental connections that physicists see between graphene and fundamental physics. Regarding graphene transport, the Raman effect probes electrons too far from the Fermi level, thus losing out on the most interesting special properties of the massless electrons very close to the Dirac point [61]. However, recent Raman measurements have probed the low-energy excitation states near the Dirac point by studying phonon softening phenomena (Section 5.4) or electronic Raman spectra [206]. As we develop probes that come closer to the Dirac point, we expect that new physics will emerge [62,72,76–82]. For example, the Klein paradox generates a 100% probability for electron tunneling when there is an electron wavefunction matching that for the hole inside an energy barrier. Due to this property, it was shown that one can modulate the electron velocity by generating a periodic potential in graphene [390]. Such an anisotropy in the electron speed could generate measurable shifts in the G' -band frequency, and then Raman spectroscopy could be used to easily quantify aspects of the Klein paradox [76,77,81].

Finally, while many new interesting applications for Raman spectroscopy on graphene will certainly come from the preparation of new related samples, there is still room for the development

of our basic knowledge. For example, our understanding related to the intensity of the DR features is marginal. Also, there is still controversy about the assignment of the 2450 cm^{-1} peak, basically because different DR features fall at this frequency, and it is not clear which of them is responsible for the peak. Of course, the relative intensity for the features related to defects depend on the number of defects. However, the relative intensity of the DR features (even those unrelated to defects) change from sample to sample. Graphene, as the prototype material, may shed light into this and other basic issues related to inelastic light scattering.

6.2. The novelties of carbon nanotubes

The Raman spectroscopy study of carbon nanotubes and their photophysics, in general, is much more mature than for graphene, and the well-established physics and experimental techniques for nanotubes have been directly applied to study graphene. In a general sense, carbon nanotubes are much more complex than graphene and thus more rich information about solid-state properties can be obtained as a function of the nanotube structure. Though carbon nanotubes have been studied intensively in the past decade, many open issues still remain. For example, very few works have focused on the spectroscopy of carbon nanotube ends, junctions or defect sites even though such spectra can easily be obtained. Double-wall carbon nanotubes are another class of carbon nanotubes that are extremely rich and have until now only been briefly studied, and triple-wall nanotubes have hardly been studied at all. The interlayer interactions in nanotubes are not so well established as in graphene. One advantage of studying nanotubes is that they have a well-defined structure, specified by two integers (n, m) , and that nanotubes have no edge structure except for the ends of a SWNT. Using this advantage, the Raman characterization of SWNTs as a function of (n, m) will provide a family of standards for SWNTs. To establish a worldwide standard should be an important issue for the future large scale use of SWNTs in practical applications.

As a more focused example, despite decades of studies, the many-peak structure of the Raman G-band is still full of effects that are not yet well understood and effects related to doping and strain are only now being studied intensively. Furthermore, the behavior of the G-band spectra upon variation of the excitation light resonance condition is still an open issue.

Carbon nanotubes are also very interesting objects for nano electro-mechanical systems (NEMS) because of their strength and stability. Using their strong optical response at the isolated nanotube level and the very high frequency of the LO and iTO modes, SWNTs can be used as very sensitive probes for electronic and structural changes in NEMS. In this sense, carbon nanotubes have already become a prototype material for the development of nanometrology. The importance of carbon nanotubes for applications is already a well-established goal [20], and here Raman spectroscopy could play a very important role as a characterization tool of the changes to the SWNT caused by external perturbations, due to the high degree of accuracy of Raman spectroscopy as a characterization tool along with the relative simplicity of its use for the characterization of carbon nanotube-based materials as a non-contact, non-destructive, room temperature measurement.

The development of standard materials based on carbon nanotubes would be of extreme importance, not only for applications, but also to establish a sensitive probe of various types of SWNT environments. The National Institute of Standards of Technology (NIST, USA) has already developed a round robin program for the measurements of the (n, m) content in a SWNT sample based on the CoMoCAT material [391]. The water-assisted CVD-grown carbon nanotubes (called “super-growth” tubes in the literature [316]) exhibit some results based on their Raman spectra which indicate that this is a special material that is closest to what is expected from a pristine SWNT (isolated from any environmental effect). These special properties are: (1) the special relation between its ω_{RBM} and tube diameter, (2) the highest measured energy for its optical transitions,

and (3) the observation of previously elusive transitions from metallic nanotubes [230]. However, it is not yet clear why this sample is special. Clarifying such a result could help in developing an effective standard reference material in the graphene area.

6.3. *Near-field Raman spectroscopy and microscopy*

The fiber-probe-based near-field systems have the potential for high spatial resolution (50–100 nm) and for the observation of photophysical phenomena in nanostructures. These systems thus far have been largely utilized for luminescence studies, but have hardly given any results on Raman spectroscopy. The near-field Raman spectroscopy and microscopy based on the tip-enhanced Raman scattering (TERS) effect first appeared in 2003 and this work had a strong impact on the photophysics field with the earliest TERS measurements on carbon nanotubes [381,382], and finally achieved a record spatial resolution of 12 nm [45]. However, the instrumentation behind this technique is still very complicated and the developments that have been achieved thus far are still carried out by very few groups in the world. Some companies are starting to produce and sell TERS systems, but the reliability of these systems is not yet in place. Once this technique becomes routine, there is no doubt about its importance to the future development of the Raman spectroscopy field as applied to nano-science. The study of subjects such as isolated defects and edges using TERS is expected to achieve a new paradigm in the near future, which will advance both science and technology.

6.4. *Time-dependent Raman and coherent phonon spectroscopy*

As pointed out in Section 2.3.6, the Fourier transformation of CP vibrations gives a spectrum that is similar to ordinary Raman spectra. It is important to note that CP spectroscopy is not just an alternative tool to Raman spectroscopy, but it is a special tool in its own right that allows observation of the phase of the vibration by which the information about the adiabatic potential for the excited states can be obtained. For example, the RBM vibration starts by opening or closing the nanotube diameter depending of the type (Type I or Type II) of semiconducting SWNTs under investigation [165]. Further, by using pulse-shaping techniques in which the frequency of the repeated laser pulse can be matched to the RBM frequency of a particular SWNT, the CP spectra only for the SWNT can be obtained among the several resonant nanotubes matched to E_{laser} .

The fast response of the transport properties in graphene is now operating in the 100 GHz range [392]. Soon this frequency will become similar to the sp^2 carbon phonon vibration frequency (47 THz for the G-band). In the near future, we may be able to directly observe each physical process contributing to the el-ph interaction and this will help us identify the energy-transfer mechanism in these optical processes. The development of attosecond lasers might bring time-dependent Raman spectroscopy to the level of this newly opened field in which specific electron-electron interactions can also be observed as a function of time.

6.5. *Conclusion and messages for the future*

The developments of Raman spectroscopy as applied to carbon nanotubes and graphene in the past decade has been truly impressive. To demonstrate this, one could develop an interesting set of lectures for a course in solid-state physics by just addressing the Raman spectroscopy on sp^2 carbon systems [1]. The level of information and details that have become available has allowed the development of a very accurate theory to describe the behavior of electrons and phonons in these systems. In this process, Raman spectroscopy has become a widely used tool for the characterization of nanomaterials. This may be the beginning of a new era where information about many-body effects and complex systems will start to be obtained with much better accuracies for

the development of new theories to explain the newly found effects. Raman spectroscopy thus helps the development of nanotechnology in its most basic sense, and allows study of physical processes that are expected to occur at the nanometer level. In following the words of Professor Richard Feynman in his lecture on 29 December 1959, that there is plenty of room for discovery at the bottom, below 10 nm spatial resolution, below 1 meV energy resolution and below 10 fs time resolution, and for the operation of materials at more than 1 THz frequency, 1000 T magnetic field, and 1 TPa pressure.

Acknowledgements

The MIT authors acknowledge the support under NSF Grant DMR 10-04147. A.J. acknowledges the financial support from the Brazilian agencies CNPq, CAPES and FAPEMIG. R.S. acknowledges a Grant-in-Aid (No. 20241023) from the MEXT, Japan. We would like to thank the referee for his/her suggestions which improved the quality of this publication.

For all figures reprinted from American Physical Society material readers may view, browse, and/or download material for temporary copying purposes only, provided these uses are for non-commercial personal purposes. Except as provided by law, this material may not be further reproduced, distributed, transmitted, modified, adapted, performed, displayed, published, or sold in whole or part, without prior written permission from the American Physical Society.

Notes

1. The B atom in Figure 1 gives a brighter STM images than the A atom, since there are electronic energy bands for the B atom near the Fermi energy.
2. The G' peak in the Raman spectra of sp^2 carbons is often called the 2D peak. It should be noted that the mechanisms involved in the 2D double resonance (DR) processes are different from those for the G' peak which involves only two phonons. The G' peak involves only two K point phonons, whereas the 2D feature arises from the second-order D that includes a DR D-band process involving a K point phonon and an elastic scattering process. In this review, we distinguish between the G' and the 2D scattering process and the actual values of their frequencies.
3. A Stokes process is a terminology used to denote the loss of photon energy in a scattering process. Here the Stokes photoluminescence process is independent of the Stokes Raman process.
4. Time-dependent perturbation theory tells us that the amplitude of the wavefunctions for excited states oscillates as a function of time if the photon energy does not match the excited-state energy, which is the physical meaning of a virtual transition.
5. A notch filter is an optical filter that suppresses a specified range of energies of the incident light.
6. By connecting monochromators in a serial way, the resolution of a monochromator is significantly improved although the actual signal becomes increasingly weak. Furthermore, extra monochromators can be used as an energy-tunable filter to reject the elastically scattered light in contrast to the notch filters, which are wavelength-specific.
7. The solution of a forced damped harmonic oscillator is not generally a Lorentzian lineshape but approaches the Lorentzian function for $\omega_q \gg \Gamma_q$. However, if ω_q approaches Γ_q , the lineshape departs from a Lorentzian function.
8. The designation π of the π band comes from its value of angular momentum which is 1.
9. Here mod denotes an integer function for evaluating the modulus for an (n, m) SWNT where we use the notation $\text{mod}(6, 3) = 0$, $\text{mod}(7, 3) = 1$ and $\text{mod}(8, 3) = 2$ as an illustrative example. Some authors use Mod 1 and Mod 2 to denote a semiconducting nanotube depending on $\text{mod}(n - m, 3) = 1$ or 2. There is thus a one-to-one correspondence between type I (II) and Mod 2 (1) semiconducting nanotubes appearing in the literature, and this is clarified in Figure 11.
10. It should be noted that there is a logarithmic 2D van Hove singularity in the density of states of graphene at the saddle point of the energy band near the M points (center of the hexagonal edges) of the BZ.

11. In time-dependent perturbation theory, the mixing (or transition) of the excited states occurs as a function of time with some finite and often measurable probability. The virtual states are defined by such a linear combination of excited states with some probability. The probability for the occupation of an excited state can be large when the energy difference between the excited states and the energy of the external field is relatively small. In such a case, we can say that the transition is resonant with the excited state.
12. Here “real absorption” means that the photo-excited electron can be in the excited states for a sufficient time, for example, 1 ns, so that the electron can be probed in the excited state. A material can scatter photons in a virtual process.
13. It is noted that not all even (odd) vibration modes under inversion symmetry are Raman (IR)-active modes.
14. The two-phonon process involving one-phonon emission and one-phonon absorption does not contribute to the Raman spectra but rather gives a correction to the effective Rayleigh spectral process.
15. Here q is the real phonon wavevector, measured from the Γ point, while in defining q_{DR} , the k and k' vectors are measured from the K point or alternatively, with respect to the K' point.
16. It is only when crystalline disorder is present that the first-order $q \neq 0$ phonons can be observed, as discussed in Section 4.3.
17. From the matrix element $\vec{\alpha}_p$, we can deduce another matrix element,

$$\begin{aligned}\vec{\beta}_p(\tau) &= \int \phi_\mu(\mathbf{r}) \nabla v(\mathbf{r} - \boldsymbol{\tau}) \phi_\nu(\mathbf{r} - \boldsymbol{\tau}) \, d\mathbf{r} \\ &= \int \phi_\nu(\mathbf{r}) \nabla v(\mathbf{r}) \phi_\mu(\mathbf{r} + \boldsymbol{\tau}) \, d\mathbf{r} = \beta_p(\tau) \hat{I}(\beta_p).\end{aligned}\tag{45a}$$

However, the integral in Equation (45a) can also be expressed by α terms [268].

18. The phonon amplitude is proportional to $A_\nu(\mathbf{q})\sqrt{\tilde{n}_\nu(\mathbf{q})}$ in which the temperature dependence of the amplitude is expressed by $\tilde{n}_\nu(\mathbf{q})$ given by Equation (47).
19. It is noted that the minus sign corresponds to a symmetric wavefunction and that the plus sign corresponds to an anti-symmetric wavefunction.
20. A virtual state is a linear combination of real states. When a virtual state is close to an exciton state, the virtual state contains a large component of the exciton states. This is the reason for the approximation used in obtaining a representation for the virtual state.
21. A cutting line is defined by the 1D BZ of an SWNT in the 2D BZ of graphene [32,135,136].
22. Other formula for ω_{RBM} can be used here, too. The difference is within $1\text{--}3 \text{ cm}^{-1}$.
23. The subscript htt in T_{htt} denotes heat treatment temperature.
24. Here core electrons refer to 1s and σ electrons. The screening by π electrons is independently considered by the polarization function within the RPA (random phase approximation) [120,148]. See Section 5.2.1 for further details.
25. The Bethe–Salpeter equation is independently solved for each value of κ . When we obtain E_{ii} values as a function of κ by solving the Bethe–Salpeter equation many times, then E_{ii} with different i values are adapted from the different κ value. Since the E_{ii} eigenvalues come from different cutting lines, there is no problem with the orthogonality of the wavefunctions.

References

- [1] A. Jorio, R. Saito, G. Dresselhaus, and M.S. Dresselhaus, *Raman Spectroscopy in Graphene Related Systems*, Wiley-VCH Verlag GmbH & Co KGaA, Weinheim, Germany, 2010.
- [2] B.T. Kelly, *Physics of Graphite*, Applied Science Publishers, London and New Jersey, 1981, p. 477.
- [3] M.M. Lucchese, F. Stavale, E.H. Martins Ferreira, C. Vilani, M.V.O. Moutinho, R.B. Capaz, C.A. Achete, and A. Jorio, *Carbon* 48(5) (2010), pp. 1592–1597.
- [4] L.M. Malard, M.H.D. Guimarães, D.L. Mafra, M.S.C. Mazzoni, and A. Jorio, *Phys. Rev. B* 79, (2009) p. 125426.
- [5] L.M. Malard, M.A. Pimenta, G. Dresselhaus, and M.S. Dresselhaus, *Phys. Rep.* 473 (2009), pp. 51–87.
- [6] R.W.G. Wyckoff, *Crystal Structures*, Wiley, 1963. Vol 6.

- [7] K.S. Novoselov, A.K. Geim, S.V. Morozov, D. Jiang, Y. Zhang, S.V. Dubonos, I.V. Grigorieva, and A.A. Firsov, *Science* 306(5696) (2004), p. 666.
- [8] A.K. Geim and A.H. MacDonald, *Phys. Today* 60(35) (2007), p. 35.
- [9] H. Lipson and A.R. Stokes, *Nature* 149(3777) (1942), p. 328.
- [10] A.W. Moore, *Highly Oriented Pyrolytic Graphite*, Vol. 11. Marcel Dekker, New York, 1973.
- [11] J. Heremans, C.H. Olk, G.L. Eesley, J. Steinbeck, and G. Dresselhaus, *Phys. Rev. Lett.* 60 (1988), p. 452.
- [12] A.W. Moore, *Nature* 221(5186) (1969), pp. 1133–1134.
- [13] A.W. Moore, *Chemistry and Physics of Carbon*, Vol. 17. Marcel Dekker, New York, 1981.
- [14] A.W. Moore, A.R. Ubbelohde, and D.A. Young, *Br. J. Appl. Phys.* 13 (1962), p. 393.
- [15] A.R. Ubbelohde, *Carbon* 7(5) (1969), pp. 523–530.
- [16] I.L. Spain, A.R. Ubbelohde, and D.A. Young, *Phil. Trans. R. Soc. London Ser. A, Math. Phys. Sci.* 262(1128) (1967), pp. 345–386.
- [17] R. Bacon, *J. Appl. Phys.* 31(2) (1960), p. 283.
- [18] M. Endo, T. Koyama, and Y. Hishiyama, *Jpn. J. Appl. Phys.* 15 (1976), pp. 2073–2076.
- [19] M.S. Dresselhaus, G. Dresselhaus, and K. Sugihara, *Graphite Fibers and Filaments 5. Springer Series in Materials Science*, Springer, Berlin, 1988.
- [20] M. Endo, M.S. Strano, and P.M. Ajayan, *Carbon Nanotubes: Advanced Topics in the Synthesis, Structure, Properties and Applications*, Vol. 111, Springer, Berlin, 2008.
- [21] A. Jorio, M.S. Dresselhaus, and G. Dresselhaus, *Carbon Nanotubes: Advanced Topics in the Synthesis, Structure, Properties and Applications*, Vol. 111, Springer, Berlin, 2008.
- [22] H.W. Kroto, J.R. Heath, S.C. O'Brien, R.F. Curl, and R.E. Smalley, *Nature* 318(6042) (1985), pp. 162–163.
- [23] M.S. Dresselhaus, G. Dresselhaus, and P.C. Eklund, *Science of Fullerenes and Carbon Nanotubes*, Academic Press, New York, NY/San Diego, CA, 1996.
- [24] S. Iijima, *Nature* 354 (1991), pp. 56–58.
- [25] A. Oberlin, M. Endo, and T. Koyama, *Carbon* 14(2) (1976), pp. 133–135.
- [26] A. Oberlin and T. Endo, *J. Cryst. Growth* 32(3) (1976), pp. 335–349.
- [27] A. Oberlin, *Carbon* 22 (1984), p. 521.
- [28] L.V. Radushkevich and V.M. Lukyanovich, *Zurn Fisic Chim.* 26 (1952), pp. 88–95.
- [29] M. Monthieux and V.L. Kuznetsov, *Carbon* 44 (2006), pp. 1621–1623.
- [30] S. Iijima and T. Ichihashi, *Nature* 363(6430) (1993), pp. 603–605.
- [31] D.S. Bethune, C.H. Klang, M.S. De Vries, G. Gorman, R. Savoy, J. Vazquez, and R. Beyers, *Nature* 363 (1993), p. 605.
- [32] R. Saito, G. Dresselhaus, and M.S. Dresselhaus, *Physical Properties of Carbon Nanotubes*, Imperial College Press, London, 1998. London.
- [33] S. Reich, C. Thomsen, and P. Ordejon, *Elastic Properties and Pressure-induced Phase Transitions of Single-walled Carbon Nanotubes*, Vol. 235, Wiley Online Library, 2003.
- [34] E. Joselevich, H. Dai, J. Liu, K. Hata, and A.H. Windle, *Carbon Nanotubes: Advanced Topics in the Synthesis, Structure, Properties and Applications*, Vol. 111, Springer, Berlin, 2008, pp. 101–164.
- [35] M.S. Arnold, A.A. Green, J.F. Hulvat, S.I. Stupp, and M.C. Hersam, *Nat. Nanotechnol.* 1(1) (2006), pp. 60–65.
- [36] M. Terrones, A.G. Souza Filho, and A.M. Rao, *Carbon Nanotubes: Advanced Topics in the Synthesis, Structure, Properties and Applications*, Vol. 111, Springer, Berlin, 2008, pp. 531–566.
- [37] M. Yudasaka, S. Iijima, and V.H. Crespi, *Carbon Nanotubes: Advanced Topics in the Synthesis, Structure, Properties and Applications*, Vol. 111, Springer, Berlin, 2008, pp. 605–629.
- [38] B.I. Yakobson, *Appl. Phys. Lett.* 72(8) (1998), p. 918.
- [39] C.D. Spataru, S. Ismail-Beigi, R. Capaz, and S.G. Louie, *Carbon Nanotubes: Advanced Topics in the Synthesis, Structure, Properties and Applications*, Vol. 111, Springer, Berlin, 2008, pp. 195–228.
- [40] T. Ando, *Carbon Nanotubes: Advanced Topics in the Synthesis, Structure, Properties and Applications*, Vol. 111, Springer, Berlin, 2008, pp. 229–250.
- [41] R. Saito, C. Fantini, and J. Jiang, *Carbon Nanotubes: Advanced Topics in the Synthesis, Structure, Properties and Applications*, Vol. 111, Springer, Berlin, 2008, pp. 251–286.

- [42] J. Lefebvre, S. Maruyama, and P. Finnie, *Carbon Nanotubes: Advanced Topics in the Synthesis, Structure, Properties and Applications*, Vol. 111, Springer, Berlin, 2008, pp. 287–319.
- [43] Y.-Z. Ma, T. Hertel, Z.V. Vardeny, G.R. Fleming, and L. Valkunas, *Carbon Nanotubes: Advanced Topics in the Synthesis, Structure, Properties and Applications*, Vol. 111, Springer, Berlin, 2008, pp. 321–352.
- [44] T.F. Heinz, *Carbon Nanotubes: Advanced Topics in the Synthesis, Structure, Properties and Applications*, Vol. 111, Springer, Berlin, 2008, pp. 353–369.
- [45] A. Hartschuh, *Carbon Nanotubes: Advanced Topics in the Synthesis, Structure, Properties and Applications*, Vol. 111, Springer, Berlin, 2008, pp. 371–392.
- [46] J. Kono, J.R. Nicholas, and S. Roche, *Carbon Nanotubes: Advanced Topics in the Synthesis, Structure, Properties and Applications*, Vol. 111, Springer, Berlin, 2008, pp. 393–421.
- [47] P. Avouris, M. Freitag, and V. Perebeinos, *Carbon Nanotubes: Advanced Topics in the Synthesis, Structure, Properties and Applications*, Vol. 111, Springer, Berlin, 2008, pp. 423–454.
- [48] J. Wu, W. Walukiewicz, W. Shan, E. Bourret-Courchesne, J.W. Ager III, K.M. Yu, E.E. Haller, K. Kissell, S.M. Bachilo, and R.B. Weisman, *Phys. Rev. Lett.* 93(1) (2004), p. 17404.
- [49] M.S. Biercuk, S. Ilani, and C.M. Marcus, *Carbon Nanotubes: Advanced Topics in the Synthesis, Structure, Properties and Applications*, Vol. 111, Springer, Berlin, 2008, pp. 455–492.
- [50] L. Kavan and L. Dunsch, *Carbon Nanotubes: Advanced Topics in the Synthesis, Structure, Properties and Applications*, Vol. 111, Springer, Berlin, 2008, pp. 567–603.
- [51] M. Kalbac, H. Farhat, L. Kavan, J. Kong, and M.S. Dresselhaus, *Nano Lett.* 8(10) (2008), pp. 3532–3537.
- [52] P.R. Wallace, *Phys. Rev.* 71(9) (1947), pp. 622–634.
- [53] H.P. Boehm, A. Clauss, U. Hofmann, and G.O. Fischer, *Z. Naturforschung B* 17(3) (1962), p. 150.
- [54] A.M. Affoune, B.L.V. Prasad, H. Sato, T. Enoki, Y. Kaburagi, and Y. Hishiyama, *Chem. Phys. Lett.* 348(1–2) (2001), pp. 17–20.
- [55] C. Berger, Z. Song, T. Li, X. Li, A.Y. Ogbazghi, R. Feng, Z. Dai, A.N. Marchenkov, E.H. Conrad, P.N. First, and W.A. de Heer, *J. Phys. Chem. B* 108(52) (2004), pp. 19912–19916.
- [56] T. Enoki, Y. Kobayashi, C. Katsuyama, V.Y. Osipov, M.V. Baidakova, K. Takai, K.I. Fukui, and A.Y. Vul, *Diam. Relat. Mater.* 16(12) (2007), pp. 2029–2034.
- [57] Y. Kobayashi, K. Fukui, T. Enoki, K. Kusakabe, and Y. Kaburagi, *Phys. Rev. B* 71(19) (2005), p. 193406.
- [58] Y. Kobayashi, K. Fukui, T. Enoki, and K. Kusakabe, *Phys. Rev. B* 73(12) (2006), p. 125415.
- [59] L.G. Cancado, M.A. Pimenta, B.R.A. Neves, G. Medeiros-Ribeiro, T. Enoki, Y. Kobayashi, K. Takai, K. Fukui, M.S. Dresselhaus, and R. Saito, *Phys. Rev. Lett.* 93(4) (2004), p. 47403.
- [60] A.K. Geim and K.S. Novoselov, *Nat. Mater.* 6(3) (2007), pp. 183–191.
- [61] A. Castro Neto, F. Guinea, N.M.R. Peres, K.S. Novoselov, and A.K. Geim, *Rev. Mod. Phys.* 81(1) (2009), pp. 109–162.
- [62] M.S. Dresselhaus and P.T. Araujo, *ACS Nano* 4(11) (2010), pp. 6297–6302.
- [63] C. Lee, X. Wei, J.W. Kysar, and J. Hone, *Science* 321(5887) (2008), p. 385.
- [64] A.A. Balandin and O.L. Lazarenkova, *Appl. Phys. Lett.* 82 (2003), p. 415.
- [65] D. Teweldebrhan and A.A. Balandin, *Appl. Phys. Lett.* 94 (2009), p. 13101.
- [66] K.I. Bolotin, K.J. Sikes, Z. Jiang, M. Klima, G. Fudenberg, J. Hone, P. Kim, and H.L. Stormer, *Solid State Commun.* 146(9–10) (2008), pp. 351–355.
- [67] S. Morozov, K. Novoselov, M. Katsnelson, F. Schedin, D. Elias, J. Jaszczak, and A. Geim, *Phys. Rev. Lett.* 100(1) (2008), p. 16602.
- [68] B. Lee, Y. Chen, F. Duerr, D. Mastrogiovanni, E. Garfunkel, E.Y. Andrei, and V. Podzorov, *Nano Lett.* 10 (2010), pp. 1407–1433.
- [69] X. Du, I. Skachko, A. Barker, and E.Y. Andrei, *Nat. Nanotechnol.* 3(8) (2008), pp. 491–495.
- [70] G. Li and E.Y. Andrei, *Nat. Phys.* 3 (2007), p. 623.
- [71] X. Du, I. Skachko, F. Duerr, A. Luican, and E.Y. Andrei, *Nature* 462 (2009), pp. 192–195.
- [72] K.S. Novoselov, A.K. Geim, S.V. Morozov, D. Jiang, M.I. Katsnelson, I.V. Grigorieva, S.V. Dubonos, and A.A. Firsov, *Nature* 438(7065) (2005), pp. 197–200.
- [73] K.S. Novoselov, E. McCann, S.V. Morozov, V.I. Fal’ko, M.I. Katsnelson, U. Zeitler, D. Jiang, F. Schedin, and A.K. Geim, *Nat. Phys.* 2(3) (2006), pp. 177–180.

- [74] R.R. Nair, P. Blake, A.N. Grigorenko, K.S. Novoselov, T.J. Booth, T. Stauber, N.M.R. Peres, and A.K. Geim, *Science (New York)* 320(5881) (2008), p. 1308.
- [75] A.F. Young and P. Kim, *Nat. Phys.* 5(3) (2009), pp. 222–226.
- [76] C.W.J. Beenakker, *Rev. Mod. Phys.* 80(4) (2008), pp. 1337–1354.
- [77] M.I. Katsnelson, K.S. Novoselov, and A.K. Geim, *Nat. Phys.* 2(9) (2006), pp. 620–625.
- [78] V.V. Cheianov, V. Fal'ko, and B.L. Altshuler, *Science* 315(5816) (2007), pp. 1252–1255.
- [79] J.M. Pereira Jr., V. Mlinar, F.M. Peeters, and P. Vasilopoulos, *Phys. Rev. B* 74(4) (2006), p. 45424.
- [80] V. Cheianov and V. Fal'ko, *Phys. Rev. B* 74(4) (2006), p. 041403.
- [81] C.W.J. Beenakker, *Phys. Rev. Lett.* 97(6) (2006), p. 67007.
- [82] F. Miao, S. Wijeratne, Y. Zhang, U.C. Coskun, W. Bao, and C.N. Lau, *Science* 317(5844) (2007), pp. 1530–1533.
- [83] A. Ossipov, M. Titov, and C. Beenakker, *Phys. Rev. B* 75(24) (2007), p. 241401.
- [84] C. Beenakker, A. Akhmerov, P. Recher, and J. Tworzydło, *Phys. Rev. B* 77(7) (2008), p. 075409.
- [85] T. Pedersen, C. Flindt, J. Pedersen, N. Mortensen, A.-P. Jauho, and K. Pedersen, *Phys. Rev. Lett.* 100(13) (2008), p. 136804.
- [86] J.S. Park, K. Sasaki, R. Saito, W. Izumida, M. Kalbac, H. Farhat, G. Dresselhaus, and M.S. Dresselhaus, *Phys. Rev. B* 80(8) (2009), p. 81402.
- [87] D.C. Elias, R.R. Nair, T.M.G. Mohiuddin, S.V. Morozov, P. Blake, M.P. Halsall, A.C. Ferrari, D.W. Boukhvalov, M.I. Katsnelson, and A.K. Geim, *Science* 323(5914) (2009), p. 610.
- [88] A.K. Geim, *Science (New York)* 324(5934) (2009), pp. 1530–1534.
- [89] C. Berger, Z. Song, X. Li, X. Wu, N. Brown, C. Naud, D. Mayou, T. Li, J. Hass, A.N. Marchenkov, E.H. Conrad, P.N. First, and W.A. de Heer, *Electronic confinement and coherence in patterned epitaxial graphene*, *Science* 312, 1191–1196 (2006).
- [90] X. Li, X. Wang, L. Zhang, S. Lee, and H. Dai, *Science* 319(5867) (2008), p. 1229.
- [91] X. Yang, X. Dou, A. Rouhanipour, L. Zhi, H.J. Räder, and K. Müllen, *J. Am. Chem. Soc.* 130(13) (2008), pp. 4216–4217.
- [92] D.V. Kosynkin, A.L. Higginbotham, A. Sinitskii, J.R. Lomeda, A. Dimiev, B.K. Price, and J.M. Tour, *Nature* 458(7240) (2009), pp. 872–876.
- [93] L. Jiao, L. Zhang, X. Wang, G. Diankov, and H. Dai, *Nature* 458(7240) (2009), pp. 877–880.
- [94] X. Jia, M. Hofmann, V. Meunier, B.G. Sumpter, J. Campos-Delgado, J.M. Romo-Herrera, H. Son, Y.-P. Hsieh, A. Reina, J. Kong, M. Terrones, and M.S. Dresselhaus, *Science* 323 (2009), pp. 1701–1705.
- [95] M. Cardona, in *Light Scattering in Solids II*, M. Cardona and G. Güntherodt, eds., Vol. 50, Springer, Berlin, 1982, pp. 19–176.
- [96] M.S. Dresselhaus, A. Jorio, M. Hofmann, G. Dresselhaus, and R. Saito, *Nano Lett.* 10 (2010), pp. 953–973.
- [97] A.C. Ferrari, Raman spectroscopy of graphene and graphite: disorder, electron–phonon coupling, doping and nonadiabatic effects, July 2007. *Solid State Communications*, 143 (2007), pp. 47–57.
- [98] D. Haberer, D.V. Vyalikh, S. Taioli, B. Dora, M. Farjam, J. Fink, D. Marchenko, T. Pichler, K. Ziegler, S. Simonucci, M.S. Dresselhaus, M. Knupfer, B. Büchner, and A. Grüneis, *Nano Lett.* 10 (2010), pp. 3360–3366.
- [99] M.S. Dresselhaus, G. Dresselhaus, and R. Saito, *Phys. Rev. B* 45(11) (1992), pp. 6234–6242.
- [100] R. Saito, T. Takeya, T. Kimura, G. Dresselhaus, and M.S. Dresselhaus, *Phys. Rev. B* 57(7) (1998), pp. 4145–4153.
- [101] E.B. Barros, N. Demir, A.G. Souza Filho, J. Mendes Filho, A. Jorio, G. Dresselhaus, and M.S. Dresselhaus, *Phys. Rev. B* 71(16), 2005.
- [102] F. Tuinstra and J.L. Koenig, *J. Chem. Phys.* 53(3) (1970), p. 1126.
- [103] A.M. Rao, E. Richter, S. Bandow, B. Chase, P.C. Eklund, K.A. Williams, S. Fang, K.R. Subbaswamy, M. Menon, A. Thess, R.E. Smalley, G. Dresselhaus, and M.S. Dresselhaus, *Science* 275(5297) (1997), pp. 187–191.
- [104] C. Thomsen and S. Reich, *Phys. Rev. Lett.* 85(24) (2000), pp. 5214–5217.
- [105] L. Alvarez, A. Righi, T. Guillard, S. Rols, E. Anglaret, D. Laplaze, and J.L. Sauvajol, *Chem. Phys. Lett.* 316(3–4) (2000), pp. 186–190.

- [106] H. Kuzmany, W. Plank, M. Hulman, Ch. Kramberger, A. Grüneis, Th. Pichler, H. Peterlik, H. Kataura, and Y. Achiba, *Eur. Phys. J. B* 22(3) (2001), pp. 307–320.
- [107] H. Telg, J. Maultzsch, S. Reich, F. Hennrich, and C. Thomsen, *Phys. Rev. Lett.* 93 (2004), p. 177401.
- [108] J. Meyer, M. Paillet, T. Michel, A. Moréac, A. Neumann, G. Duesberg, S. Roth, and J.-L. Sauvajol, *Phys. Rev. Lett.* 95(21) (2005), p. 217401.
- [109] M. Milnera, J. Kürti, M. Hulman, and H. Kuzmany, *Phys. Rev. Lett.* 84(6) (2000), pp. 1324–1327.
- [110] S. Lefrant, J.P. Buisson, J. Schreiber, O. Chauvet, M. Baibarac, and I. Baltog, *Synth. Met.* 139(3) (2003), pp. 783–785.
- [111] A. Jorio, R. Saito, J. Hafner, C. Lieber, M. Hunter, T. McClure, G. Dresselhaus, and M.S. Dresselhaus, *Phys. Rev. Lett.* 86(6) (2001), pp. 1118–1121.
- [112] A.C. Ferrari, J. Meyer, V. Scardaci, C. Casiraghi, M. Lazzeri, F. Mauri, S. Piscanec, D. Jiang, K. Novoselov, S. Roth, and A. Geim, *Phys. Rev. Lett.* 97(18) (2006), p. 187401.
- [113] D. Graf, F. Molitor, K. Ensslin, C. Stampfer, A. Jungen, C. Hierold, and L. Wirtz, *Nano Lett.* 7(2) (2007), pp. 238–242.
- [114] A. Gupta, G. Chen, P. Joshi, S. Tadigadapa, and P.C. Eklund, *Nano Lett.* 6(12) (2006), pp. 2667–2673.
- [115] K. Sasaki, R. Saito, M.S. Dresselhaus, K. Wakabayashi, T. Enoki, *New J. Phys.* 12 (2010), p. 103015.
- [116] C.V. Raman and K.S. Krishnan, *Nature* 121(3048) (1928), p. 501.
- [117] G. Landsberg and L. Mandelstam, *Naturwissenschaften* 16 (1928), pp. 772–772.
- [118] F. Bassani, G. Pastori Parravicini, and R.A. Ballinger, *Electronic States and Optical Transitions in Solids*, Pergamon Press, New York, 1975.
- [119] N.W. Ashcroft and N.D. Mermin, *Solid State Physics*, Holt, Rinehart and Winston, New York, 1976.
- [120] T. Ando, *J. Phys. Soc. Jpn.* 66(4) (1997), pp. 1066–1073.
- [121] F. Wang, G. Dukovic, L.E. Brus, and T.F. Heinz, *Science* 308(5723) (2005), p. 838.
- [122] J. Maultzsch, R. Pomraenke, S. Reich, E. Chang, D. Prezzi, A. Ruini, E. Molinari, M.S. Strano, C. Thomsen, and C. Lienau, *Phys. Rev. B* 72(24) (2005), p. 241402.
- [123] S.Y. Zhou, G.-H. Gweon, J. Graf, A.V. Fedorov, C.D. Spataru, R.D. Diehl, Y. Kopelevich, D.-H. Lee, S.G. Louie, and A. Lanzara, *Nat. Phys.* 2(9) (2006), pp. 595–599.
- [124] A. Bostwick, T. Ohta, T. Seyller, K. Horn, and E. Rotenberg, *Nat. Phys.* 3(1) (2006), pp. 36–40.
- [125] A. Grüneis, C. Attacalite, T. Pichler, V. Zabolotnyy, H. Shiozawa, S. Molodtsov, D. Inosov, A. Koitzsch, M. Knupfer, J. Schiessling, R. Follath, R. Weber, P. Rudolf, L. Wirtz, and A. Rubio, *Phys. Rev. Lett.* 100(3) (2008), p. 37601.
- [126] K. Sugawara, T. Sato, S. Souma, T. Takahashi, and H. Suematsu, *Phys. Rev. Lett.* 98(3) (2007), p. 36801.
- [127] W. Kohn, *Phys. Rev. Lett.* 2 (1959), p. 393.
- [128] S.D.M. Brown, A. Jorio, P. Corio, M.S. Dresselhaus, G. Dresselhaus, R. Saito, and K. Kneipp, *Phys. Rev. B* 63(15) (2001), p. 155414.
- [129] U. Fano, *Phys. Rev.* 124(6) (1961), pp. 1866–1878.
- [130] E.H. Martins Ferreira, M.V.O. Moutinho, F. Stavale, M.M. Lucchese, R.B. Capaz, C.A. Achete, and A. Jorio, *Phys. Rev. B* 82(12) (2010), p. 125429.
- [131] A.C. Ferrari and J. Robertson, *Phys. Rev. B* 61(20) (2000), pp. 14095–14107.
- [132] R.J. Nemanich, S.A. Solin, and R.M. Martin, *Phys. Rev. B* 23(12) (1981), pp. 6348–6356.
- [133] H. Richter, Z.P. Wang, and L. Ley, *Solid State Commun.* 39(5) (1981), pp. 625–629.
- [134] I.H. Campbell and P.M. Fauchet, *Solid State Commun.* 58(10) (1986), pp. 739–741.
- [135] G.G. Samsonidze, R. Saito, A. Jorio, M.A. Pimenta, A.G. Souza Filho, A. Grüneis, G. Dresselhaus, and M.S. Dresselhaus, *J. Nanosci. Nanotechnol.* 3(6) (2003), pp. 431–458.
- [136] R. Saito, K. Sato, Y. Oyama, J. Jiang, G.G. Samsonidze, G. Dresselhaus, and M.S. Dresselhaus, *Phys. Rev. B* 71 (2005), p. 153413.
- [137] M.S. Dresselhaus, G. Dresselhaus, A.M. Rao, A. Jorio, A.G. Souza Filho, G.G. Samsonidze, and R. Saito, *Indian J. Phys.* 77B (2003), pp. 75–99.
- [138] R. Saito, J. Jiang, A. Grüneis, K. Sato, Y. Oyama, G.G. Samsonidze, S.G. Chou, G. Dresselhaus, M.S. Dresselhaus, L.G. Cançado, C. Fantini, A. Jorio, and M.A. Pimenta, *Mol. Cryst. Liquid Cryst.* 455 (2006), pp. 287–294.

- [139] J. Jiang, R. Saito, A. Grüneis, S.G. Chou, G.G. Samsonidze, A. Jorio, G. Dresselhaus, and M.S. Dresselhaus, *Phys. Rev. B* 71 (2005), pp. 45417–45419.
- [140] K. Nakada, M. Fujita, G. Dresselhaus, and M.S. Dresselhaus, *Phys. Rev. B* 54 (1996), pp. 17954–17961.
- [141] S. Reich, C. Thomsen, and J. Maultzsch, *Carbon Nanotubes, Basic Concepts and Physical Properties*, Wiley-VCH, Berlin, 2004.
- [142] E.B. Barros, A. Jorio, G.G. Samsonidze, R.B. Capaz, A.G. Souza Filho, J. Mendes Filho, G. Dresselhaus, and M.S. Dresselhaus, *Phys. Rep.* 431(6) (2006), pp. 261–302.
- [143] Y.W. Son, M.L. Cohen, and S.G. Louie, *Phys. Rev. Lett.* 97(21) (2006), p. 216803.
- [144] Y.W. Son, M.L. Cohen, and S.G. Louie, *Nature* 444(7117) (2006), pp. 347–349.
- [145] J. Maultzsch, S. Reich, and C. Thomsen, Raman scattering in carbon nanotubes revisited, *Phys. Rev. B* 65 (2002), p. 3402.
- [146] H. Telg, J. Maultzsch, S. Reich, and C. Thomsen, *Phys. Rev. B* 74(11) (2006), p. 115415.
- [147] C.D. Spataru, S. Ismail-Beigi, L.X. Benedict, and S.G. Louie, *Phys. Rev. Lett.* 92(7) (2004), p. 77402.
- [148] J. Jiang, R. Saito, G.G. Samsonidze, A. Jorio, S.G. Chou, G. Dresselhaus, and M.S. Dresselhaus, *Phys. Rev. B* 75 (2007), pp. 35407–35413.
- [149] V.G. Kravets, A.N. Grigorenko, R.R. Nair, P. Blake, S. Anissimova, K.S. Novoselov, and A.K. Geim, *Phys. Rev. B* 81(15) (2010), p. 155413.
- [150] M.Y. Sfeir, T. Beetz, F. Wang, L. Huang, X.M. Henry Huang, M. Huang, J. Hone, S. O'Brien, J.A. Misewich, T.F. Heinz, L. Wu, Y. Zhu, and L.E. Brus, *Science* 312(5773) (2006), pp. 554–556.
- [151] C. Casiraghi, A. Hartschuh, H. Qian, S. Piscanec, C. Georgi, A. Fasoli, K.S. Novoselov, D.M. Basko, and A.C. Ferrari, *Nano Lett.* 9(4) (2009), pp. 1433–1441.
- [152] M.J. O'Connell, S.M. Bachilo, C.B. Huffman, V.C. Moore, M.S. Strano, E.H. Haroz, K.L. Rialon, P.J. Boul, W.H. Noon, and C. Kittrell, *Science* 297(5581) (2002), p. 593.
- [153] S.M. Bachilo, L. Balzano, J.E. Herrera, F. Pompeo, D.E. Resasco, and R. Bruce Weisman, *J. Am. Chem. Soc.* 125(37) (2003), pp. 11186–11187.
- [154] S.G. Chou, F. Plentz, J. Jiang, R. Saito, D. Nezich, H.B. Ribeiro, A. Jorio, M.A. Pimenta, G.G. Samsonidze, and A.P. Santos, *Phys. Rev. Lett.* 94(12) (2005), p. 127402.
- [155] R.C.C. Leite and S.P.S. Porto, *Phys. Rev. Lett.* 17(1) (1966), pp. 10–12.
- [156] M. Freitag, J. Chen, J. Tersoff, J.C. Tsang, Q. Fu, J. Liu, and Ph. Avouris, *Phys. Rev. Lett.* 93(7) (2004), p. 76803.
- [157] S. Essig, C.W. Marquardt, A. Vijayaraghavan, M. Ganzhorn, S. Dehm, F. Hennrich, F. Ou, A.A. Green, C. Sciascia, F. Bonaccorso, K.-P. Bohnen, H.v. Lohneysen, M.M. Kappes, P.M. Ajayan, M.C. Hersam, A.C. Ferrari, and R. Krupke, *Nano Lett.* 10 (2010), p. 1589.
- [158] Y. Chen, R.C. Haddon, S. Fang, A.M. Rao, P.C. Eklund, W.H. Lee, E.C. Dickey, E.A. Grulke, J.C. Pendergrass, and A. Chavan, *J. Mater. Res.* 13(9) (1998), pp. 2423–2431.
- [159] U.J. Kim, C.A. Furtado, X. Liu, G. Chen, and P.C. Eklund, *J. Am. Chem. Soc.* 127(44) (2005), pp. 15437–15445.
- [160] J. Kastner, T. Pichler, H. Kuzmany, S. Curran, W. Blau, D.N. Weldon, M. Delamesiere, S. Draper, and H. Zandbergen, *Chem. Phys. Lett.* 221(1–2) (1994), pp. 53–58.
- [161] A. Gambetta, C. Manzoni, E. Menna, M. Meneghetti, G. Cerullo, G. Lanzani, S. Tretiak, A. Piryatinski, A. Saxena, and R.L. Martin, *Nat. Phys.* 2(8) (2006), pp. 515–520.
- [162] Y.-S. Lim, K.-J. Yee, J.-H. Kim, E.H. Háróz, J. Shaver, J. Kono, S.K. Doorn, R.H. Hauge, and R.E. Smalley, *Nano Lett.* 6(12) (2006), pp. 2696–2700.
- [163] K. Ishioka, M. Hase, M. Kitajima, L. Wirtz, A. Rubio, and H. Petek, *Phys. Rev. B* 77 (2008), p. 121402(R).
- [164] K. Kato, K. Ishioka, M. Kitajima, J. Tang, R. Saito, and H. Petek, *Nano Lett.* 8(10) (2008), pp. 3102–3108.
- [165] A. Jones, A. Ballestad, T. Li, M. Whitwick, J. Rottler, and T. Tiedje, *Phys. Rev. B* 79(20) (2009), pp. 205419–205434.
- [166] K.S. Krishnan and C.V. Raman, *Proc. R. Soc. Lond. Ser. A* 115(772) (1927), pp. 549–554.
- [167] M.S. Dresselhaus, G. Dresselhaus, R. Saito, and A. Jorio, *Raman Spectroscopy of Carbon Nanotubes*, Vol. 409, Elsevier, the Netherlands, 2005.
- [168] J. Klett, R. Hardy, E. Romine, C. Walls, and T. Burchell, *Carbon* 38(7) (2000), pp. 953–973.

- [169] A.C. Ferrari and J. Robertson, *Phil. Trans. R. Soc. Lond. A* 362 (2004), pp. 2477–2512.
- [170] L.G. Cançado, M.A. Pimenta, B.R.A. Neves, M.S.S. Dantas, and A. Jorio, *Phys. Rev. Lett.* 93, 247401 (2004).
- [171] A. Jorio, A.G. Souza Filho, G. Dresselhaus, M.S. Dresselhaus, A. Swan, M. Ünlü, B. Goldberg, M.A. Pimenta, J. Hafner, C.M. Lieber, and R. Saito, *Phys. Rev. B* 65(15) (2002), p. 155412.
- [172] A.C. Ferrari and J. Robertson, *Phys. Rev. B* 64(7) (2001), p. 75414.
- [173] M.J. Pelletier, *Analytical Applications of Raman Spectroscopy*, Wiley-Blackwell, Oxford, UK, 1999, p. 478.
- [174] M.A. Pimenta, G. Dresselhaus, M.S. Dresselhaus, L.G. Cancado, A. Jorio, and R. Saito, *Phys. Chem. Chem. Phys.* 9(11) (2007), pp. 1276–1290.
- [175] C. Fantini, A. Jorio, M. Souza, M.S. Strano, M.S. Dresselhaus, and M.A. Pimenta, *Phys. Rev. Lett.* 93(14) (2004), p. 147406.
- [176] Y. Kumazawa, H. Kataura, Y. Maniwa, I. Umezumi, S. Suzuki, Y. Ohtsuka, and Y. Achiba, *Synth. Met.* 103(1–3) (1999), pp. 2555–2558.
- [177] R. Saito, G. Dresselhaus, and M.S. Dresselhaus, *Phys. Rev. B* 61 (2000), pp. 2981–2990.
- [178] A.M. Rao, P.C. Eklund, S. Bandow, A. Thess, and R.E. Smalley, *Nature* 388(6639) (1997), pp. 257–259.
- [179] K. Kneipp, H. Kneipp, P. Corio, S. Brown, K. Shafer, J. Motz, L. Perelman, E. Hanlon, A. Marucci, G. Dresselhaus, and M.S. Dresselhaus, *Phys. Rev. Lett.* 84(15) (2000), pp. 3470–3473.
- [180] P. Corio, S.D.M. Brown, A. Marucci, M.A. Pimenta, K. Kneipp, G. Dresselhaus, and M.S. Dresselhaus, *Phys. Rev. B* 61(19) (2000), pp. 13202–13211.
- [181] S. Lefrant, *Curr. Appl. Phys.* 2(6) (2002), pp. 479–482.
- [182] K. Kneipp, A. Jorio, H. Kneipp, S. Brown, K. Shafer, J. Motz, R. Saito, G. Dresselhaus, and M.S. Dresselhaus, *Phys. Rev. B* 63(8) (2001), p. 81401.
- [183] G. Goncalves, P.A.A.P. Marques, C.M. Granadeiro, H.I.S. Nogueira, M.K. Singh, and J. Gracio, *Chem. Mater.* 21(20) (2009), pp. 4796–4802.
- [184] L. Gao, W. Ren, B. Liu, R. Saito, Z.-S. Wu, S. Li, C. Jiang, F. Li, and H.-M. Cheng, *ACS Nano* 3(4) (2009), pp. 933–9.
- [185] X. Ling, L. Xie, Y. Fang, H. Xu, H. Zhang, J. Kong, M.S. Dresselhaus, J. Zhang, and Z. Liu, *Nano Lett.* 10(2) (2010), pp. 553–561.
- [186] F. Schedin, E. Lidorikis, A. Lombardo, V.G. Kravetsand, A.K. Geim, A.N. Grigorenko, K.S. Novoselov, and A.C. Ferrari, *ACS Nano* 4 (2010), p. 5617.
- [187] W. Ren, R. Saito, L. Gao, F. Zheng, Z. Wu, B. Liu, M. Furukawa, J. Zhao, Z. Chen, and H.-M. Cheng, *Phys. Rev. B* 81(3) (2010), p. 35412.
- [188] A. Hartschuh, H.N. Pedrosa, L. Novotny, and T.D. Krauss, *Science* 301(5638) (2003), p. 1354.
- [189] K. Ikeda and K. Uosaki, *Nano Lett.* 9(4) (2009), pp. 1378–1381.
- [190] A. Zumbusch, G.R. Holtom, and X. Sunney Xie, *Phys. Rev. Lett.* 82(20) (1999), pp. 4142–4145.
- [191] A. Das, B. Chakraborty, S. Piscanec, S. Pisana, A.K. Sood, and A.C. Ferrari, *Phys. Rev. B* 79(15) (2009), p. 155417.
- [192] L.M. Malard, D.C. Elias, E.S. Alves, and M.A. Pimenta, *Phys. Rev. Lett.* 101(25) (2008), p. 257401.
- [193] S. Piscanec, M. Lazzeri, J. Robertson, A.C. Ferrari, and F. Mauri, *Phys. Rev. B* 75(3) (2007), p. 35427.
- [194] S. Piscanec, M. Lazzeri, F. Mauri, A.C. Ferrari, and J. Robertson, *Phys. Rev. Lett.* 93(18) (2004), p. 185503.
- [195] A. Das, S. Pisana, B. Chakraborty, S. Piscanec, S.K. Saha, U.V. Waghmare, K.S. Novoselov, H.R. Krishnamurthy, A.K. Geim, and A.C. Ferrari, *Nature Nanotechnology*, 3, 210–215, (2008).
- [196] K. Sasaki, R. Saito, G. Dresselhaus, M.S. Dresselhaus, H. Farhat, and J. Kong, *Phys. Rev. B* 77 (2008), p. 245441.
- [197] M. Lazzeri and F. Mauri, *Phys. Rev. Lett.* 97(26) (2006), p. 266407.
- [198] K. Ishikawa and T. Ando, *J. Phys. Soc. Jpn.* 75(8) (2006), p. 84713.
- [199] V.N. Popov and P. Lambin, *Phys. Rev. B* 73(8) (2006), p. 854635607.
- [200] J. Yan, E.A. Henriksen, P. Kim, and A. Pinczuk, *Phys. Rev. Lett.* 101(13) (2008), p. 136804.
- [201] H. Farhat, H. Son, G. Samsonidze, S. Reich, M.S. Dresselhaus, and J. Kong, *Phys. Rev. Lett.* 99(14) (2007), p. 145506.

- [202] M. Kalbac, L. Kavan, H. Farhat, J. Kong, and M.S. Dresselhaus, *J. Phys. Chem. C* 113(5) (2009), pp. 1751–1757.
- [203] M. Kalbac, H. Farhat, L. Kavan, J. Kong, K. Sasaki, R. Saito, and M.S. Dresselhaus, *ACS Nano* 3 (2009), pp. 2320–2328.
- [204] H. Farhat, K. Sasaki, M. Kalbac, M. Hofmann, R. Saito, M.S. Dresselhaus, and J. Kong, *Phys. Rev. Lett.* 102(12) (2009), pp. 268041–4.
- [205] K. Sasaki, H. Farhat, R. Saito, and M.S. Dresselhaus, *Phys. E* 42(8) (2010), pp. 2005–2015.
- [206] H. Farhat, S. Berciaud, M. Kalbac, R. Saito, T. Heinz, M.S. Dresselhaus, and J. Kong, unpublished.
- [207] A.V. Baranov, A.N. Bekhterev, Y.S. Bobovich, and V.I. Petrov, *Opt. Spectrosc.* 62 (1987), pp. 612–616.
- [208] J. Maultzsch, S. Reich, and C. Thomsen, *Phys. Rev. B* 70(15) (2004), p. 155403.
- [209] R. Saito, A. Grüneis, G.G. Samsonidze, V.W. Brar, G. Dresselhaus, M.S. Dresselhaus, A. Jorio, L.G. Cançado, C. Fantini, and M.A. Pimenta, *New J. Phys.* 5 (2003), p. 157.
- [210] R. Saito, A. Jorio, A.G. Souza Filho, G. Dresselhaus, M.S. Dresselhaus, and M. Pimenta, *Phys. Rev. Lett.* 88(2) (2001), p. 27401.
- [211] R. Saito, A. Grüneis, L.G. Cançado, M.A. Pimenta, A. Jorio, A.G. Souza Filho, M.S. Dresselhaus, and G. Dresselhaus, *Mol. Cryst. Liq. Cryst.* 387 (2002), pp. 287–296.
- [212] I. Pócsik, M. Hundhausen, M. Koósa, and L. Ley, *J. Non-Cryst. Solids* 227–230 (1998), pp. 1083–1086.
- [213] D. Mafra, G. Samsonidze, L. Malard, D. Elias, J. Brant, F. Plentz, E. Alves, and M. Pimenta, *Phys. Rev. B* 76(23) (2007) 233407.
- [214] R. Vidano and D.B. Fischbach, *J. Am. Ceram. Soc.* 61(1–2) (1978), pp. 13–17.
- [215] R.P. Vidano and L.J. Fischbach, *Solid State Commun.* 39(2) (1981), pp. 341–344.
- [216] L.G. Cançado, M.A. Pimenta, R. Saito, A. Jorio, L.O. Ladeira, A. Grueneis, A.G. Souza-Filho, G. Dresselhaus, and M.S. Dresselhaus, *Phys. Rev. B* 66(3) (2002), p. 35415.
- [217] J. Zimmermann, P. Pavone, and G. Cuniberti, *Phys. Rev. B* 78(4) (2008), p. 45410.
- [218] M. Lazzeri, C. Attacalite, L. Wirtz, and F. Mauri, *Phys. Rev. B* 78(8) (2008), p. 81406.
- [219] D.M. Basko, *Phys. Rev. B* 78(11) (2008), p. 115432.
- [220] D.M. Basko, S. Piscanec, and A.C. Ferrari, *Phys. Rev. B* 80(16) (2009), p. 165413.
- [221] T. Shimada, T. Sugai, C. Fantini, M. Souza, L.G. Cançado, A. Jorio, M.A. Pimenta, R. Saito, A. Grüneis, and G. Dresselhaus, *Carbon* 43(5) (2005), pp. 1049–1054.
- [222] M.A. Pimenta, E.B. Hanlon, A. Marucci, P. Corio, S.D.M. Brown, S.A. Empedocles, M.G. Bawendi, G. Dresselhaus, and M.S. Dresselhaus, *Brazilian J. Phys.* 30(2) (2000), pp. 423–427.
- [223] R.J. Nemanich and S.A. Solin, *Phys. Rev. B* 20(2) (1979), pp. 392–401.
- [224] P.H. Tan, Y.M. Deng, and Q. Zhao, *Phys. Rev. B* 58(9) (1998), pp. 5435–5439.
- [225] E.F. Atunes, A.O. Lobo, E.J. Corat, V.J. Trava-Airoldi, A.A. Martin, and C. Verissimo, *Carbon* 44(11) (2006), pp. 2202–2211.
- [226] P.H. Tan, C.Y. Hu, J. Dong, W.C. Shen, and B.F. Zhang, *Phys. Rev. B* 64(21) (2001), p. 214301.
- [227] V.W. Brar, G.G. Samsonidze, M.S. Dresselhaus, G. Dresselhaus, R. Saito, A. Swan, M. Ünlü, B. Goldberg, A.G. Souza Filho, and A. Jorio, *Phys. Rev. B* 66(15) (2002), p. 155418.
- [228] M. Pimenta, A. Marucci, S. Empedocles, M. Bawendi, E. Hanlon, A. Rao, P. Eklund, R. Smalley, G. Dresselhaus, and M.S. Dresselhaus, *Phys. Rev. B* 58(24) (1998), pp. R16016–R16019.
- [229] P.T. Araujo, A. Jorio, M.S. Dresselhaus, K. Sato, and R. Saito, *Phys. Rev. Lett.* 103(14) (2009), p. 146802.
- [230] P.T. Araujo, P.B.C. Pesce, M.S. Dresselhaus, K. Sato, R. Saito, and A. Jorio, *Phys. E* 42 (2010), pp. 1251–1261.
- [231] Y. Miyauchi, R. Saito, K. Sato, Y. Ohno, S. Iwasaki, T. Mizutani, J. Jiang, and S. Maruyama, *Chem. Phys. Lett.* 442(4–6) (2007), pp. 394–399.
- [232] A.R.T. Nugraha, R. Saito, K. Sato, P.T. Araujo, A. Jorio, and M.S. Dresselhaus, *Appl. Phys. Lett.* 97(9) (2010), p. 91905.
- [233] K. Sato, R. Saito, Y. Oyama, J. Jing, L.G. Cancado, M.A. Pimenta, A. Jorio, G.G. Samsonidze, G. Dresselhaus, and M.S. Dresselhaus, *Chem. Phys. Lett.* 427(1–3) (2006), pp. 117–121.
- [234] S. Uryu and T. Ando, *Phys. Semicond. B* 893 (2007), pp. 1033–1034.
- [235] R.A. Jishi, L. Venkataraman, M.S. Dresselhaus, and G. Dresselhaus, *Chem. Phys. Lett.* 209 (1993), pp. 77–82.

- [236] R. Nicklow, N. Wakabayashi, and H.G. Smith, *Phys. Rev. B* 5(12) (1972), pp. 4951–4962.
- [237] J.L. Wilkes, R.E. Palmer, and R.F. Willis, *J. Electron Spectrosc. Rel. Phenom.* 44(1) (1987), pp. 355–360.
- [238] T. Aizawa, R. Souda, S. Otani, Y. Ishizawa, and C. Oshima, *Phys. Rev. B* 42(18) (1990), pp. 11469–11478.
- [239] R. Al-Jishi and G. Dresselhaus, *Phys. Rev. B* 26(8) (1982), pp. 4514–4522.
- [240] S. Siebentritt, R. Pues, K.-H. Rieder, and A.M. Shikin, *Phys. Rev. B* 55(12) (1997), pp. 7927–7934.
- [241] C. Mapelli, C. Castiglioni, G. Zerbi, and K. Müllen, *Phys. Rev. B* 60(18) (1999), pp. 12710–12725.
- [242] C.D. Spataru, S. Ismail-Beigi, L.X. Benedict, and S.G. Louie, *Appl. Phys. A Mater. Sci. Process.* 78(8) (2004), pp. 1129–1136.
- [243] R. Saito, A. Jorio, J. Jiang, K. Sasaki, G. Dresselhaus, and M.S. Dresselhaus, *Optical Properties of Carbon Nanotubes and Nanographene*, Oxford University Press, Oxford, UK, 2010.
- [244] A. Grüneis, J. Serrano, A. Bosak, M. Lazzeri, S.L. Molodtsov, L. Wirtz, C. Attaccalite, M. Krisch, A. Rubio, F. Mauri, and T. Pichler, *Phys. Rev. B* 80(8) (2009), p. 85423.
- [245] M. Furukawa, Thesis. Master's Thesis, Tohoku University, 2010.
- [246] K. Sasaki, M. Yamamoto, S. Murakami, R. Saito, M.S. Dresselhaus, K. Takai, T. Mori, T. Enoki, and K. Wakabayashi, *Phys. Rev. B* 80(15) 155450 (2009).
- [247] N. Mounet and N. Marzari, *Phys. Rev. B* 71(20) (2005), p. 205214.
- [248] D. Sanchez-Portal, E. Artacho, J.M. Solar, A. Rubio, and P. Ordejon, *Phys. Rev. B* 59 (1999), pp. 12678–12688.
- [249] O. Dubay and G. Kresse, *Phys. Rev. B* 67(3) (2003), p. 35401.
- [250] J.-C. Charlier, P. Eklund, J. Zhu, and A.C. Ferrari, *Electron and phonon properties of graphene: their relationship with carbon nanotubes*, Vol. 111, Springer Series on Topics in Applied Physics, Springer, Berlin, 2008, pp. 625–680.
- [251] P.H. Tan, L. An, L.Q. Liu, Z.X. Guo, R. Czerw, D.L. Carroll, P.M. Ajayan, N. Zhang, and H.L. Guo, *Phys. Rev. B* 66(24) (2002), p. 245410.
- [252] J. Hone, *Phonons and Thermal Properties of Carbon Nanotubes*, Vol. 80, Springer, Berlin, 2001, pp. 273–286.
- [253] D. Porezag, Th. Frauenheim, Th. Köhler, G. Seifert, and R. Kaschner, *Phys. Rev. B* 51(19) (1995), pp. 12947–12957.
- [254] G.G. Samsonidze, R. Saito, N. Kobayashi, A. Grüneis, J. Jiang, A. Jorio, S.G. Chou, G. Dresselhaus, and M.S. Dresselhaus, *Appl. Phys. Lett.* 85 (2004), pp. 5703–5705.
- [255] A. Grüneis, C. Attaccalite, L. Wirtz, H. Shiozawa, R. Saito, T. Pichler, and A. Rubio, *Phys. Rev. B* 78(20) (2008), p. 205425.
- [256] S. Reich, J. Maultzsch, C. Thomsen, and P. Ordejón, *Phys. Rev. B* 66(3) (2002), p. 35412.
- [257] J. Slonczewski and P. Weiss, *Phys. Rev.* 109(2) (1958), pp. 272–279.
- [258] M. Koshino and T. Ando, *Phys. Rev. B* 77(11) (2008), p. 115313.
- [259] J.C. Slater and G.F. Koster, *Phys. Rev.* 94(6) (1954), pp. 1498–1524.
- [260] J.J.P. Stewart, *MOPAC93.00*, Fujitsu Limited, Tokyo, Japan, 1993.
- [261] M.J. Frisch, G.W. Trucks, H.B. Schlegel, G.E. Scuseria, M.A. Robb, J.R. Cheeseman, G. Scalmani, V. Barone, B. Mennucci, G.A. Petersson, H. Nakatsuji, M. Caricato, X. Li, H.P. Hratchian, A.F. Izmaylov, J. Bloino, G. Zheng, and D.J. Sonnenb, *Gaussian 09, Revision A.1*, Gaussian, Inc., Wallingford, CT, 2009.
- [262] A. Grüneis, R. Saito, G.G. Samsonidze, T. Kimura, M.A. Pimenta, A. Jorio, A.G. Souza Filho, G. Dresselhaus, and M.S. Dresselhaus, *Phys. Rev. B* 67(16) (2003), pp. 165402–165407.
- [263] Y. Oyama, R. Saito, K. Sato, J. Jiang, G.G. Samsonidze, A. Grüneis, Y. Miyauchi, S. Maruyama, A. Jorio, G. Dresselhaus, and M.S. Dresselhaus, *Carbon* 44(5) (2006), pp. 873–879.
- [264] R. Saito, A. Grüneis, G.G. Samsonidze, G. Dresselhaus, M.S. Dresselhaus, A. Jorio, L.G. Cancado, M.A. Pimenta, and A.G. Souza Filho, *Appl. Phys. A* 78(8) (2004), pp. 1099–1105.
- [265] J. Jiang, R. Saito, A. Grüneis, G. Dresselhaus, and M.S. Dresselhaus, *Carbon* 42 (2004), pp. 3169–3176.
- [266] G.G. Samsonidze, E.B. Barros, R. Saito, J. Jiang, G. Dresselhaus, and M.S. Dresselhaus, *Phys. Rev. B* 75 (2007), p. 155420.

- [267] J. Jiang, R. Saito, A. Grüneis, G. Dresselhaus, and M.S. Dresselhaus, *Chem. Phys. Lett.* 392 (2004), pp. 383–389.
- [268] J. Jiang, R. Saito, G.G. Samsonidze, S.G. Chou, A. Jorio, G. Dresselhaus, and M.S. Dresselhaus, *Phys. Rev. B* 72 (2005), pp. 235408–235411.
- [269] J. Jiang, R. Saito, A. Grüneis, S. Chou, G. Samsonidze, A. Jorio, G. Dresselhaus, and M.S. Dresselhaus, *Phys. Rev. B* 71(20) (2005), p. 205420.
- [270] A. Grüneis, *Resonance Raman spectroscopy of single wall carbon nanotubes*, Ph.D. thesis, Tohoku University, Sendai, Japan, September 2004.
- [271] R. Saito and H. Kamimura, *J. Phys. Soc. Jpn.* 52(2) (1983), p. 407.
- [272] T. Ando, *J. Phys. Soc. Jpn.* 74(3) (2005), pp. 777–817.
- [273] J. Jiang, R. Saito, K. Sato, J. Park, G.G. Samsonidze, A. Jorio, G. Dresselhaus, and M.S. Dresselhaus, *Phys. Rev. B* 75(3) (2007), p. 35405.
- [274] M. Rohlffing and S.G. Louie, *Phys. Rev. B* 62(8) (2000), pp. 4927–4944.
- [275] V. Perebeinos, J. Tersoff, and P. Avouris, *Phys. Rev. Lett.* 92(25) (2004), p. 257402.
- [276] R.B. Capaz, C. Spataru, S. Ismail-Beigi, and S.G. Louie, *Phys. Rev. B* 74(12) (2006), pp. 5–8.
- [277] E.B. Barros, R.B. Capaz, A. Jorio, G.G. Samsonidze, A.G. Souza Filho, S. Ismail-Beigi, C.D. Spataru, S.G. Louie, G. Dresselhaus, and M.S. Dresselhaus, *Phys. Rev. B* 73(24) (2006), p. 241406.
- [278] J.S. Park, Y. Oyama, R. Saito, W. Izumida, J. Jiang, K. Sato, C. Fantini, A. Jorio, G. Dresselhaus, and M.S. Dresselhaus, *Phys. Rev. B* 74 (2006), p. 165414.
- [279] Z. Yu and L.E. Brus, *J. Phys. Chem. B* 105(29) (2001), pp. 6831–6837.
- [280] S. Reich, C. Thomsen, and P. Ordejón, *Phys. Rev. B*, 64, (2001) p. 195416.
- [281] P.K. Eklund, G. Dresselhaus, M.S. Dresselhaus, and J. Fischer, *Phys. Rev. B* 16(8) (1977), pp. 3330–3333.
- [282] A.W. Bushmaker, V.V. Deshpande, S. Hsieh, M.W. Bockrath, and S.B. Cronin, *Nano Lett.* 9(8) (2009), pp. 2862–2866.
- [283] Y. Wu, J. Maultzsch, E. Knoesel, B. Chandra, M. Huang, M. Sfeir, L.E. Brus, J. Hone, and T.F. Heinz, *Phys. Rev. Lett.* 99(2) (2007), p. 27402.
- [284] L.M. Malard, J. Nilsson, D.C. Elias, J.C. Brant, F. Plentz, E.S. Alves, A.H. Castro-Neto, and M.A. Pimenta, *Phys. Rev. B* 76(20) (2007), p. 201401.
- [285] N. Ferralis, R. Maboudian, and C. Carraro, *Phys. Rev. Lett.* 101(15) (2008), p. 156801.
- [286] T.M.G. Mohiuddin, A. Lombardo, R.R. Nair, A. Bonetti, G. Savini, R. Jalil, N. Bonini, D.M. Basko, C. Galiotis, N. Marzari, K.S. Novoselov, A.K. Geim, and A.C. Ferrari, *Phys. Rev. B* 79 (2009), p. 205433.
- [287] M. Huang, H. Yan, C. Chen, D. Song, T.F. Heinz, and J. Hone, Phonon softening and crystallographic orientation of strained graphene studied by Raman spectroscopy, May 2009.
- [288] S. Pisana, M. Lazzeri, C. Casiraghi, K.S. Novoselov, A.K. Geim, A.C. Ferrari, and F. Mauri, *Nat. Mater.* 6(3) (2007), pp. 198–201.
- [289] J. Yan, Y. Zhang, P. Kim, and A. Pinczuk, *Phys. Rev. Lett.* 98(16) 166802 (2007).
- [290] Y. Wang, Z. Ni, T. Yu, Z.X. Shen, H. Wang, Y. Wu, W. Chen, and A.T. Shen Wee, *J. Phys. Chem. C* 112(29) (2008), pp. 10637–10640.
- [291] C. Casiraghi, S. Pisana, K.S. Novoselov, A.K. Geim, and A.C. Ferrari, *Appl. Phys. Lett.* 91 (2007), p. 233108.
- [292] G. Compagnini, F. Giannazzo, S. Sonde, V. Raineri, and E. Rimini, *Carbon* 47(14) (2009), pp. 3201–3207.
- [293] I.O. Maciel, N. Anderson, M.A. Pimenta, A. Hartschuh, H. Qian, M. Terrones, H. Terrones, J. Campos-Delgado, A.M. Rao, L. Novotny, and A. Jorio, *Nat. Mater.* 7(11) (2008), pp. 878–883.
- [294] X. Wang, L. Zhi, and K. Müllen, *Nano Lett.* 8(1) (2008), pp. 323–327.
- [295] Z. Ni, Y. Wang, T. Yu, Y. You, and Z. Shen, *Phys. Rev. B* 77(23) (2008), p. 235403.
- [296] D.M. Basko, *Phys. Rev. B* 76(8) (2007), p. 81405.
- [297] J.S. Park, A. Reina Cecco, R. Saito, J. Jiang, G. Dresselhaus, and M.S. Dresselhaus, *Carbon* 47 (2009), pp. 1303–1310.
- [298] L.G. Cançado, A. Reina, J. Kong, and M.S. Dresselhaus, *Phys. Rev. B* 77(24) (2008), p. 245408.
- [299] P. Lespade, A. Marchand, M. Couzi, and F. Cruege, *Carbon* 22(4–5) (1984), pp. 375–385.
- [300] P. Lespade, R. Al-Jishi, and M.S. Dresselhaus, *Carbon* 20(5) (1982), pp. 427–431.
- [301] H. Wilhelm, M. Lelaurain, E. McRae, and B. Humbert, *J. Appl. Phys.* 84 (1998), p. 6552.

- [302] R.J. Nemanich and S.A. Lucovsky, *Solid State Commun.* 23(2) (1977), pp. 117–120.
- [303] L.G. Cancado, K. Takai, T. Enoki, M. Endo, Y.A. Kim, H. Mizusaki, A. Jorio, L.N. Coelho, R. Magalhaes-Paniago, and M.A. Pimenta, *Appl. Phys. Lett.* 88(16) (2006), p. 163106.
- [304] P. Poncharal, A. Ayari, T. Michel, and J.L. Sauvajol, *Phys. Rev. B* 79(19) (2009), p. 195417.
- [305] A. Reina, H.B. Son, L.Y. Jiao, B. Fan, M.S. Dresselhaus, Z.F. Liu, and J. Kong, *J. Phys. Chem. C* 112(46) (2008), pp. 17741–17744.
- [306] A. Reina, S. Thiele, X. Jia, S. Bhaviripudi, M.S. Dresselhaus, J.A. Schaefer, and J. Kong, *Nano Res.* 2 (2009), pp. 509–516.
- [307] C.H. Lui, Z. Li, Z. Chen, P.V. Klimov, L.E. Brus, and T.F. Heinz, *Nano Lett.* 11(1) (2011), pp. 164–169.
- [308] M.S. Dresselhaus and R. Kalish, *Ion Implantation in Diamond, Graphite and Related Materials*, Springer Series in Materials Science, Springer, Berlin, 1992.
- [309] A. Jorio, M.M. Lucchese, F. Stavale, E.H. Martins Ferreira, M.V.O. Moutinho, R.B. Capaz, and C.A. Achete, *J. Phys.: Condens. Matter* 22(33) (2010), p. 334204.
- [310] A. Grüneis, R. Saito, T. Kimura, L.G. Cançado, M.A. Pimenta, A. Jorio, A.G. Souza Filho, G. Dresselhaus, and M.S. Dresselhaus, *Phys. Rev. B* 65(15) (2002), pp. 155405–155407.
- [311] A.K. Gupta, T.J. Russin, H.R. Gutierrez, and P.C. Eklund, *ACS Nano* 3 (2009), pp. 45–52.
- [312] B. Krauss, P. Nemes-Incze, V. Skakalova, L.P. Biro, K. von Klitzing, and J.H. Smet, *Nano Lett.* (11)(10) (2010), pp. 4544–4548.
- [313] M.S. Dresselhaus, G. Dresselhaus, and A. Jorio, *J. Phys. Chem. C* 111 (2007), pp. 17887–17893.
- [314] P.T. Araujo, I.O. Maciel, P.B.C. Pesce, M.A. Pimenta, S.K. Doorn, H. Qian, A. Hartschuh, M. Steiner, L. Grigorian, and K. Hata, *Phys. Rev. B* 77(24) (2008), p. 241403.
- [315] G.D. Mahan, *Phys. Rev. B* 65(23) (2002), p. 235402.
- [316] K. Hata, D.N. Futaba, K. Mizuno, T. Namai, M. Yumura, and S. Iijima, *Science* 306(5700) (2004), p. 1362.
- [317] S.M. Bachilo, M.S. Strano, C. Kittrell, R.H. Hauge, R.E. Smalley, and R.B. Weisman, *Science* 298(5602) (2002), p. 2361.
- [318] M.S. Strano, *J. Am. Chem. Soc.* 125(51) (2003), pp. 16148–16153.
- [319] S.K. Doorn, D.A. Heller, P.W. Barone, M.L. Usrey, and M.S. Strano, *Appl. Phys. A* 78(8) (2004), pp. 1147–1155.
- [320] T. Michel, M. Paillet, P. Poncharal, A. Zahab, J.-L. Sauvajol, J.C. Meyer, and S. Roth, *Carbon Nanotubes* 222(II) (2006), pp. 121–122.
- [321] P.T. Araujo, S.K. Doorn, S. Kilina, S. Tretiak, E. Einarsson, S. Maruyama, H. Chacham, M.A. Pimenta, and A. Jorio, *Phys. Rev. Lett.* 98(6) (2007), p. 67401.
- [322] P.T. Araujo, C. Fantini, M.M. Lucchese, M.S. Dresselhaus, and A. Jorio, *Appl. Phys. Lett.* 95(26) (2009), p. 261902.
- [323] J.S. Soares, L.G. Cançado, E.B. Barros, and A. Jorio, *Phys. Stat. Solidi B* 247(11–12) (2010), pp. 2835–2837.
- [324] J.S. Soares, A.P.M. Barboza, P.T. Araujo, N.M. Barbosa Neto, D. Nakabayashi, N. Shadmi, T.S. Yarden, A. Ismach, N. Geblinger, E. Joselevich, C. Vilani, L.G. Cancado, L. Novotny, G. Dresselhaus, M.S. Dresselhaus, B.R.A. Neves, M.S.C. Mazzoni, and A. Jorio, *Nano Lett.* 10(12) (2010), pp. 5043–5048.
- [325] R. Pfeiffer, C. Kramberger, F. Simon, H. Kuzmany, V.N. Popov, and H. Kataura, *Eur. Phys. J. B* 42(3) (2004), pp. 345–350.
- [326] R. Pfeiffer, F. Simon, H. Kuzmany, and V.N. Popov, *Phys. Rev. B* 72(16) (2005), p. 161404.
- [327] R. Pfeiffer, F. Simon, H. Kuzmany, V.N. Popov, V. Zolyomi, and J. Kurti, *Phys. Stat. Solidi B* 243(13) (2006), pp. 3268–3272.
- [328] R. Pfeiffer, H. Peterlik, H. Kuzmany, F. Simon, K. Pressl, P. Knoll, M.H. Rummeli, H. Shiozawa, H. Muramatsu, Y.A. Kim, T. Hayashi, and M. Endo, *Phys. Stat. Solidi B* 245(10) (2008), pp. 1943–1946.
- [329] H. Kuzmany, W. Plank, R. Pfeiffer, and F. Simon, *J. Raman Spectrosc.* 39(2) (2008), pp. 134–140.
- [330] F. Villalpando-Paez, H. Muramatsu, Y.A. Kim, H. Farhat, M. Endo, M. Terrones, and M.S. Dresselhaus, *Nanoscale* 2(3) (2010), pp. 406–411.
- [331] F. Villalpando-Paez, H. Son, D. Nezich, Y.P. Hsieh, J. Kong, Y.A. Kim, D. Shimamoto, H. Muramatsu, T. Hayashi, M. Endo, M. Terrones, and M.S. Dresselhaus, *Nano Lett.* 8 (2008), pp. 3879–3886.

- [332] X. Zhao, Y. Ando, L.-C. Qin, H. Kataura, Y. Maniwa, and R. Saito, *Chem. Phys. Lett.* 361(1–2) (2002), pp. 169–174.
- [333] M.S. Dresselhaus and P.C. Eklund, *Adv. Phys.* 49 (2000), pp. 705–814.
- [334] S.D.M. Brown, P. Corio, A. Marucci, M.S. Dresselhaus, M.A. Pimenta, and K. Kneipp, *Phys. Rev. B* 61(8) (2000), pp. 5137–5140.
- [335] P.T. Araujo and A. Jorio, *Phys. Stat. Solidi B* 245(10) (2008), pp. 2201–2204.
- [336] G.S. Duesberg, W.J. Blau, H.J. Byrne, J. Muster, M. Burghard, and S. Roth, *Chem. Phys. Lett.* 310(1–2) (1999), pp. 8–14.
- [337] J. Azoulay, A. Débarre, A. Richard, and P. Tchénio, *J. Phys. IV* 10(8) (2000), pp. 8–223.
- [338] A. Jorio, A.G. Souza Filho, G. Dresselhaus, M.S. Dresselhaus, R. Saito, J. Hafner, C. Lieber, F. Matinaga, M. Dantas, and M.A. Pimenta, *Phys. Rev. B* 63(24) (2001), p. 245416.
- [339] J.H. Hafner, C.L. Cheung, T.H. Oosterkamp, and C.M. Lieber, *J. Phys. Chem. B* 105(4) (2001), pp. 743–746.
- [340] A. Jorio, C. Fantini, M.S.S. Dantas, M.A. Pimenta, A.G. Souza Filho, G.G. Samsonidze, V.W. Brar, G. Dresselhaus, M.S. Dresselhaus, A. Swan, M. Ünlü, B. Goldberg, and R. Saito, *Phys. Rev. B* 66(11) (2002), p. 115411.
- [341] A.G. Souza Filho, A. Jorio, J. Hafner, C. Lieber, R. Saito, M. Pimenta, G. Dresselhaus, and M.S. Dresselhaus, *Phys. Rev. B* 63(24) (2001), p. 241404R.
- [342] K. Sato, R. Saito, J. Jiang, G. Dresselhaus, and M.S. Dresselhaus, *Phys. Rev. B* 76 (2007), p. 195446.
- [343] K. Sato, R. Saito, J. Jiang, G. Dresselhaus, and M.S. Dresselhaus, *Vib. Spectrosc.* 45(2) (2007), pp. 89–94.
- [344] P.B.C. Pesce, P.T. Araujo, P. Nikolaev, S.K. Doorn, K. Hata, R. Saito, M.S. Dresselhaus, and A. Jorio, *Appl. Phys. Lett.* 96 (2010), p. 51910.
- [345] S. Doorn, P. Araujo, K. Hata, and A. Jorio, *Phys. Rev. B*, 78, 165408. (2008).
- [346] V.N. Popov, *New J. Phys.* 6 (2004), p. 17.
- [347] S. Maruyama, R. Kojima, Y. Miyauchi, S. Chiashi, and M. Kohno, *Chem. Phys. Lett.* 360(3–4) (2002), pp. 229–234.
- [348] P. Nikolaev, M.J. Bronikowski, R.K. Bradley, F. Rohmund, D.T. Colbert, K.A. Smith, and R.E. Smalley, *Chem. Phys. Lett.* 313(1–2) (1999), pp. 91–97.
- [349] T. Ando, *J. Phys. Soc. Jpn.* 79(2) (2010), p. 4706.
- [350] M.S. Dresselhaus, G. Dresselhaus, A. Jorio, A.G. Souza Filho, and R. Saito, *Carbon* 40(12) (2002), pp. 2043–2061.
- [351] A. Jorio, G. Dresselhaus, M.S. Dresselhaus, M. Souza, M.S.S. Dantas, M.A. Pimenta, A.M. Rao, R. Saito, C. Liu, and H.M. Cheng, *Phys. Rev. Lett.* 85(12) (2000), pp. 2617–2620.
- [352] A. Jorio, M.A. Pimenta, A.G. Souza Filho, G.G. Samsonidze, A.K. Swan, M.S. Ünlü, B.B. Goldberg, R. Saito, G. Dresselhaus, and M.S. Dresselhaus, *Phys. Rev. Lett.* 90(10) (2003), p. 107403.
- [353] H. Ajiki and T. Ando, *Phys. B: Condens. Matter* 201 (1994), pp. 349–352.
- [354] A.G. Marinopoulos, L. Reining, A. Rubio, and N. Vast, *Phys. Rev. Lett.* 91(4) (2003), p. 46402.
- [355] G.S. Duesberg, I. Loa, M. Burghard, K. Syassen, and S. Roth, *Phys. Rev. Lett.* 85(25) (2000), pp. 5436–5439.
- [356] J. Hwang, H.H. Gommans, A. Ugawa, and H. Tashiro, *Phys. Rev. B* 62 (2000), pp. R13310–R13313.
- [357] A. Jorio, A.G. Souza Filho, V. Brar, A. Swan, M. Ünlü, B. Goldberg, A. Righi, J. Hafner, C.M. Lieber, R. Saito, G. Dresselhaus, and M.S. Dresselhaus, *Phys. Rev. B* 65(12) (2002), p. R121402.
- [358] A. Rao, A. Jorio, M.A. Pimenta, M. Dantas, R. Saito, G. Dresselhaus, and M.S. Dresselhaus, *Phys. Rev. Lett.* 84(8) (2000), pp. 1820–1823.
- [359] C. Thomsen, S. Reich, P.M. Rafailov, and H. Jantoliak, *Phys. Stat. Solidi B* 214 (1999), pp. 15–16.
- [360] M. Souza, A. Jorio, C. Fantini, B.R.A. Neves, M.A. Pimenta, R. Saito, A. Ismach, E. Joselevich, V.W. Brar, G.G. Samsonidze, G. Dresselhaus, and M.S. Dresselhaus, *Phys. Rev. B* 69(24) (2004), p. R15424 1–4.
- [361] P. Corio, A. Jorio, N. Dimer, and M.S. Dresselhaus, *Chem. Phys. Lett.* 392 (2004), pp. 396–402.
- [362] L. Kavan, L. Dunsch, H. Kataura, A. Oshiyama, M. Otani, and S. Okada, *J. Phys. Chem. B* 107(31) (2003), pp. 7666–7675.

- [363] A.W. Bushmaker, V.V. Deshpande, S. Hsieh, M.W. Bockrath, and S.B. Cronin, *Nano Lett.* 9(2) (2009), pp. 607–611.
- [364] R. Saito, A. Jorio, J. Hafner, C.M. Lieber, M. Hunter, T. McClure, G. Dresselhaus, and M.S. Dresselhaus, *Phys. Rev. B* 64(8) (2001), pp. 85312–85319.
- [365] K. Sasaki, R. Saito, G. Dresselhaus, M.S. Dresselhaus, H. Farhat, and J. Kong, *Phys. Rev. B* 78 (2008), pp. 235405–235411.
- [366] J.C. Tsang, M. Freitag, V. Perebeinos, J. Liu, and P. Avouris, *Nat. Nanotechnol.* 2(11) (2007), pp. 725–730.
- [367] A.G. Souza-Filho, A. Jorio, G.G. Samsonidze, G. Dresselhaus, R. Saito, and M.S. Dresselhaus, *Nanotechnology* 14 (2003), pp. 1130–1139.
- [368] N. Geblinger, A. Ismach, and E. Joselevich, *Nat. Nanotechnol.* 3(4) (2008), pp. 195–200.
- [369] A. Jorio, C. Fantini, M.A. Pimenta, R.B. Capaz, G.G. Samsonidze, G. Dresselhaus, M.S. Dresselhaus, J. Jiang, N. Kobayashi, and A. Grüneis, *Phys. Rev. B* 71(7) (2005), p. 75401.
- [370] J. Kürti, V. Zólyomi, M. Kertesz, and G.Y. Sun, *New J. Phys.* 5 (2003), p. 125.
- [371] C. Fantini, A. Jorio, M. Souza, and L.O. Ladeira, *Phys. Rev. Lett.* 93 (2004), p. 87401.
- [372] C. Fantini, A. Jorio, M. Souza, R. Saito, G.G. Samsonidze, M.S. Dresselhaus, and M.A. Pimenta, in *Proceedings of the XVIII International Winter School on the Electronic Properties of Novel Materials*, H. Kuzmany, J. Fink, M. Mehring, and S. Roth, eds., Vol. 786, pp. 178–181, American Institute of Physics, Woodbury, NY, 2005.
- [373] R. Saito, T. Takeya, T. Kimura, G. Dresselhaus, and M.S. Dresselhaus, *Phys. Rev. B* 59(3) (1999), pp. 2388–2392.
- [374] S.G. Chou, H. Son, M. Zheng, R. Saito, A. Jorio, G. Dresselhaus, and M.S. Dresselhaus, *Chem. Phys. Lett.* 443(4–6) (2007), pp. 328–332.
- [375] A.G. Souza Filho, A. Jorio, A.K. Swan, M.S. Ünlü, B.B. Goldberg, R. Saito, J. Hafner, C.M. Lieber, M.A. Pimenta, G. Dresselhaus, and M.S. Dresselhaus, *Phys. Rev. B* 65(8) (2002), p. 85417.
- [376] A.G. Souza Filho, A. Jorio, G. Dresselhaus, M.S. Dresselhaus, R. Saito, A.K. Swan, M.S. Ünlü, B.B. Goldberg, J.H. Hafner, C.M. Lieber, and M.A. Pimenta, *Phys. Rev. B* 65(3) (2001), p. 35404.
- [377] A.G. Souza-Filho, A. Jorio, G.G. Samsonidze, G. Dresselhaus, M.A. Pimenta, M.S. Dresselhaus, A.K. Swan, M.S. Ünlü, B.B. Goldberg, and R. Saito, *Phys. Rev. B* 67 (2003), p. 035427-1–7.
- [378] G.G. Samsonidze, R. Saito, A. Jorio, A.G. Souza-Filho, A. Grüneis, M.A. Pimenta, G. Dresselhaus, and M.S. Dresselhaus, *Phys. Rev. Lett.* 90 (2003), p. 27403.
- [379] A.G. Souza Filho, A. Jorio, G.G. Samsonidze, G. Dresselhaus, M.S. Dresselhaus, A.K. Swan, M. Ünlü, B.B. Goldberg, R. Saito, and J.H. Hafner, *Chem. Phys. Lett.* 354(1–2) (2002), pp. 62–68.
- [380] R. Saito, A. Jorio, A.G. Souza Filho, G. Dresselhaus, M.S. Dresselhaus, A. Grüneis, L.G. Cançado, and M.A. Pimenta, *Jpn. J. Appl. Phys.* 41(Part 1, No. 7B) (2002), pp. 4878–4882.
- [381] L. Novotny and B. Hecht, *Principles of Nanooptics*, Cambridge University Press, 2006, p. 558.
- [382] A. Hartschuh, E.J. Sánchez, X.S. Xie, and L. Novotny, *Phys. Rev. Lett.* 90(9) (2003), p. 95503.
- [383] I.O. Maciel, M.A. Pimenta, M. Terrones, H. Terrones, J. Campos-Delgado, and A. Jorio, *Phys. Stat. Solidi B* 245(10) (2008), pp. 2197–2200.
- [384] I.O. Maciel, J. Campos-Delgado, E. Cruz-Silva, M.A. Pimenta, B.G. Sumpter, V. Meunier, F. López-Urias, E. Muñoz-Sandoval, H. Terrones, M. Terrones, and A. Jorio *Nano Lett.* 9(6) (2009), pp. 2267–2272.
- [385] I.O. Maciel, J. Campos-Delgado, M.A. Pimenta, M. Terrones, H. Terrones, A.M. Rao, and A. Jorio, *Phys. Stat. Solidi B* 246(11–12) (2009), pp. 2432–2435.
- [386] C. Georgi and A. Hartschuh, *Appl. Phys. Lett.* 97(14) (2010), p. 143117.
- [387] H. Qian, C. Georgi, N. Anderson, A.A. Green, M.C. Hersam, L. Novotny, and A. Hartschuh, *Nano Lett.* 8(5) (2008), pp. 1363–1367.
- [388] N. Anderson, A. Hartschuh, and L. Novotny, *Nano Lett.* 7(3) (2007), pp. 577–582.
- [389] L.G. Cançado, A. Hartschuh, and L. Novotny, *J. Raman Spectrosc.* 40(10) (2009), pp. 1420–1426.
- [390] C.H. Park, L. Yang, Y.W. Son, M.L. Cohen, and S.G. Louie, *Nat. Phys.* 4(3) (2008), pp. 213–217.
- [391] A. Jorio, C. Fantini, M.A. Pimenta, D.A. Heller, M.S. Strano, M.S. Dresselhaus, Y. Oyama, J. Jiang, and R. Saito, *Appl. Phys. Lett.* 88(2) (2009), p. 23109.
- [392] Y.-M. Lin, C. Dimitrakopoulos, K.A. Jenkins, D.B. Farmer, H.-Y. Chiu, A. Grill, and Ph. Avouris, *Science* 327(5966) (2010), p. 662.